University of Alberta

Surface and Borehole Seismic Images at the International Continental Drilling Program Outokumpu Borehole: Implications for Reflectivity of the Crystalline Crust

by

Xuefeng Duo

A thesis submitted to the Faculty of Graduate Studies and Research
in partial fulfillment of the requirements for the degree of

Master of Science

in

Geophysics

Department of Physics

Fall 2011
Edmonton, Alberta

Abstract

The study area, Outokumpu, is a hard rock area and it is well known for its unconventional Precambrian massive Cu-Co-Zn sulphide deposits (~1.97 Ga) which were discovered in 1910. This study was conducted to understand the seismic reflection characteristic in hard rock environment in Outokumpu, Finland. The geophysical techniques involved data processing for two 2D surface seismic lines and a vertical seismic profiling data, generating synthetic seismogram, and joint interpretation of seismic reflection. Due to the complex physical properties in hard rock area, special attention paid in data processing includes the definition of geometries, preserving the high-frequency information, noise suppression and deconvolution. These efforts provided high resolution seismic results. The subsurface structure of Outokumpu-type assemblage is observed. Moreover, there is a remarkable consistency between seismic surface results and the VSP result.

Acknowledgements

I am greatly indebted to my supervisor, Dr. Douglas Schmitt, for his help and encouragement throughout my study. And I appreciate his valuable advice and suggestions. I am also thankful to Dr. Jeff Gu for teaching me a lot about the seismology and for his technical assistance.

I am grateful to the Experimental Geophysics Group. Special thanks to Heather Schijns for so much help and patience. I also thank Oluwafemi Ogunsuyi, Helen Yam, and Oluwaseyi Idowu for their ideas and help. And I extend my thanks to Suvi Heinonen for providing me her processing data.

I acknowledge GEDCO for providing Vista™ seismic processing software and for their technical support.

Finally, I am especially grateful to my parents for their love and support. And I would also like to thank my husband for his encouragement and for always being there for me.

Table of Contents

1.0 Introduction.....1

1.1 Physical Properties and Seismic Imaging in Hard Rock Environments.....1

1.1.1 Physical Properties of Hard Rock……1

1.1.2 Seismic Imaging in Hard Rock Environment……7

1.2 Outokumpu Area Geology……12

1.3 Seismic Survey in Outokumpu……..19

1.4 The Outokumpu Scientific Drill Hole……25

1.5 Summary……32

2.0 2D Seismic Surface Survey.....34

2.1 Introduction……..……...……...35

2.2 Seismic Survey and Data Acquisition...…….……55

2.3 Data Quality.....61

2.4 Data Processing…….....67

2.4.1 Defining Geometry and Processing Flows……68

2.4.2 Trace Editing and Static……70

2.4.3 Noise Attenuation……..76

2.4.4 Amplitude Compensation……..83

2.4.5 Deconvolution……89

2.4.6 Stack Velocity Analysis……..91

2.4.7 Residual statics correction……101

2.4.8 Stack……102

2.4.9 Seismic Image Migration……105

2.5 Comparison with earlier results……111

2.6 Conclusions……118

3.0 Vertical Seismic Profiling……..……121

3.1 Introduction…….……121

3.2 Geometries and Acquisition of Vertical Seismic Profiling.……125

3.3 Data Quality Analysis…….127

3.4 Processing of VSP Data……..132

3.4.1 Trace Editing……...……132

3.4.2 First break Picking and P-wave Velocities Calculation……...133

3.4.3 Noise Attenuation ……..140

3.4.4 Wavefield Separation……..……148

3.4.5 Deconvolution……...……...154

3.4.6 Static Time Shifting.……....154

3.4.7 Corridor Stack……..…..…….……157

3.5 Conclusions.....161

4.0 Joint Interpretation of Seismic Surface and Borehole Data……**163**

4.1 Evaluation of processing…….....163

4.2 Final results…….……...…167

4.2.1 Crooked 2D Seismic Lines……..169

4.2.2 Zero-offset VSP……...……171

4.2.3 Velocity……174

4.2.4 Synthetic……..…176

4.3 Joint Interpretation.....179

4.4 Discussion.....189

4.5 Conclusions.....190

4.6 Future work.....192

References.....194

Appendix.....209

List of Tables

Table 1-1 The definition of some rock types found in Outokumpu area……16
Table 2-1 Processing sequence and parameters for 2D seismic lines……..75

List of Figures

Figure 1.1 Density of some igneous and metamorphic host rocks (from compilations of Hallenburg (1984) and Olhoeft and Johnson (1989)). Reproduced with the permission of Douglas R. Schmitt…….…….....4

Figure 1.2 Intrinsic compressional and shear wave velocities of common igneous and metamorphic rocks; summary values from compilations in Schon (1996). Reproduced with the permission of Douglas R. Schmitt……5

Figure 1.3 P-wave velocities versus densities of some base metal ore minerals. F = felsic; M = mafic; SED = sediments, including carbonates (c); SERP = serpentinite; UM, ultramafic. Dashed lines represent the constant impedance (Z); bar shows minimum impedance contrast (about 2.5) required to give strong reflections (R = 0.06). Figure was reprinted with authorization under the Fair Use Permission of SEG……..……6

Figure 1.4 Geographic location of Outokumpu, Finland. Reproduced with the permission of GTK……..…….……...13

Figure 1.5 Geological map of Outokumpu area. Figure was reprinted with authorization under the Non-Commercial Reproduction policy of Taylor & Francis.……....14

Figure 1.6 Magnetic high-resolution map of the Outokumpu area. The hammers show the locations of the most important mines and ore in this area. Anomaly zones are generally related to the traces of thrust surfaces separating overlapping thrust sheets. Reproduced with the permission of GTK……..17

Figure 1.7 Filtered magnetic map. Wavelength is above 2000 m. The high amplitude anomalies have been emphasized with red colour. Crosses, boxes and triangles respectively show the location of mines, prospects and mineralized outcrops. Reproduced with the permission of GTK……18

Figure 1.8 Location of FIRE transects in the central part of the Fennoscandian Shield. Reproduced with the permission of GTK…….…20

Figure 1.9 OKU-soundings (redlines) were done as a part of FIRE. Blue lines show the two crooked 2-D seismic lines (Line_2000 and Line_3000) which were done in May2006. The green circle shows the location of the Outokumpu deep drill hole. Reproduced with the permission of GTK.……22

Figure 1.10 A 3D visualization of the OKU-soundings as a part of the FIRE high

resolution seismic reflection sections with a geological map of the surface. The Outokumpu Deep Drill Hole is marked as red line. Reproduced with the permission of GTK……...…23

Figure 1.11 The migrated OKU-1 section. The deep hole is marked with red line. The Outokumpu-type assemblage at the depth of 1300-1750 m is showed in the yellow oval. And green oval covers an additional potential event at the depth of 2000-2500 m. Blue oval covers a reflector at the depth of near 1000 m. Reproduced with the permission of GTK……...……..24

Figure 1.12 Logging records (left), lithologies (middle) from coring and the geology information (right) in deep drill hole……26

Figure 1.13 The OUTO FAC40 televiewer data from the Outokumpu deep drill dole….28

Figure 2.1 The wavelength and amplitude of a wave……37

Figure 2.2 Phase velocity (Vp) and group velocity (Vg) of waves……38

Figure 2.3 Wave types on a shot gather from line_2000……41

Figure 2.4 Reflected and transmitted waves generated by a wave normally incident on an interface…….43

Figure 2.5 Reflected and refracted waves generated by a wave obliquely incident on an interface…….45

Figure 2.6 The vertical resolution (a) of separable expression (blue line) and resolvable expression (orange dot line) and the horizontal resolution (b) in seismic exploration based on a velocity model (c)……48

Figure 2.7 A cartoon of source-receiver geometry and seismic wave types in a shot……51

Figure 2.8 A cartoon for surface seismic geometry (a), a CMP gather (b) generated from (a), NMO (normal moveout) correction (c) and stacked trace (d)……52

Figure 2.9 A cartoon to show the crooked line geometry……..53

Figure 2.10 A cartoon of a stacking chart in a 2D seismic survey (a) and the stack profile (b) from (a)……56

Figure 2.11 A simple processing procedure……...57

Figure 2.12 (a) geometry of line_2000.(b) the definition of bin grids. Sources are marked by red squares. Blue squares are receivers. And black points show CMP positions.

Surface lines are shown as dark green lines. The rectangles are bin grids……..59

Figure 2.13 (a) geometry of line_3000.(b) the definition of bin grids. Sources are marked by red squares. Blue squares are receivers. And black points show CMP positions. Surface lines are shown as dark green lines. The rectangles are bin grids……..60

Figure 2.14 (a) Line_2000 raw shot record (shotpoint 2020). (b) Shot2020 from 0 ms to 2000 ms after gain. (c) Amplitude spectrum of shot2020……63

Figure 2.15 (a) Line_3000 raw shot record (shotpoint 30860). (b) Shot30860 from 0 ms to 1000 ms after gain (c) Amplitude spectrum of shot30860……..…..64

Figure 2.16 Raw shot gathers from shot2000 and shot2196 to show the amplitude difference between different shots……65

Figure 2.17 (a) Subsurface folds of line_2000. (b) Subsurface folds of line_3000……...69

Figure 2.18 Shot gathers from line_2000. (a) Before refraction static correction. (b) After refraction static correction…….73

Figure 2.19 Shot gathers from line_3000. (a) Before refraction static correction. (b) After refraction static correction……74

Figure 2.20 F-K filtering to attenuate the linear noise.(a) a shot gather from line_2000 in F-K domain, (b) F-K rejecting pie slices on the shot gather, (c) the shot gather in F-K domain after F-K filtering……78

Figure 2.21 F-K filtering to attenuate the linear noise. (a) a shot gather from line_3000 in F-K domain, (b) F-K rejecting pie slices on the shot gather, (c) the shot gather in F-K domain after F-K filtering…….79

Figure 2.22 A shot record from line_2000. (a) Before F-K filtering. (b) After F-K filtering. (c) The difference between (a) and (b)……..81

Figure 2.23 A shot record from line_3000. (a) Before F-K filtering. (b) After F-K filtering. (c) The difference between (a) and (b)……..82

Figure 2.24 Comparison of amplitude compensation from line_2000. (a) Raw recording before amplitude compensation. (b) After amplitude compensation……87

Figure 2.25 Comparison of amplitude compensation from line_3000. (a) Raw recording before amplitude compensation. (b) After amplitude compensation……88

Figure 2.26 Deconvolution results from line_2000. (a) the shot gathers before (top) and

after (bottom)the deconvolution, (b) the autocorrelation before (top) and after (bottom) the deconvolution, (c) the amplitude spectrum before (top) and after (bottom)the deconvolution……92

Figure 2.27 Deconvolution results from line_3000. (a) the shot gathers before (top) and after (bottom)the deconvolution , (b) the autocorrelation before (top) and after (bottom) the deconvolution, (c)the amplitude spectrum before (top) and after (bottom)the deconvolution……93

Figure 2.28 Velocity analysis from line_2000. (a)Semblance. Black line is the velocity picking line on current CMP supergather. Yellow and green lines are the velocity picking lines on next and former CMP supergathers, respectively. (b)CVS, red points are the velocities picked. (c) CMP supergather……94

Figure 2.29 Velocity analysis from line_3000. (a)Semblance, Black line is the velocity picking line on current CMP supergather. Yellow and green lines are the velocity picking lines on next and former CMP supergathers, respectively. (b)CVS, red points are the velocities picked. (c) CMP supergather……95

Figure 2.30 Velocity field of line_2000……....99

Figure 2.31 Velocity field of line_3000……...100

Figure 2.32 A portion of stack profiles from line_2000.Top is the first stack profile without residual static correction. And the bottom one is the stack profile with twice residual static correction……103

Figure 2.33 A portion of stack profiles from line_3000. Top is the first stack profile without residual static correction. And the bottom one is the stack profile with three times residual static correction……...104

Figure 2.34 A portion of stack profile of line_2000 before (top) and after (bottom) F-X 2D predictive filter……..106

Figure 2.35 A portion of stack profile of line_3000 before (top) and after (bottom) F-X 2D predictive filter……..107

Figure 2.36 The final stack profile from line_2000……108

Figure 2.37 The final stack profile from line_3000……109

Figure 2.38 Migration principles. (a) Migration corrects the dipping reflection segment C′D′ on a time profile to its actual location of CD. C′D′ moves to updip direction and becomes shorter. (b) Migration collapses diffractions back to their original

source point……110

Figure 2.39 Migration profile of line_2000……112

Figure 2.40 Migration profile of line_3000……113

Figure 2.41 Line_2000 old stack result from Suvi Heinonen……..115

Figure 2.42 Current stack result of line_2000 in the same grid with the earlier result…116

Figure 2.43 Comparison between the current stack result (a) and the earlier stack result (b) of line_2000 from 0 ms to 1000 ms……117

Figure 3.1 Schematics of zero-offset VSP survey, far-offset VSP survey, deviated-well VSP survey and walk-a-way VSP survey……122

Figure 3.2 Zero-offset VSP geometry: Red point is the shot position. The green points are receivers' positions……..128

Figure 3.3 (a) Zero-offset VSP raw data (b) Amplitude spectrum of raw VSP data……129

Figure 3.4 Wave types identified from the raw VSP data in time domain (a) and frequency-wavenumber domain (b)……131

Figure 3.5 The first breaks picking. (a) a portion of the first breaks picking on VSP data, (b) all the first breaks picking points in the zero-offset VSP data……..134

Figure 3.6 P-wave interval velocities calculated from the picked first break time of VSP data with different lengths of windows. (a) with 30-point length window; (b) with 50-point length window; (c) with 70-point length window; (d) the correlation coefficient of the local linear slope method when the length of window is 50 points……...136

Figure 3.7 Measures of interval velocities in Outokumpu deep drill hole. (a) sonic log interval velocities (black solid line) with corresponding Backus average (orange solid line) and arithmetic average (dotted white line). (b) the geology information. (c) sonic log averages from (a) compared to values of the interval velocities (dotted black line)obtained from the seismic travel time of Figure 3.5 by local linear slope method. (d) density log with Backus average……..138

Figure 3.8 (a) Trace 615 from 0 ms to 500 ms. (b) Trace 615 after removing the 50Hz harmonic noise. (c) The harmonic noise estimated from (a)……..142

Figure 3.9 (a) Amplitude spectra of trace 615. (b) Amplitude spectra of trace 615 after

removing the 50Hz harmonic noise. (c) Amplitude spectra of the harmonic noise estimated from raw data……..143

Figure 3.10 (a) The data with noise in frequency and wavenumber domain, and the F-K filter pie slices for tube wave attenuation are displayed. (b) The data without 50Hz harmonic noise in frequency and wavenumber domain……144

Figure 3.11 Comparison of VSP data before (a) and after (b) tube waves attenuation…147

Figure 3.12 A cartoon of the wavefield separation by median filter. Lines with upward arrows are upgoing waves; Lines with downward arrows are downgoing waves. (a) raw data. (b) data after static correction to flatten downgoing waves (solid arrows). (c) enhanced downgoing wavefield (heavier solid arrows) by median filter. (d) upgoing wavefield (solid arrows) after subtracting the downgoing wavefield. (e) data after static correction to flatten upgoing waves (solid arrows).(f) enhanced upgoing wavefield (heavier solid arrows) by median filter…….151

Figure 3.13 The wavefield separation by median filter on Outokumpu VSP data. (a) data after noise attenuation and amplitude compensation. (b) data after static correction to flatten downgoing waves.(c) enhanced downgoing wavefield by median filter. (d) upgoing wavefield after subtracting the downgoing wavefield. (e) data after static correction to flatten upgoing waves.(f) enhanced upgoing wavefield by median filter……..153

Figure 3.14 (a) upgoing wavefield after deconvolution. (b) upgoing wavefield delayed by twice first breaking time. The mute zone for corridor stacking is displayed on (b)……155

Figure 3.15 Autocorrelation plots: Top is the autocorrelation from upgoing wavefield before deconvolution; Bottom is the autocorrelation from upgoing wavefield after deconvolution……..156

Figure 3.16 Comparison of synthetic (a), vertical summation (b) and the corridor stack (c)……...……159

Figure 3.17 Final corridor stack result of VSP data. (a) with 2m depth receiver increment. (b) with 10m depth receiver increment. (c) with 20m depth receiver increment…….160

Figure 4.1 A 3D view of the surface seismic and the zero-offset VSP results in Outokumpu……..168

Figure 4.2 The final stack results of line_2000 (a) and line_3000 (b)……170

Figure 4.3 The migration profiles of line_2000 (a) and line_3000 (b)……172

Figure 4.4 Final corridor stack result of VSP data. (a) with 2m depth receiver increment. (b) with 10m depth receiver increment. (c) with 20m depth receiver increment…….173

Figure 4.5 Measures of interval velocities in Outokumpu deep drill hole. (a) sonic log interval velocities (black solid line) with corresponding Backus average (orange solid line) and arithmetic average (dotted white line). (b) the geology information. (c) sonic log averages from (a) compared to values of the interval velocities (dotted black line)obtained from the seismic travel time of Figure 3.5 by local linear slope method. (d) density log with Backus average…….175

Figure 4.6 Synthetic seismogram: From left to right, they are the density log, the acoustic log, calculated acoustic impedance, reflection coefficient, the synthetic seismogram, and geology information from the deep drill hole…….177

Figure 4.7 Comparison of synthetic seimogram (a) and VSP corridor stack (b)…….180

Figure 4.8 Comparison of seismic stack result of line_2000 and VSP result……...183

Figure 4.9 Comparison of seismic stack result of line_3000 and VSP result. In order to reveal details, the comparison in region A is expanded and shown on Figure 4.10……..185

Figure 4.10 An expanded portion of the region A from the Figure 4.9……186

Figure A.1 An example of a seismic vibrator……..….210

Figure A.2 (a) An 8 s sweep in the time domain; the frequency range for this figure is 1-5 Hz for display purpose, (b) the instantaneous frequency of the sweep as a function of time, (c) the autocorrelation of the sweep……212

Figure A.3 Vibroseis source sweep, response and correlation.....213

List of Symbols and Abbreviations

$\overline{V}$	Time-weighted RMS velocity
A	AGC factor; Constant
a	Amplitude
A_0	Amplitude of the incident wave
A_1	Amplitude of the reflected wave
A_2	Amplitude of the transmitted wave
B	Constant
D, D_0	Spherical divergence factor
$e(t)$	Impulse response
$f(t)$	Ricker wavelet
k	Wavenumber; Bulk modulus
N	Number of sampling points in a window
$n(t)$	Random noise
r	Radius of the spherical wavefront
R	Reflection coefficient
R_f	First Fresnel zone
T	Period of wave
t	Travel time
T	Transmission coefficient; Travel time; Offset
t_0	Travel time at zero offset
v	Stacking velocity; Propagation speed of wave

V	Propagation speed of wave
v_0	Velocity of the deposit; Peak frequency
V_1	Velocity in the first layer
V_A	Simple arithmetic mean velocity
V_B	'Backus' long-wavelength average velocity
v_c	Velocity of the country rock
v_g	Group velocity
V_i	Interval velocity in *i*th layer
V_{LP}	P-wave interval velocity
v_P	Phase velocity; Velocity of compressional wave
V_P, v_1, v_2	Velocity of compressional wave
V_{rms}	RMS velocity
v_S	Velocity of shear wave
$w(t)$	Seismic wavelet
x	Position; offset
$x(t)$	Seismogram
x-t	Space-time
Z, Z_1, Z_2	Acoustic impedance
Z_0	Acoustic impedance of the deposit
Z_C	Acoustic impedance of the country rock
θ_1	Incidence angle
θ_2	Refraction angle
λ	Wavelength of wave; First Lamé parameter

μ	Shear modulus
ρ, ρ_1, ρ_2	Density of the material
ρ_0	Density of the deposit
ρ_c	Density of the country rock
ω	Frequency
2D	Two dimensional
3D	Three dimensional
AGC	Automatic gain control
AMPL	Acoustic impedance
CDMO	Cross-dip-moveout
CDP	Common depth point
CMP	Common midpoint
COP	Common offset point
CRP	Common receiver point
CSP	Common shot point
CVS	Constant velocity stack
FIRE	Finnish Reflection Experiment
F-K	Frequency-wavenumber
F-X	Frequency-space
GFZ	German Research Center for Geosciences
GPS	Global Positioning System
GR	Gamma rays
GTK	Geological Survey of Finland

ICDP	International Continental Scientific Drilling Program
KTB	German Continental Deep Drilling Program
MD	Measured depth
NEDRA	A Russian company
NKSB	North Karelian Schist Belt
NMO	Normal moveout
OKU	Outokumpu
P-wave	Compressional wave
RMS	Root mean square
RUNT	Travel time
S/N	Signal-to-noise
SP	Spontaneous potential
S-wave	Shear wave
TVD	True depth
Tw	Tube wave
VSP	Vertical seismic profiling

1.0 Introduction

This thesis presents the study of the seismic reflection characteristics in the hard rock environment at Outokumpu, Finland. The principal research techniques used in this thesis consist of surface seismic reflection and vertical seismic profiling. Meanwhile, the processing techniques on two 2D seismic lines and a vertical seismic profiling are discussed. This chapter provides introductory material describing the geology, the physical properties of metamorphic rocks and sulphide minerals, the seismic reflection characteristics in hard rock environments, and the seismic exploration history in Outokumpu, Finland.

1.1 Physical Properties and Seismic Imaging in Hard Rock Environments

1.1.1 Physical Properties of Hard Rock

Rocks are classified into three main types: sedimentary rocks, igneous rocks and metamorphic rocks. ‘Hard rock’ is admittedly a somewhat ambiguous term used primarily in the mining community to describe low porosity metamorphic and igneous rocks. Another somewhat ambiguous term used in this community is ‘crystalline’ to describe these same types of materials, this despite the fact that all rocks are composed of mineral crystals. These terms ‘hard’ and ‘crystalline’ will be used throughout the thesis in describing the metamorphic assemblages at Outokumpu.

Metamorphic rocks are the most voluminous at Outokumpu. Metamorphic rocks form deep in the earth where high temperature and pressure can make profound physical and chemical changes on the existing rocks (sedimentary rock, igneous rock or another older metamorphic rock) (Blatt *et al.*, 1996). The process is called metamorphism. Metamorphic rocks make up a large part of earth's crust. A simple classification of metamorphic rocks is not readily accomplished because they can be formed from essentially any pre-existing rock type. As such, the 'protolith' is important in describing the rock type. For example, a metamorphosed sedimentary rock is referred to as a 'metasediment'. The original minerals will still exist or they may have been chemically converted by the conditions of pressure, temperature, strain, and available fluids during the metamorphic cycle. Another way to characterize the metamorphic rocks is through their mineral texture into foliated and nonfoliated rocks. The latter grouping consists of nearly monomineralic rocks such as quartzite and marble in which the mineral grains have equant shape and are not crystallographically aligned. The former foliated rocks are often broken initially into three categories of 1) slates that have a well defined cleavage plane, 2) schists in which micas will show a preferential alignment, and 3) gneisses that show clear banding of phyllitic (micas) and granular (quartz, feldspars) and preferential mineralogical alignments.

Phanertic (i.e. plutonic or intrusive) igneous rocks are hard, crystalline rocks which formed through the cooling and solidification of magma or lava either at, or below, the

earth's surface (Le Maitre *et al.*, 2002). Such plutonic igneous rocks were, surprisingly, found as granite pegmatite intrusions in the Outokumpu well. They make up 95% of upper 16 kilometres of earth's crust (Klein and Hurlbut Jr, 1985).

Economic minerals in hard rock environments mainly include gold, copper, nickel, zinc and lead, which come from igneous and metamorphic rocks. As such, understanding the physical properties of hard rock is essential when exploring for mineral deposits in hard rock environments.

In sedimentary basins, the rock types are often quite distinct from one another and in the absence of other disruptive forces are for the most part layered and distinguishable over many kilometres. In contrast, due to the formation processes, metamorphic rocks are highly deformed and fragmented which make the overall geological structure more heterogeneous than would be found in sedimentary rocks. Structures in hard rock environment are often complex and steeply dipping (Salisbury and Snyder, 2007) and may have undergone many cycles of faulting, ductile deformation, and igneous intrusion. In addition, ore deposits found within such structures normally have fairly small sizes (< 1 km across) (Salisbury and Snyder, 2007). Laboratory studies show velocities and densities of hard rock are typically higher than sedimentary rock (Schmitt *et al.*, 2003) (Fig. 1.1 and Fig. 1.2). Ore minerals display a much higher densities and wide varied velocities. But they have relatively lower impedance difference (Salisbury *et al.*, 1996) (Fig. 1.3).

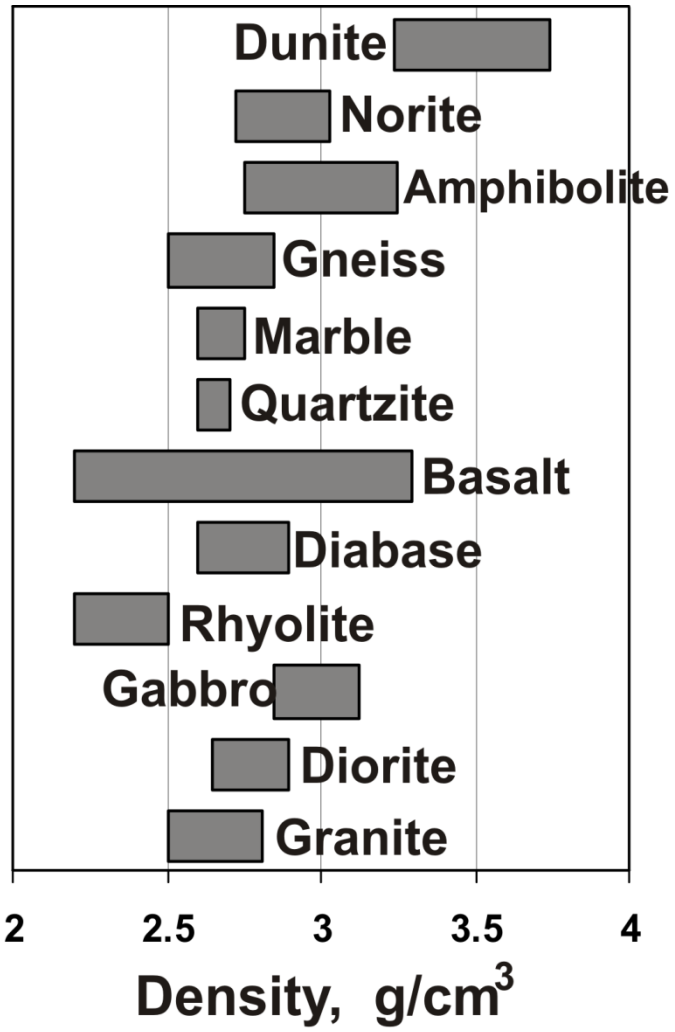

(Schmitt *et al.*, 2003)

Figure 1.1 Density of some igneous and metamorphic host rocks (from compilations of Hallenburg (1984) and Olhoeft and Johnson (1989)). Reproduced with the permission of Douglas R. Schmitt.

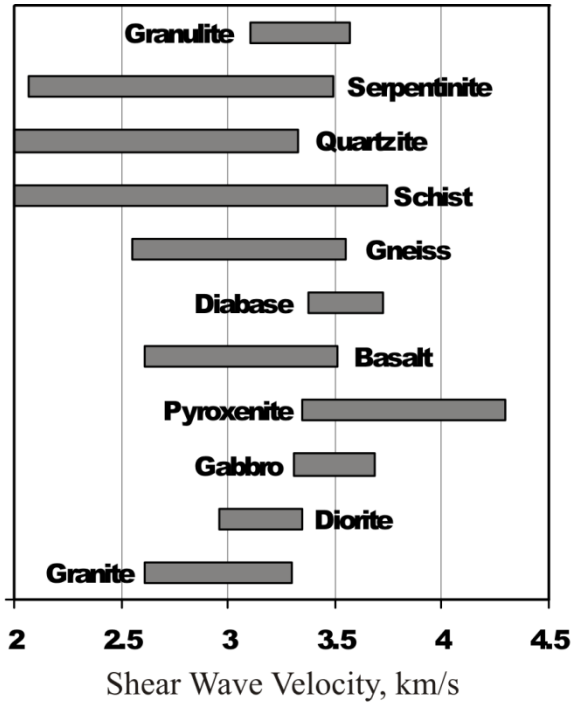

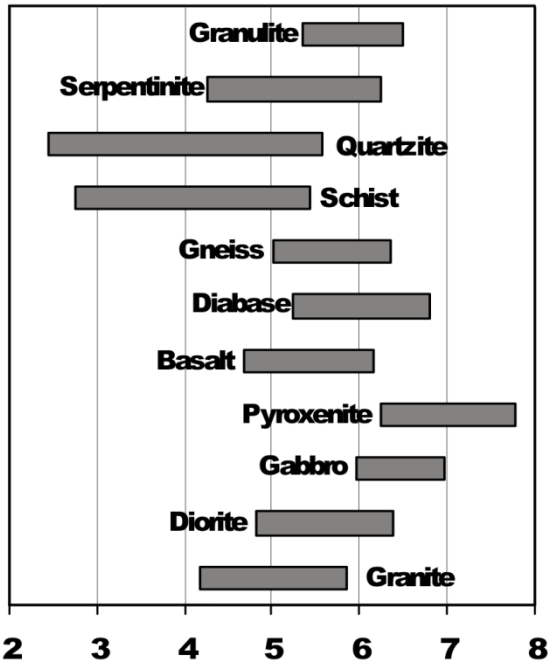

(Schmitt *et al.*, 2003)

Figure 1.2 Intrinsic compressional and shear wave velocities of common igneous and metamorphic rocks; summary values from compilations in Schon (1996). Reproduced with the permission of Douglas R. Schmitt.

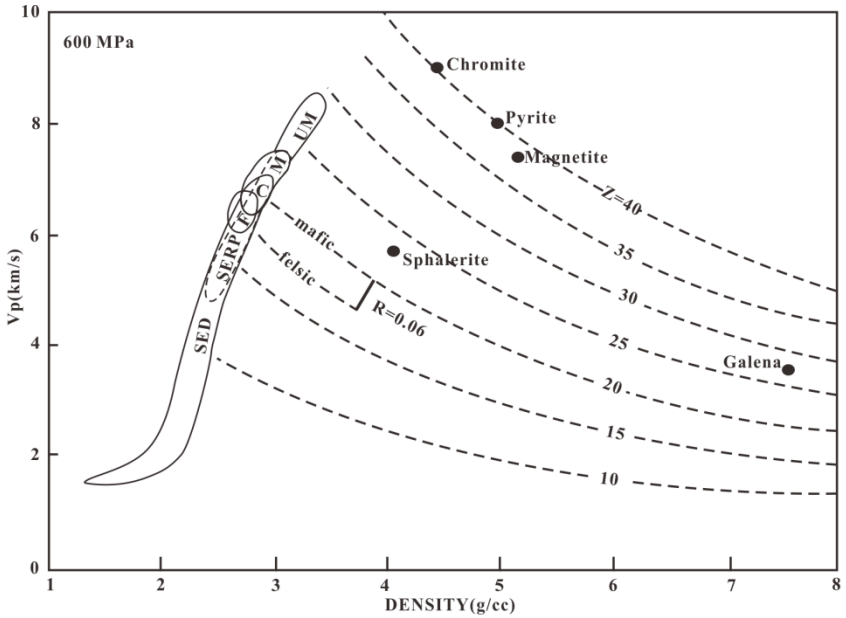

(Salisbury *et al.*, 1996)

Figure 1.3 P-wave velocities versus densities of some base metal ore minerals. F = felsic; M = mafic; SED = sediments, including carbonates (c); SERP = serpentinite; UM, ultramafic. Dashed lines represent the constant impedance (Z); bar shows minimum impedance contrast (about 2.5) required to give strong reflections (R = 0.06). Figure was reprinted with authorization under the Fair Use Permission of SEG. http://economicgeology.org/misc/permissions.dtl

1.1.2 Seismic Imaging in Hard Rock Environments

Seismic methods have not been employed much in mining exploration in hard rock terranes. Instead many traditional techniques including geological field mapping, electromagnetic surveying, drilling, and potential field techniques (gravity and magnetics) have long been used in the mining industry to locate metal deposits. They are effective at discovering shallow deposits. However, as the search for these mineral resources must seek progressively deeper into the earth these methods become less economic by themselves; and considering the long-term profitability in mining industry new deep exploration techniques are required. For example, electromagnetic methods are good at finding electrically conductive zones, but the problem with this is that these methods cannot distinguish an economic ore body from more abundant graphite conductors. As the anomalies detected today are at depths in excess of 1 km, drilling each one to find that which is economic is not practical. As such, it becomes important to attempt to further distinguish economic ores; and seismic techniques that are sensitive to density and elastic properties provide one such new way to evaluate a given anomaly detected by the more traditional methods.

Seismic reflection techniques have been widely used for oil exploration in sedimentary basins for over 80 years. And with seismic reflection techniques, it is possible to image structures accurately at depth range interesting for mining purposes. Further, in recent decades, many successful cases of finding minerals by using seismic exploration methods

have been presented (White *et al.*, 2000, Dehghannejad *et al.*, 2010, Adam *et al.*, 2000, Eaton *et al.*, 2010). It is demonstrated that seismic reflection techniques might be utilized as valuable geophysical tools to improve the understanding of the mineral structures, and to enhance the capabilities for detecting deep ore deposits. This is particularly true as the maximum depth of base metal mining is reaching 3 km.

Additionally, seismic reflection techniques are also used to understand the structure of the crust. For example, extensive studies were done in Kola Superdeep Borehole, Russia and the German Continental Deep Drilling Program (KTB) (Ganchin *et al.*, 1998, Smithson *et al.*, 2000, Harjes *et al.*, 1997, Luschen *et al.*, 1996, Ayarza *et al.*, 2000, Carr *et al.*, 1996, Rabbel *et al.*, 2004). The survey methods included not only the borehole measurements, but also surface reflection seismic and vertical seismic profiling techniques. In practice, the seismic reflection survey can be useful to determine the crustal seismic structure. It was shown that the upper crust is reflective; and the understanding of the Earth's continental crust was greatly improved. However, seismic reflection techniques must be modified to adapt to the different physical properties in hard rock environments.

In principle, the impedance difference is critical to whether or not a deposit can be detected by seismic reflection techniques (Salisbury *et al.*, 1996, Salisbury *et al.*, 2000, Salisbury and Snyder, 2007). The acoustic impedance difference between the deposit and country rock must be large enough to generate strong reflections or at least to scatter the seismic waves. The acoustic impedance of a given rock type is the product of its density

and the velocity of seismic compressional wave propagating through it. If the wave is normally incidence on a reflecting interface between two different rock types, the reflection coefficient *R* of the reflected wave amplitude can be expressed as:

$$R = \frac{v_0\rho_o - v_C\rho_C}{v_0\rho_0 + v_C\rho_C} = \frac{Z_0 - Z_C}{Z_0 + Z_C} \tag{1-1}$$

where v_0 and ρ_0 are the velocity and density of medium 1, respectively, and v_C and ρ_c are the velocity and density of medium 2, respectively. Hence, Z_0 is the acoustic impedance of medium 1 and Z_C is the acoustic impedance of medium 2. According to Salisbury et al. (Salisbury *et al.*, 2000), a minimum value of R = 0.06 (Fig. 1.3), which was acquired in practice, is required to produce a strong reflection in most geologic settings.

Additionally, the acquisition parameters used in seismic surveys also govern whether or not deposits can be imaged. In terms of the physical properties of hard rock, the signal-to-noise ratio is particularly low due to the inherent heterogeneous structural characteristics and low impedance differences (and hence small reflection amplitudes). Further, based on experience, it is often difficult to obtain a stable and lateral continuous reflector in hard rock areas on a seismic profile. Usually, high frequency seismic exploration techniques with high fold acquisition layouts are employed in hard rock areas with the aim to generate high resolution images (Lu *et al.*, 2010, Milkereit and Green, 1992, Milkereit *et al.*, 1994, Salisbury *et al.*, 2000). Recently, for example, Lu et al. (2010) successfully obtained effective reflections from shallow layers to the Moho in the Luzong

metallic ore area by applying a changeable seismic survey with 40 m receiver spacing, 240 m source spacing, 60 fold in general. In the area of the ore concentration, however, they reduced spacing to a 10 m receiver spacing and a 80 m source spacing. This increased the seismic fold to 90 in the ore concentration zone. In Ontario, a high-resolution seismic survey with 30-140 Hz, 20 m source and receiver spacing, 120-fold coverage and 4 s records was applied by Milkereit et al., (1992) to image the Sudbury structure. A new model of the deep complex Sudbury structure was developed from this data that was with the observed regional magnetic and gravity fields.

2D or 3D seismic surface exploration technology is often used in hard rock areas not so much to directly detect an ore body but to develop models of the geological structure. 2D seismic surface exploration is a fast and economical way to map simple structures. 3D seismic surface exploration requires a complicated layout and costs considerably more than a 2D seismic survey. Thus, it is used to delineate potential deposits in detail (Malehmir and Bellefleur, 2009, Milkereit *et al.*, 2000, Schmelzbach *et al.*, 2007). As a complement to seismic surface exploration imaging, vertical seismic profiling (VSP) technology is also useful in mapping structures, especially steeply dipping structures and fractures in crystalline rocks (Carr *et al.*, 1996, Luschen *et al.*, 1996, Miao *et al.*, 1994, Miao *et al.*, 1995, Rabbel *et al.*, 2004, White *et al.*, 1994, Cosma *et al.*, 2001, Willenberg *et al.*, 2008).

Some geophysical results from boreholes contribute to the understanding of reflectivity in

crystalline rock masses. Such seismic data can also be used to determine the in situ seismic wave speeds, calibrate the seismic travel time-to-depth of surface reflection surveys, and to assist in tying seismic results with well logging surveys. In order to obtain high resolution results, the receiver intervals during vertical seismic profiling acquisition are usually smaller than in regular acquisition. Finally, the shorter one-way source to receiver paths in vertical seismic profiling improve the signal-to-noise ratio because the overburden path is eliminated.

Based on the requirements about high resolution, special considerations are also needed for data processing. It involves careful analysis on subsurface conditions, geometry, data quality, and geologic features and numerous iterative tests on processing parameters and sequences. Static correction, high-pass filter, and noise suppression are especially important to give a clear image of the deposit.

Consequently, even though complex physical properties, discontinuous structures and small differences in acoustic impedances make acquisition and processing of seismic data challenging both in theory and in practice, deposits in hard rock environments can be detected and located by high resolution seismic surface reflection and borehole vertical seismic profiling. This thesis provides a new case study in which both surface and borehole seismic data were simultaneously obtained allowing for the firm interpretation of some strong seismic reflectors that had been seen in earlier surveys.

1.2 Outokumpu Area Geology

The study area near the town of Outokumpu, Finland, is a hard rock area located in southeast Finland (Fig. 1.4). It is the site of a historic base metal mine, and well known for its unconventional Precambrian massive Cu-Co-Zn sulphide deposits (~1.97 Ga) discovered in 1910. Since then, a number of studies have been carried out in this area involving geologic, geochemical, and geophysical methods. Many papers have been published about the study of the evolution of the Outokumpu area (Gaal *et al.*, 1971, Koistinen, 1981, Park, 1988, Ruotoistenmaki and Tervo, 2006, Santti *et al.*, 2006, Sorjonen-Ward, 1997, Kontinen and Peltonen, 2002, Kontinen and Peltonen, 2003). They gave a detailed description and the evolution of the ore potential zones in this area.

The Outokumpu-type assemblage is located tectonically at a conjunction zone named the North Karelian Schist Belt (NKSB) between the late Archean Karelain cratonic domain in the northeast, and the Paleoproterozoic Svecofennian domain (Fig. 1.5). In this region, the lithologies are basically composed of four associations: 1) foliated granitoids and stromatic migmatites that are the dominant lithologies in the late Archean basement, 2) Paleopreoterozoic metamorphosed terrestrial to passive margin marine meta-sediments with mafic intrusions and volcanic eruptions, 3) serpentinites and their hydrothermally altered derivates with minor volcanics and gabbros enclosed within sulfidic and carbonaceous black schists and thick-bedded turbiditic greywacke. These materials which make up the mineralized Outokumpu-type assemblage, and 4) relative young

Figure 1.4 Geographic location of Outokumpu, Finland.
Reproduced with the permission of GTK.

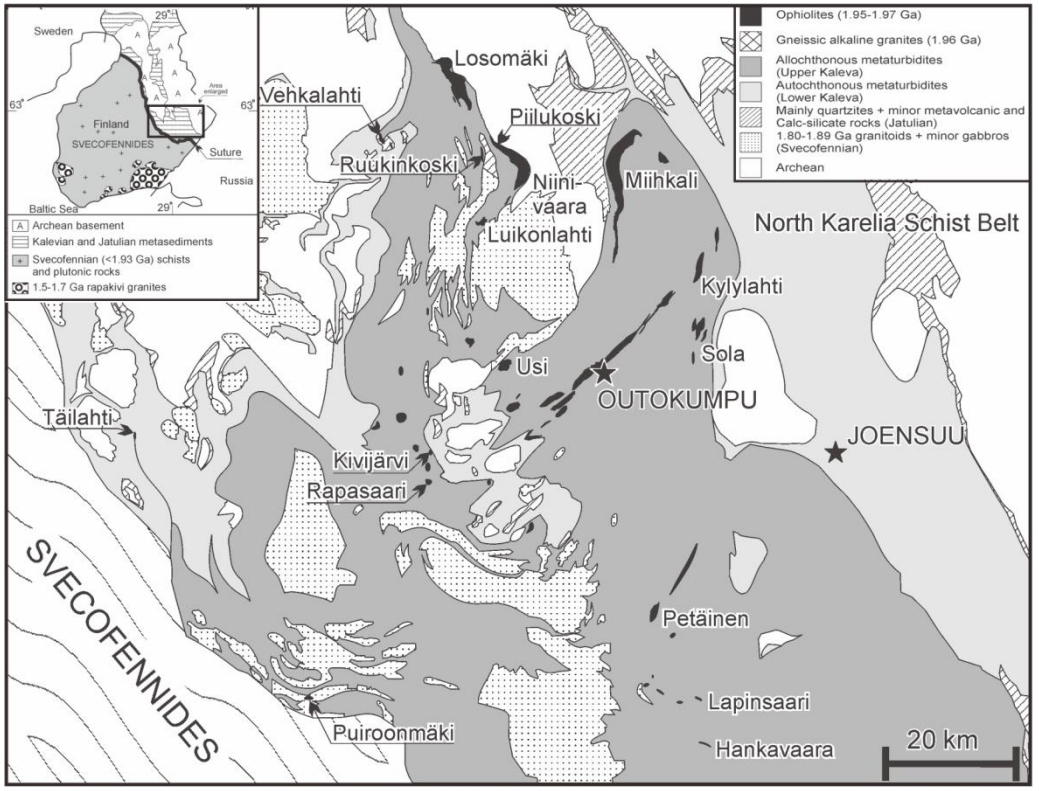

(Modified from Santti *et al.*, 2006)

Figure 1.5 Geological map of Outokumpu area. Figure was reprinted with authorization under the Non-Commercial Reproduction policy of Taylor & Francis. https://s100.copyright.com/AppDispatchServlet

granodioritic to tonalitic intrusions (1.80-1.89 Ga) which truncated early tectonic fabrics (Sorjonen-Ward, 1997, Santti *et al.*, 2006).

The tectonic evolution of the region during the Late Paleoproterozoic is characterized by episodes of sedimentation, rifting and magmatism including:

1) 2.5-2.1 Ga predominantly mafic magmatism with subsequent stable platform terrestrial to shallow marine sedimentation,

2) 2.1-2.0 Ga rifting and subsidence indicated by mafic volcanics, sills and dykes as well as clastic turbidites, carbonates, iron formations and graphitic schists,

3) 1.97-1.95 Ga renewed rifting which leaded to the formation of oceanic crust,

4) 1.95-1.85 Ga transition from divergent to convergent tectonics indicated by monotonous metapsammites and Outokumpu nappe emplacement (Sorjonen-Ward, 1997).

The ultramafic massifs of variable size enclosed by metasediments of the Outokumpu-type assemblage are interpreted to be metamorphosed ophiolites (Table 1-1) that were distributed over an area of more than 5000 km^2 (Kontinen and Peltonen, 2002, Kontinen and Peltonen, 2003) (Fig. 1.5). These massifs represent fragments of a dominantly ultramafic oceanic floor (Santti *et al.*, 2006). The ophiolites are intimately associated with semimassive polymetallic Cu-Co-Zn-Ni-Ag-Au-As sulphides and

disseminated Ni sulphides which form the polymetallic Outokumpu ore deposits (Kontinen and Peltonen, 2002, Kontinen and Peltonen, 2003). At present, these ore bodies are mainly exposed along the thrust belts, which are highlighted by magnetic anomalies as shown in Fig. 1.6 and Fig. 1.7 (Ruotoistenmaki and Tervo, 2006). These shallow outcrops were easily found and led to the development of the historic Outokumpu mine. However, the Outokumpu mine is closed now as the nearer surface deposits have been depleted; and there have been research efforts to extend the mining carried out by the Finnish Geological Survey (GTK –the Geological Survey of Finland).

Table 1-1 The definition of some rock types found in Outokumpu area.

Rock Type	**Definition**
Ophiolite	A typical sequence of rocks in the oceanic crust: from bottom to top: ultrabasic rocks, gabbro, sheeted dikes, pillow basalts, and sea-floor sediments, which usually indicate a divergent zone and a sea-floor environment.
Serpentinite	A rock composed of one or more serpentine group minerals.
Diopside skarn	Diopside skarn is a type of skarn that contains diopside pyroxene. Here, skarn means a type of metamorphic rock derived from limestone or dolostone, which is most often formed at the contact zone between intrusions of granitic magma and carbonate country rocks.
Quartzite	A metamorphic rock consisting largely or entirely of quartz; most quartzites are formed by metamorphism of sandstone.
Pegmatite	Any extremely coarse-grained igneous rock with interlocking crystals is referred to as pegmatite. Most are of granitic composition.
Black Schist	Schist is a type of metamorphic rock containing abundant particles of mica, characterized by strong foliation, and originating from a metamorphism. Black Schists are metamorphic black shales.

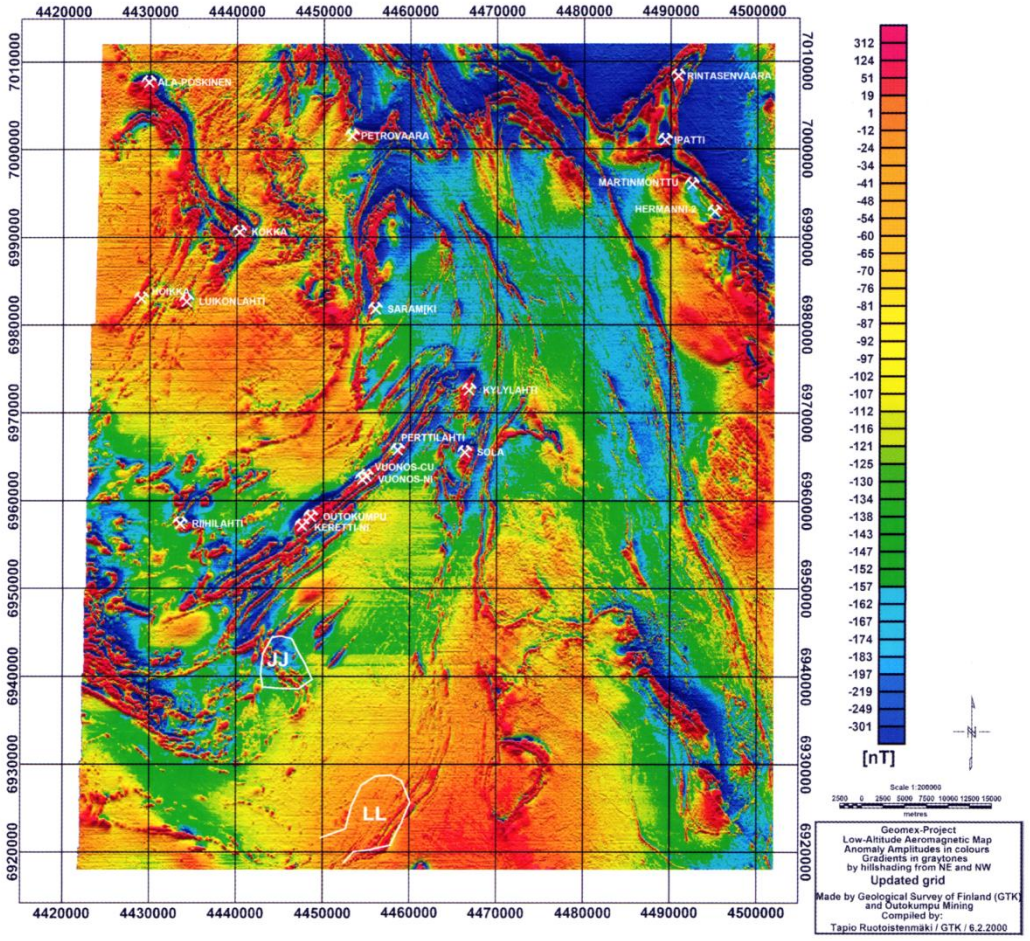

(Ruotoistenmaki and Tervo, 2006)

Figure 1.6 Magnetic high-resolution map of the Outokumpu area. The hammers show the locations of the most important mines and ore in this area. Anomaly zones are generally related to the traces of thrust surfaces separating overlapping thrust sheets. Reproduced with the permission of GTK.

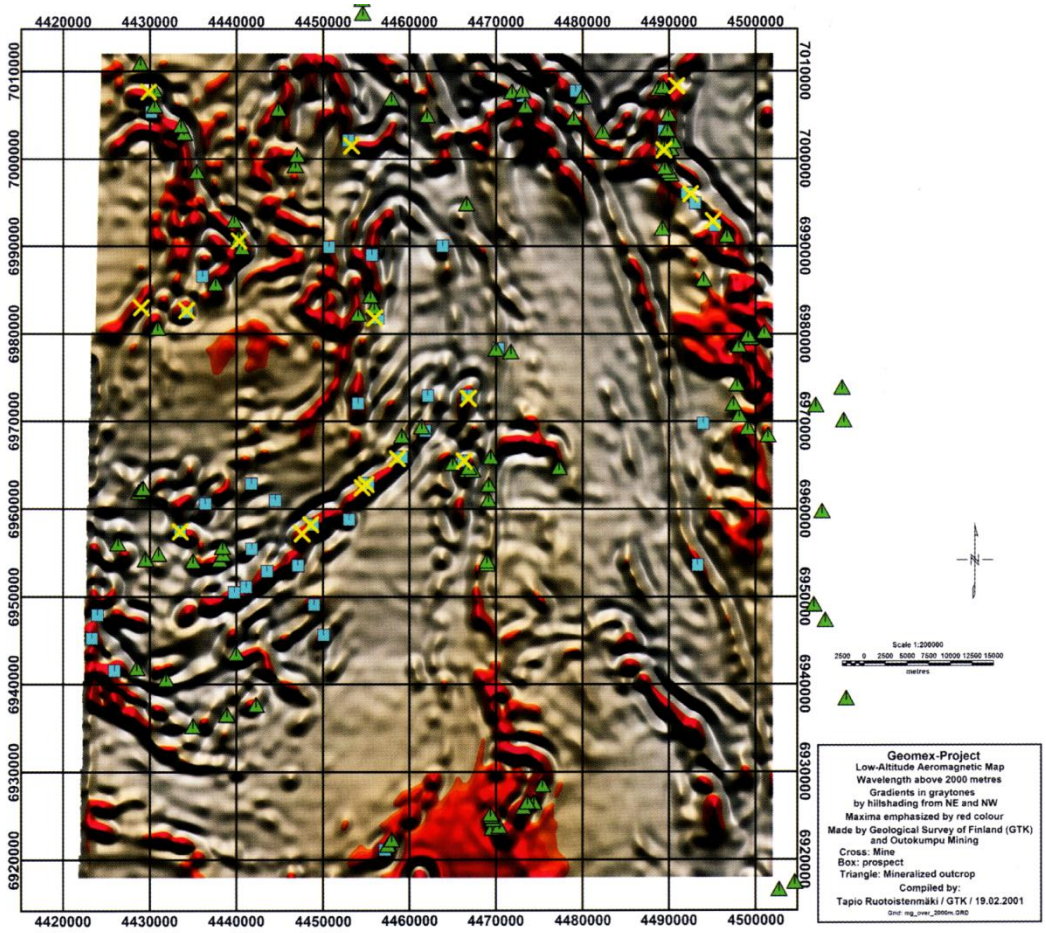

(Ruotoistenmaki and Tervo, 2006)

Figure 1.7 Filtered magnetic map. Wavelength is above 2000 m. The high amplitude anomalies have been emphasized with red colour. Crosses, boxes and triangles respectively show the location of mines, prospects and mineralized outcrops. Reproduced with the permission of GTK.

1.3 Seismic Surveys in Outokumpu

A reflection seismic survey is the method of using seismic waves to investigate the subsurface structures by recording the characteristics and travel time of the reflected waves on the interfaces between different layers in the earth. It involves sources to generate seismic waves and geophones to record returned energy. In a 2D seismic survey, sources and geophones are placed along a survey line. After processing, a seismic profile with subsurface information along this survey line can be obtained.

From 2001 to 2003, a series of crustal-scale reflection seismic vibrator surveys were performed as a lithosphere project FIRE (Finnish Reflection Experiment) by a national consortium (Geological Survey of Finland, Institute of Seismology of the University of Helsinki, Institute of Geosciences and the Sodankylä Geophysical Observatory of the University of Oulu) (Kukkonen *et al.*, 2006). The project includes four long FIRE transects (Fig. 1.8), over the Fennoscandian Shield in Finland with a total length of 2135 km. Five (minimum four) 15.4-ton vibrators applying peak forces of about 10 tons/vibrator were used to generate the seismic signal. Those vibrators used a linearly increasing sweep from 12 to 80 Hz and they were activated with a source point interval of 100m. The receiving geophone group interval was 50 m with a maximum source-receiver offset of 9050 m. The record length after correlation was 30 s (corresponding to about 100 km depth into the earth). The four transects were designed to cross all of the major geological units in Finland. FIRE 3, which runs across the Outokumpu formation in

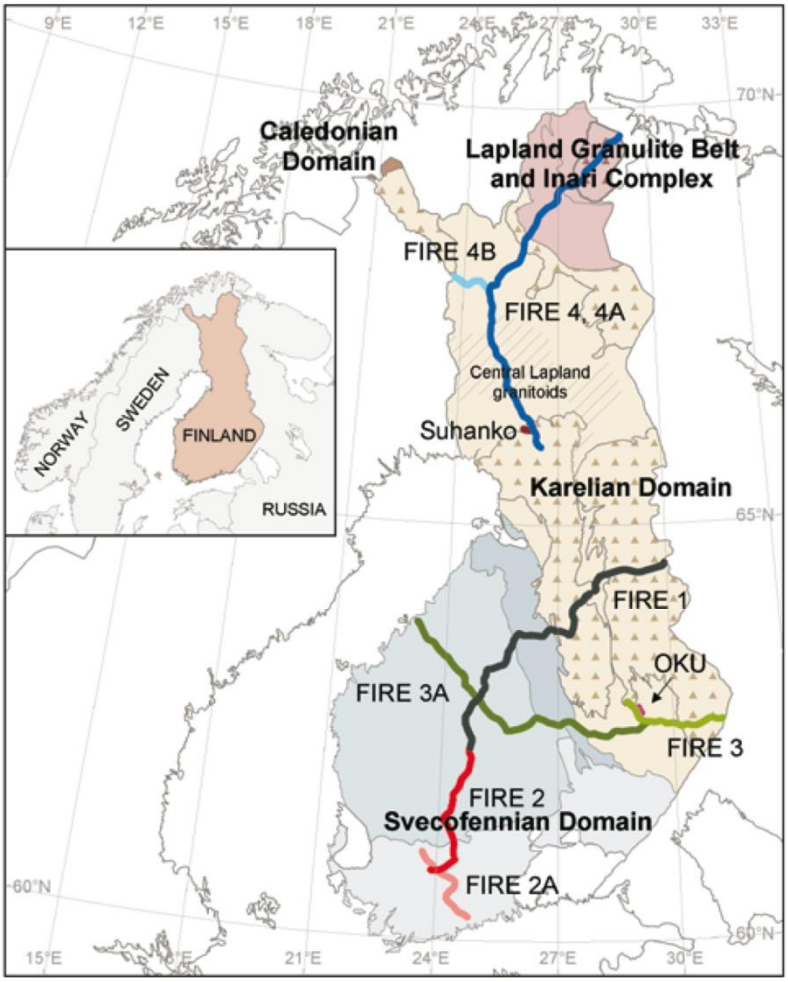

(Kukkonen *et al.*, 2006)

Figure 1.8 Location of FIRE transects in the central part of the Fennoscandian Shield. Reproduced with the permission of GTK.

NW-SE direction (Fig. 1.8), showed a distinct strong reflector in the Outokumpu area at 1.3-1.5 km depth.

In August 2002, a higher resolution seismic reflection survey (Fig. 1.9) was also carried out as a part of the FIRE project in order to improve the understanding on the structure of Outokumpu formation and to test the practicality of seismic reflection technology in ore exploration (Kukkonen, 2004, Kukkonen, 2007). This survey contains three intersecting profiles (OKU-1, OKU-2 and OKU-3), each about 10 km long. OKU-1 and OKU-2 were parallel and 6 km apart from each other. They run in a NW-SE direction across the geologic strike of the formation. OKU-3 connected them by running parallel to the strike. In addition, OKU-1 runs along the same path as a portion of the much longer FIRE 3 which allows a correlation between them to better understand the large scale features of the crust. The OKU series profiles were acquired with a 25 m geophone group interval and a 50 m source interval giving a fold from 78 to 119. The frequency band of signal was higher than for the deep FIRE profiles and extended from 30-130 Hz, the recording length was 6 s.

The final results (Fig. 1.10) exhibited strong reflectors between 1 km and 3 km on all three sections. Those reflectors can be followed through the entire OKU-3 profile (Kukkonen, 2004, Kukkonen, 2007). Interpretation of the FIRE lines in the vicinity of Outokumpu (FIRE 3, OKU-1, OKU-2, and OKU-3) suggested that the Outokumpu-type assemblage (Fig. 1.11) could be seen extending laterally from the mining district at the

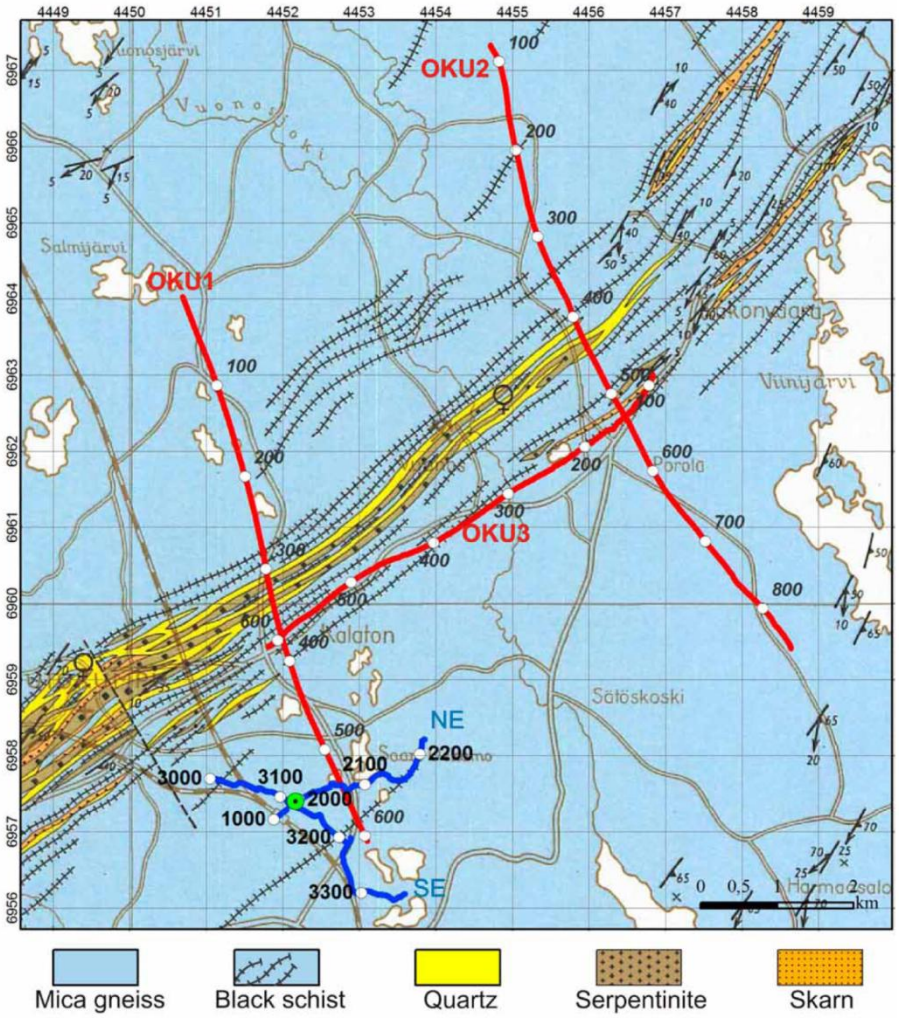

(Heinonen *et al.*, 2011)

Figure 1.9 OKU-soundings (redlines) were done as a part of FIRE. Blue lines show the two crooked 2-D seismic lines (Line_2000 and Line_3000) which were done in May2006. The green circle shows the location of the Outokumpu deep drill hole. Reproduced with the permission of GTK.

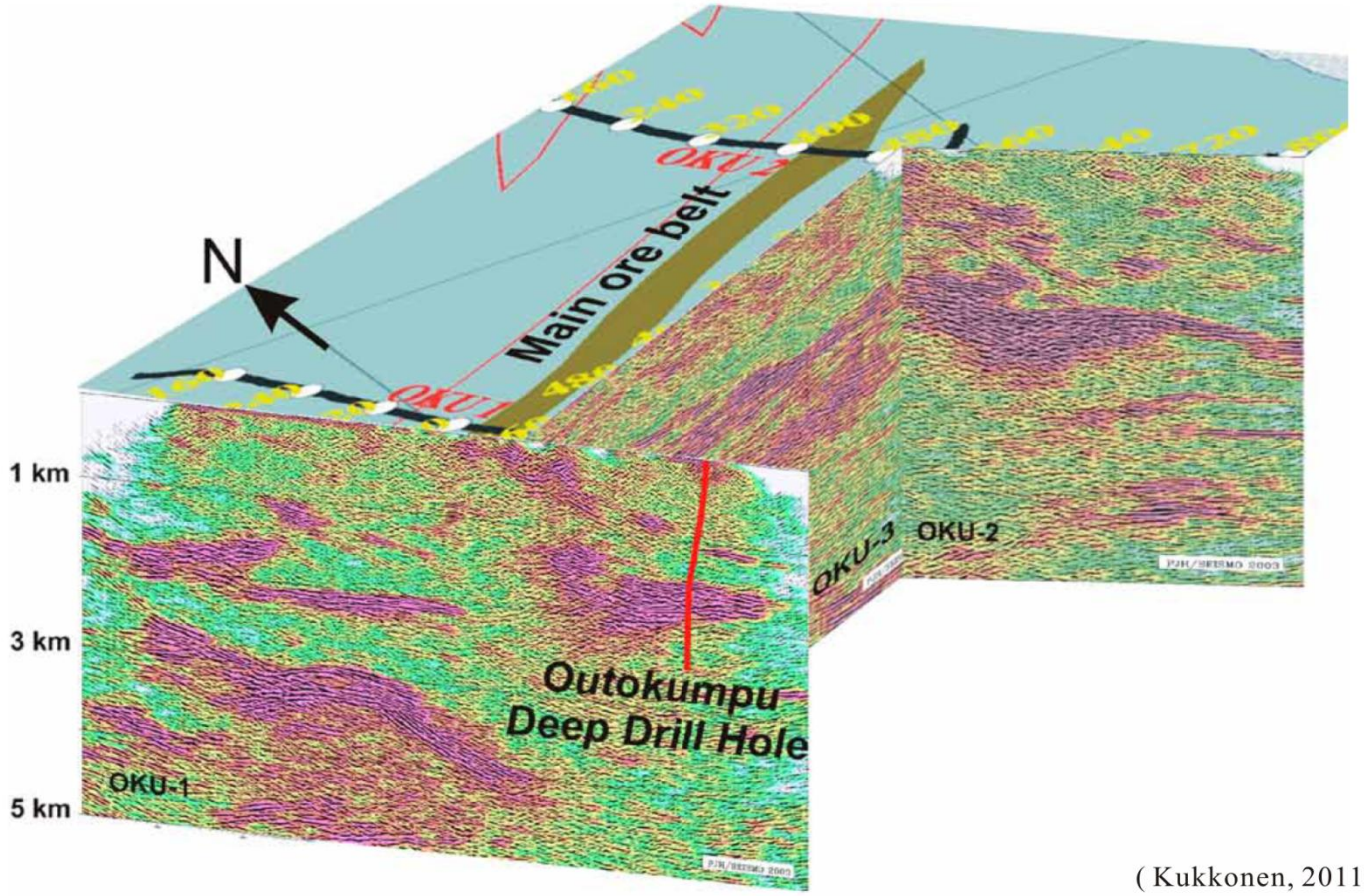

(Kukkonen, 2011)

Figure 1.10 A 3D visualization of the OKU-soundings as a part of the FIRE high resolution seismic reflection sections with a geological map of the surface. The Outokumpu Deep Drill Hole is marked as red line. Reproduced with the permission of GTK.

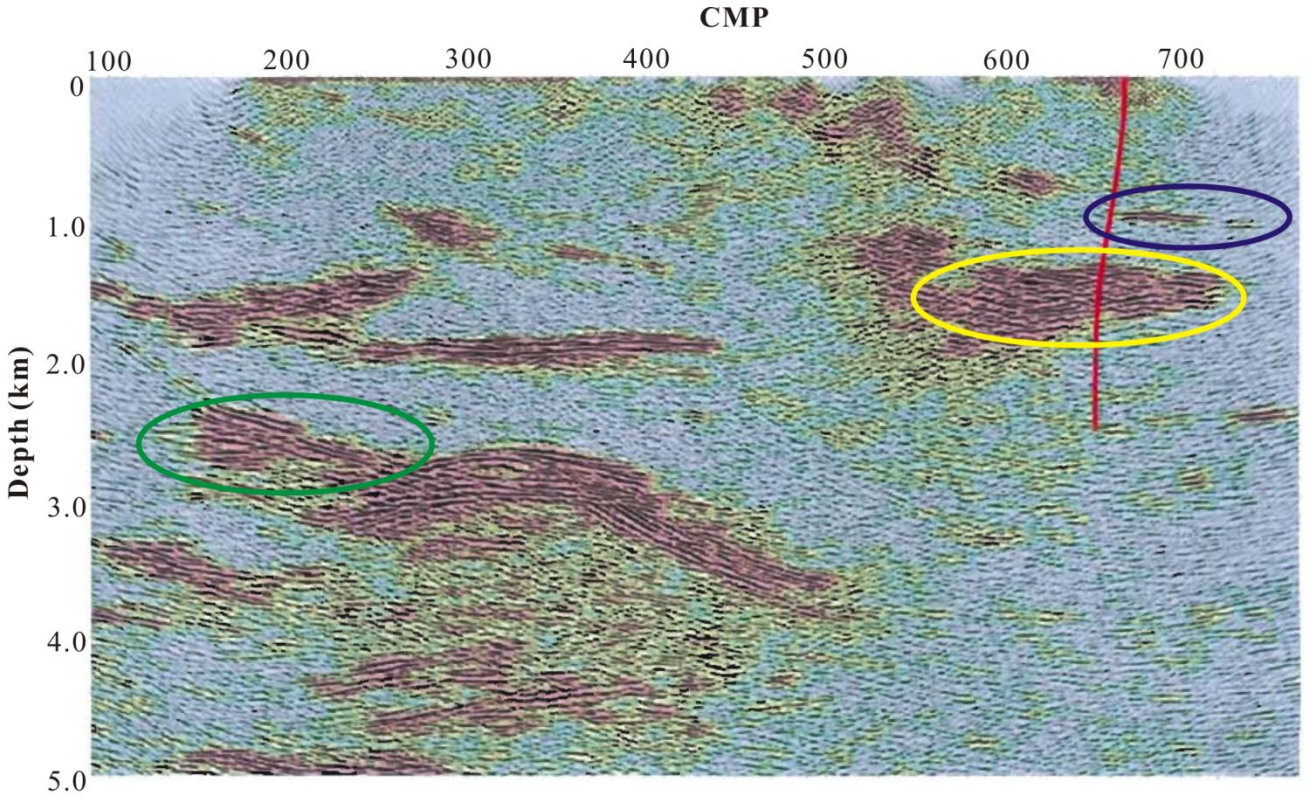

(Edited from Heikkinen and Kukkonen, 2007)

Figure 1.11 The migrated OKU-1 section. The deep hole is marked with red line.The Outokumpu-type assemblage at the depth of 1300-1750 m is showed in the yellow oval. And green oval covers an additional potential event at the depth of 2000-2500 m. Blue oval covers a reflector at the depth of near 1000 m. Reproduced with the permission of GTK.

depth of 1300-1750 m. At the depth of near 1000 m, a strong reflector can also be observed from OKU-1 profile (Fig. 1.11), which could be caused by a fracture zone located at 967 m in the OKU-1 deep drill hole (Heinonen *et al.*, 2011). However, an additional event was also observed at the depth of 2000-2500 m, and it was believed that this event had some potential for prospectively also. This anomaly together with the potential of sampling the Outokumpu-type assemblage to look for minerals motivated the drilling in 2004-2005 of a 2,516 m deep research borehole by the Outokumpu Deep Drilling Project of the Geological Survey of Finland (GTK) in order to understand the deep structure and geophysical and petrophysical properties of the ore belt.

1.4 The Outokumpu Scientific Drill Hole

The Outokumpu deep hole (OKU-1) is located on the SE side of the main ore belt, and about 400 m west from the FIRE OKU-1 line (Fig. 1.9). The borehole was nearly completely cored with unusually sized large core (216 mm diameter), this core now resides at the storage facilities of the GTK. The borehole did not intersect the anticipated seismic anomaly seen in the FIRE lines at the expected depth of 1.0-1.2 km, this is likely due to the fact that the spatial extent of the anomaly was small relative to the distance from the trace of the FIRE line and the actual borehole position. Indeed, aside from 33 m of glacial materials at the surface, the borehole cored through a uniform 1314 m of various schists (Fig. 1.12) and a biotite gneiss that, despite the differences in the geological assignations, do not significantly differ from the perspective of physical

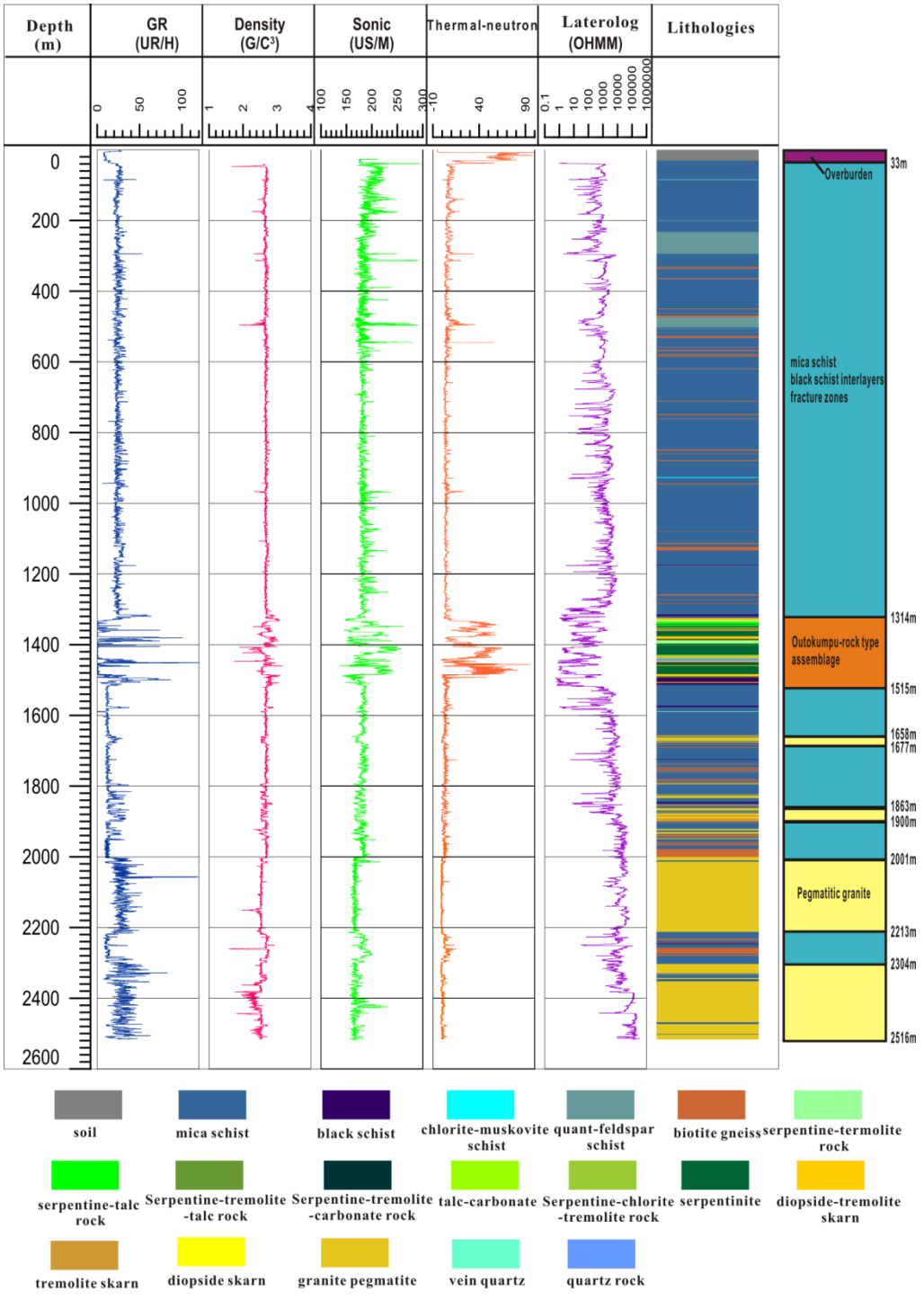

Figure 1.12 Logging records (left), lithologies (middle)from coring and the geology information(right) in deep drill hole.

property variations. Even geologically, the core interpreters referred to the thick 1300 m section of biotite schist/gneisss in jest as ‘monotonite’. About 10% of the rock types, those lying from 1314 m to 1515m, consist of serpentinite, diopside skarn, quartzite and black schist (Table 1-1). These latter rocks have a high potential to host mineral deposits and these are the Outokumpu-type assemblage believed to have ophiolitic origin as described earlier. The schists reappear beneath the 200 m thick Outokumpu-type assemblage rocks, and, somewhat unexpectedly, these are interrupted by a series of pegmatitic granites (Table 1-1). These pegmatite zones were completely unexpected.

Geophysical logs were obtained by a Russian company NEDRA during the drilling breaks. Twenty different logs were obtained in this well, including natural gamma rays (GR), lateral, laterolog, microlaterolog, spontaneous potential (SP), mud resistivity, inductive conductivity, caliper, acoustic (P-wave), gamma ray, epithermal neutron, thermal neutron, neutron-gamma, density, temperature, spectral gamma-ray, lithology, magnetic, and inclinometer. Some logging records and lithologies according to the coring from the deep drill hole are displayed on Fig. 1.12 (Kukkonen, 2007).

Another set of logs, OUTO FAC40 ultrasonic televiewer data (Fig. 1.13), was carried out in the deep drill hole from September 22 to 25, 2006 by the Operational Support Group of ICDP (International Continental Scientific Drilling Program) at GFZ (German Research Center for Geosciences) Potsdam. This 3600 oriented image of borehole shows the runtime (travel time) as a function of drilling mud properties and hole size and the

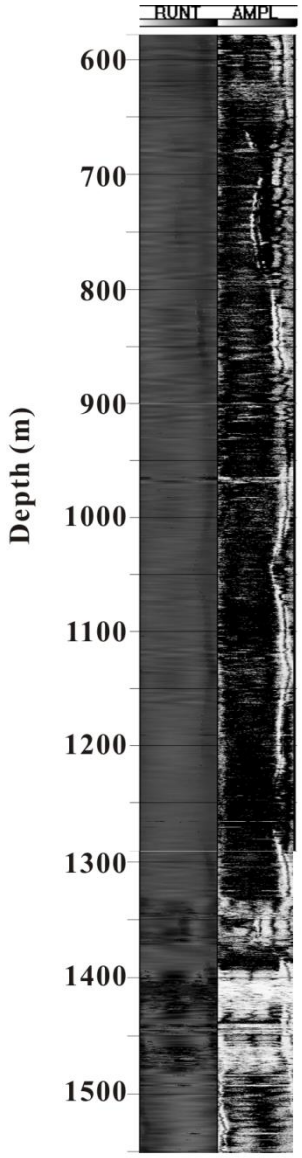

Figure 1.13 The OUTO FAC40 televiewer data from the Outokumpu Deep Drill Hole.

amplitude of reflected signal as a function of drilling mud, hole size, wall micro-rugosity and wellbore acoustic impedance contrasts (Prensky, 1999). It is mainly used to display fractures and other geological features. The data has been north oriented. For AMPL image (acoustic impedance), dark color has higher amplitude than the light color. On RUNT (travel time) image, dark color means a longer travel time than light color. And fractures are usually displayed on AMPL image as sine curves.

The geophysical logs show large variations through the Outokumpu-type assemblage between 1314 m to 1515 m depth (Fig. 1.12) on GR, thermal-neutron, laterolog, density, sonic and the televiewer data. Outside of this Outokumpu-type assemblage section, the density remains quite uniform and nearly constant through a given lithology; the pegmatite zones have slightly lower density than the schists.

Substantial transit-time sonic log (and hence *Vp* velocity) variations can also be observed through the Outokumpu assemblage. Similar patterns can be recognized from laboratory measurements on core samples (Elbra *et al.*, 2011, Kern *et al.*, 2009).

Kern et al. (2009) measured the elastic wave velocities, chemistry and modal mineralogy of 13 selected samples in the Outokumpu deep drill hole. P- and S- wave velocities were measured in the three foliation-related structural velocities as a function of pressure which was up to 600 MPa. The strong anisotropy of P- and S- wave velocities, which was found to be strongly related to foliation, was revealed. Further, it was revealed that the in

situ elastic wave velocity is very sensitive to the state of microfracturing.

Elbra et al. (2011) focused on the petrophysical measurements. The pressure during the P- and S-wave measurement ranged from 3 to 40 MPa depending on the sample depth. According to Elbra et al (2011), the various lithological units can be identified on the basis of their petrophysical properties. The density shows a little variation through the uppermost part of the core. It decreases a little with depth with a range from 2700 kg m^{-3} to 2800 kg m^{-3}. The schist series exhibits the lowest density, about 2636 kg m^{-3}. But the ophiolitic complex (Outokumpu-type assemblage), which is from 1314 m to 1515 m, shows a greater variations in density from as low as 2514 kg m^{-3} to as great as 3158 kg m^{-3}. Elbra et al. (2011) measured the V_P at *in situ* pressure. It increases with depth. The average V_p for upper schist series is 5509 m/s. The ophiolitic complex exhibits an average 5622 m/s on V_P. But Elbra et al. (2011) note that their measured velocities may be significantly affected by drilling induced microfracturing. This is consistent with Kern et al. (Kern *et al.*, 2009).

Despite those seismic reflection surveys in Outokumpu area, the Outokumpu-type assemblage is still incompletely understood. The Outokumpu deep drill hole provides improved knowledge about the physical properties of upper crustal rocks. However, seismic reflection survey may reveal much wider area and not suffering from microfracturing caused by coring related disturbances on the rock (Kern *et al.*, 2009, Kern *et al.*, 2001). However, Shijns et al, (2011) suggest that a pervasive series

microcracks, possibly related to the in situ state of stress, may have an important influence on the overall seismic anisotropy of the area.

After the deep drill hole was drilled in Outokumpu, a VSP survey was conducted in May 2006 in an ICDP funded collaboration of the Finnish GTK, the Institute of Seismology at the University of Helsinki, and the University of Alberta (Fig. 1.9). Simultaneous with the walk-a-way VSP acquisition of this study (Schijns et al, 2011, Schijns et al, 2009), 2-D seismic reflection surveys were obtained (Fig. 1.9). VSP is a three letter acronym for Vertical Seismic Profiling. It is one of techniques of seismic measurement, and usually used for correlation with surface seismic data. The energy source for VSP measurement is placed on the surface, near the well head or with a distance to the wellhead. And geophones are fixed on the wall of the well, far below the surface, which is one big difference between VSP measurement and surface seismic survey.

This VSP survey in Outokumpu deep drill hole consists of a zero-offset VSP, a far-offset VSP, and a series of walkaway VSP's with the receiver at three different depths of 1000 m, 1750 m, and 2500 m. The zero offset VSP (see Chapter 3) was recorded at 2 m depth increments from 2500 m to 50 m, which allows us to get a high resolution profile. The VSP survey was done in order to determine detailed structure of the bedrock nearby the deep drill hole and combine straight measurements done in deep drill hole to surface measurements. Besides the VSP survey, the 2D surface seismic survey consists of two crooked seismic lines which were acquired at a 1 ms sampling period, 5 s recording

length aimed at high resolution seismic imaging and further refining the geology model. They were almost perpendicular to each other, but there unfortunately was no crossing point among the seismic lines and the deep drilled hole.

The work in this thesis continues the examination of this unique seismic data set. This work builds on the earlier studies of Suvi Heinonen (Heinonen *et al.*, 2011) who processed some of the reflection data and of Schijns et al (2009) who developed a detailed model of the near surface velocity structure that is necessary to correct the data. In this thesis I process all of the surface reflection data and the zero-offset VSP data. These data are then combined to examine in more detail the reflectivity in the crystalline crust in the vicinity of the OKU borehole.

1.5 Summary

This study area, Outokumpu, is a hard rock area. The Outokumpu-type assemblage, which lies from 1314 m to 1515m, consists of serpentinite, diopside skarn, quartzite and black schist. These rocks have a high potential to host massive Cu-Co-Zn sulphide deposits (~1.97 Ga) which were first discovered in 1910. From logging information and laboratory measure, the Outokumpu-type assemblage section reveals an abnormal density and velocity variation comparing to the other rather uniform lithological zones. Even though seismic reflection technology has seldom used for ore exploration due to the complex properties and structures of hard rocks, some successful cases of finding minerals by using modified

seismic reflection methods have been presented in recent decades. In this thesis, a zero offset VSP survey and two 2D seismic lines, which were recorded in 2006, were used to study the seismic reflection characteristic of sulphide deposits in Outokumpu. More details are described in the following chapters.

2.0 2D Seismic Surface Survey

Although the central theme of this thesis will focus on the zero-offset vertical seismic profile (VSP) collected at Outokumpu in Chapter 3, much of that VSP's value is lost without the ability to use it to better understand the reflectivity observed in surface profiles. As noted above, there has been a good deal of 2D seismic reflection profiling obtained in the vicinity of the well as part of the FIRE project. That data led to the siting of the well in order to attempt to intercept both the Outokumpu-type assemblage and a tantalizing shallower prospective seismic event. During the VSP surveys, we were also simultaneously able to obtain even higher spatial resolution, but shorter, seismic profiles radiating from the borehole. The description of these 2D lines is the focus of this chapter.

It needs to be mentioned that the work here builds on earlier processing analyses of Heinonen (Heinonen *et al.*, 2011), and the near surface static corrections constructed by Schijns et al. (2009).

This chapter covers the seismic processing of the high resolution Outokumpu 2D seismic profiles. The chapter starts with a brief background, history, and applications of reflection seismology in order to assist the nonexpert reader in understanding the work. The seismic survey and processing methods will be subsequently described after analysis of data acquisition and quality of these two 'crooked' 2D seismic lines. The processing sequence mainly includes defining geometry, amplitude compensation, noise attenuation,

deconvolution, velocity analysis, CMP stacking and image migration. Special considerations are given to the problems associated with crooked lines and quality control.

2.1 Introduction

Reflection seismology plays a prominent role in investigating the earth's interior structure, studying earthquakes, locating coal, mineral deposits and hydrocarbon resources and delineating near-surface geology for engineering studies. In principle, there is nothing limiting the depth that reflection profiles can be obtained but this of course is highly dependent on the strength of the seismic source employed. Artificial sources such as vibrators and explosions are typically limited to depths of at most 100 km. However, there has been much progress in recent years with the use of earthquake sources to help image even deeper; and intelligent use of arrays of seismometers are now extending reflection profiles to the 670 km discontinuity if not deeper. Recent work in this area has been reviewed by Gu (Gu, 2010).

Obtaining reflection seismic profiles usually contains three stages: data acquisition, processing, and interpretation. With the combination of other geophysical, borehole and geologic data, seismic profiles can provide reliable information about the structure and distribution of rock types (Sheriff and Geldart, 1982). The reflection seismology technique basically involves generating seismic waves and recording the time that waves

travelled from the source to a series of geophones (Lay and Wallace, 1995). The traveltimes depend upon the properties of rocks and the structure of beds.

In mathematics and science, a wave is a disturbance. It is a transfer of energy through space and time. Amplitude is the height of the wave. The wavelength is the distance from one wave top, or crest, to the next. The time required for a wave to travel one wavelength is its period (Fig. 2.1). Frequency is the number of periods a wave completes per unit time. Period and frequency are inverses of one another. The wave can be described by one-dimensional scalar wave equation (Stein and Wysession, 2003) :

$$\frac{\partial^2 u(x,t)}{\partial x^2} = \frac{1}{v^2}\frac{\partial^2 u(x,t)}{\partial t^2} \tag{2-1}$$

where u is the displacement, x is the position, t is the time, and v is the propagation speed of the wave. The propagation velocity of the waves depends on density and elasticity of the medium. There are two types of velocities that are associated with waves: phase velocity and group velocity (Main, 1993) (Fig. 2.2). Phase velocity is the rate at which the phase of the wave propagates in space. It is described by the wavelength λ and period T.

$$v_p = \frac{\lambda}{T} \tag{2-2}$$

or by the wave's angular frequency ω and wavenumber k

$$v_p = \frac{\omega}{k} \tag{2-3}$$

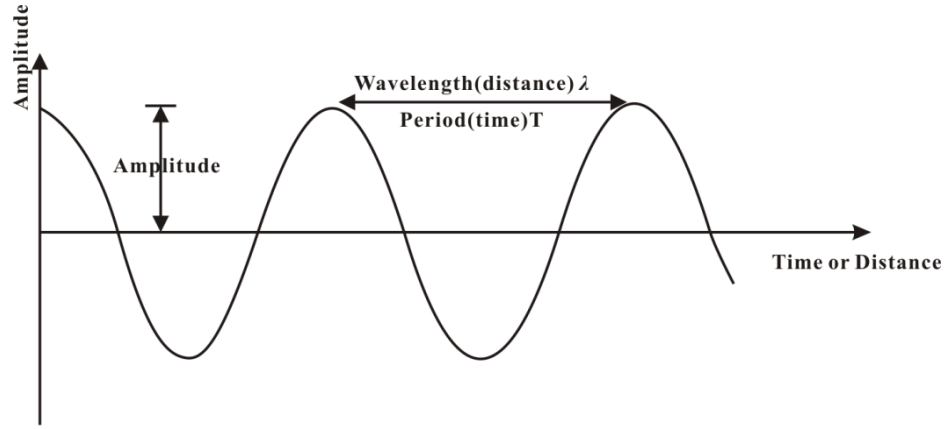

Figure 2.1 The wavelength and amplitude of a wave.

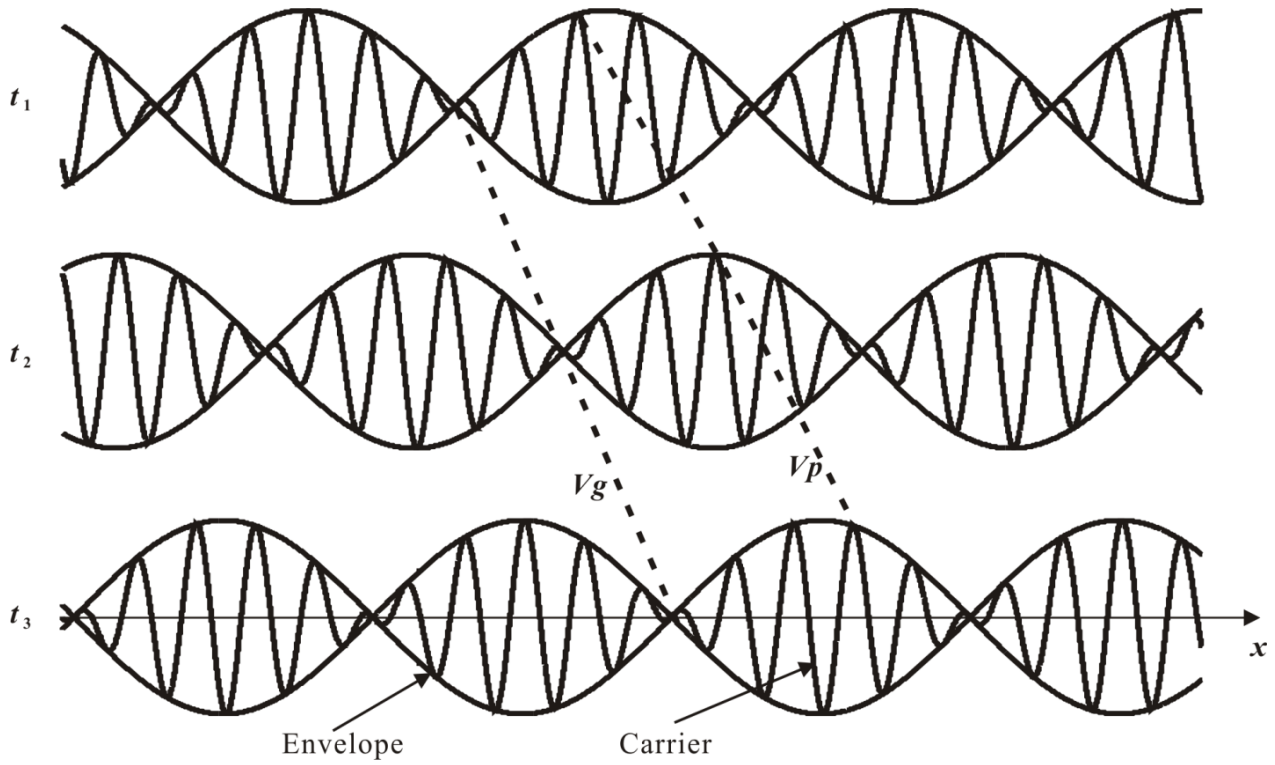

Figure 2.2 Phase velocity (*Vp*) and group velocity (*Vg*) of waves.

where $\omega = 2\pi f$, and $k = 2\pi / \lambda$.

The group velocity v_g is defined by the equation:

$$v_g = \frac{\partial \omega}{\partial k} \tag{2-4}$$

Seismic waves are waves of mechanical elastic energy that travel through the earth. When the seismic energy is released from sources, two different wave types are generated: body waves and surface waves (Fig. 2.3). The energy of body waves propagates through the earth, and those remaining energy of surface waves spreads out over the surface. Body waves can be further classified into P-waves or compression waves and S-waves or shear waves by the types of particle motion in their wavefronts. For P-waves, the particle motion is parallel to the direction of propagation. For S-waves, the particle motion is perpendicular, or transverse, to the direction of propagation. The propagation velocity of the waves depends on density and elasticity of the medium and tends to increase with depth. The velocity of P-waves is given by

$$v_p = \sqrt{\frac{k + \frac{4}{3}\mu}{\rho}} = \sqrt{\frac{\lambda + 2\mu}{\rho}} \tag{2-5}$$

where k is the bulk modulus, λ is the first Lamé parameter, μ is the shear modulus, and ρ is the density of the material that the wave propagates. The velocity of S-waves is given by

$$v_s = \sqrt{\frac{\mu}{\rho}} \tag{2-6}$$

In liquids and gases, μ is zero. So S-waves can only propagate in solid materials. And the P-waves travel usually about twice as fast as S-waves and can travel through any medium. P-waves are the dominant waves in reflection profiling as they are usually more easily generated. Further, because they arrive first their coda tend to obscure the later S-waves.

Surface waves (Fig. 2.3) travel more slowly than body waves and exist whenever there is a interface separating media with different elastic properties (Lay and Wallace, 1995). Their amplitudes decrease with increasing distance from the surface. Analogously to body waves, there are two types of surface waves, Love waves and Rayleigh waves that are classified by the types of particle motion in their wavefronts. Rayleigh waves are combinations of P and SV waves and propagate along a free surface of a solid. The particles in the wavefront of the Rayleigh wave are polarized to vibrate in the vertical plane. They are also known as ground roll. Love waves are essentially horizontally polarized shear waves (SH waves). The particle motion of a Love wave forms a horizontal line perpendicular to the direction of propagation. Love waves travel faster than Rayleigh waves. Although surface waves can in principle be used to study shallow structures (e.g. Beaty *et al.*, 2002) most reflection imaging surveys utilize only the compressional P-waves. Surface waves are treated as coherent noise which needs to be removed or attenuated from the data in order that reflections are highlighted.

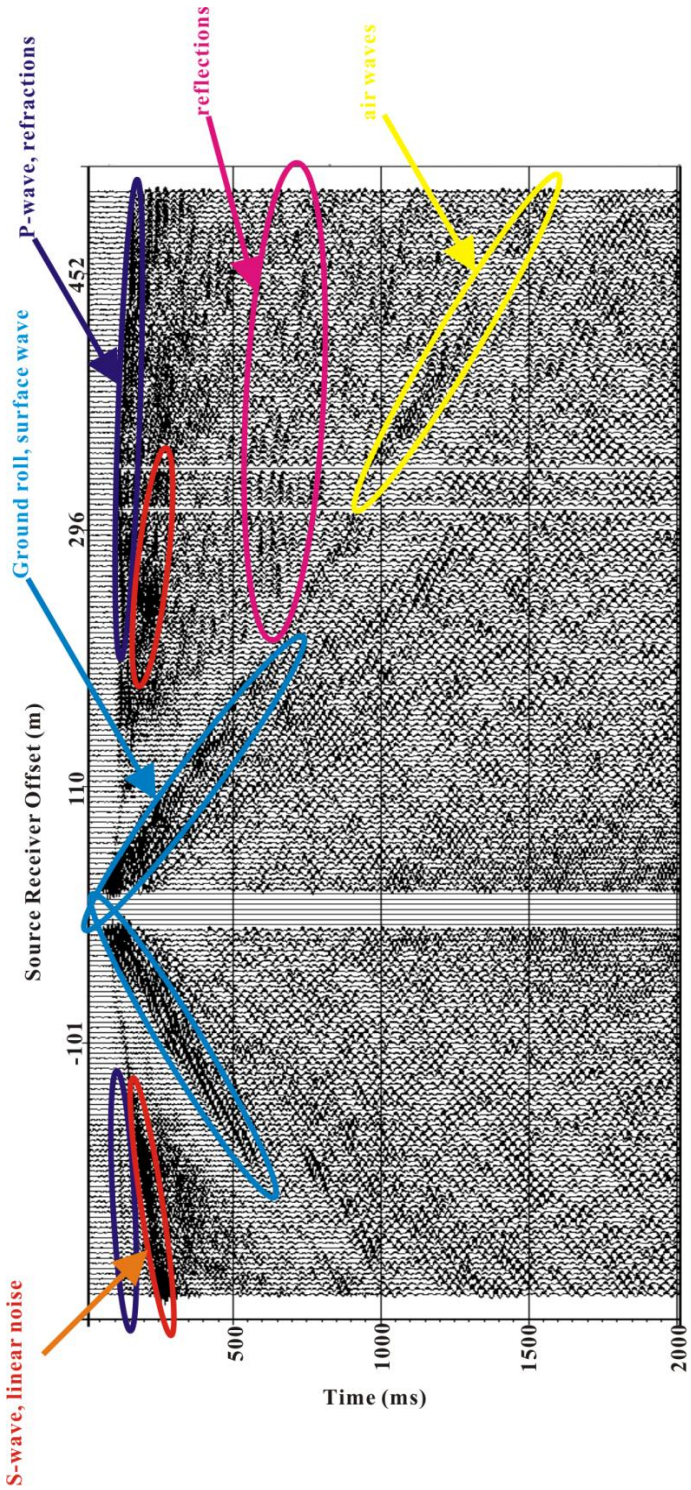

Figure 2.3 Wave types on a shot gather from line_2000.

When seismic waves propagating within the earth encounter an interface between two different media or an abrupt change in the elastic properties, part of energy will be reflected and the remaining energy will be transmitted. When a compressional wave is normally incident on the interface (Fig. 2.4), a transmitted wave travels vertically through the interface with a zero angle of incidence and a reflected wave returns back along the track of the incident wave (Kearey and Brooks, 1984). The total energy of the reflected wave and the transmitted wave equals to the energy of the incident wave.

The reflection coefficient *R* is described by

$$R = A_1 / A_0 \tag{2-7}$$

where A_0 is the amplitude of the incident wave, and A_1 is the amplitude of the reflected wave. For a normally incident wave, *R* is given by

$$R = \frac{\rho_2 v_2 - \rho_1 v_1}{\rho_2 v_2 + \rho_1 v_1} = \frac{Z_2 - Z_1}{Z_2 + Z_1} \tag{2-8}$$

where ρ_1, v_1, Z_1 and ρ_2, v_2, Z_2 are the density, P-wave velocity and acoustic impedance in the first and second layers, respectively. (See also Chapter 1).

The transmission coefficient *T* is described by:

$$T = A_2 / A_0 \tag{2-9}$$

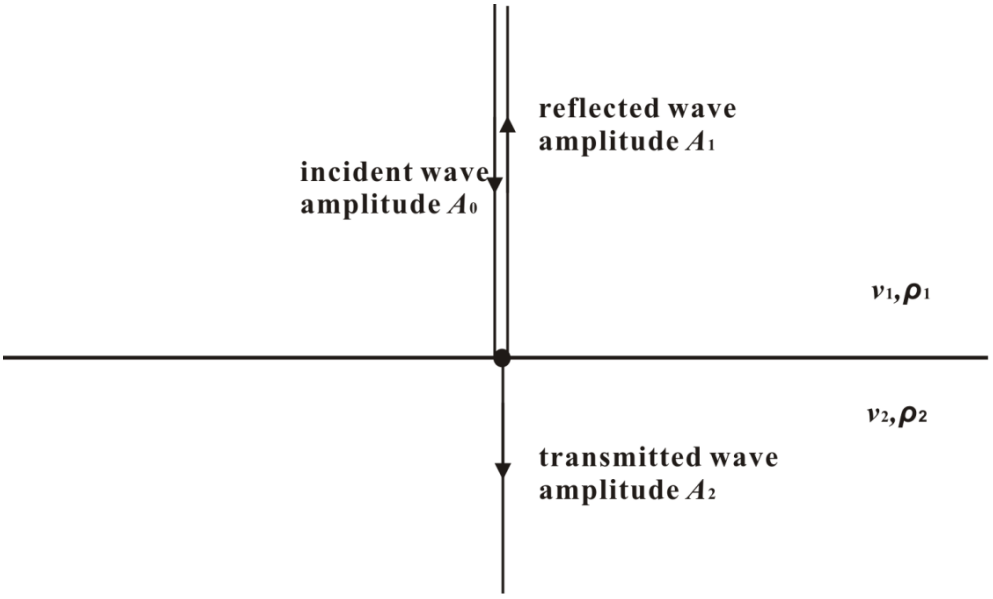

(kearey and Brooks, 1984)

Figure 2.4 Reflected and transmitted waves
generated by a wave normally incident on an interface

And for a normally incident wave, this is given by

$$T = \frac{2Z_1}{Z_2 + Z_1} \tag{2-10}$$

Typically, the reflection coefficient R is less than ± 0.2. Most of the seismic energy incident on a interface is transmitted, and only a small proportion is reflected (Kearey and Brooks, 1984).

When a seismic wave is obliquely incident on the interface, the reflected and transmitted waves are generated as in the case of normally incidence (Fig. 2.5). The transmitted wave travels with a changed direction and is referred to as a refracted wave. The relationship between the angles of incidence and refraction is described by Snell's law:

$$\frac{\sin\theta_1}{\sin\theta_2} = \frac{v_1}{v_2} \tag{2-11}$$

where θ_1 and θ_2 are the incidence angle and the refraction angle, respectively. v_1 and v_2 are the velocities of wave in different materials.

Both reflections and refractions are useful waves in exploration seismology. Refracted arrivals are used to map the weathered layer and determine velocities in near surface, which are applied to calculate the statics for sources and receivers. However, this study makes little use of refracted information and hence the reader is referred to any of various references on applied seismology (e.g., Kearey and Brooks, 1984). However, this study

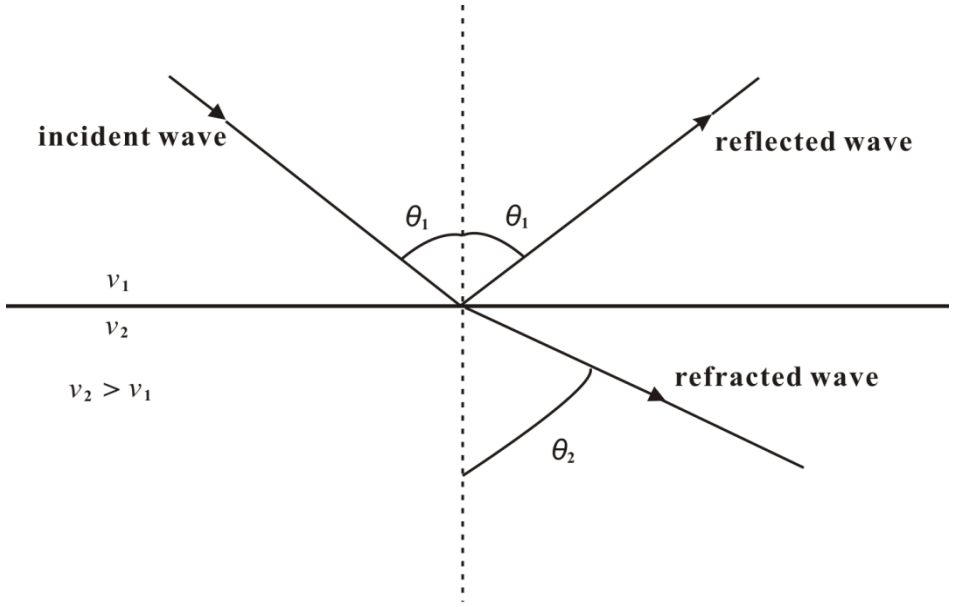

Figure 2.5 Reflected and refracted waves
generated by a wave obliquely incident on an interface.

does employ the surface travel time corrections developed by Schijns et al (2009) from tomographic analysis of the refracted waves.

Reflection information is what we mainly used to map the more detailed structure of the subsurface. The history can be traced back to 1917 when Reginald A. Fessenden issued his patent on the application of seismic waves to exploration. Then, this technique has been developed very rapidly. It is mainly used to reduce risk in the petroleum industry. Wells are now rarely drilled without existing seismic information beforehand to elucidate the buried geological structures. Techniques of acquiring and processing reflection data have also been developed to a very high level due to extensive applications in petroleum exploration, which will be described later.

How detailed the structure information obtained could be obtained is really a problem of the seismic resolution possible. Seismic resolution describes the ability to individually distinguish two close features. There are both vertical and horizontal limits to the resolution.

The vertical resolution depends primarily on the frequency content of the signal. The vertical resolution criterion is often expressed as being equal to $\lambda/2$ (a separate limit), where λ is the predominant wavelength of the incident wavelet. So the measured anomalies are separately distinguishable. A resolvable limit of resolution is expressed as $\lambda/4$ (Widess, 1973). In this case, two anomalies are close together, but still can be

individually distinguished. When two anomalies merge, it is impossible for their signatures to be well separated and they cannot be resolved.. So a layer, which is thinner than the $\lambda/4$ of the incident wavelet, could not be detected by seismic surveys. The vertical resolution can be increased by shortening the wavelength, i.e. increasing the frequency (Fig. 2.6 (a)). However, high frequency signals suffer more attenuation; consequently the vertical resolution decreases with the depth. The deeper the layer, the lower the frequency can be received.

Horizontal resolution describes how close two reflecting points can be separated horizontally. It is usually estimated from the width of the first Fresnel zone, R_f, which is expressed as (Sheriff, 1989):

$$R_f = \frac{v}{2}\sqrt{\frac{t}{f}} \tag{2-12}$$

where v is the seismic velocity; f is the frequency and t is two-way reflection time traveled by the seismic waves from the surface to the reflecting interface and back. The first Fresnel zone may be approximately described as an area on the reflecting surface from which scattered, seismic waves arriving back at the receiver interfere constructively and arrival at about same time. As such, any arrivals from this patch cannot be individually resolved. Subsurface features smaller than the Fresnel zone usually cannot be resolved using seismic waves although they might be still detected via their scattering response. High frequency (or equivalently shorter wavelengths) narrows the Fresnel zone.

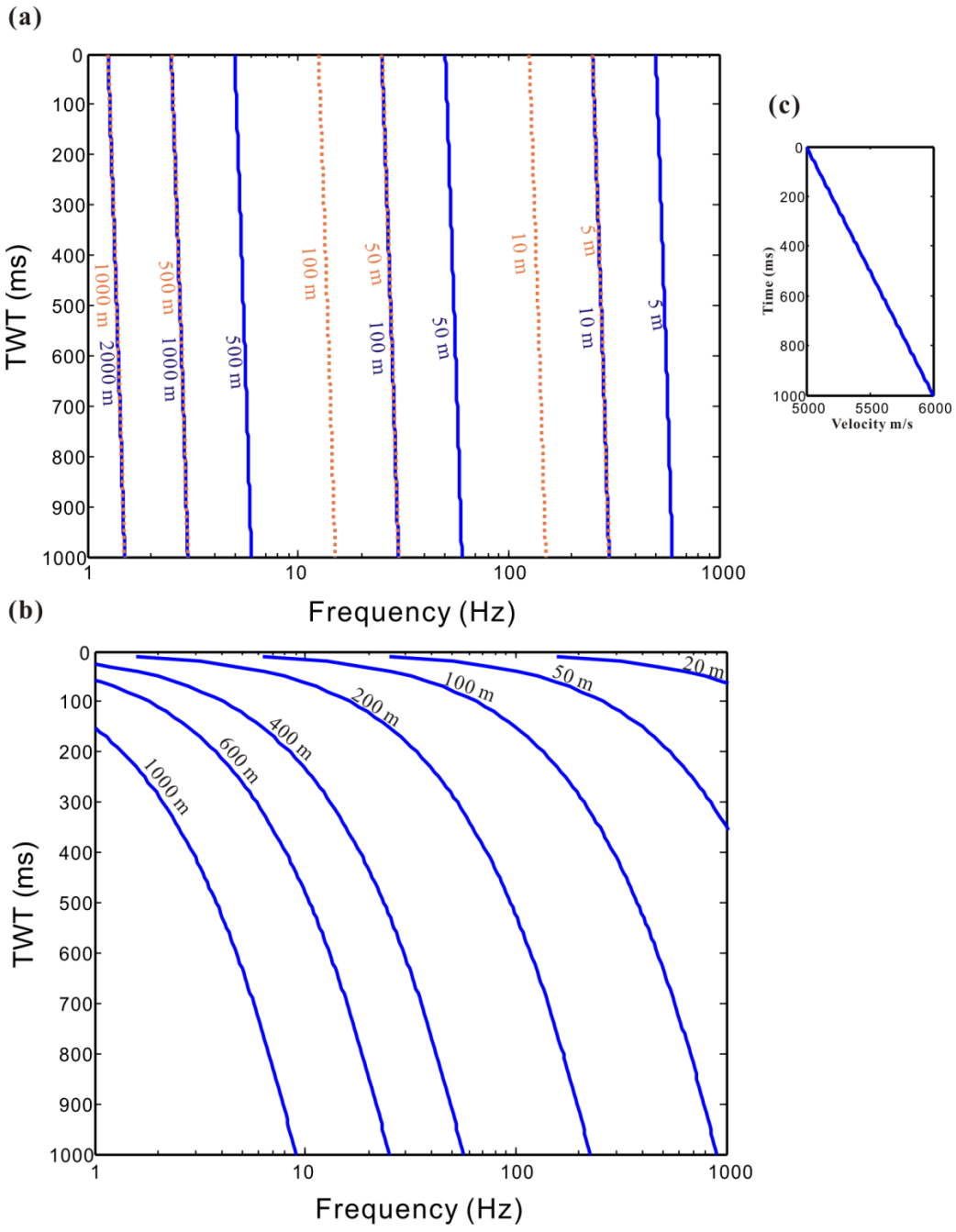

Figure 2.6 The vertical resolution (a) of separable expression (blue line) and resolvable expression (orange dot line) and the horizontal resolution (b) in seismic exploration based on a velocity model (c)

But it not only depends on the frequency, but also on the velocity and depth of reflectors (Yilmaz, 2001).

Fig. 2.6 shows the vertical and horizontal resolution variation as frequencies of 1-1000 Hz with a model (Fig. 2.6 (c)) of velocity linearly increasing with depth from 5000 m/s to 6000 m/s. These velocities are illustrative of those observed at Outokumpu. Both the vertical resolution and the horizontal resolution decrease with depth and increase with frequency without considering of the earth filtering to higher frequencies. The horizontal resolution has more rapid decrease than the vertical resolution in depth, and less increase with frequency. At the frequency of 250 Hz, the resolvable vertical resolution is between 5 m and 10 m, but the horizontal resolution is about 200 m.

The seismic reflection survey generates a structure image in the earth's interior. It can be carried out on land or on water. Depending on the purpose of exploration or economical reason, it can be a 2D or 3D survey. The 3D seismic acquisition is much more complicated and more expensive than 2D seismic. The result of 3D seismic survey can be thought as a volume of data which can be sliced in arbitrary ways to produce seismic lines in arbitrary directions; consequently, the volume of data is huge. 3D methods had not been accepted extensively until computer technologies were rapidly developed in 1970s (Nelson, 1983).

A 2D seismic survey is relatively cheap and easy to implement. The energy source is

placed on the same surface line with a number of receivers (Fig. 2.7). Seismic work is carried out along the line where the seismic profile is desired, although surface features and culture must be considered in the layout. Data acquisition consists of activating the source and simultaneously triggering the seismic recording system that acquires the signals from the otherwise passive geophones. As sources and receivers move along the line, subsurface structure under the line is able to be delineated after data processing (Fig. 2.8).

Sometimes, due to the surface situation or exploration needs, a survey line could be crooked due to local culture and topography, this is the case at Outokumpu. When the survey line is crooked (Fig. 2.9), the common midpoints (CMP) cannot all fall on the same location as in a ideal 'straight' 2D seismic survey. The CMP points are distributed in areal patches instead of at points. To cover them, a rectangle bin grid is chose as Fig. 2.9 shows. The surface line (Processing line) could be straight or curved (Wu *et al.*, 1995, Kashubin and Juhlin, 2010) depending on the need of processing and how crooked the survey line is. However, neither of them would be able to follow the survey line exactly. Usually it is defined by following the density of CMP points (Wu, 1996). This irregular survey brings some special problems, such as variable fold coverage and uneven offset distribution. Further, some difficulties would be introduced into processing, too. It needs to deal with the less effectiveness in conventional stack and migration caused by the existence of the cross-dip which means that the subsurface reflectors have a dip angle in

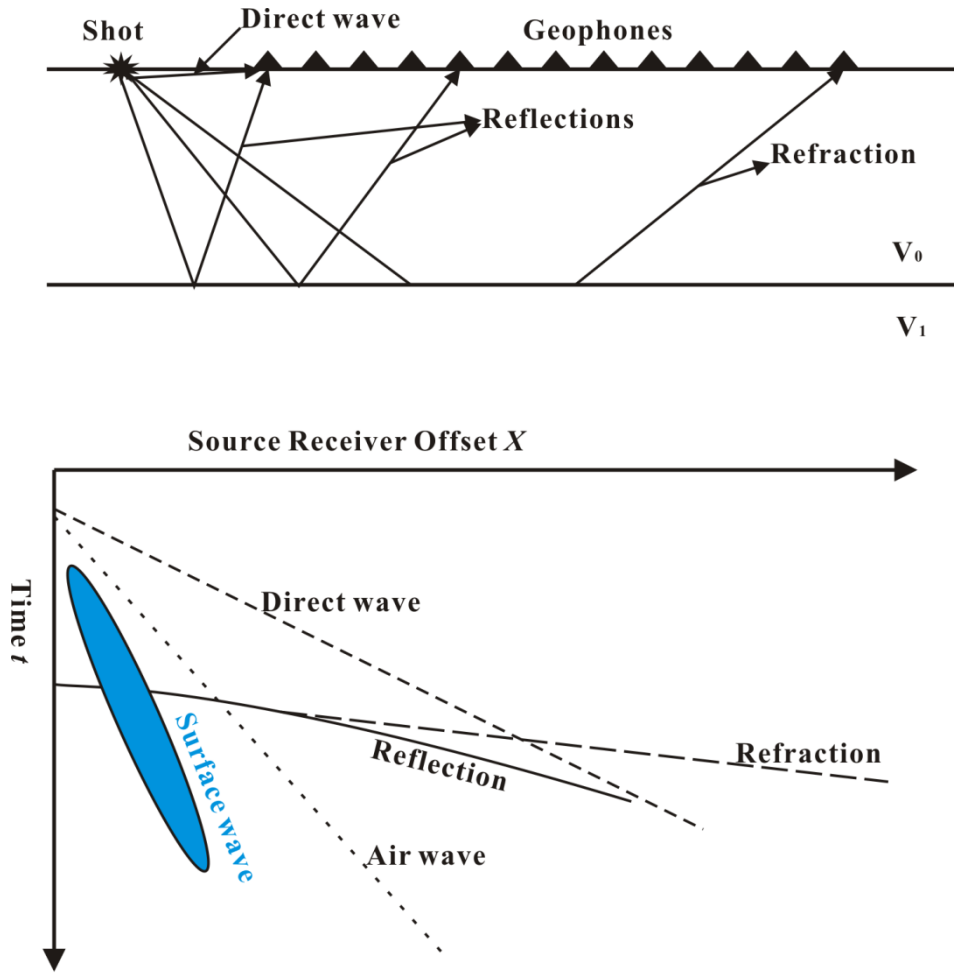

Figure 2.7 A cartoon of source-receiver geometry and seismic wave types in a shot.

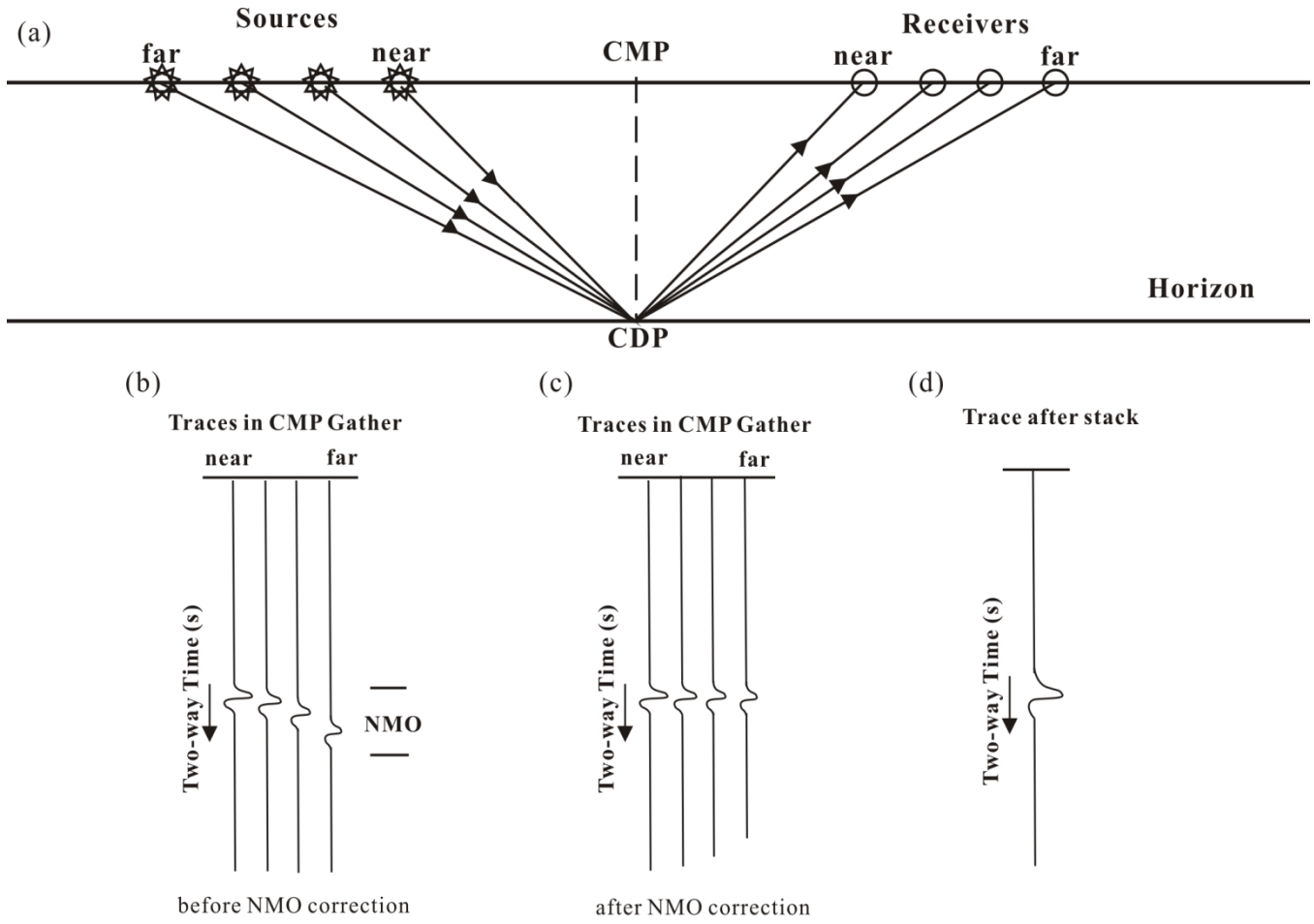

Figure 2.8 A cartoon for surface seismic geometry (a), a CMP gather (b) generated from (a), NMO (normal moveout) correction (c) and stacked trace (d).

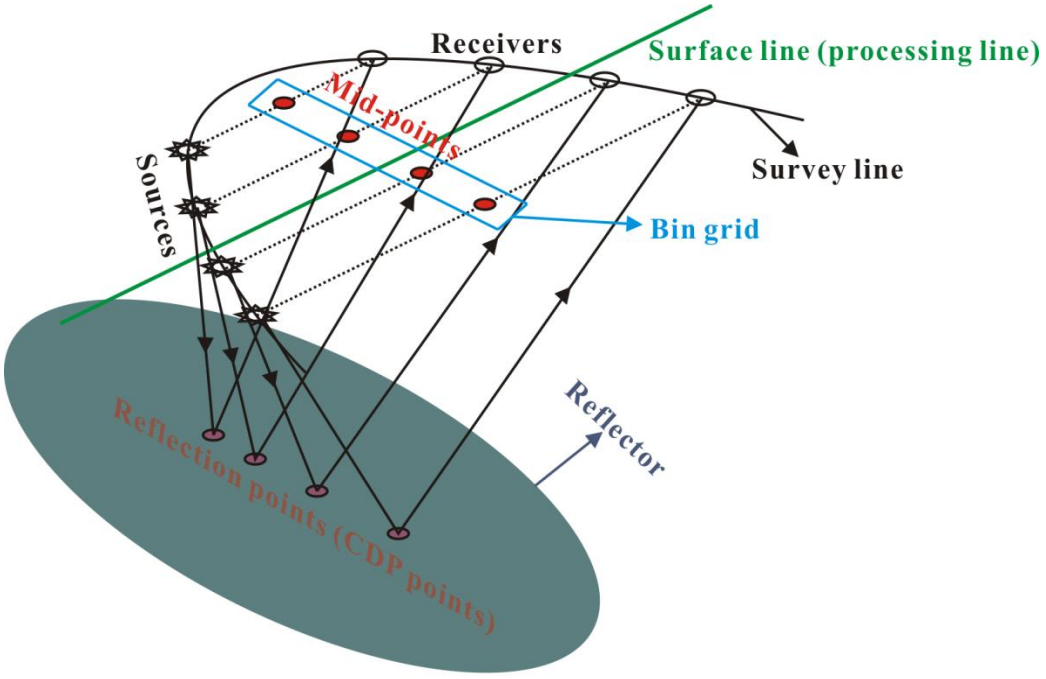

Figure 2.9 A cartoon to show the crooked line geometry

the direction perpendicular the surface line (Nedimovic, 2000). This issue will appear with the data analyzed in this chapter.

Some successful examples of handling crooked-line geometries have been published. Wu et al. (Wu *et al.*, 1995) and Nedimovic and West (Nedimovic and West, 2003a) both presented a cross-dip stack method applied by correcting the cross-dip-moveout (CDMO) before stack. And Nedimovic and West (2003a) also presented another method they called amplitude stacking that proved to be effective to improve the stack imaging. Kashubin and Juhlin (2010) produced 'alternative CDP binning strategies', which involves changing the orientation of the bins according to the estimated cross-dip to better align the reflection events. In addition to these methods that focus on stack imaging, Schmelzbach et al. (2008) presented a diffraction imaging scheme to enhance the image. Further, Nedimovic and West (2003b) provided a 3D Kirchhoff Prestack migration algorithm to construct a 3D image volume from the data obtained; in this way a 2D crooked survey instead provides some 3D information along the profile Successful processing can even provide the strikes and dips information of reflectors (Bellefleur *et al.*, 1998).

The data recorded from receivers is in digital form as a number of shot gathers (Fig. 2.7). As shots and receivers are moved forward along the survey line in a fixed interval, multiple-fold seismic records are obtained. As Fig. 2.8 (a) showed, there are a certain number (fold) of traces from different shots and receivers at a common depth point (CDP)

which is assumed to lie below the corresponding common midpoint (CMP) on the surface. Fold is used to describe how many traces bottom within same CMP point. Fold is determined by the number of 'live' receivers in a spread and the spacing between the source points in a regular seismic survey. Shot gathers will be sorted into CMP gathers like Fig. 2.8 (b).

In one CMP gather the reflection traveltime curve as a function of offset is approximately a hyperbola. The time difference between traveltime at a given offset and at zero offset is called normal moveout (NMO) (Yilmaz, 2001). And the NMO correction is the method to remove the time differences caused by different offsets. After NMO correction (Fig. 2.8 (c)), traces in a same CMP gather will be summed together to generate a strong seismic stacking trace (Fig. 2.8 (d)). So a stack profile can be gained after all the CMP gathers are summed (Fig. 2.10). A simple processing sequence is illustrated by Fig. 2.11. The data acquired in the field includes not only the desired reflections for imaging but also refractions, surface waves and multiples (Fig. 2.7). Further, we also need to face other amplitude, frequency, and velocity problems before we can map the subsurface. So it is really necessary to process the data before interpretation.

2.2 Seismic Survey and Data Acquisition

These two crooked seismic lines (line_2000 and line_3000, Fig. 1.10) in Outokumpu were recorded in 2006 by University of Alberta, the GTK (Geological Survey of Finland)

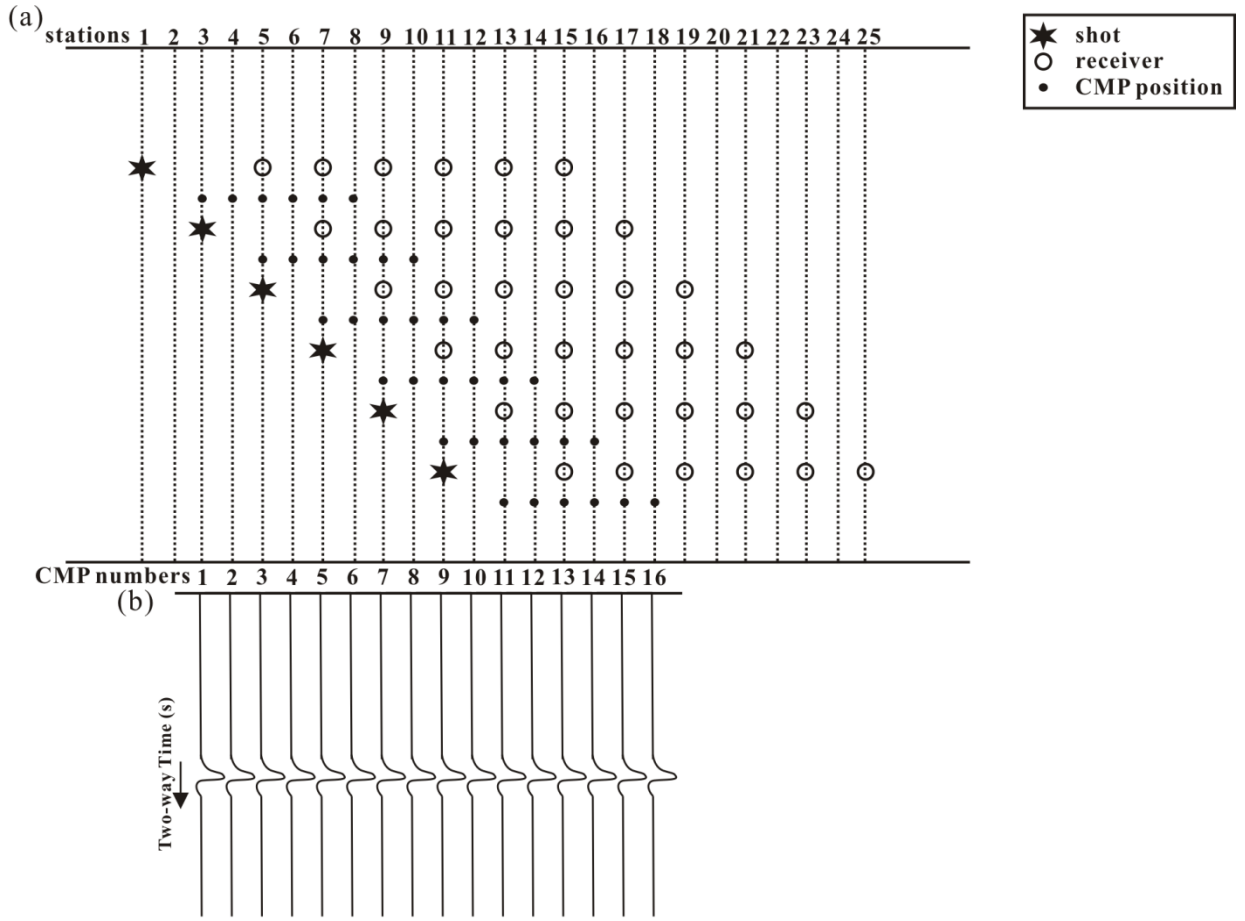

Figure 2.10 A cartoon of a stacking chart in a 2D seismic survey (a) and the stack profile (b) from (a).

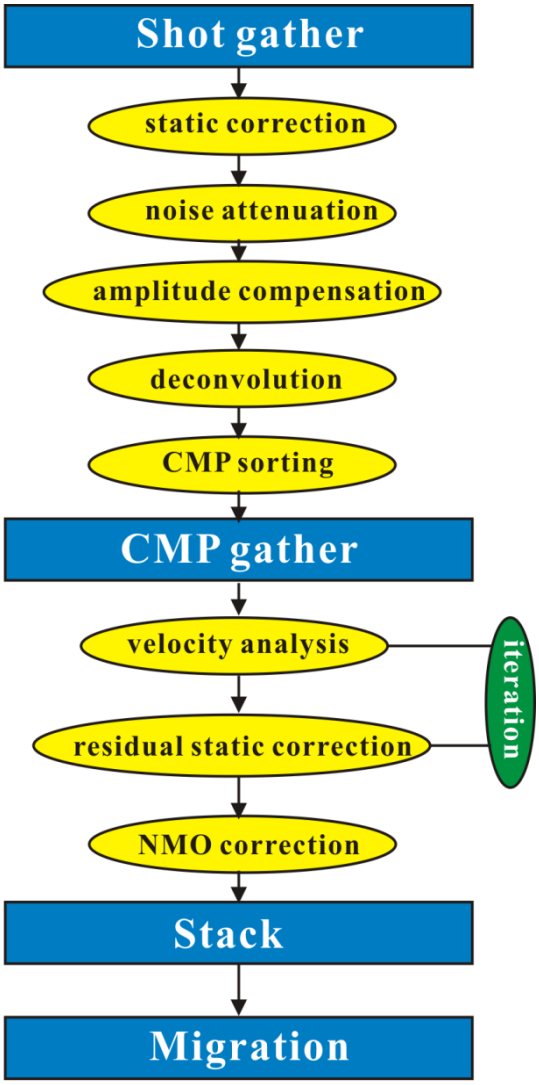

Figure 2.11 A simple processing procedure

and Institute of Seismology of University of Helsinki as part of a project funded by the International Continental Drilling Program. These profiles were obtained near the OKU-1 deep drill hole in order to improve the determining the detailed underground structure. Acquisition of the lines was complicated by the irregular topography (Schijns *et al.*, 2009), natural features, and human occupation. As such, obtaining truly straight lines was impossible. Further, the two profiles were almost perpendicular to each other, but the local culture did not allow for a crossing point among the lines and the deep drilled hole.

Seismic data were acquired with a 1 ms sampling period on 216 channels using a semi-distributed system (Geode®, Geometrics, California). A high-frequency vertical seismic vibrator (IVI MinivibTM, Industrial Vehicles International, Oklahoma) source employed an 8 s linear taper sweep with frequencies 15–250 Hz with a nominal force of 25 kN (~5500 lbs). The nominal source gap was 20m, and receiver gap was 4m. The total recording length is 5 seconds.

From the geometry figures of Fig. 2.12 and Fig. 2.13, we can see these two 2D seismic lines were particularly crooked for the reason of avoiding houses and other buildings. Sources are shown as red squares, and receivers are blue squares. Line_2000 was covered by both sources and geophones, but line_3000 could not be completely covered by geophones due to time constraints. Indeed, these reflection profiles were really only obtained while taking advantage of the fact that the walk-a-way VSP's were being obtained. As noted by Schijns et al (2009), however, obtaining these surface profiles was

(a)

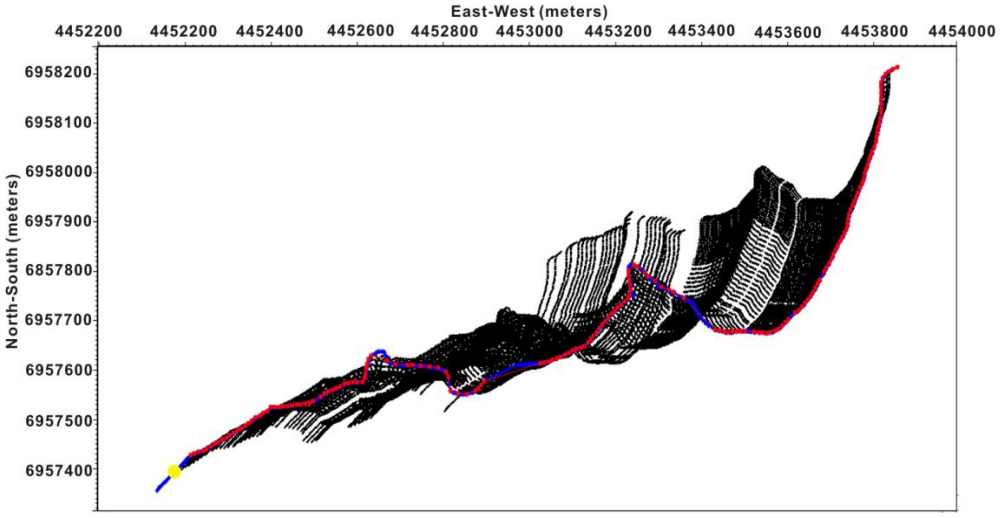

(b)

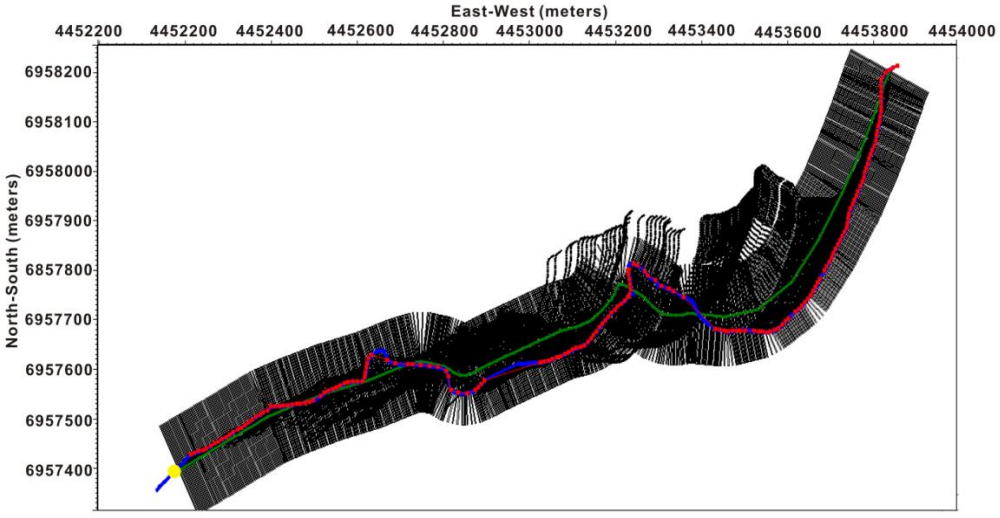

Figure 2.12 (a) geometry of line_2000.(b) the definition of bin grids. Sources are marked by red squares. Blue squares are receivers. And black points show CMP positions. Surface lines are shown as dark green lines. The rectangles are bin grids. The deep drill hole is shown as yellow points.

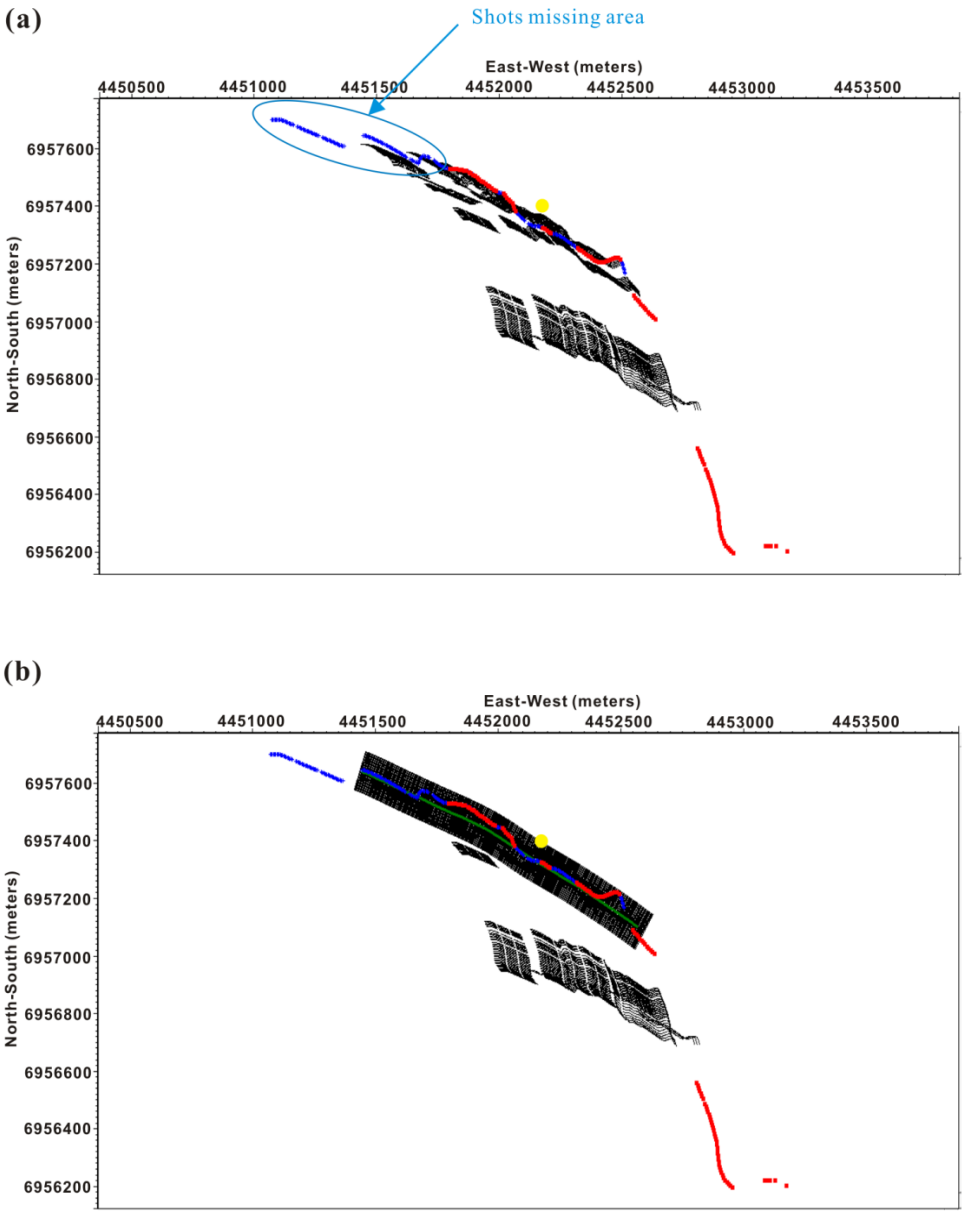

Figure 2.11

Figure 2.13 (a) geometry of line_3000.(b) the definition of bin grids. Sources are marked by red squares. Blue squares are receivers. And black points show CMP positions. Surface lines are shown as dark green lines. The rectangles are bin grids. The deep drill hole is shown as yellow points.

critical to properly processing the walk-a-way seismic data later. Additionally, the shot points were more limited in this line because of local infrastructure.

The surface, or processing profiles are shown on the geometry figures as dark green lines, these were defined by following the density of common-midpoint (CMP) (dark points) in Vista™ software, and they were adjusted manually to follow the survey lines where they deviated the survey lines too far. The CMP points distribute in a wide area since the survey lines were seriously crooked. Relatively large bin spacing was defined to cover as many CMP points as possible. However, some of the CMP points still can not be included in this coverage; and this information is unfortunately lost. This is one problem that this irregular survey introduced for data processing (Wu, 1996). And at the same time, since the corresponding CDP (common depth point) points in one bin grid lie in a range not at a point as normally 2D seismic survey does, this has an impact on the resolution of stacking and migration if a cross-dip exists.

2.3 Data Quality

Seismic reflection surveying is the technology to detect the subsurface structures by using reflections. However, as we know, noise, refractions and other events always interfere with the desired reflection signals (Fig. 2.3). This is particularly important here as the reflections we expect in these metamorphic terranes are quite weak. Noise can be classified as linear noise and non-linear noise. And it is unavoidable during the seismic

acquisition. Moreover, when different types of waves arrive at the geophones at the same time they are difficult to separate. In order to increase the reflection signal compared to the background noise, the quality of data needs to be analyzed at the beginning to determine how those noise differs from signals. And on the basis of this analysis, then we can select processing flows and parameters to attenuate noise.

Several analysis means will help us to understand the quality of the data: recognizing the type of interference waves, amplitude characteristics, and the frequency properties.

Examining the raw data from shot gathers (Fig. 2.14 (a) and Fig. 2.15 (a)), amplitude is attenuated from shallow to deep on each shot gather due to the fact that the energy of waves is dissipated while they propagate, which will be discussed in details in later section. The attenuation is more serious on line_2000 than on line_3000. Further, energy differences between shot points also exists on different positions of line_2000 (Fig. 2.16) and line_3000 after examining whole data set, this is due to the changing ground conditions along the lines that ranged from excellent coupling on the snow covered dirt roads to poor coupling in zones covered loose sands or gravels. After balancing the energy loss by AGC (automatic gain control), several types of interference waves can be revealed from shot gathers: surface waves (ground roll), air waves, linear noise and random noise (Fig. 2.14 (b) and 2.15 (b)). Reflections cannot easily be seen with such a strong noisy background.

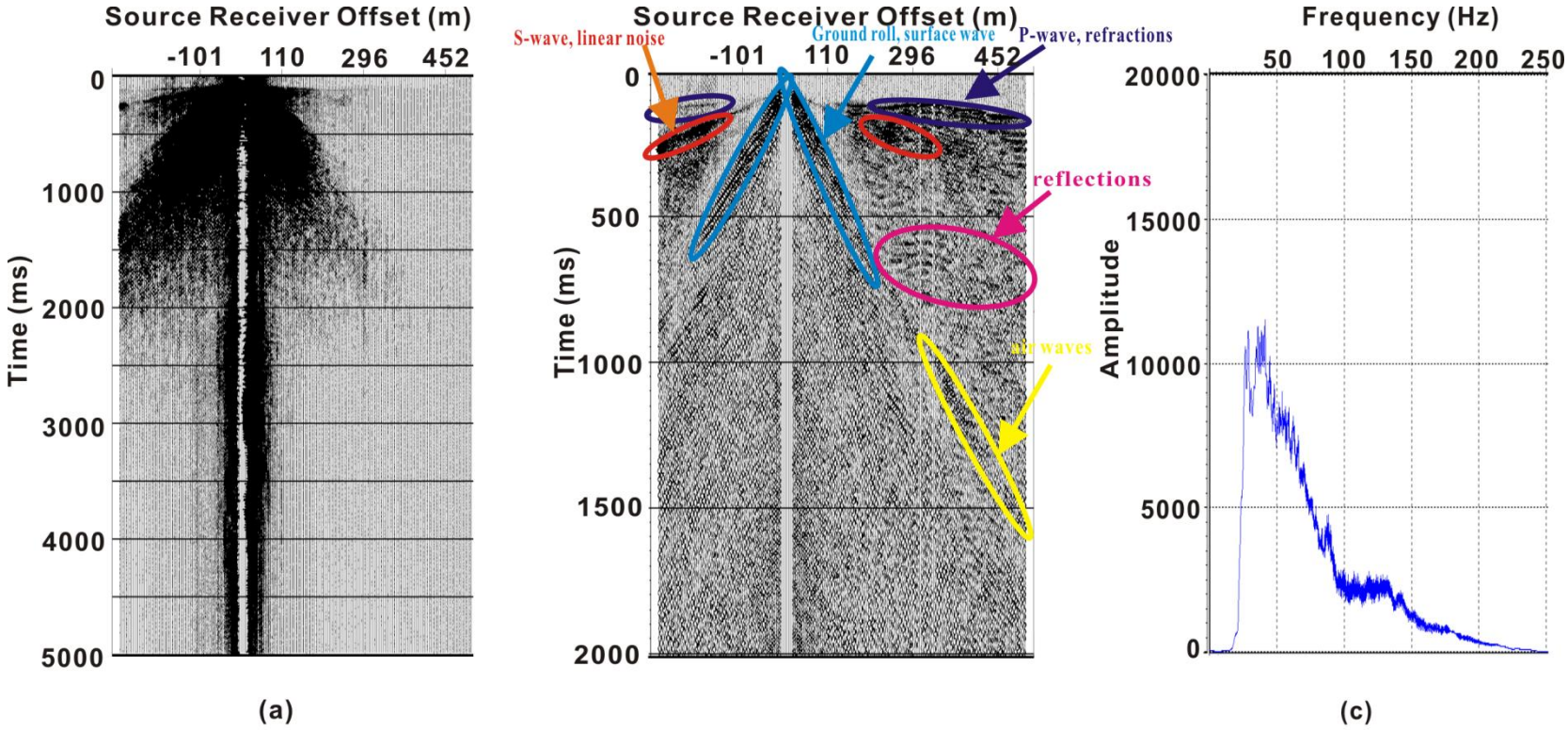

Figure 2.14 (a) Line_2000 raw shot record (shotpoint 2020).
(b) Shot2020 from 0 ms to 2000 ms after gain. (c) Amplitude spectrum of shot2020

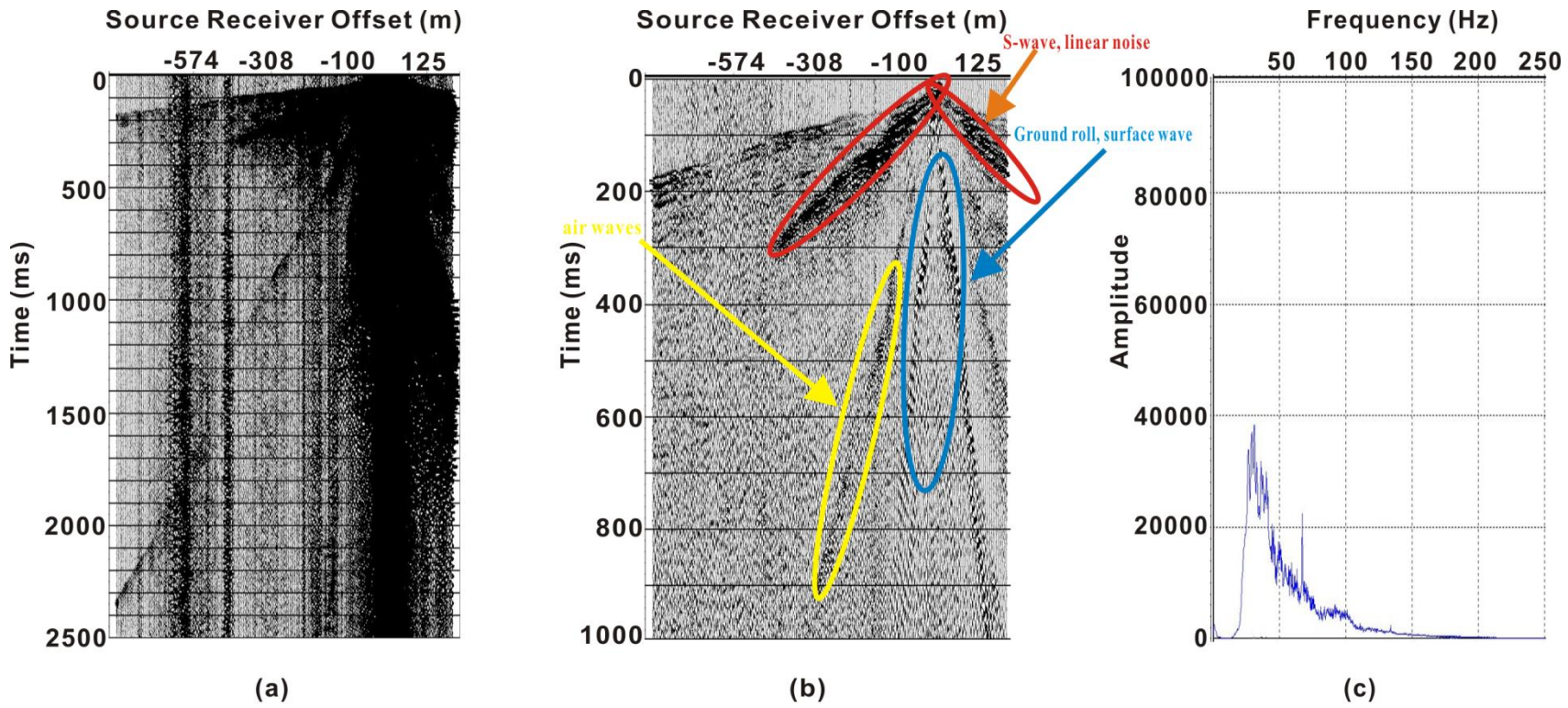

Figure 2.15 (a) Line_3000 raw shot record (shotpoint 30860).
(b) Shot30860 from 0 ms to 1000 ms after gain (c) Amplitude spectrum of shot30860.

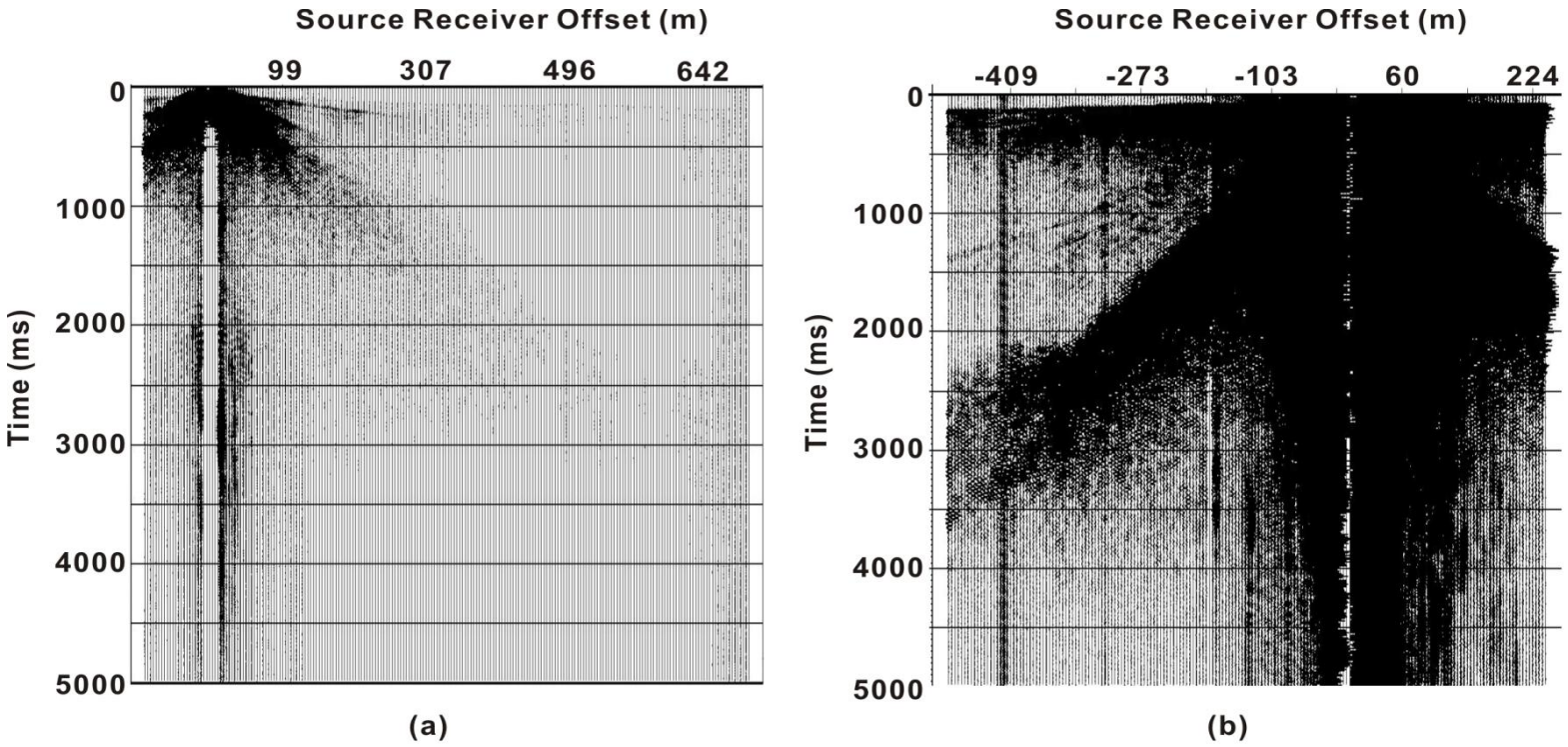

Figure 2.16 Raw shot gathers from shot2000 and shot2196 to show the amplitude difference between different shots.

The surface waves are also commonly known as ground roll. They have low group velocity, large amplitudes and sometimes low frequency. It usually can be attenuated by bandpass filtering if the frequency content of the surface waves differs significantly from the desired signal. Alternatively, a two-dimensional F-K filter can be applied, and as this is used extensively later its discussion is delayed.

Air waves are essentially the unavoidable audible sound waves produced by the seismic source while it is active. These travel with a ~340 m/s velocity and are also a serious problem for seismic processing. The problem with them is that the sound waves usually include frequencies much above those for the waves propagating in the earth. As such, they are highly aliased (improperly sampled) by the data acquisition system. There are no effective ways to completely remove them from records except muting (i.e. zeroing) them out by choosing a narrow corridor along their propagation path. However, reflections in this corridor zone will be muted at the same time. As there is no perfect solution to do this it must be performed with care.

Shear waves (Fig. 2.14) are also treated as noise since we only need the P-wave reflections, here. The shear wave refraction has a higher velocity (about 1800 m/s) than the surface wave and falls within the same frequency band as the desired signal. It can be identified in the frequency-wavenumber F-K domain as linear noise. Surgical mutes may be applied to it, but this will result in the loss of some of the desired signal. So usually a narrow F-K filter is used to attenuate it on the base of no spatial aliasing generated.

In addition, the amplitude spectra (Fig. 2.14 (c) and Fig. 2.15 (c)) show that the frequency band of effective amplitudes mainly lies between 30 Hz to 180Hz for line_2000, and 30 Hz to 150 Hz for line_3000. It may vary from shot to shot; and a general examination on each shot is needed. The final bandpass filter parameters were consequently determined based on this shot by shot examination. The low frequency part is considered to be dominated by surface wave due to the high amplitude.

To sum up, line_2000 and line_3000 are both noisy data sets with low signal-to-noise ratio. This is another challenge for the data processing.

2.4 Data Processing

The purpose of seismic processing is to organize the shot gathers collected in the field, to edit out poor signals, to condition desired signals, to re-sort them into common midpoint (CMP) gathers, and finally to correct the traveltimes so they can be added together to enhance the signal to noise of the coherent events. Seismic data processing usually follows a basic routine (e.g., Fig. 2.11) but it may be varied for specific needs. The determination of whole processing sequence was based on the geometry and quality of these 2D seismic data. While only the final results are shown, it is important to note that a great deal of testing of different parameters and techniques, not all of which are successful and consequently not shown here, is essential before determining parameters for each step. Detailed information is discussed in later sections.

2.4.1 Defining Geometry and Processing Flows

With crooked line acquisition, the CMP gathers have inconsistent fold coverage and uneven offset distribution (Nedimovic and West, 2003a). The CMP points cover a wide area surrounding the survey lines as already shown in Fig. 2.12 (a) and Fig. 2.13 (a) above. Surface lines did not follow shot lines or receiver lines exactly since survey lines were crooked. The surface profiles were defined by following the distribution of CMP points and as close to the survey line as possible, which are shown as dark green lines on Fig. 2.12 (b) and Fig. 2.13 (b). The bin spacing needs to be large enough to catch the scattered CMP points but a larger area will lead to higher uncertainty about the image if a cross-dip exists (Nedimovic and West, 2003a). As a result, some CMP points were not included in the bins; they gave no contribution to the final image. Note that line_3000 was less crooked than line_2000 and has a relatively narrower CMP distribution range. Hence, a bin spacing with 2 m in the surface line direction since the receiver gap is 4 m, and 100 m wide in the perpendicular direction of the surface line was chosen in order to cover most of CMP points for line_2000. Correspondingly, the bin spacing for line_3000 was 2 m in the surface line direction and 80 m wide in the perpendicular direction. Subsurface folds are displayed on Fig. 2.17, which do not distribute uniformly. On line_2000, besides the both edges of survey line, low fold coverage also can be observed from CMP 560 to CMP 620 and around CMP 720 by reason of seriously crooked survey line. It is obviously that line_2000 has more irregular fold coverage than line_3000.

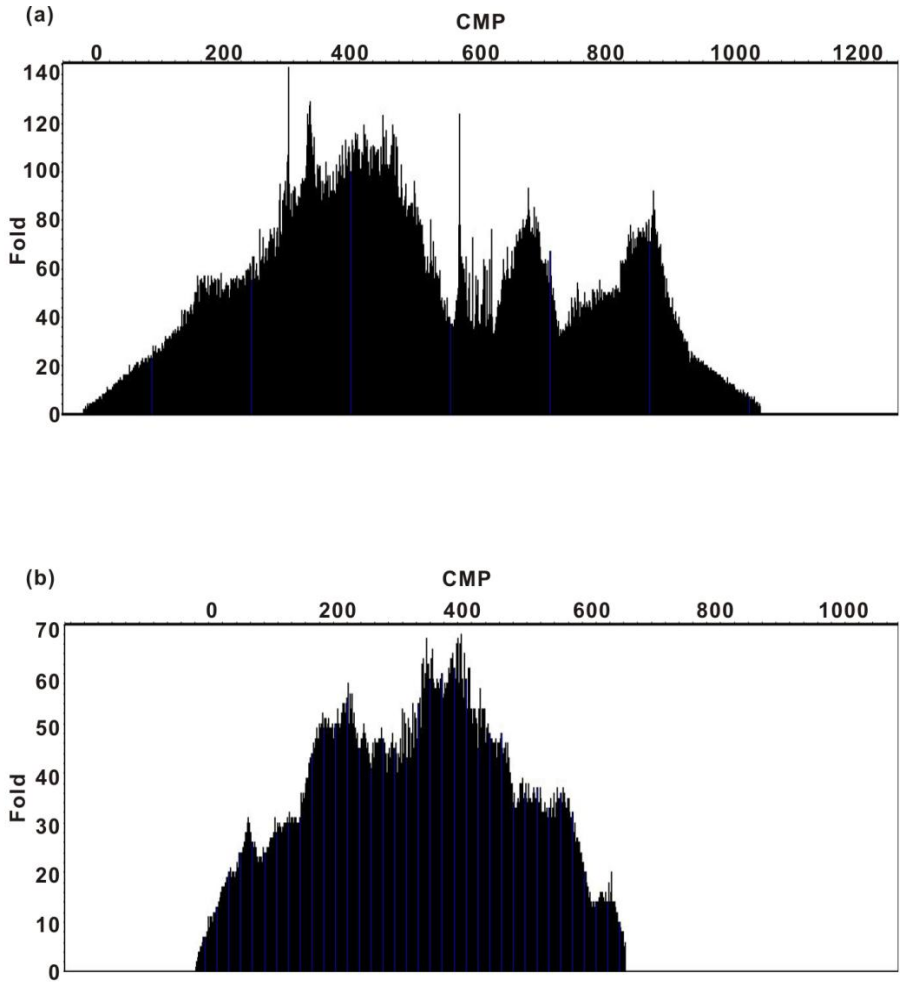

Figure 2.17 (a) Subsurface folds of line_2000. (b) Subsurface folds of line_3000.

However, Line_3000 has much lower fold coverage than line_2000. The fold coverage in line_3000 is all lower than 70 comparing with 120 in line_2000.

According to the quality analysis, a series of processing flows and parameters were tested. And the processing was mostly performed on Vista™ software. Table 2.1 shows the final processing procedure and key parameters.

2.4.2 Trace Editing and Static Corrections

The trace editing operation is to delete or omit dead and exceptionally noisy traces which are normally called bad traces or abnormal traces. These bad traces can be revealed by abnormally high amplitude and frequency spike which are usually dangerous if included in the final stack as they contain little or no useful coherent energy. They could cause processing algorithm to be unstable or create false events in the image. Accordingly, detecting and editing of bad traces was performed on records one by one, and it needs to be done carefully and manually. Trace editing may decrease the fold coverage, but it enhances the resolution of stack profile by eliminating directly those traces that contain minimal useful information.

'Statics' are corrections which are applied to seismic data to eliminate travel time shifts of the reflection times caused by variations of topography and of velocity of the near-surface. The static corrections are made to make sure that all the records are from a common fixed datum. This correction involves two factors. The first is the elevation differences between

the shot and receiver points. The second is the seismic velocity structure of the topmost 'weathered' layer which usually has an abnormally low velocity. This result in rapid lateral shifts in the travel time of even flat lying deep reflections and may cause false indication of subsurface structures on the seismic section.

The elevation information can be obtained from elevation changes in trace headers (as obtained by differential GPS (Global Positioning System) surveying during the field campaign). The variations of the low velocities and thicknesses of the weathered layers can be derived from the arrival time of recordings using various methods including seismic tomography as carried out by Schijns et al (2009). In the Outokumpu seismic survey, elevations of shots and receivers range from 88m to 108 m with the biggest elevation difference among shots and receivers being about 20 m. The static correction is a combined weathering and election correction. It is calculated based on the first break time of seismic recordings. Because of the rapidly varying topography and the extreme variations in velocities between the near surface materials of glacial origins and the metamorphic bedrock the static corrections are quite severe. Indeed, Schijns et al. (2009) had to develop a laterally varying two dimensional velocity model of the near surface materials in order to be able to properly analyze the walk-a-way VSP data so obtained. Meanwhile, since Schijns et al. (2009) only calculated the statics for the shots locations as was needed for her VSP analysis, here the statics for receiver positions were generated by interpolating between her shot position values. This could be achieved only because shots

and receivers followed the same trajectory on the surface. This may not be exactly accurate, but as the spacing between the shots was nominally only 20 m, it is enough for long wavelength corrections. Some errors can be corrected after residual static correction. However, by the reason that line_3000 was not completely covered by shots and receivers, the statics for receivers in the shots missing area (Fig. 2.13) all kept a constant value which was obtained from the closest shot. So this resulted in relatively big correction errors in shots missing area.

The near surface traveltime effects obscured many features of the data, and the removal of these was crucial to the successful processing and interpretation of the data. After applying the refraction statics on sources and receivers, the fixed datum is 12 m above the sea level. The records after statics correction are shown on Fig. 2.18 and Fig. 2.19. The effect is very pronounced in Fig. 2.18 where the large bump in the traveltimes was largely removed.

The overall continuity of reflectors is an important criterion to evaluate the effectiveness of the refraction static correction. But in this case the deeper and weak reflectors are not readily seen in the shot gathers before noise attenuation. It also can see that the statics correction yield substantial improvements on the seismic records. Line_2000 has a more observable change than line_3000 because line_2000 has a more serious static problem. However, some errors still exist due to the fact that velocities and thicknesses can never

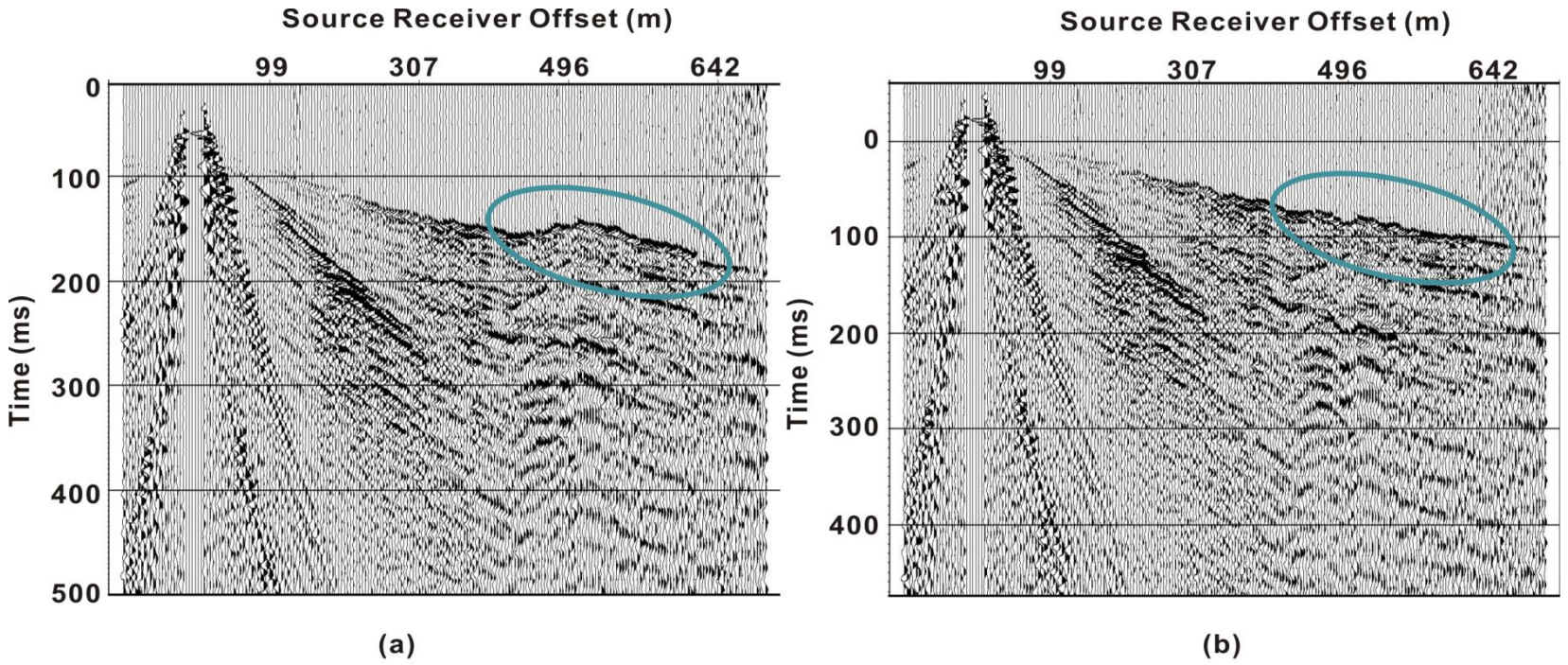

Figure 2.18 Shot gathers from line_2000. (a) Before refraction static correction. (b) After refraction static correction.

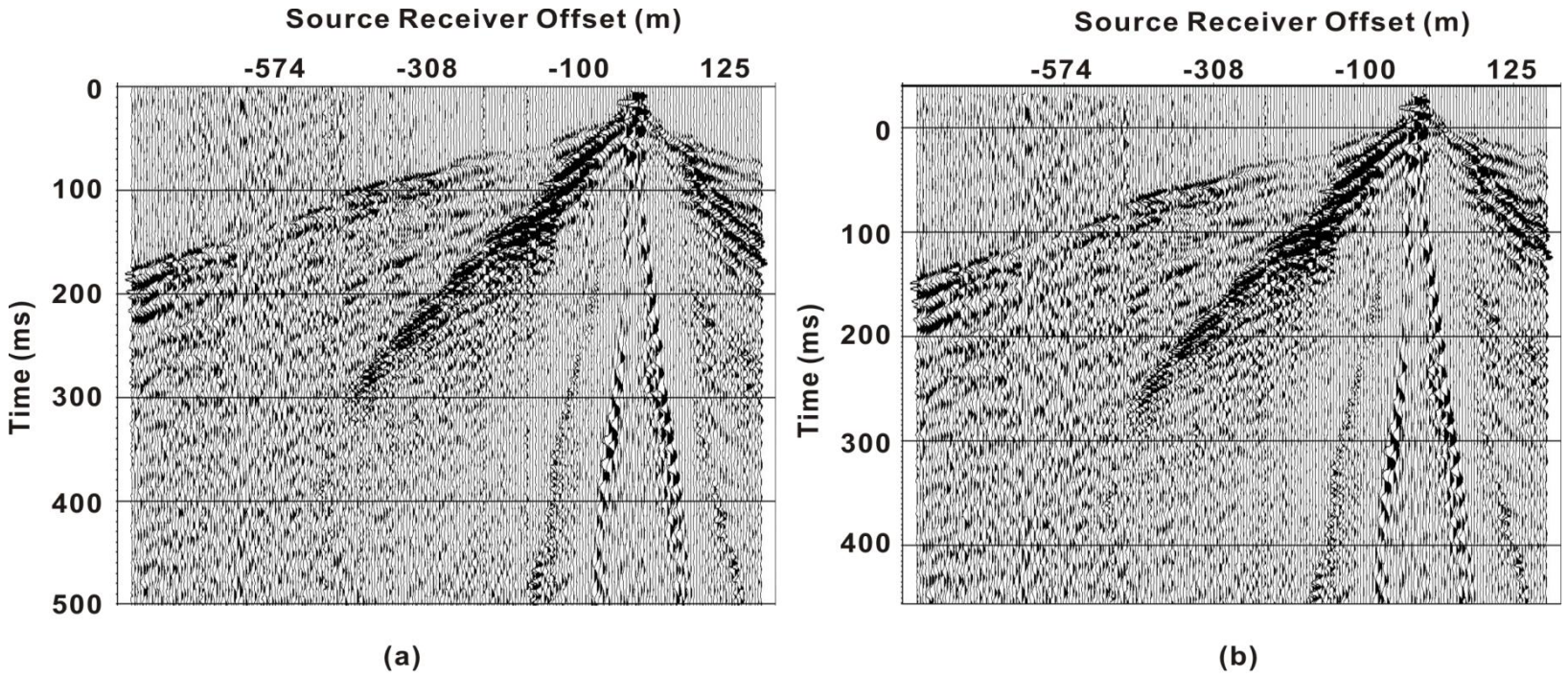

Figure 2.19 Shot gathers from line_3000. (a) Before refraction static correction. (b) After refraction static correction.

Table 2.1 Processing sequence and parameters for 2D seismic lines

Processing Step	**Parameters**	
	Line_2000	**Line_3000**
Geometry Definition		
Lmo		
Trace editing		
Applying refraction statics		
Bandpass filtering	30-40-170-190	30-40-130-150
Spherical divergence compensation	Time-velocity pairs	Time-velocity pairs
Surface consistent compensation		
F-K filtering		
Spiking deconvolution	Operator length:200ms	Operator length:200ms
Autocorrelation		
Predictive deconvolution	Operator length:200ms Prediction lag: 18ms	Operator length:200ms Prediction lag: 18ms
F-X 2D prediction	Filter length: 3 traces	Filter length: 3 traces
CMP sorting		
Initial velocity analysis		
NMO correction and first stacking		
First residual statics calculation		
Second stacking		
Second velocity analysis		
NMO correction and Third stacking		
Second residual statics calculation		
Fourth stacking		
Time-variant bandpass filter	-200-400ms: 30-40-90-100 400-1000ms: 30-40-150-180 1000-5000ms: 30-40-90-100	-200-400ms: 35-45-90-100 400-1000ms: 30-40-120-150 1000-5000ms: 30-40-100-120
F-X 2D prediction	Filter length: 3 traces	Filter length: 3 traces
Velocity smoothing		
Kirchhoff migration	100%velocity 200 traces in diffraction	100%velocity 200 traces in diffraction

be precisely modeled and especially because the crooked lines are not usually perfectly modeled by two-dimensional models since three-dimensional heterogeneities exist. These errors can be corrected during a residual statics analysis which will be discussed later.

2.4.3 Noise Attenuation

Both line_2000 and line_3000 have very low signal-noise ratio. According to the data quality analysis, the noise mainly includes random noise, surface waves, airwaves, linear noise and high frequency interference which can be identified from Fig. 2.14 (b) and Fig. 2.15 (b). From the average amplitude spectrum picture for a shot shown on Fig. 2.14 (c) and Fig. 2.15 (c), low frequency part from 25 Hz to 40 Hz for both line_2000 and line_3000 is mainly dominated by surface waves. Therefore, bandpass filtering was used to reduce surface waves. To avoid removing some reflections in this frequency band inadvertently, the parameters has to be chosen carefully, and need to be test and determined after comparisons of filtering results.

To further suppress noise, F-K velocity filtering was applied to seismic data. F-K velocity filtering removes unwanted energy based on velocity properties of seismic wave modes. Seismic wave modes can differ in two fundamental ways (Hardage, 2000). One is the direction of velocity propagation and the other is the magnitudes of velocities. Therefore, noises that can not be isolated in time domain might be isolated in frequency-wavenumber domain. In the frequency-wavenumber domain, velocities are

equal to the frequency *f* over the wavenumber *k* according to

$$V = \frac{2\pi f}{k} = \frac{\omega}{k} \tag{2-13}$$

where ω is the angular frequency. For a fixed velocity (i.e. nondispersive), the plot of frequency versus wavenumber is a straight line. Surface waves and linear noise usually have lower frequency and low velocities. In our case, velocity of surface waves is about 190 m/s. The velocity of airwaves is about 340 m/s but they have a much broader range of frequencies. A second strong linear arrival (possibly a direct wave or a shear wave) has a velocity of 1400 m/s. Each seismic record was divided into negative offset and positive offset parts, and was transformed into frequency-wavenumber domain from space-time domain by using a 2D Fourier transform (Fig. 2.20 (a) and Fig. 2.21 (a)). Different F-K filtering 'pie slices' were tested. Big pie slice including not only the 1400 m/s arrival waves may artificially act the F-K filter on signal. Some false events might be generated. So a relatively narrow F-K filter pie slice including only the linear events was finally chose. Since data with positive offsets was transformed into the negative wavenumber half plane in F-K domain and data with negative offsets was transformed into the positive wavenumber half plane in F-K domain, a F-K filtering pie slice in negative wavenumber half plane was applied to positive offset data part. And a F-K filtering pie slice in positive wavenumber half plane was applied to negative offset data part. This was carried out manually on a shot gather by shot gather basis. Then the filtered seismic data was transformed back into the *x-t* space-time domain. The

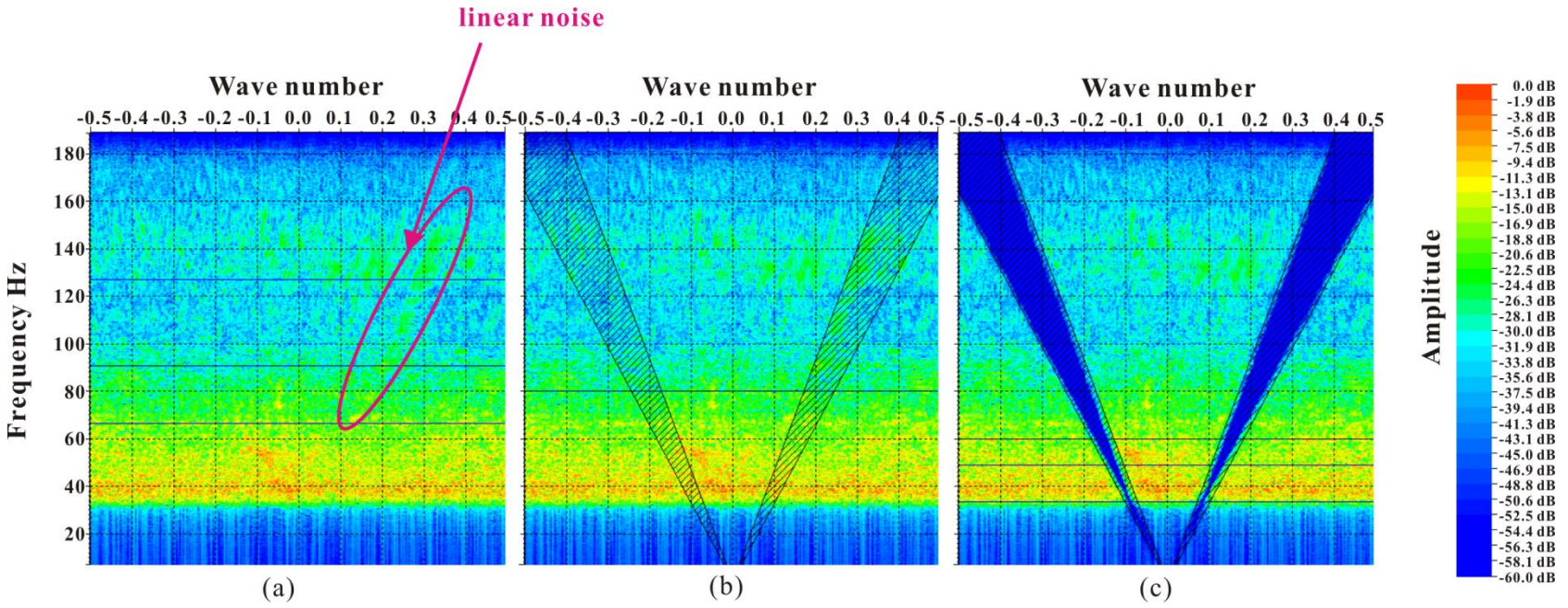

Figure 2.20 F-K filtering to attenuate the linear noise.(a) a shot gather from line_2000 in F-K domain, (b) F-K rejecting pie slices on the shot gather, (c) the shot gather in F-K domain after F-K filtering

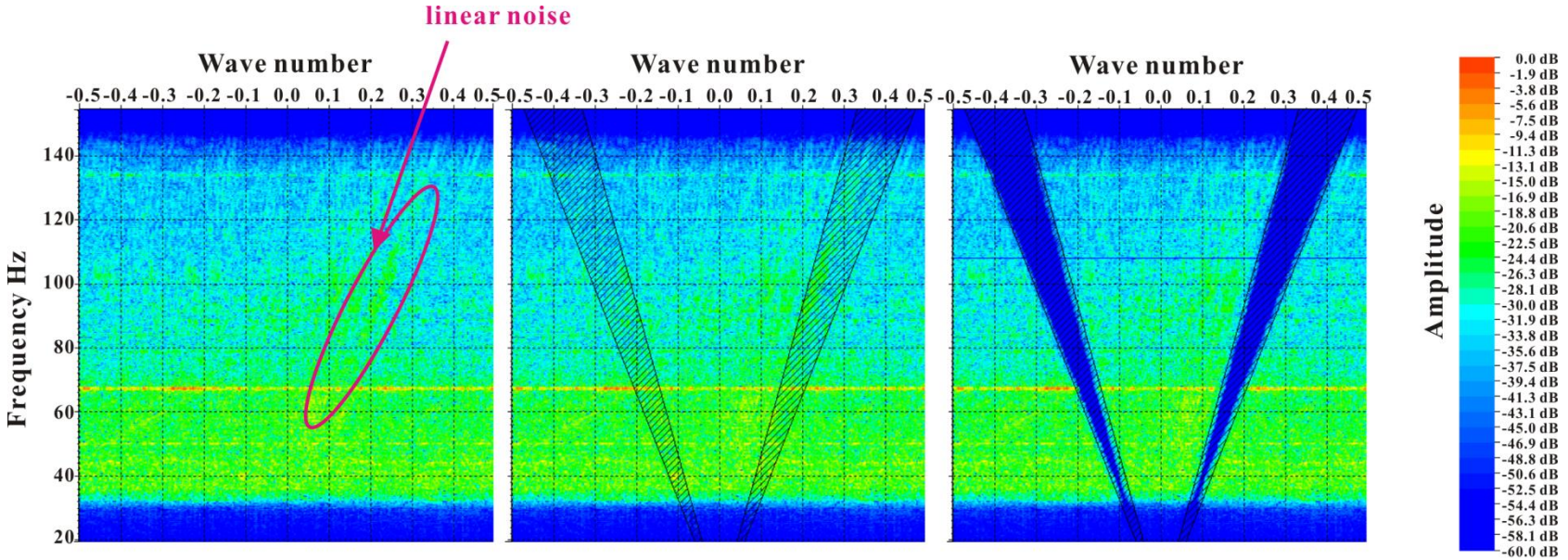

Figure 2.21 F-K filtering to attenuate the linear noise. (a) a shot gather from line_3000 in F-K domain, (b) F-K rejecting pie slices on the shot gather, (c) the shot gather in F-K domain after F-K filtering

differences between data before F-K filtering and data after F-K filtering must be inspected to make sure that no signal was filtered. The effect of F-K filtering depends on the size of pie slices and also on the quality of seismic data.

F-K filtering was used twice on both line_2000 and line_3000 to attenuate the ground roll and the 1400 m/s linear noise arrival with different pie slices, respectively. The data lying in the pie slices (Fig. 2.20 (b) and Fig. 2.21 (b)) were eliminated in F-K domain, which also are shown on Fig. 2.22 (c) and Fig. 2.23 (c). Fig. 2.20 and Fig. 2.21 show the F-K filtering on linear noise in F-K domain. And Fig. 2.22 and Fig. 2.23 show an example of F-K filtering on shot gathers from line_2000 and line_3000 respectively. By inspecting the difference between (a) and (b), linear noise and some ground roll were attenuated by the F-K filtering. The application of the F-K shown in Fig. 2.22 is somewhat disappointing as little difference is seen before and after. That in Fig. 2.23 is much more positive as a series of hyperbolic shaped events appear particularly at the expected depths for the Outokumpu-type assemblage in Fig. 2.23 (b) that are not readily visible in Fig. 2.23 (a). Although noise was not removed completely, further processing might achieve even better results.

Perhaps more important than the filtering, the summing of the appropriately time corrected seismic traces such that the desired coherent reflections add together referred to as ‘stacking’ in the seismic processing vernacular is the simplest and most powerful method to reduce random noise. All traces gathered from a same CMP point will be

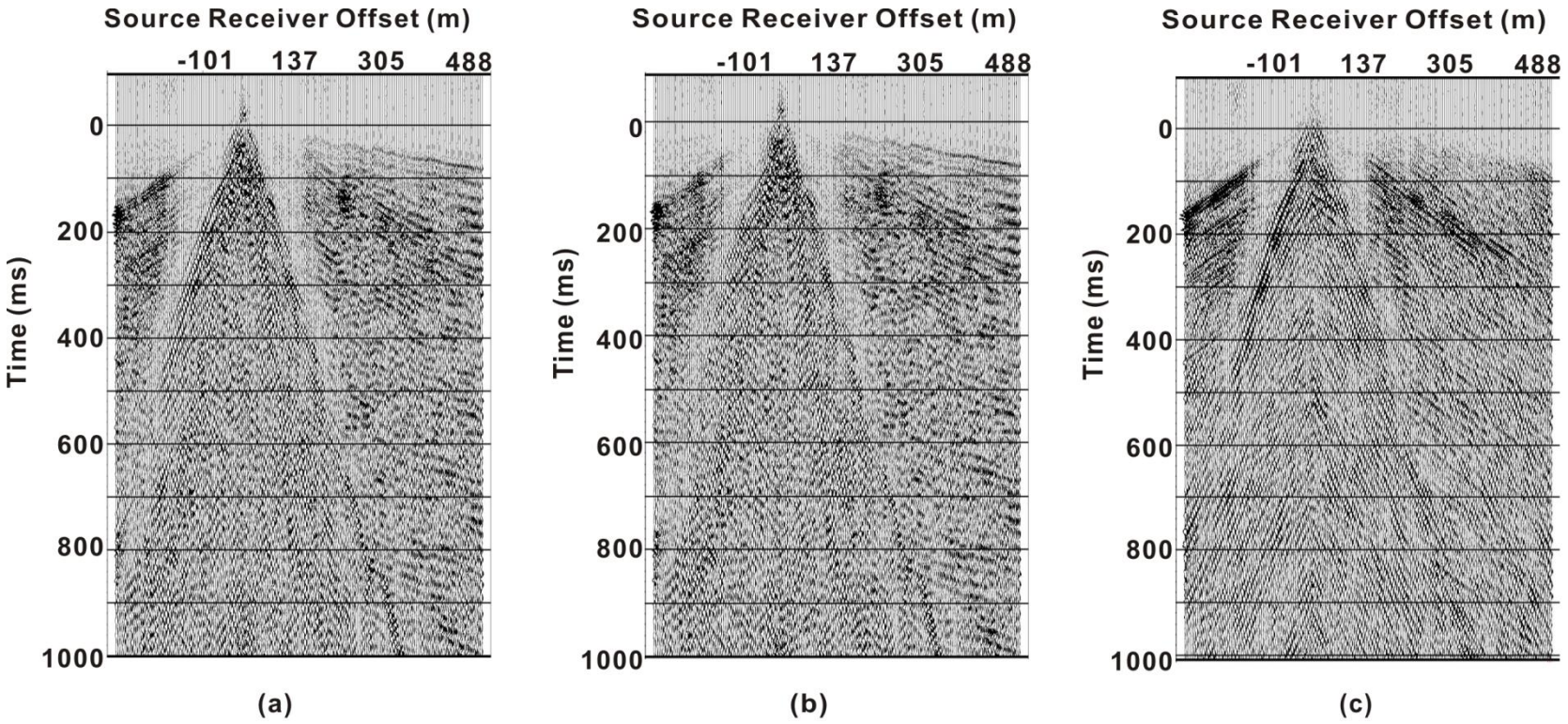

Figure 2.22 A shot record from line_2000. (a) Before F-K filtering. (b) After F-K filtering. (c) The difference between (a) and (b).

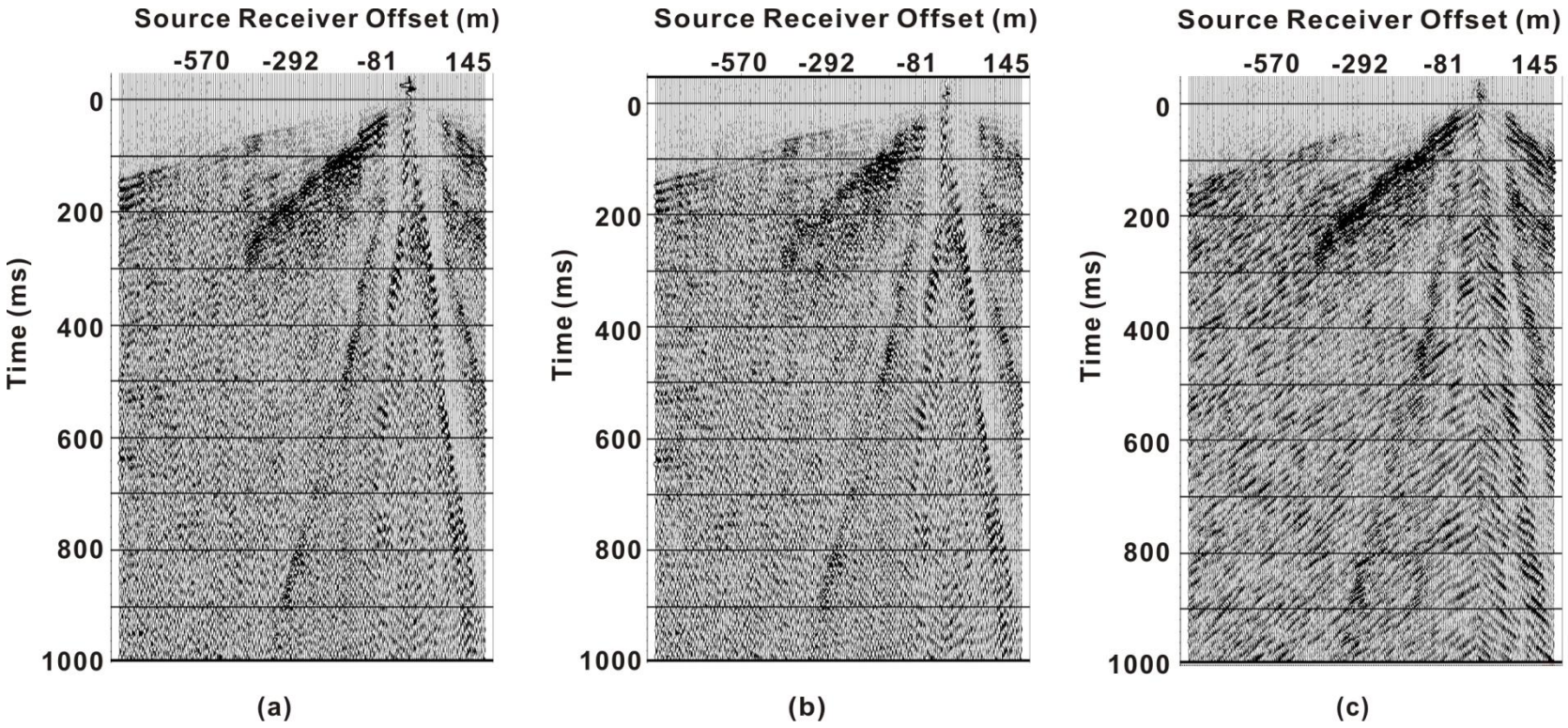

Figure 2.23 A shot record from line_3000. (a) Before F-K filtering. (b) After F-K filtering. (c) The difference between (a) and (b)

corrected by stacking velocities and added together. As a result, reflectors which have same phase will be enhanced. And random noise which is uncorrelated from trace to trace and has different phases will be largely attenuated after stacking.

The F-X 2D predictive method is generally used after stacking in order to attenuate remaining noise to increase signal-noise ratio (Chase, 1992). It can also be applied to either common-offset or common shot gathers prior to stacking. It works by first transforming data into frequency-offset domain. Then a Wiener prediction filter is applied to each mono-frequency series on each trace. The data is then transformed back to the space-time domain. The effect is to "smooth" the data across space (x). Of course care must be exercised in the application of such procedures as, while it may provide an image that is more appealing to the eye, it may also have smoothed out some important structure.

Noise can also be suppressed by applying spiking deconvolution, predictive deconvolution, and time-variant bandpass filtering (Scheuer and Oldenburg, 1988). The resolution is improved step by step and these techniques will be discussed in more detail shortly.

2.4.4 Amplitude Compensation

In seismic surveying, seismic waves are propagated through the earth’s interior and return to surface after refraction or reflection at geological boundaries. As seismic waves

propagate, the energy is dissipated and the amplitude of the wave gradually diminishes (Lowrie, 2007). The factors which affect amplitude are generally known, which include simple geometric divergence, the spread of wavefront, scattering, and absorption. In a homogeneous medium, simple geometric energy attenuation is proportional to $1/r^2$, and amplitude attenuation is proportionate to 1/r, where r is the radius of the spherical wavefront emanating from the point source. Scattering due to the heterogeneities in the earth also causes the amplitude decrease (Wu, 1989). This occurs in a discontinuous medium or a medium with rapid variations of velocities and densities. The energy is not lost. It is redistributed into other directions, and the wave types may change, too. The factors that affect the scattering include source frequency, rocks' physical properties, and the propagation distance. The absorption happens due to the imperfect elastic properties of medium and part of this energy is converted to frictional heat. The attenuation of seismic waves by absorption is dependent on frequency. High frequencies are attenuated more rapidly than are low frequencies (Lowrie, 2007).

Amplitude decays as the traveltime increases as offset gets further. The severity of the amplitude decay differs from common shot gather to common shot gather for a variety of reasons (Fig. 2.16).

To compensate for amplitude loss, three methods were used. The first is a somewhat empirical spherical divergence (spreading) correction. In a common form, the spherical divergence is corrected by (Wang and McCowan, 1989)

$$D = A * T^{B} \tag{2-14}$$

where, A and B are constants, and T is either the travel time or the offset. A and B are determined empirically. But a fixed divergence factor as a function of traveltime couldn't correct the divergence completely. More precise correction is developed by Newman (Newman, 1973). It works by using square law spherical spreading method to approximate the effect of amplitude loss. The divergence factors are established from a priori knowledge of the velocity in the first layer together with information which is obtained from the timing of reflected events and the time-weighted RMS (root mean square) velocity (Newman, 1973).

$$D_0 = \frac{t\overline{V^2}}{V_1} \tag{2-15}$$

where

$t = \sum_{i=1}^{n} t_i$, the two-way reflection time

$\overline{V}$, the time-weighted RMS velocity, which is given by:

$$\overline{V}^2 = \sum_{i=1}^{N} V_i^2 t_i \Big/ \sum_{i=1}^{N} t_i \tag{2-16}$$

where V_i is the interval velocity in ith layer. V_1 is the velocity in the first layer.

It works well on short offset distances where the NMO is very nearly hyperbolic. It should be noted that the spherical divergence (spreading) correction is based on an assumption of the earth model consisting of horizontal, isotropic layers. However, the energy loss due to the geometrical spreading can be fairly compensated.

In my case, the time and velocity information were obtained from the velocity files analyzed in line_2000 by Suvi Heinonen in 2007. They were applied on both two seismic lines.

As we noted, an amplitude difference still exists in different shot gathers because of near-surface variations, differences of source strength/coupling, and other acquisition factors. This influences all common-midpoint based processing since traces in a CMP gather are from different shot gathers. Consequently, it is necessary to counterbalance this energy discrepancy in the early stages of processing. To achieve this, a surface consistent amplitude compensation method was used in Vista^{TM} software. It decomposed amplitudes of raw data into CSP (common shot point), CRP (common receiver point), CMP and COP (common offset point) components. Then balance factors for each trace were calculated from these four components, and applied to raw data to balance amplitude in a surface-consistent way (Taner and Koehler, 1981, Cary and Lorentz, 1993). The effect of amplitude compensation is shown on Fig. 2.24 and Fig. 2.25.

After spherical amplitude compensation and surface consistent amplitude compensation,

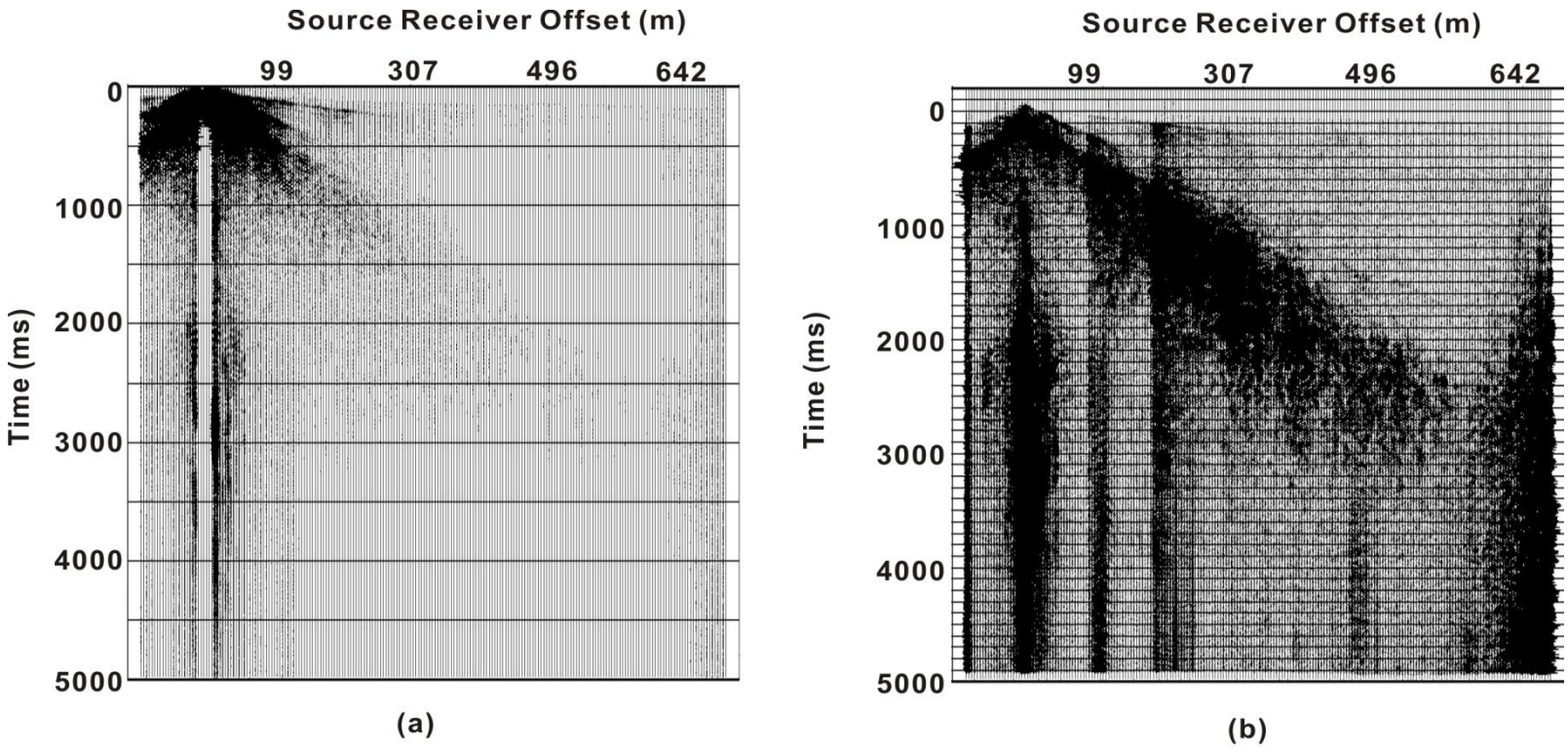

Figure 2.24 Comparison of amplitude compensation from line_2000.
(a) Raw recording before amplitude compensation. (b) After amplitude compensation.

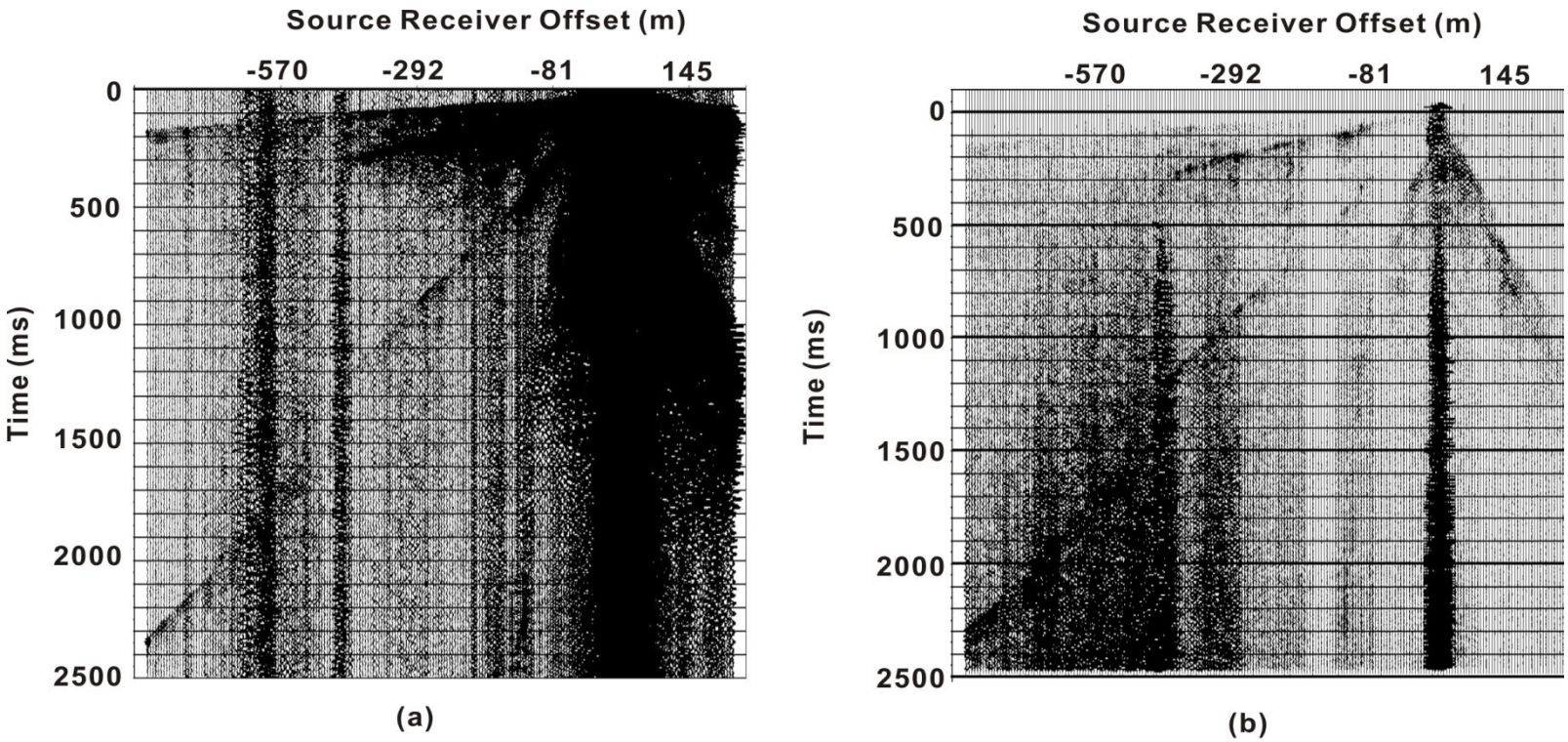

Figure 2.25 Comparison of amplitude compensation from line_3000.
(a) Raw recording before amplitude compensation. (b) After amplitude compensation.

energy losses have still not been corrected completely. Another compensation method known as AGC (automatic gain control) was also applied. AGC works by applying a gain to equalize the amplitude base on the traveltime. It is given by

$$A = \sqrt{\frac{\sum_{i=1}^{N} a_i^2}{N}} \tag{2-17}$$

where, N is the number of sampling points in a window, a is the amplitude. Traces will be divided in number of windows. In each window, A is calculated and assigned to the middle of the window. And the window slides along the trace till all the amplitude factors, A, are calculated for all the windows. It can improve the visibility of deep data, but it destroys the true-relative amplitudes (Eaton and Wu, 1996). So, in order to preserve potential information in true-relative amplitudes, AGC was used only before stacking to raise weaker signals. No AGC or other gain was used on CMP gather.

2.4.5 Deconvolution

Deconvolution is the converse of convolution, and it can be thought of as an inverse filtering of the data. It is normally applied to improve seismic data by compressing the wavelet to increase time resolution or by attenuating multiples and reverberations prior to a final stack. The earth which consists of layers of rocks with different seismic impedance is treated as a filter and so the forward seismic recording of the data can be considered as a convolutional process. That is, the recorded seismogram *x(t)* is the result of the

convolution of seismic wavelet with the earth's impulse response with added random noise, as shown in equation 2-18 (from Yilmaz, 2001).

$$x(t) = w(t) * e(t) + n(t) \tag{2-18}$$

where *x(t)* is the recorded seismogram, *w(t)* is the seismic wavelet, *e(t)* is the earth's impulse response, and *n(t)* is the random noise.

Deconvolution is used to try to recover the impulse response *e(t)* out of the recorded seismogram *x(t)* by deconvolving out the input wavelet *w(t)* that was filtered by the earth. If this could be done perfectly, then one would have the highest resolution seismogram possible, i.e. one that would have a spike with the reflection strength amplitude at each reflecting event in the earth. Of course, this is the ideal and can never in practice be fully achieved but, regardless, substantial improvements can still be made.

Spiking deconvolution was applied after the noise removal described in the previous section to compress the wavelet to a spike. A minimum phase seismic wavelet is required for obtaining a stable inverse. If the wavelet is not minimum phase, we will not get a perfect zero-lag spike (Yilmaz, 2001). However, the result is still acceptable. After testing with different operator lengths, 200 ms was finally chose for the spike deconvolution.

Predictive deconvolution was applied after spiking deconvolution to attenuate multiples. Multiple reverberations are often a problem in reflection seismic data as they can appear

as false events, can results in erroneous velocity analyses, or interfere with the desired but weaker primary reflections. Predictive deconvolution is one means to attempt to attenuate such reverberations. Predictive deconvolution assumes that the primary reflections are inherently unpredictable while the more periodic multiples are predictable (Yilmaz, 2001). The key parameter in predictive deconvolution is the prediction lag which is related to the periodicities of multiples. After testing on different prediction lags, 18 ms was utilized at last. Comparing shot gather and frequency spectrum before deconvolution with same record after spiking and predictive deconvolution (Fig. 2.26 (c) and Fig. 2.27 (c)), we can see deconvolution broadened frequency range, increased main frequency value, and improved data quality effectively. On the shot gather after deconvolution from line_2000 (Fig. 2.26 (a)), the reflections became stronger and more continuous. Additionally, from autocorrelation pictures before and after deconvolution (Fig. 2.26 (b) and Fig. 2.27 (b)), wavelet was compressed, and multiples were suppressed successfully.

2.4.6 Stack Velocity Analysis

Velocities are the most important information in seismic data processing. They are the basis of stacking, migration, and time-depth conversion. In data processing, NMO velocities are analyzed to correct the normal moveout like Fig. 2.28 and Fig. 2.29 shows. For a perfectly flat-lying layered geology this is identical with the time-normalized root mean square (RMS) velocity described above in Equation 2-19. As shown in many texts, the traveltime curves of different reflectors from a horizontally layered geology are

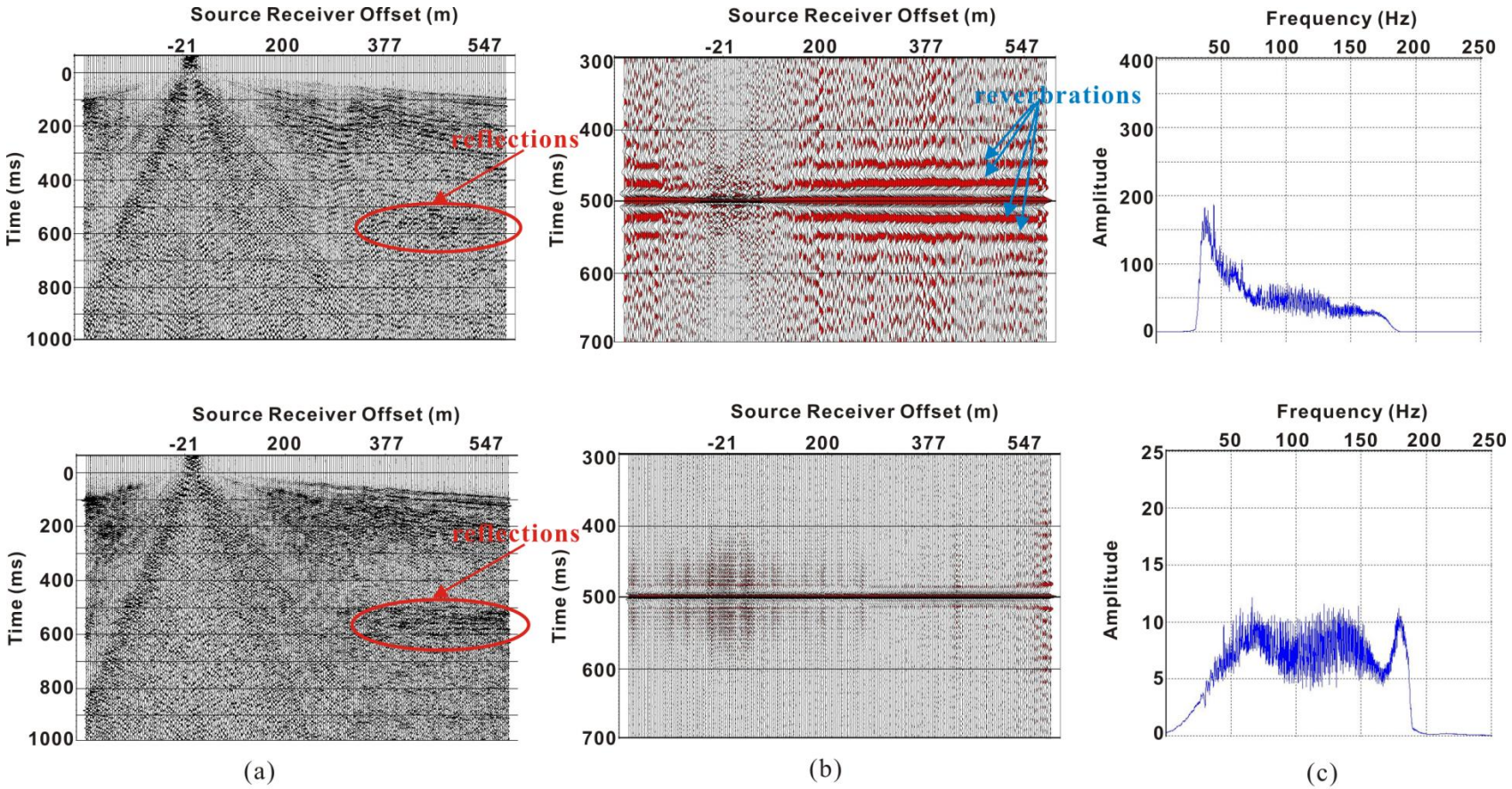

Figure 2.26 Deconvolution results from line_2000.
(a) the shot gathers before (top) and after (bottom)the deconvolution , (b) the autocorrelation before (top) and after (bottom) the deconvolution, (c) the amplitude spectrum before (top) and after (bottom)the deconvolution.

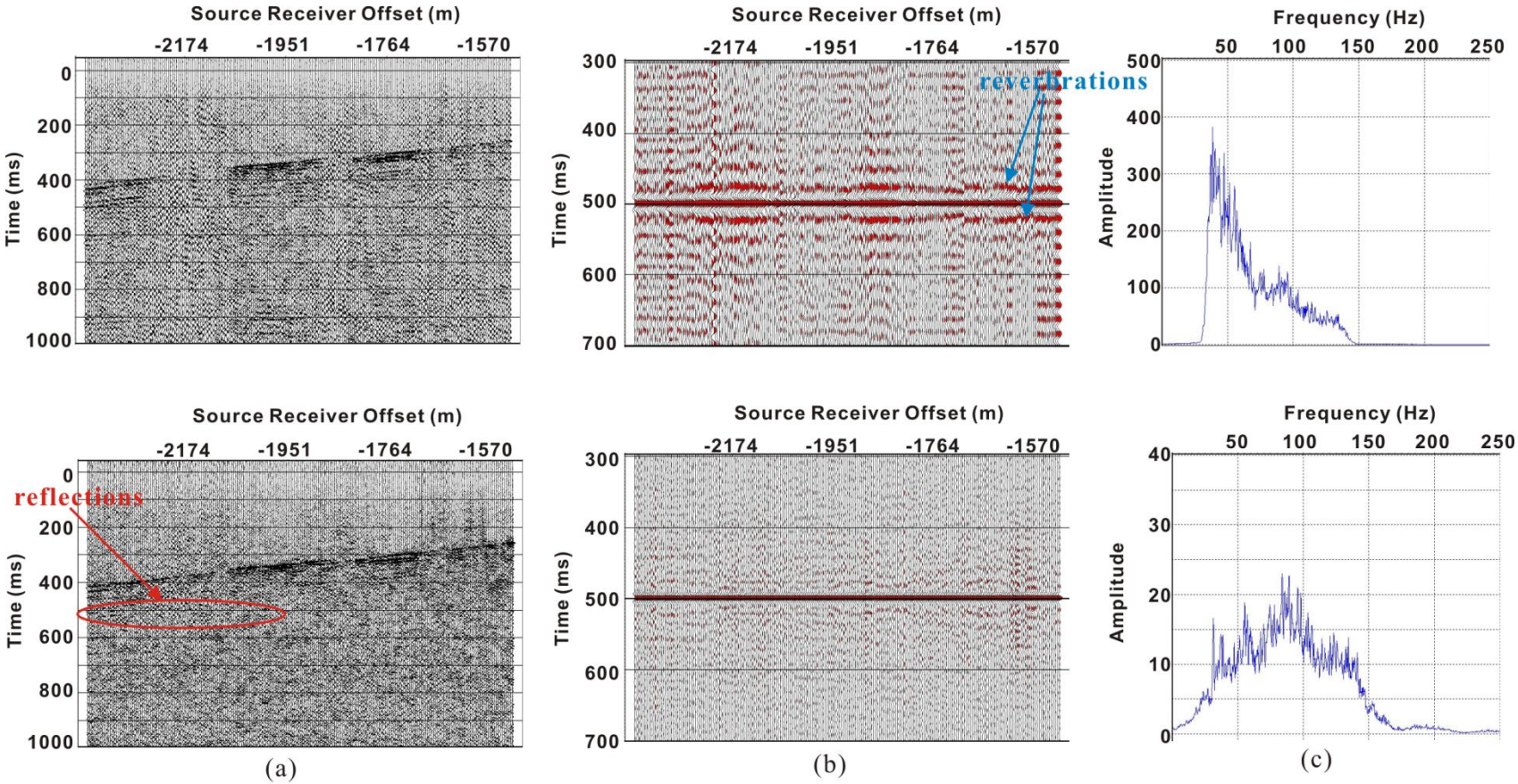

Figure 2.27 Deconvolution results from line_3000.
(a) the shot gathers before (top) and after (bottom)the deconvolution , (b) the autocorrelation before (top) and after (bottom) the deconvolution, (c)the amplitude spectrum before (top) and after (bottom)the deconvolution.

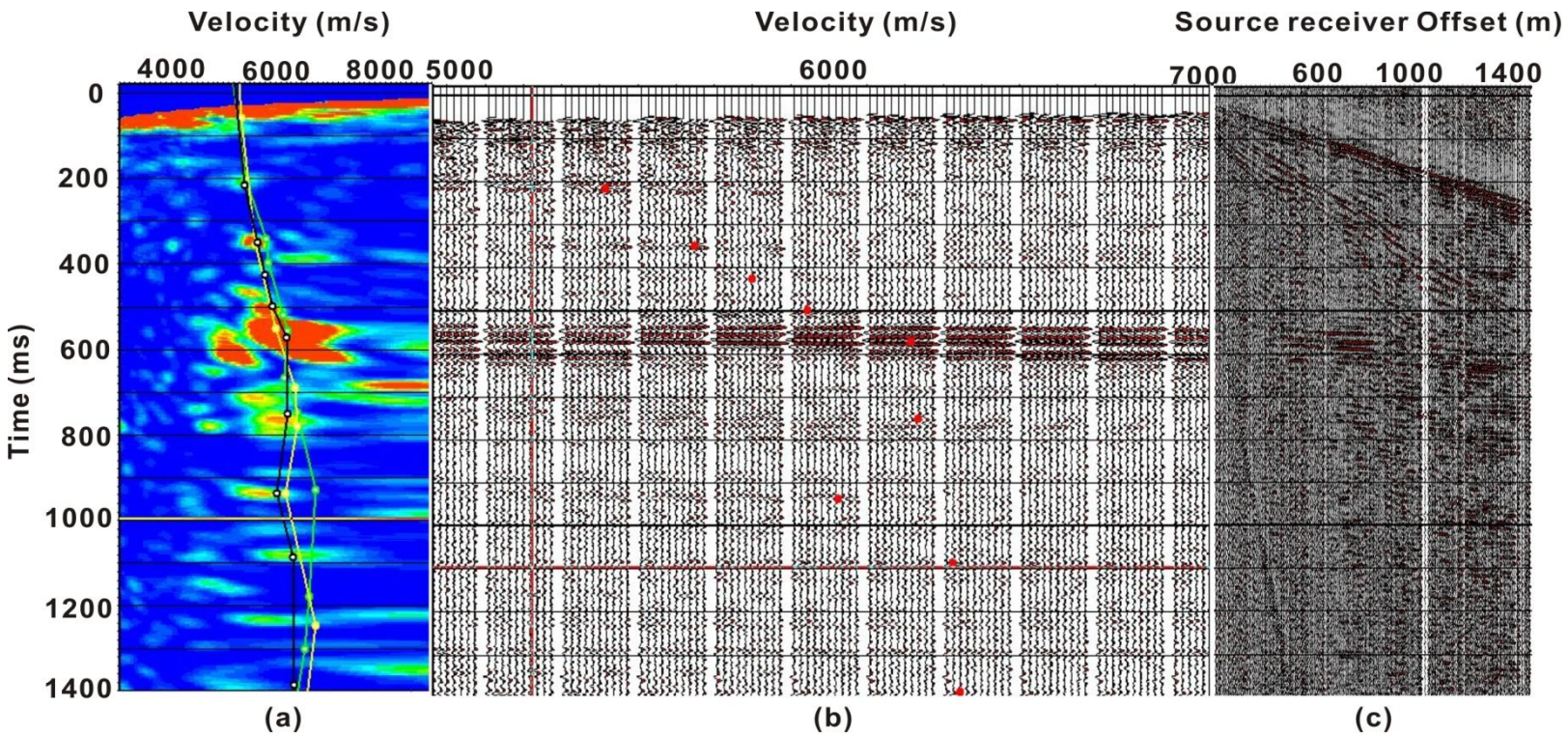

Figure 2.28 Velocity analysis from line_2000. (a)Semblance. Black line is the velocity picking line on current CMP supergather. Yellow and green lines are the velocity picking lines on next and former CMP supergathers, respectively. (b)CVS, red points are the velocities picked. (c) CMP supergather.

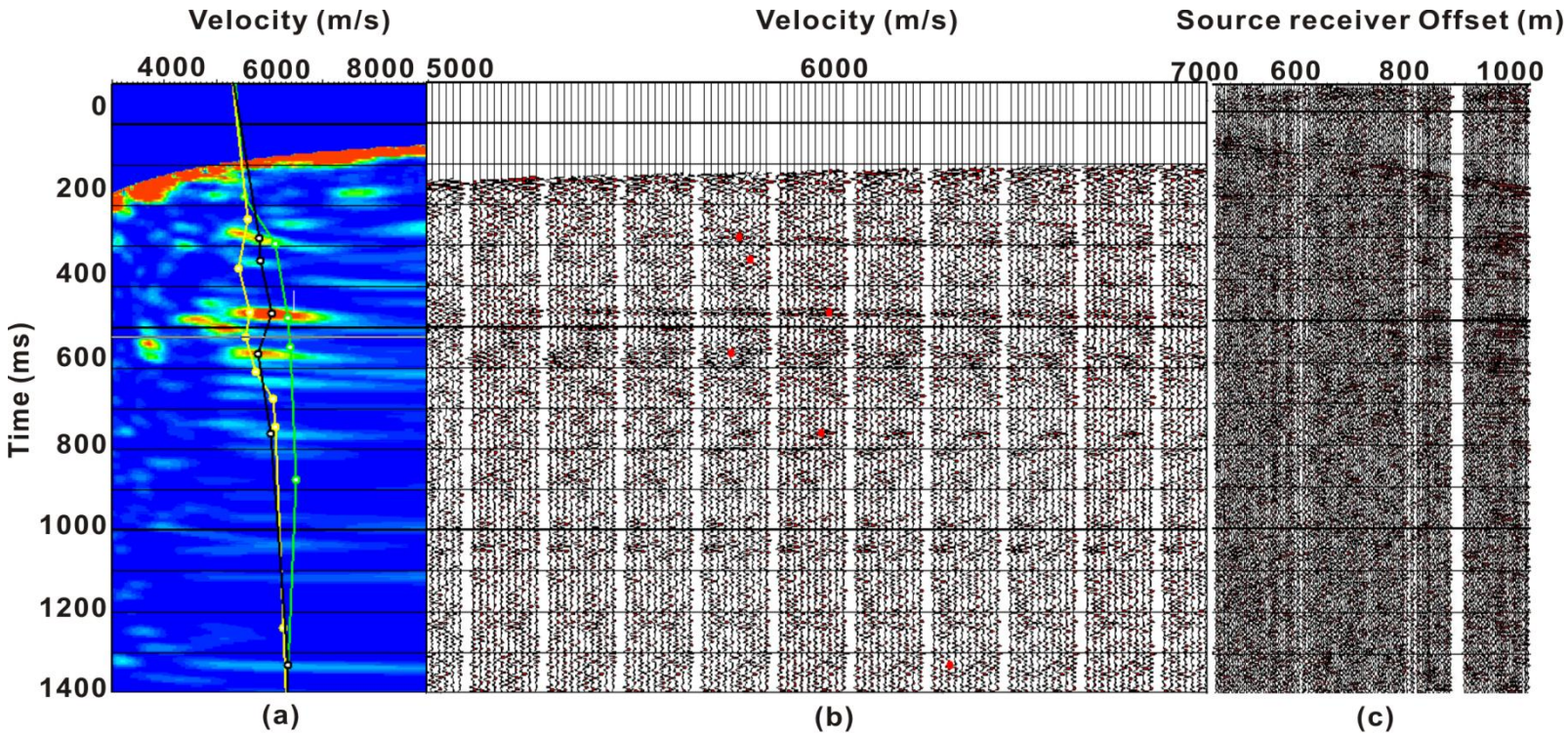

Figure 2.29 Velocity analysis from line_3000. (a)Semblance, Black line is the velocity picking line on current CMP supergather. Yellow and green lines are the velocity picking lines on next and former CMP supergathers, respectively. (b)CVS, red points are the velocities picked. (c) CMP supergather.

approximately described by:

$$t^2 = t_0^2 + \frac{x^2}{v^2} \tag{2-19}$$

where x is the offset between source and receiver, v is stacking velocity, and t_0 is the traveltime to the reflecting interface at zero offset (i.e., x = 0). So, the NMO correction can be derived and given by:

$$\Delta t = t - t_0 = t_0 \left[\sqrt{1 + (\frac{x}{v t_0})^2} - 1 \right] \tag{2-20}$$

Furthermore, the empirically derived stacking velocity is generally equal to NMO correction velocity (or root mean square (RMS) velocity).

The RMS velocity is used to flatten via correction the seismic reflections on each CMP gather before stacking. Use of V_{rms} values that are lower than the actual ones will 'overcorrect' the reflections, such that the image of the corrected reflection will be concave up with a 'smile'. In contrast, too high values for V_{rms} will undercorrect the reflections and they will remain downward concave as a 'frown'. When a proper velocity is used, the reflections are flattened; they may then be added up together ('stacked') to give a stronger event by improving the signal to noise ratio.

Hence, one of the most important parts of seismic processing is finding the appropriate function V_{rms} (x, t_o) that will allow all of the traces in each CMP to be appropriately

summed. When we use the actual data to find V_{rms} (x, to) then the results is called the 'stacking' velocity. Two ways for velocity analysis were used here to determine the stacking velocities. One is called semblance which is based on computing the velocity spectrum. On velocity spectrum, velocity is a function of two-way time. The signal coherency is calculated by means of hyperbolic searches of CMP gathers for a large number of narrow time windows where various stacking velocities are assumed (Taner and Koehler, 1969). Stacking velocities were interpreted by choosing the highest coherency points.

When the semblance velocity spectrum is insufficient to provide accuracy in velocity analysis, another technique, the constant velocity stack (CVS) is often used to assist in determining the stacking velocity. The CVS method stacks CMP gathers with a range of constant velocities. And the velocity estimation is based on the amplitude and continuity of stacked events.

Base on the importance of velocity analysis to the quality of stacking, usually a reliable velocity function is obtained by using a combination of the CVS method and the velocity spectrum. This is done interactively within the Vista™ software. Fig. 2.28 and Fig. 2.29 show examples of velocity analysis. Velocity analysis was performed on selected super CMP gathers, every 50 CMPs for first velocity analysis and every 25 CMPs for the second velocity analysis. The super gathers were constructed by combining 11 adjacent CMP gathers together. This can increase the accuracy of velocity analysis in low fold

coverage area and low signal-to-noise ratio area. Fig. 2.28 (a) and Fig. 2.29 (a) show the velocity spectra derived from the super gather as in Fig. 2.28 (c) and Fig. 2.29 (c). For each spectrum, the velocity was scanned from 3000 m/s to 9000 m/s every 50 m/s. the vertical axis is the two-way time from 0 to 5 seconds for line_2000 and from 0 to 2.5 seconds for line_3000. Red indicates the maximum coherency values. The panel of CVS analysis is shown on Fig. 2.28 (b) and Fig. 2.29 (b). The velocity scan range is from 3000 m/s to 9000 m/s. Red points are velocities chosen as the best stack response (i.e. the optimal $V_{rms}(x, t_0)$.

The whole velocity-time pairs were picked based on semblance, CVS and CMP gather information. Complete velocity fields across the entire profile were generated by spatially interpolating velocity-time pairs, which were shown on Fig. 2.30 and Fig. 2.31. The velocity field was used to flatten CMP gathers, and stack. These velocities were also used for migration.

From velocity fields, velocities vary from 4000 m/s to 7000 m/s in depth. And line_2000 and line_3000 both have a relative stable velocity variation in lateral direction. Velocities have more changes in the shallow part than in the deep part. This can explained because there are more interference waves in shallow layers, like shear waves and surface waves, which will affect the accuracy of velocity analysis. And also inadequate static correction could be another reason. In the objective zone around 500 ms, the velocity varies from 5500 m/s to 6500 m/s, which can also be identified from Fig. 2.30 and Fig. 2.31.

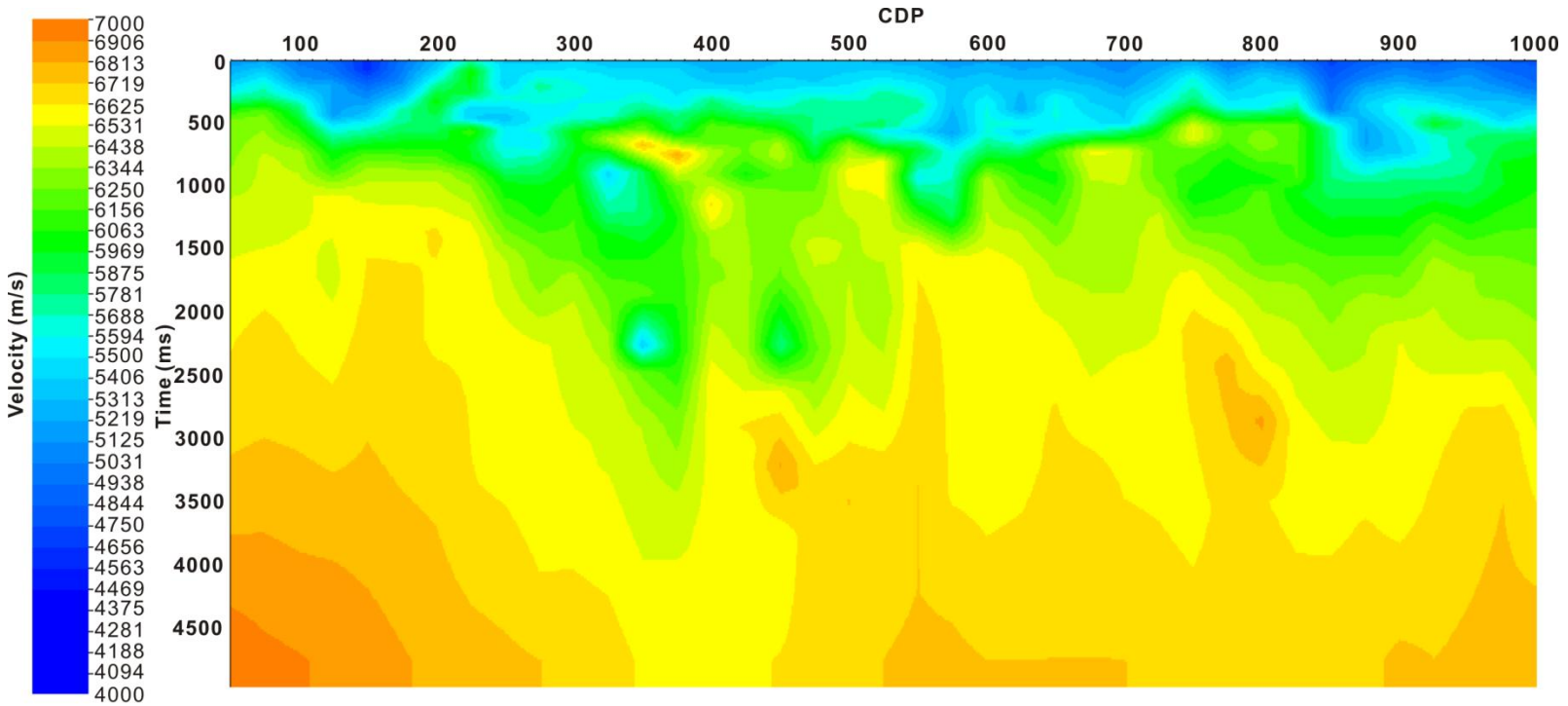

Figure 2.30 Velocity field of line_2000

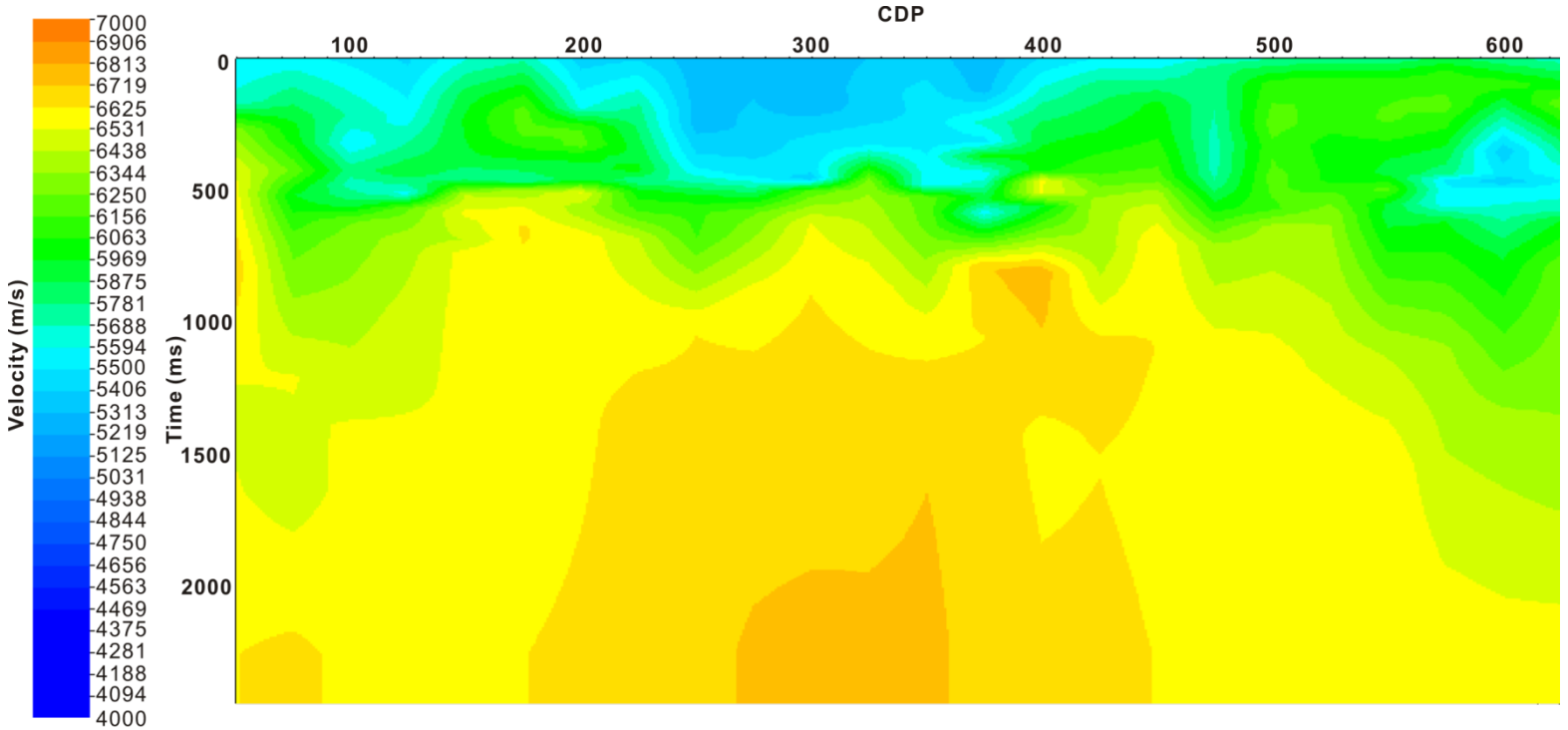

Figure 2.31 Velocity field of line_3000.

2.4.7 Residual statics correction

On the beginning of data processing, refraction statics were applied to the data to remove the impact from the irregularities in the near-surface. These corrections generally remove long-wavelength anomalies. But short-wavelength anomalies still exist and the first round refraction statics cannot capture these smaller scale variations. These also need to be corrected to image subsurface structures accurately. These secondary static corrections are referred to as residual statics correction. This usually follows velocity analysis and normally will be performed iteratively with velocity analysis.

There are several different methods which can achieve residual statics correction. In this project, residual statics corrections were calculated by using a stack power maximization algorithm employed in Vista™ software which was presented by Ronen and Claerbout (1985). This method calculates static values by minimizing the difference between modeled and actual traveltime deviations associated with a reflection event on moveout-corrected gathers (Yilmaz, 2001). It involves several important parameters which need to be chosen with care, especially for the current data with low signal-to-noise ratio. It includes model building, correlation windows, and maximum allowable time shifts. The correlation window usually covers all the objective zones at least, and could be as long as the whole time length of data. The maximum allowable time shift and model building should be made by examining the stack response. When the static values are close to one time sample interval (here 1 ms), the iteration between

velocity analysis and residual static calculations should be completed.

After testing on different parameters, a window from 300 ms to 800 ms was defined and the biggest time shift was limited in 24 ms. Two iterations of velocity analyses and residual statics corrections were carried out on line_2000, and three iterations for line_3000. These iterations are necessary to consistently improve the stacking function and static corrections.

The effectiveness of residual static corrections can be observed from Fig. 2.32 for a portion of line_2000 and Fig. 2.33 for a portion of line_3000. These comparisons between the profiles with and without residual static corrections, the continuity of reflections and resolution of stack have been improved. This is especially obvious in Fig. 2.32 where new events appear at depths near 900 ms below the main expected reflectors at 500 ms. The effect is perhaps more pronounced in Fig. 2.33 where the 500 ms reflector package was initially very difficult to discern.

2.4.8 Stack

Common-depth point or Common midpoint stacking was performed based on all the reflections were flattened by NMO correction. The process is summing traces in the same CMP gather up, and then divided by fold to produce the final CMP trace. The plotting of all of the CMP traces generates a seismic profile.

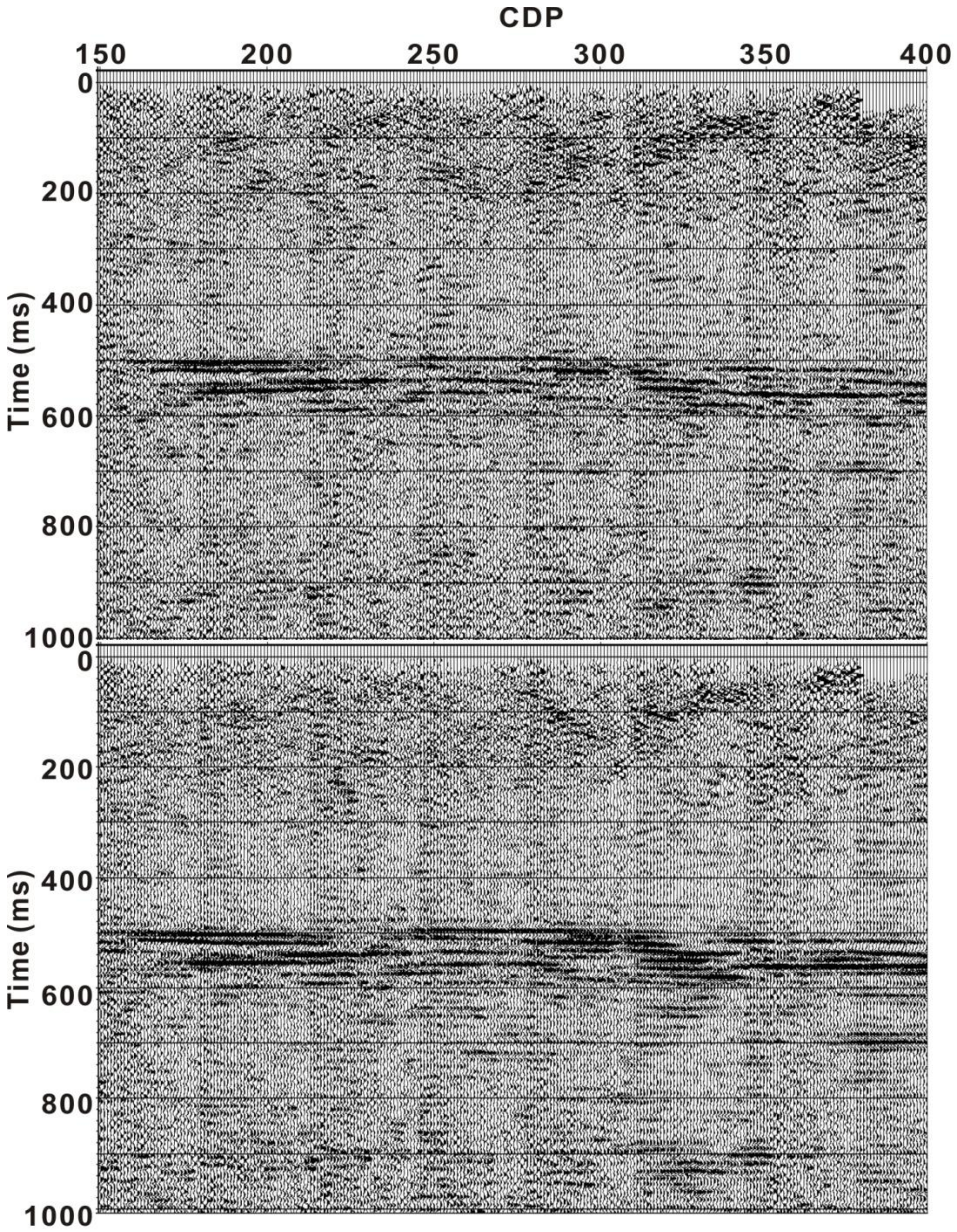

Figure 2.32 A portion of stack profiles from line_2000.
Top is the first stack profile without residual static correction.
And the bottom one is the stack profile with twice residual static correction.

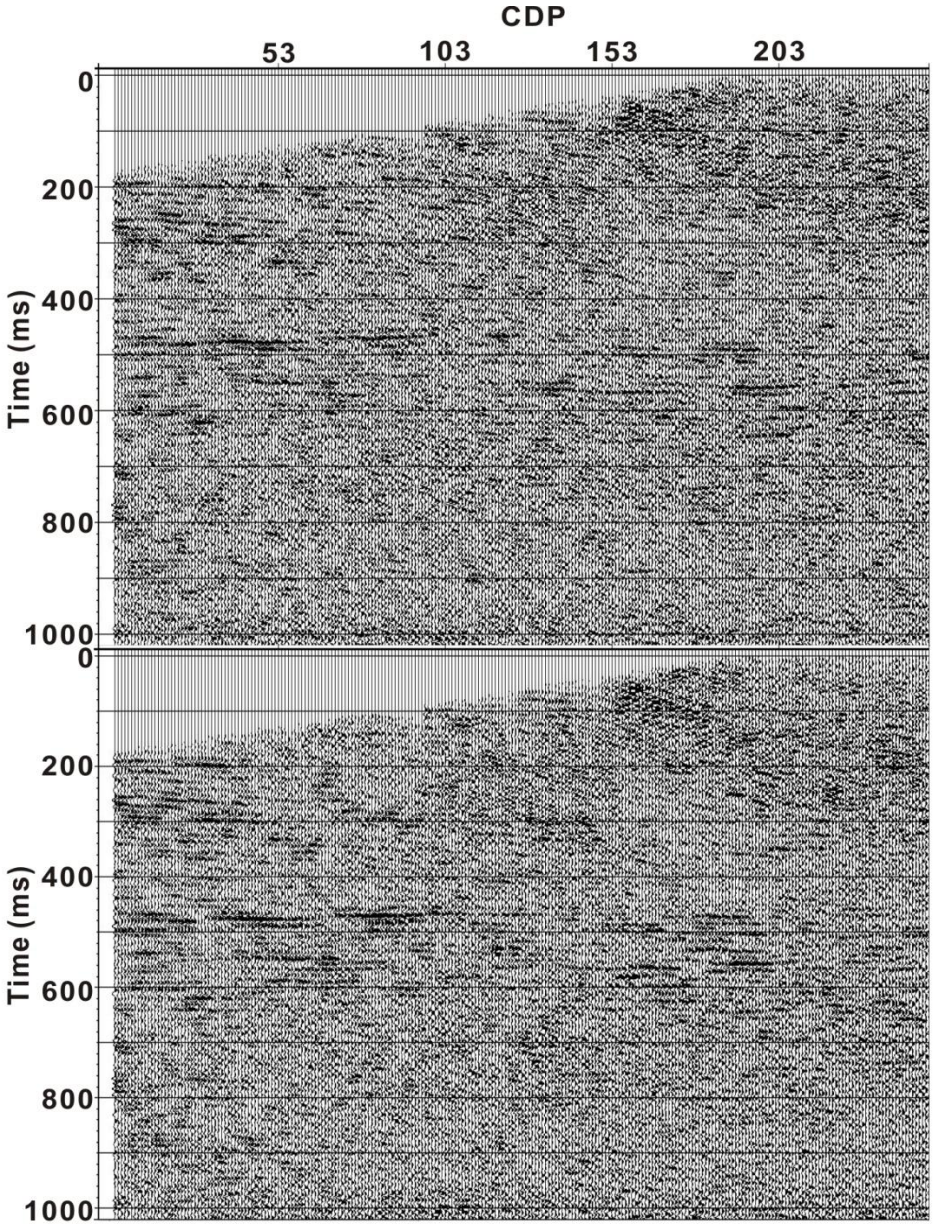

Figure 2.33 A portion of stack profiles from line_3000.
Top is the first stack profile without residual static correction.
And the bottom one is the stack profile with three times residual static correction

After stacking, an F-X 2D prediction method was utilized on stack profile to improve signal-to-noise ratio. This method is discussed on the noise attenuation section. The comparisons before and after F-X 2D prediction filter are displayed on Fig. 2.34 (line_2000) and Fig. 2.35 (line_3000). The signal-to-noise ratio on both line_2000 and line_3000 are effectively improved, especially in those oval areas. In addition, a time-variant bandpass filter was applied. For the shallow part of data, a relatively narrower bandpass filter was chose to attenuate some high frequency noise. The final stack profile is shown on the Fig. 2.36 and Fig. 2.37.

2.4.9 Seismic Image Migration

The common midpoint stack is originally set up to attenuate noise without attenuating the reflections. It is based on the assumption of horizontal layers. It is not strictly valid for dipping layers. Migration is required because some reflectors are not horizontal as we assumed. 'Migration' involves moving ('migrating') dipping reflectors to their actual geometric locations (Fig. 2.38 (a)) and collapsing diffractions back to their original source point (Fig. 2.38(b)). Basically it is an image reconstructing process to create a more accurate image of the subsurface. There are three basic approaches to migration: finite-difference methods, frequency domain methods, and Kirchhoff method migrations (Yilmaz, 2001). Each method has its own suitable conditions and computational costs. Migration can be performed either after stacking on the final CMP traces or perhaps more preferably before stacking (i.e. pre-stack) on the individual traces.

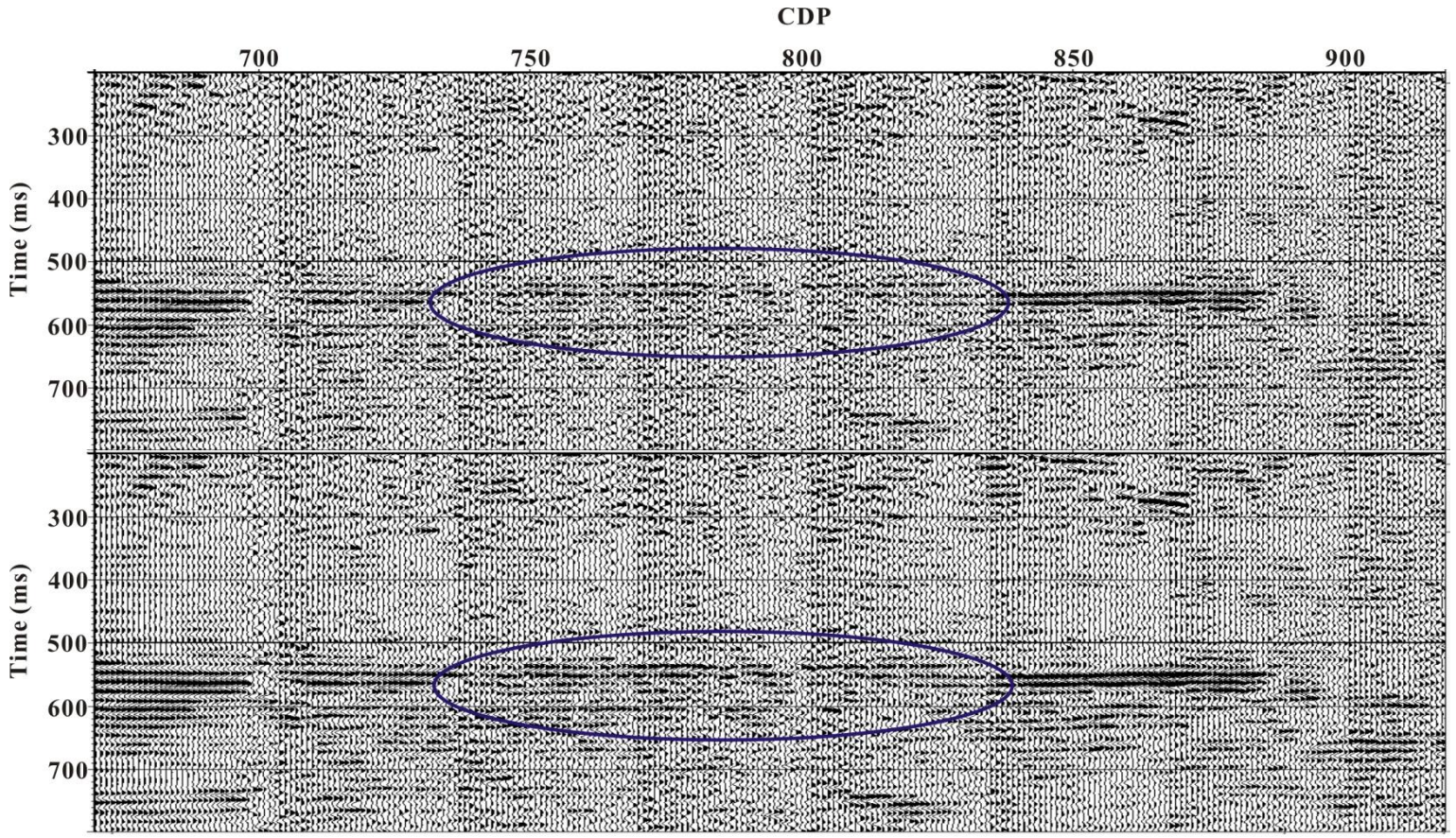

Figure 2.34 A portion of stack profile of line_2000 before (top) and after (bottom) F-X 2D predictive filter

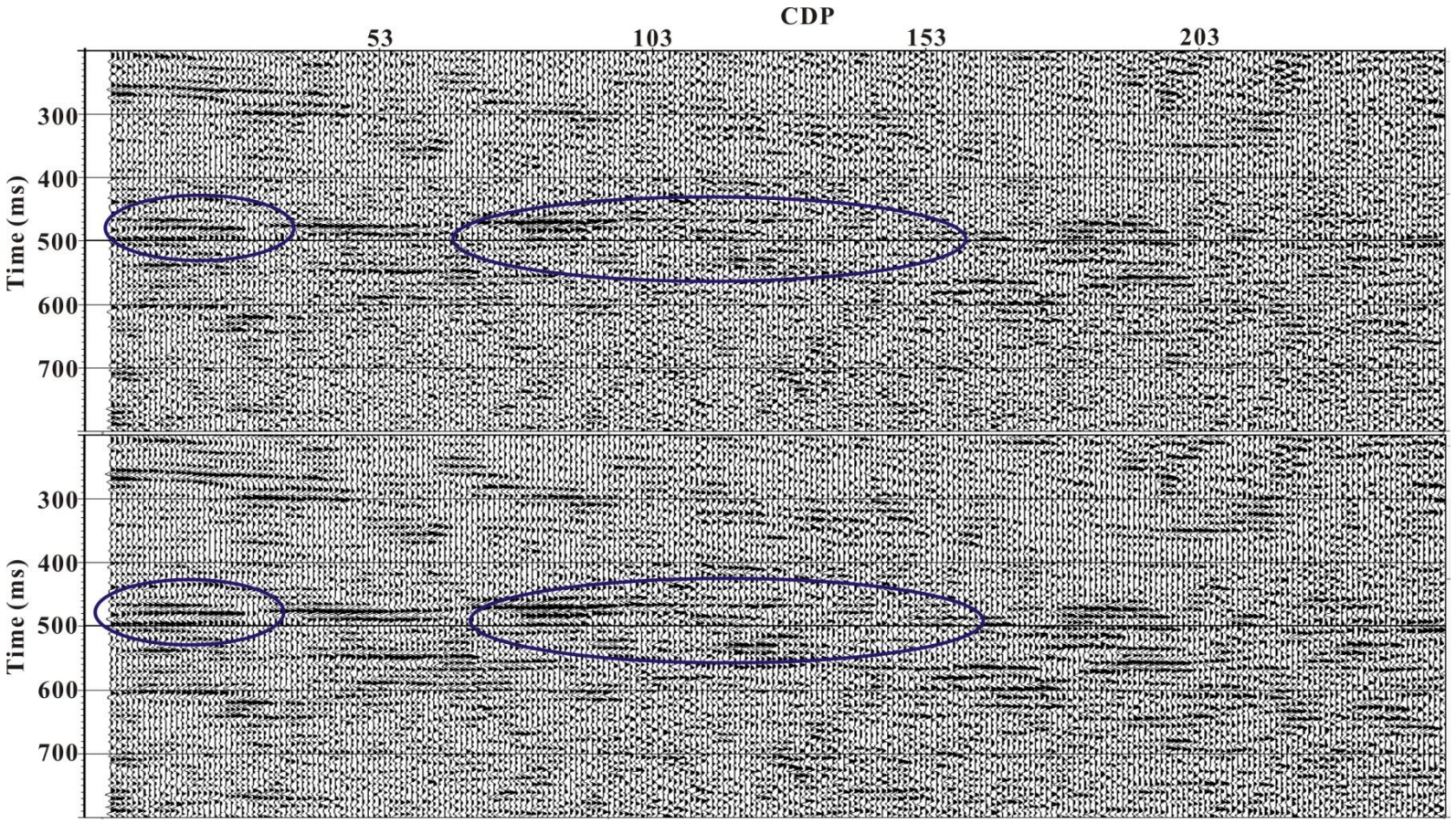

Figure 2.35 A portion of stack profile of line_3000 before (top) and after (bottom) F-X 2D predictive filter

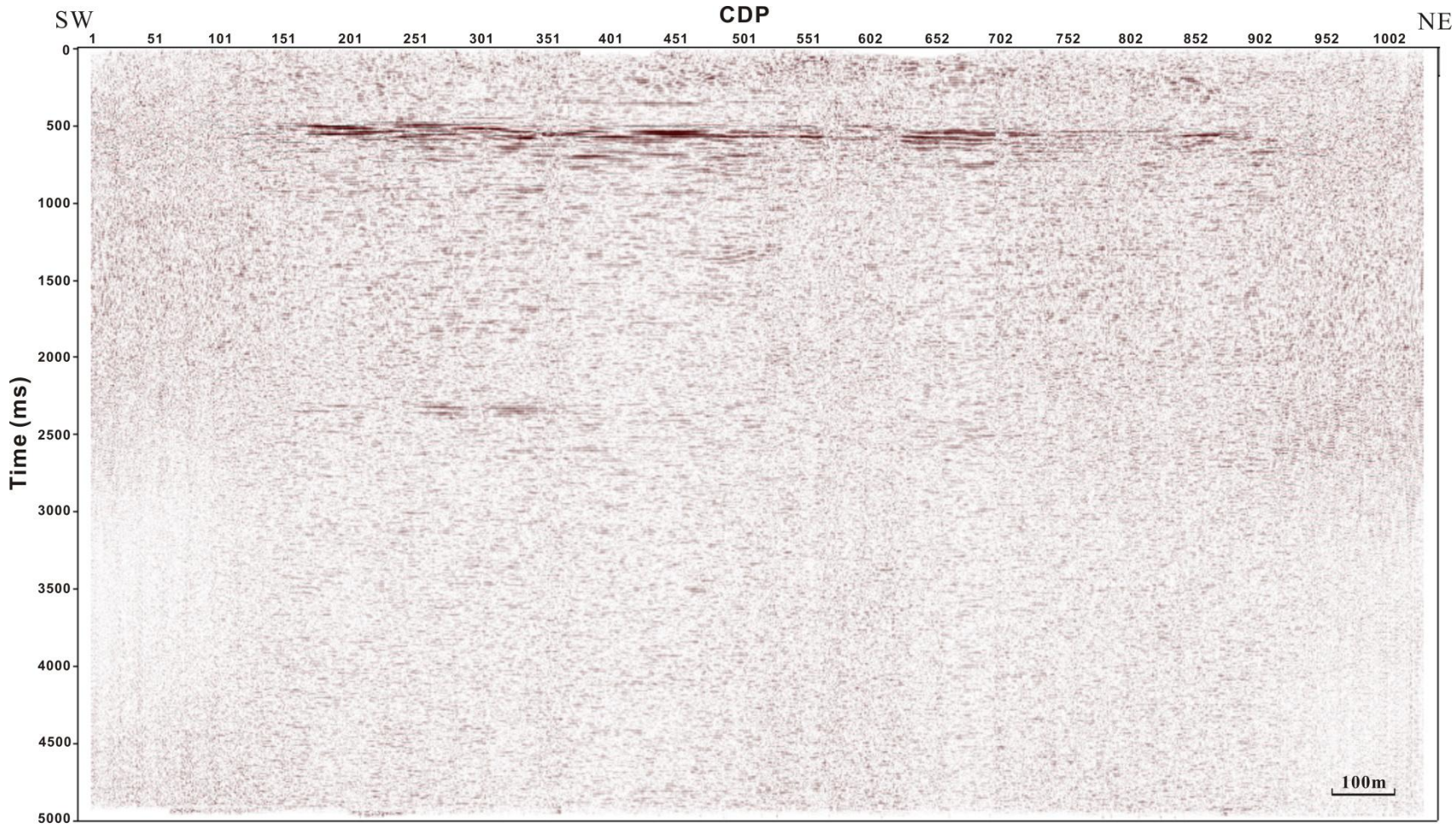

Figure 2.36 The final stack profile from line_2000.

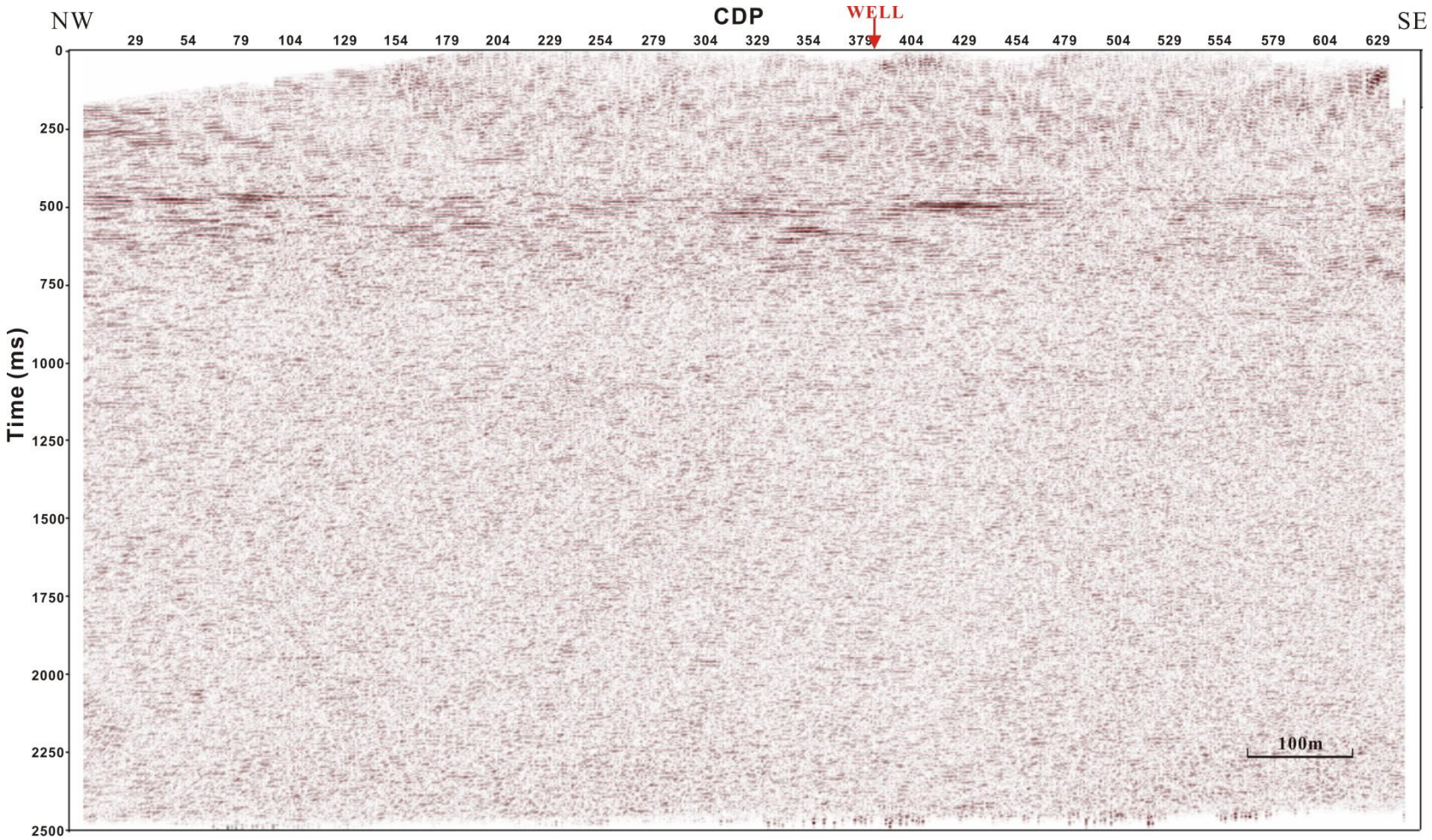

Figure 2.37 The final stack profile from line_3000.

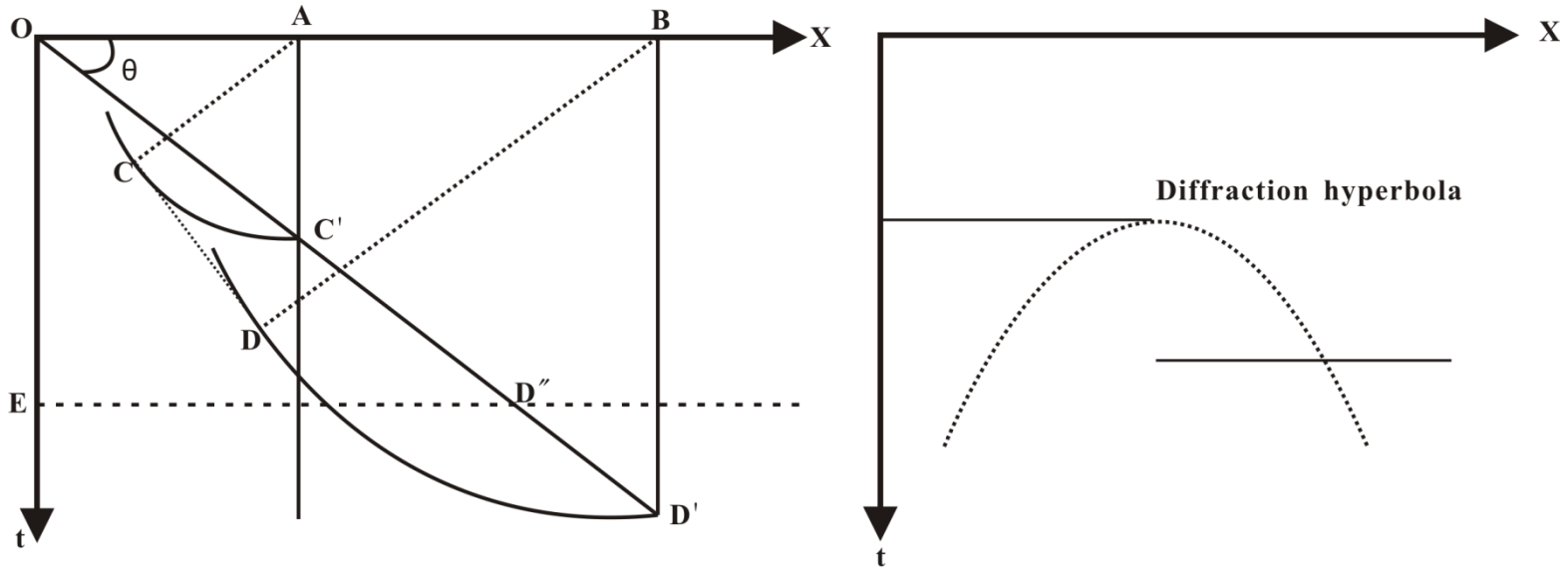

Figure 2.38 Migration principles. (a) Migration corrects the dipping reflection segment *C´D´* on a time profile to its actual location of *CD*. *C´D´* moves to updip direction and becomes shorter. (b) Migration collapses diffractions back to their original source point.

Kirchhoff migration is based on the integral solution to the scalar wave equation and it is perhaps the least expensive (in terms of computer time) and simplest to understand. It can handle all dips up to 90 degrees, but has limited ability in handling lateral velocity variations (Yilmaz, 2001). In this research area, based on the small variation in lateral velocities and the effect of different migration approaches, Kirchhoff migration was implemented on the data. In Kirchhoff migration, two parameters are critical to the migration process: the velocity field and the migration aperture. Migration aperture defines the range of data included in the migration of each point. It usually should be bigger than two times the horizontal shift distance of migration of the steepest reflector. A small aperture could cause undermigration and bring fake horizontal events. The velocity field used for migration ordinarily needs to be smoothed to prevent the process from producing artificial structures in the image due to abrupt lateral velocity variations. Further, the velocity may also need to be further corrected to avoid undermigration and overmigration. The output of migration is intended to represent the geological cross-section along the line traverse even though it often is displayed in time (Yilmaz, 2001). Fig. 2.39 and Fig. 2.40 show the migration profile of line_2000 and line_3000, respectively. A 100% velocity field (see Fig. 2.30 and Fig. 2.31) with a 200 trace each side aperture was utilized in the migration.

2.5 Comparison with earlier results

It is useful to compare this latest processing attempt to the old processing result which

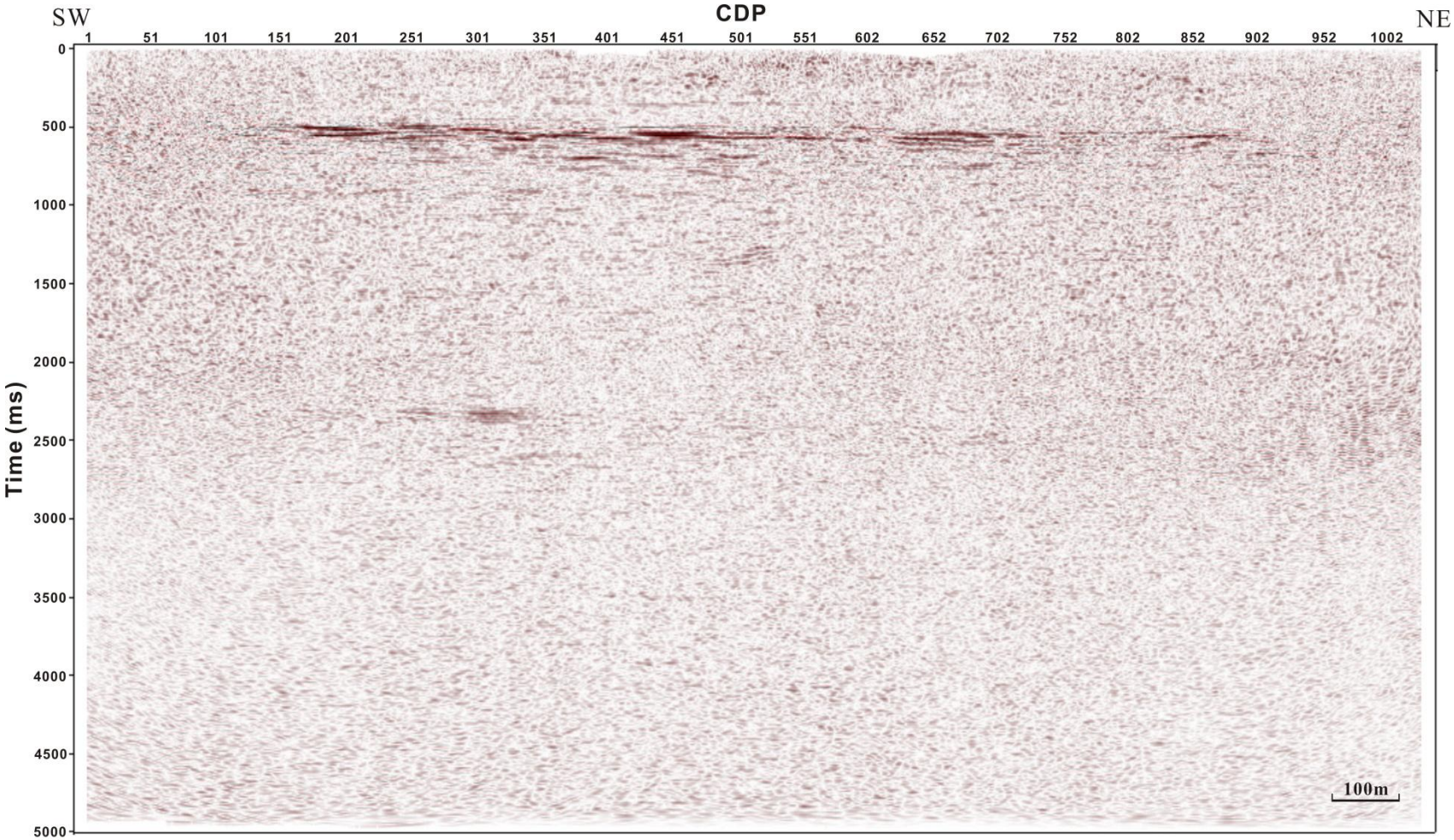

Figure 2.39 Migration profile of line_2000.

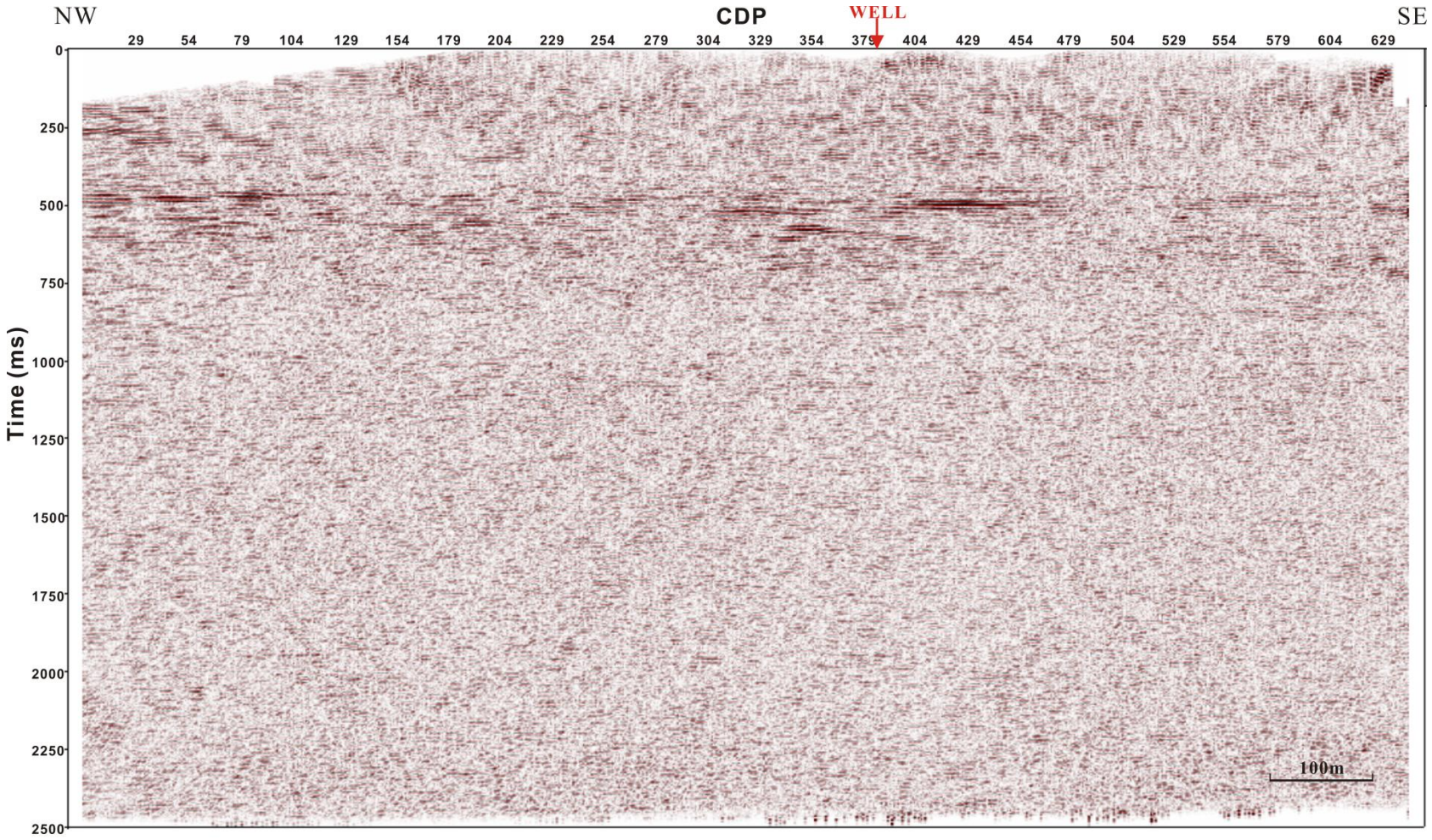

Figure 2.40 Migration profile of line_3000.

was finished in 2007 by Suvi Heinonen (Fig. 2.41). Here a new the definition of survey line was defined and new bin grids adapted. The entire processing sequence and parameters were also modified. Meanwhile, the quality controls were exerted to each step. The bin grid in new result was 2 m x 100 m which makes it much longer than old result that used a 5 m x 100 m bin size. To compare, a result with a big grid of 5 m x 100 m was also generated from original result which is showed on Fig. 2.42. And old profile had a shorter surface line and less CDP traces than new profile due to the different definition of geometries.

The comparison is presented on Fig. 2.43. Only 1 s length profiles are displayed in order to show more details. From comparison, this latest processing was able to reveal additional features and appears to better resolve the reflectors. There is only a 20 ms time difference between the latest profile and earlier profile, and this is likely caused by the application of different static corrections and reference elevation datum. More detailed information can be observed on new profile (Fig. 2.43 (a)) around the expected Outokumpu-type assemblage zone. And the continuity has been improved greatly. Other than the layer around 500 ms, one strong layer can also clearly recognized from line_2000 at 340 ms from CMP 108 to CMP 244, which can only be seen a little bit from old profile. And line_2000 also exhibits some other strong layers at 2.3 s from CMP 60 to CMP 200, which are not revealed on old profile. Below 2.5 s, there is no comparison since old profile was only processed from 0 to 2 s.

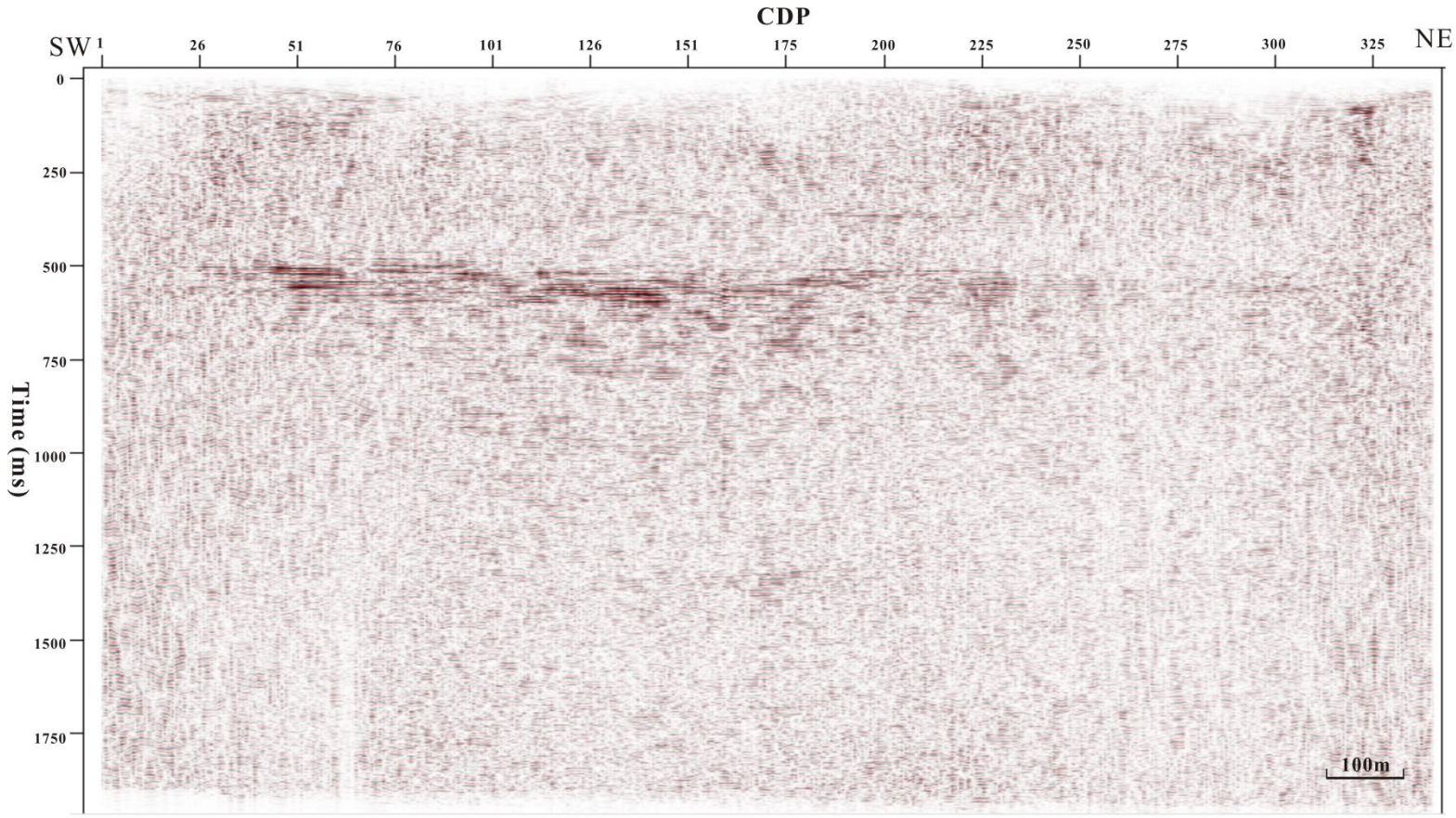

Figure 2.41 Line_2000 stack result from Suvi Heinonen

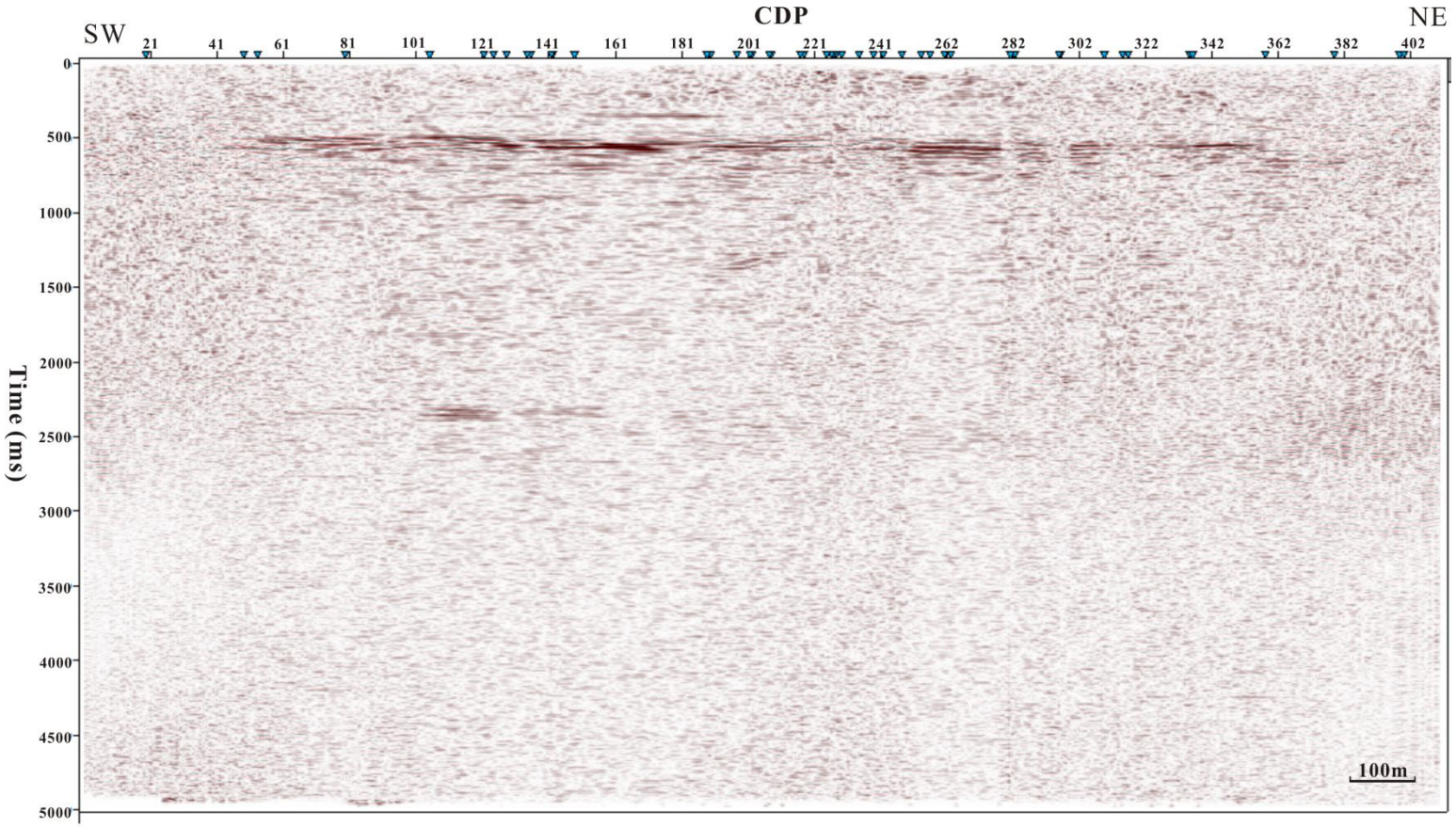

Figure 2.42 Current stack result of line_2000 in the same grid with the earlier result

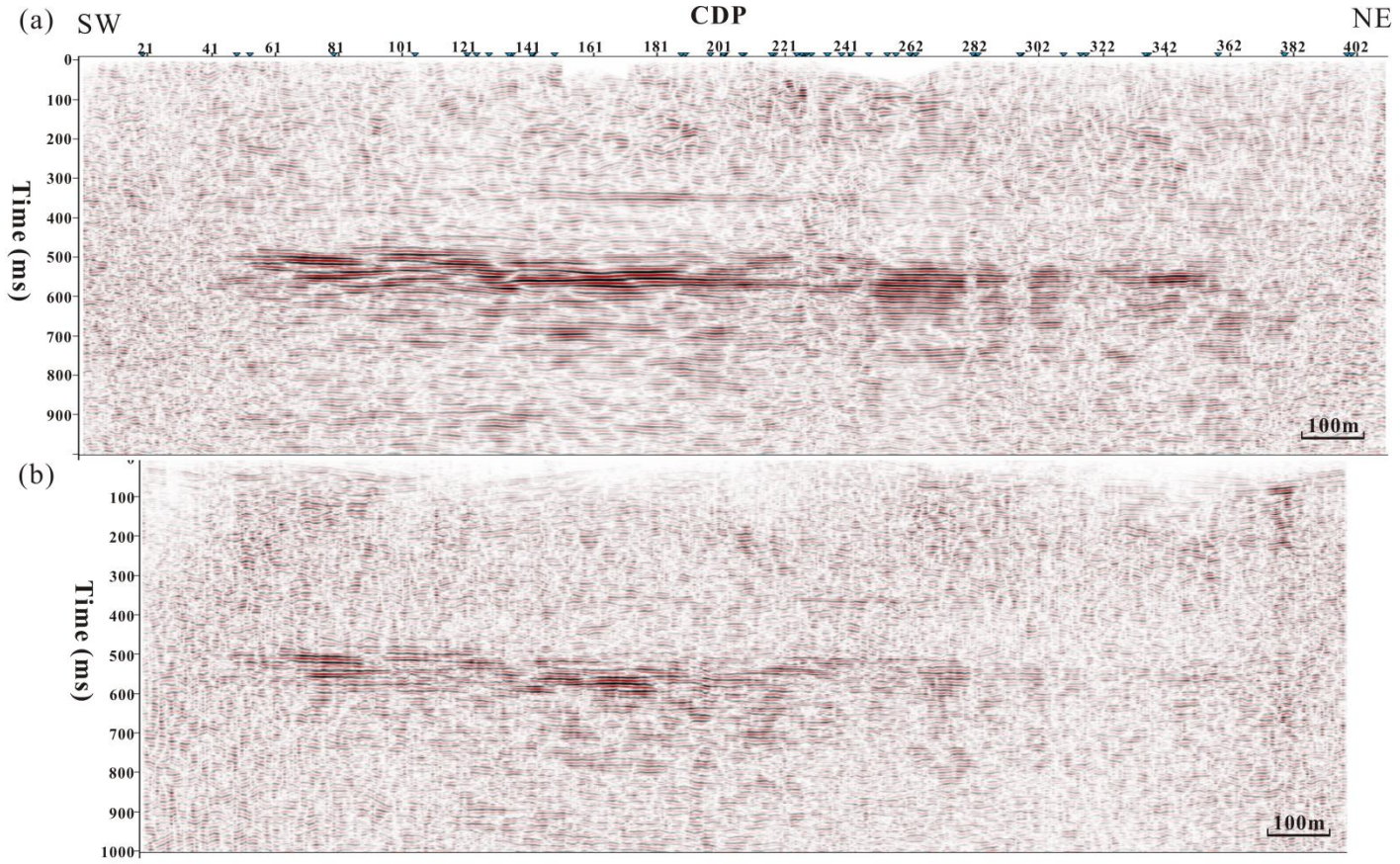

Figure 2.43 Comparison between the current stack result (a) and the earlier stack result (b) of line_2000 from 0 ms to 1000 ms

Line_3000 was not attempted earlier so there is no comparison for it available.

2.6 Conclusions

This 2D seismic survey was acquired on high-frequency vertical seismic vibrator and had a relatively high fold to generate high resolution images. However, by the reason of the special properties of hard rocks, the signal to noise ratios on both line_2000 and Line_3000 is quite low. Moreover, the two seismic lines are seriously crooked, which introduces some special difficulties for data processing. Based on the analysis on geometry and data quality, the final processing sequence and parameters were determined after repeated testing and comparison. Special attention was given to the definition of surface lines and bin grids, the preservation of high frequency information, methods and parameters of noise attenuation, and deconvolution. Line_2000 and line_3000 had essentially the same processing sequence, but with a few different parameters according to their different data quality (Table 2-1).

Seismic data processing describes the series of computational procedures that begin with the raw seismic data obtained in the field and end with a final 2D ‘profile’ or 3D ‘volume’ that highlights the times or depths of different reflecting geological horizons in the earth. These profiles may then be interpreted to delineate the subsurface geological structure.

Seismic processing flow usually follows a basic routine. It involves the application a series of computational algorithms to the seismic data as guided by the geophysicist.

There is no a single universal sequence that can be applied to every dataset. For each step, judgements are needed based on the quality of datasets. For an unknown dataset, a series of test on parameters and algorithms are necessary, which helps processor to make a decision. And the experience of a processor plays an important part in the processing. In this processing, numerous tests were performed almost on every step. Only the successful results are displayed here. For instance, in order to attenuate the linear noise, simple mute and F-K filtering with different pie size were tested. Due to the fact it is really necessary to keep the weak signal in the dataset as much as we can, simple mute method was discarded. But it is still very useful for some datasets which have strong reflections. And for the deconvolution step, sometimes people use predictive deconvolution first then followed spike deconvolution to attenuate the multiples and then compress the wavelet. But in this case, predictive deconvolution did not work well because it was hard to estimate the multiples on a very noisy data. So a spike deconvolution was performed first, which compressed the wavelet and also improved the signal-to-noise ratio, then followed by a predictive deconvolution. By comparing the results between these two different deconvolution sequences, the latter one was chose for a better improvement.

Considering the complications caused by irregular geometry and poor data quality, the two seismic lines were processed successfully. The final results show strong and distinct reflectors around 500 ms which are associated with the Outokumpu-type assemblage known to host massive sulphide bodies. Reflectors on line_2000 are more continuous

than those on line_3000. And line_2000 appears to have a higher signal-to-noise ratio than line_3000 even though it crooked more seriously than the other. The reason that line_3000 has a relatively low resolution is considered as the fact that line_3000 has lower fold coverage because it was not fully covered by receivers and sources. We will return to the interpretation these profiles in Chapter 5 where they will be integrated with the borehole seismic data.

3.0 Vertical Seismic Profiling

This chapter presents the results of the vertical seismic profiling (VSP) measurements in the OKU-1 borehole at Outokumpu, Finland. The VSP data was obtained from the 2.5 km deep International Continental Drilling Program (ICDP) research borehole. A variety of different VSP geometries were acquired including a zero-offset VSP (Fig. 3.1a) that is the principle contribution in this thesis, one far-offset VSP (Fig. 3.1b) , and a series of walk-a-way VSP (Fig. 3.1d) surveys being analyzed for seismic anisotropy in related research (Schijns *et al.*, 2011) .

The zero offset VSP survey was carried out in order to determine detailed velocity and reflectivity structure of the rock mass near the deep drill hole. This chapter focuses on the processing of zero-offset VSP data. It starts with an introduction of VSP measurements including the definition of VSP's, some history, and its applications. This introductory material is followed by acquisition, geometry and processing of the OKU-1 zero-offset VSP data. Data processing of zero-offset VSP mainly consists of defining the geometry, calculating the interval velocity, the noise attenuation, wavefield separation, deconvolution and corridor stacking. Details of this are described in later sections.

3.1 Introduction

Vertical seismic profiling (commonly abbreviated to the shorter name VSP which is used hereafter) is a rapidly developing area of geophysical technology. It is a measurement

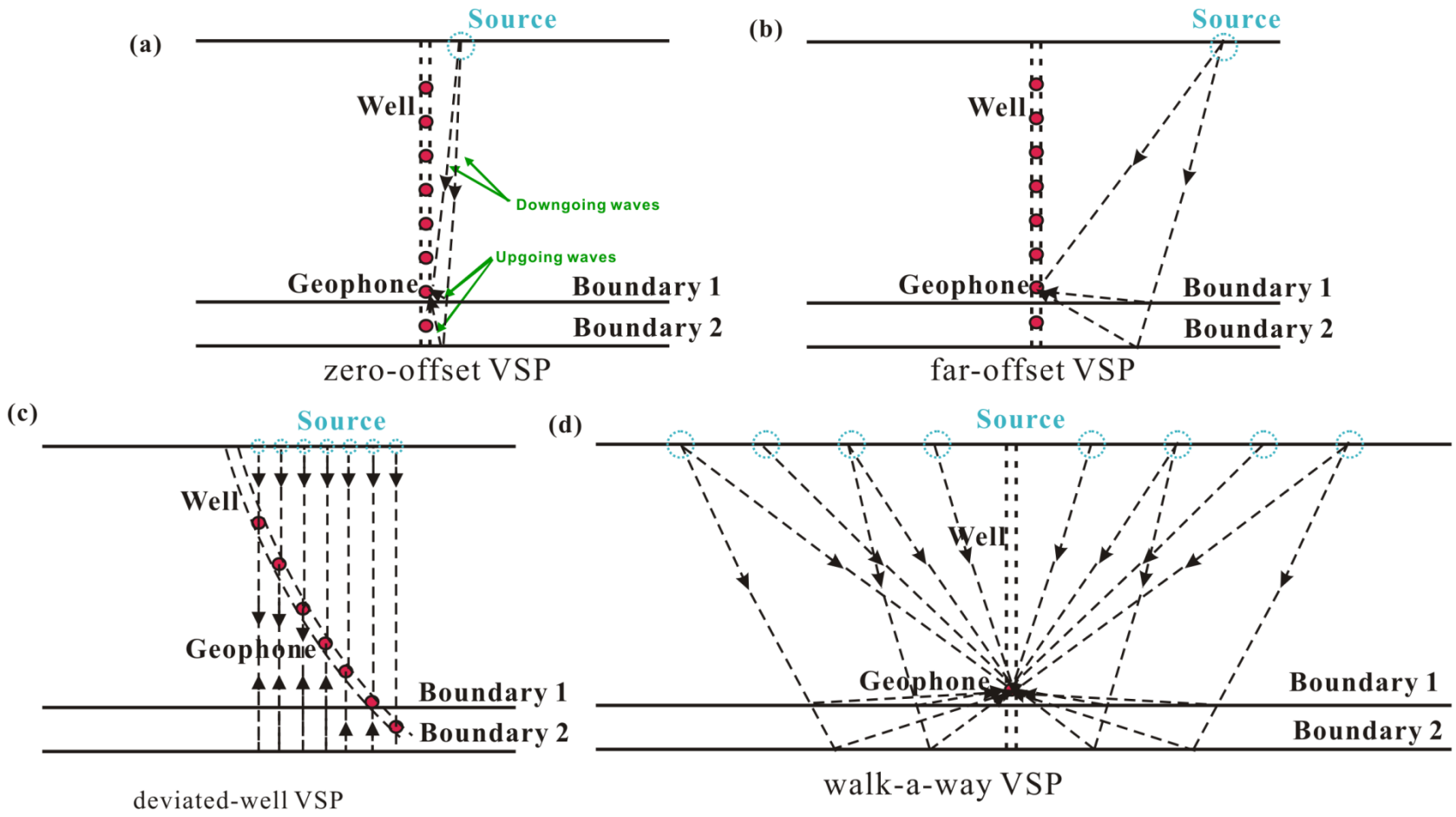

Figure 3.1 Schematics of zero-offset VSP survey, far-offset VSP survey, deviated-well VSP survey and walk-a-way VSP survey

procedure that a seismic source generating a signal is placed near the surface of a drilled well and geophones are fixed at various depths inside the wellbore to record reflected seismic energy (Hardage, 2000). Early variants of this were called ‘check shots’ and they were invaluable in calibrating the travel times of a seismic wave to a given depth in the earth. In the absence of additional information, the depths estimated from surface reflection seismic data are notoriously prone to error and hence a VSP is necessary to determine a true time to depth function. Further, modern processing techniques described below even allow for better adjustment of the actual reflections seen in the borehole to the actual reflection profile.

A geophone placed on the earth’s surface records only upgoing waves travelling from below. In contrast, because a VSP geophone is located far below the earth’s surface when recording, it responds to both the upgoing and the downgoing seismic wavefields (Fig. 3.1). This is the principal difference between VSP and surface seismic data because downgoing events cannot be identified in data recorded by geophones positioned on the earth’s surface. So since the receivers are located down the borehole and closer to the target, the accuracy relative to surface measurement is improved. Meanwhile because the seismic energy travels only one way through the earth and particularly only once through the highly attenuating near surface materials, VSP data suffers less frequency-dependent attenuation (Zimmerman and Chen, 1993). In principle, the VSP has a potential capacity to provide a more detailed seismic image of the subsurface, thereby enhancing the

reliability of a geological interpretation (Cassell, 1984). However, this is at the expense of lateral coverage. In addition, relative to the sonic logs, VSP data have a signal bandwidth closer to the seismic data. As a result, VSP data often provide more reliable correlation of well control to seismic data than synthetic seismograms derived from sonic logs. So, as noted, VSP's provide a direct measure of the travel time to depths in the earth.

The major use of borehole data was limited primarily to the calculation of seismic wave propagation transit times until the work of Jolly (1953), Riggs (1955), and Levin and Lynn (1958) who described a full wave type study. They suggested that in addition to the measurement of travel times to depths in the earth, the seismic response that follows the direct arrivals can also be used to determine the seismic wavelet attenuation. As a result, workers started to pay attention to the recordings beyond the first arrivals.

Soviet geophysicists developed the studies of VSP applications from the 1960s to 1970s. Their work was described by a major investigation by (Gal'perin, 1974). And these were followed in the late 1970s by workers outside of the Soviet Union. Since then, the vertical seismic profiling techniques evolved rapidly and the VSP became an important tool in the 1990s.

As a powerful tool in a variety of seismic exploration situations, vertical seismic profiles are applied to many aspects. Vertical seismic profiling is mainly used to measure the

variations of seismic velocity with depth because a vertical seismic profile is closely related to a velocity survey since the source and receiver geometry is the same for both measurements. First arrival times can be used to calculate the interval velocities. The full waveform data recorded in a vertical seismic profile can improve the structural, stratigraphic, and lithological interpretation of surface seismic recordings (Hardage, 2000, Stewart and Disiena, 1989, Boyer and Mari, 1997). Meanwhile, the separation of the upgoing and downgoing wavefields provides a method to study the acoustic response of earth in detail (Kennett *et al.*, 1980, Balch, 1982, Balch and Lee, 1984). Vertical seismic profiling can also be applied to measure seismic attenuation, estimate reflector dips, and determine the location of fault planes. Finally, appropriate processing of the observed seismic records produces highly reliable ties between a well log and surface seismic profiles. That is, the VSP data is the only way to truly calibrate a seismic reflection record.

3.2 Geometries and Acquisition of Vertical Seismic Profiling

VSP surveys usually utilize surface sources and borehole receivers, although in some cases downhole sources too have been employed. Depending on the relative alignment of the source and receiver configurations, VSP surveys can generally categorized as either a zero-offset VSP or an offset VSP. Four basic types of VSP surveys are usually distinguished, which includes zero-offset VSP, far-offset VSP, walkaway VSP and deviated-well VSP (Oristaglio, 1985) (Fig. 3.1).

Acquisition of zero-offset VSP data involves a surface source that is located at a single point at the surface close to the wellhead and a geophone clamped at various, usually uniformly spaced, depths to the borehole wall. The source and receivers are treated as vertically aligned. Traces are recorded several times at the same depth. The geophone is then moved to a new depth and recording is repeated. Traditionally this was carried out with a single 3-component geophone due to limitations of wirelines. Recent digital systems, however, can allow for literally hundreds of individual receivers to be placed in a chain down the borehole making the measurements rapid.

The final profile is displayed in depth and time. The VSP records both upgoing and downgoing waves (Fig. 3.1). The seismic ray paths from the source to the receiver are considered nearly vertical and have lengths that are very close to the depth of the receiver. Consequently, zero-offset VSP surveys provide information about the subsurface only within the Fresnel zone centered at the well.

The conventional zero-offset VSP is typically recorded at relatively large receiver gaps of 10 m or more; in many cases this spacing results in a seriously under-sampling of the wavefield, but this large spacing is usually dictated by the high costs for such surveys in industry. In contrast, in the OKU-1 zero-offset survey the equipment and personnel were all supplied directly by the project; this allowed a geophone station to be recorded every two meters starting at 2500 m and ending at 50 m (near the bottom of the surface casing). The zero-offset survey was recorded from April 28 2006 to April 30 2006 with a source

(IVI Minvib®) which was 33.5 m away from the borehole. 8 s sweeps from 15 Hz to 250 Hz in frequency were used. After correlation, the record length was 5 second with 1 ms sampling rate. The fold ranges from 1 to 5 (i.e. depending on noise conditions records were repeated at each depth up to 5 times and these were summed to improved the signal to noise). Fig. 3.2 shows the 3D geometry of the zero-offset VSP from Outokumpu, the borehole deviation is apparent and the borehole drifts towards W and NW by 250 m at the furthest deviation.

3.3 Data Quality Analysis

In a quality VSP survey, the geophones are locked rigidly against the wellbore wall in order that they transduce the proper signal. A loose geophone is problematic as the signal observed is then highly contaminated because the geophone are not properly coupled to the earth; the geophones are essential free to move on the wireline and this is obviously picked up in the signal. Meanwhile the borehole provides a relatively noise-free environment for VSP recording. However, some noise is unique for vertical seismic profiling.

The final raw data zero-offset VSP data set is shown in Fig. 3.3a. These data (Fig. 3.3 (a) and (b)) that amplitude decay resulting from spherical spreading, scattering and absorption also exists in the VSP data just as it does with the surface seismic data described in the previous chapter. The frequency has almost same bandwidth in this

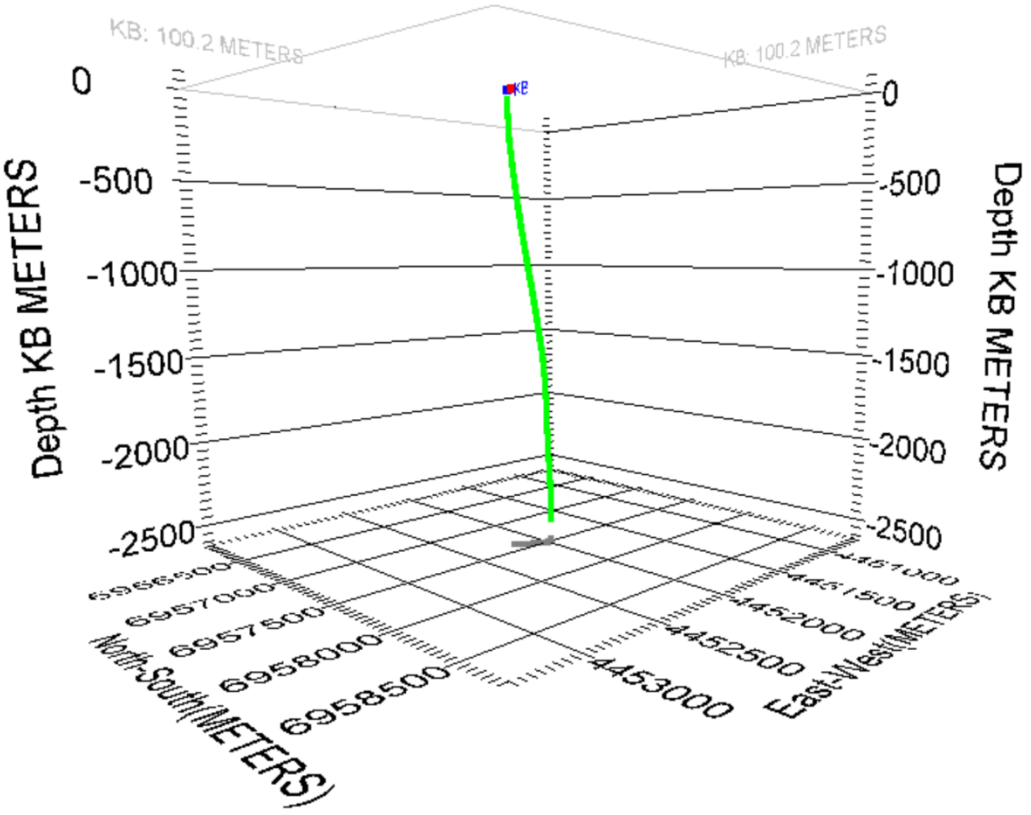

Figure 3.2 Zero-offset VSP geometry: Red point is the shot position. The green points are receivers' positions.

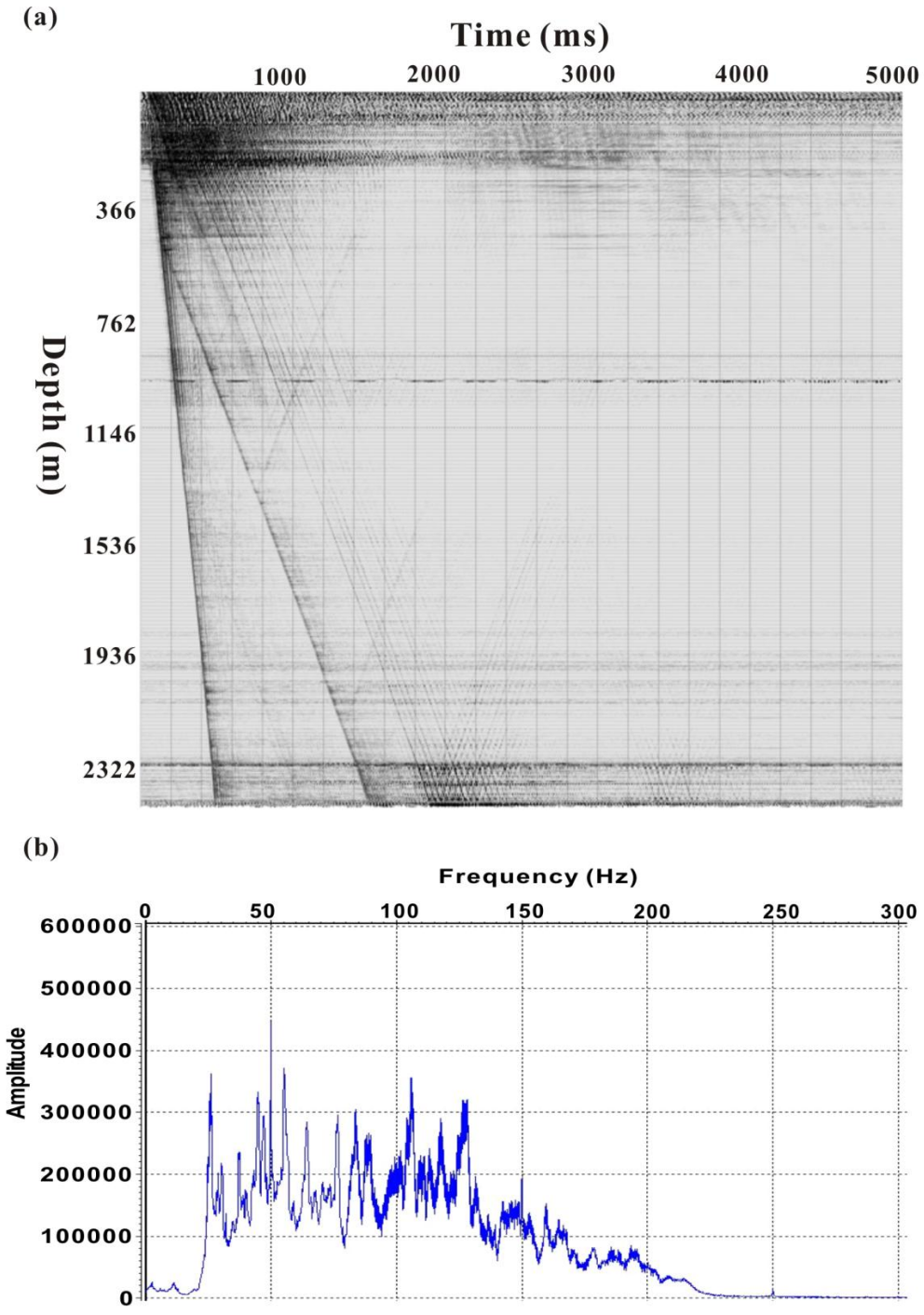

Figure 3.3 (a) Zero-offset VSP raw data (b) Amplitude spectrum of raw VSP data

zero-offset VSP data as those 2D surface seismic data on amplitude spectrum. The high frequency components were attenuated less than they were in the surface seismic data (Fig. 2-14 (c) and Fig. 2-15 (c)) since the seismic waves only travel one way in VSP survey. Additional, it is easy to see from the raw data (Fig. 3.4 (a)) with AGC gain that there are several kinds of interference waves.

In addition to random noise, tube waves, which are low-velocity, high-amplitude events propagating along the interface between the borehole wall and the borehole fluid, are visible in the profile and travel with a velocity of 1430m/s. The tube waves also reflect strongly from the bottom of the well borehole and from fracture zones (Tw4, Tw5, Tw2, Tw6 in Fig. 3.4 (a)) and these travel back up towards the surface. There is also substantial harmonic noise with 50 Hz contaminating most of the traces which can be seen clearly from the frequency-wavenumber F-K domain (Fig. 3.4 (b)). This harmonic signal is electrical noise from the local power grid that, in Europe, operates at 50 Hz.

All of these make the S/N ratio of the data quite low, which makes it very difficult to separate the signal from the noise. Moreover unlike surface seismic surveys, the VSP records both upgoing waves and downgoing waves. One can observe that the downgoing waves are so dominant that the primary upgoing reflections can hardly be identified on the data (Fig. 3.4a).

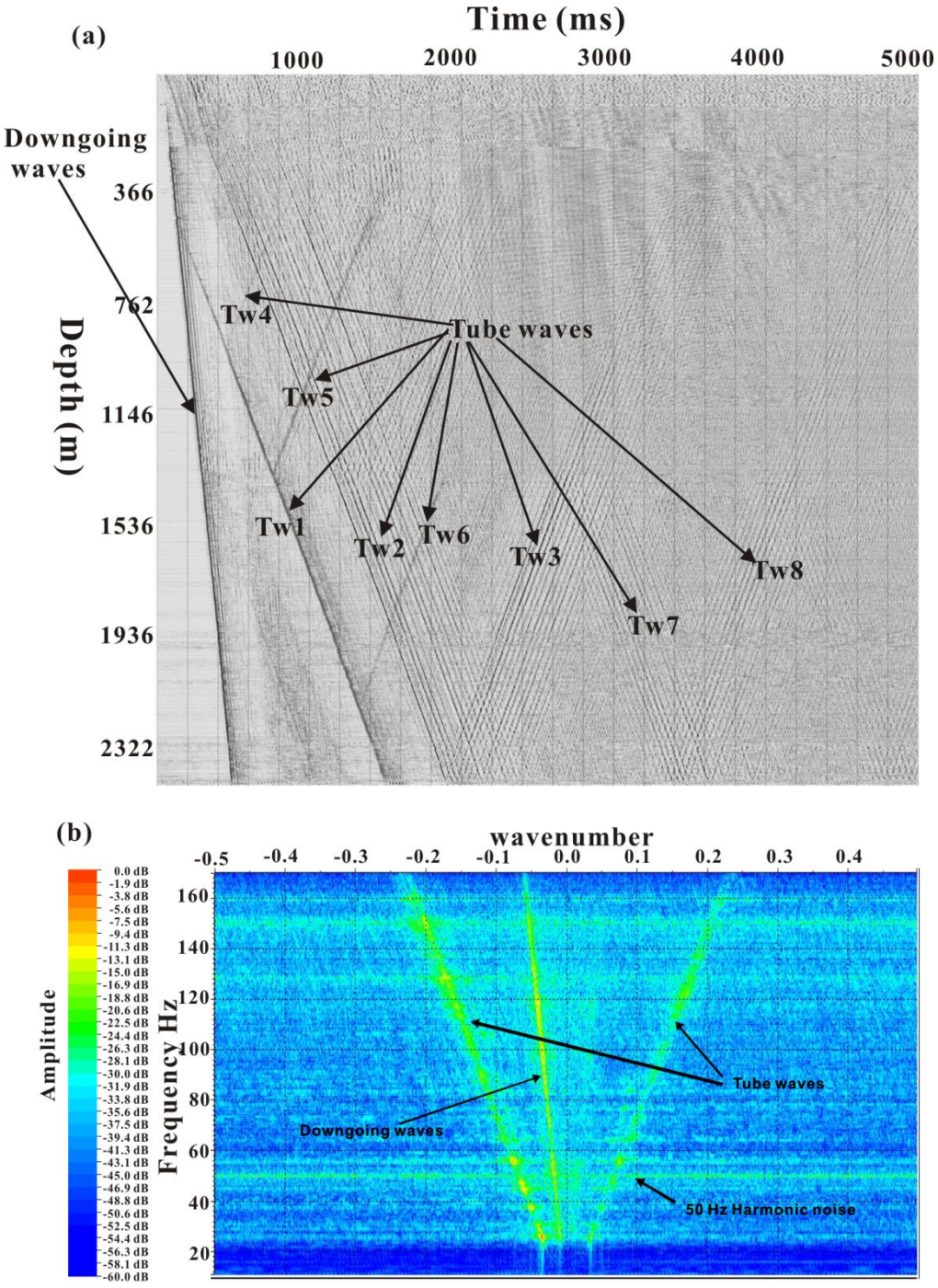

Figure 3.4 Wave types identified from the raw VSP data in time domain (a) and frequency-wavenumber domain (b).Harmonic noise is the electrical noise from the local power grid. Tube waves are low-velocity, high-amplitude events propagating along the interface between the borehole wall and the borehole fluid.

3.4 Processing of VSP Data

VSP data are often used to find the depths at which seismic reflections originate and hence assist in the interpretation of surface reflection seismic profiles. However, facing the unprocessed data, several problems are apparent according to the data quality analysis, which makes it necessary to processing the data in order to achieve a desired interpretation. The basic theory of processing techniques is well known, and many of them are borrowed from surface seismic processing. However, techniques used in VSP processing have been modified (Lee and Balch, 1983) according to the unique geometry of the VSP.

For the general zero-offset VSP data processing, it is assumed that the source offset is small compare to the depth of interest, and the dip of the rock layers is negligible. Due to the unique conditions of each VSP data, a different processing procedure is required for the different types of surveys. The details of the processing steps vary according to the specific data set. Here, this section presents a detailed processing procedure for Outokumpu high resolution zero-offset VSP data.

3.4.1 Trace Editing

In order to eliminate bad traces which contain excessive noise or spurious events from the data set, every trace was plotted separately for an initial quality check. And bad traces were deleted from data to improve the signal-to-noise ratio. This editing process is

somewhat subjective and may be repeated several times.

3.4.2 First break Picking and P-wave Velocities Calculation

A vertical seismic profile is closely related to a velocity or 'check-shot' survey since the source and receiver geometry is the same for both measurements. First break times are the critical information needed to determine the P-wave velocity (Dix, 1939, Dix, 1945, Stewart, 1984). The picking of first arrivals is affected by the quality of raw data. So a fairly unambiguous arrival time picking (Fig. 3.5) could be made if the data has a low signal-to-noise ratio.

First break picking is about picking the first arrivals of refracted waves. Because it is unavoidable to record some type of noise preceding the first break time, the real first break time can be very difficult to pick. Usually, the first prominent peak following the first arrival will be picked as the first break time. The error is considered to be minimal compared to the inconstant picking from trace to trace. Before manual picking the first arrivals, AGC scaling was added to data to attenuate the anomalous amplitude and enhance picking accuracy. Troughs of the first breaks were picked on Vista^{TM} software manually (Fig. 3.5 (a)). Most of these first breaks were clear to pick except those traces that came from the shallow section (above ~150 m depth) due to the poor coupling of the geophone package to the wellbore in this uppermost zone. The entire set of (1306 traces) picked times is shown in Fig. 3.5 (b). Those picks are then used to calculate the P-wave interval

velocities which were compared with the sonic log measurements below.

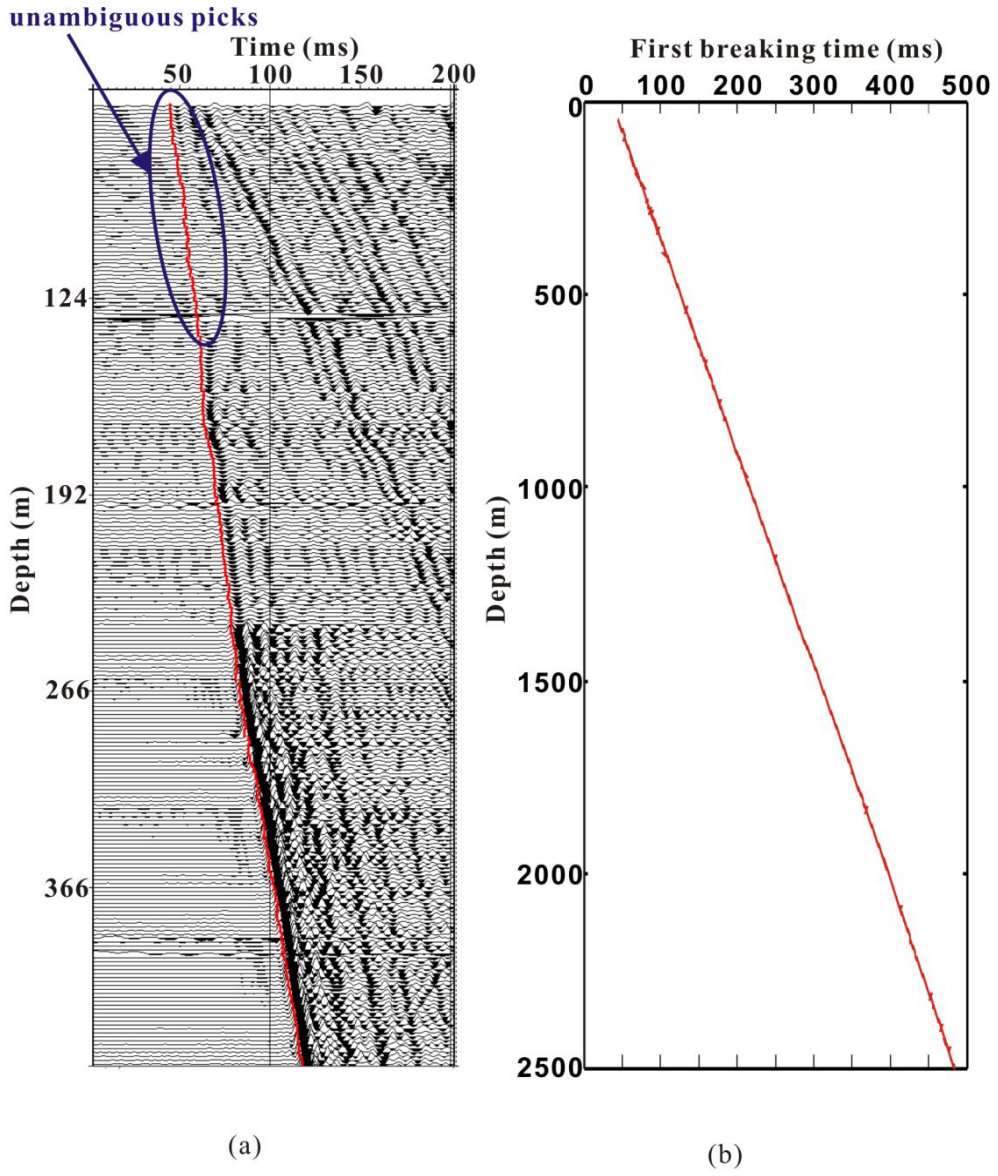

Figure 3.5 The first breaks picking. (a) a portion of the first breaks picking on VSP data, (b) all the first breaks picking points in the zero-offset VSP data.

Determination of the P-wave velocities from the picked times is in principle straightforward but this is also complicated by the close 2 m spacing between the measurements. For a wave speed of 6000 m/s, the wavefront requires only 1/3000 seconds (0.33 ms) that is only a fraction of the 1 ms sampling period employed. Since the travel times can be picked to at best 1 ms, the inherent error in timing results cannot allow one to calculate the velocities from the simple ratio of the geophone spacing with the time differences between adjacent geophone stations. Consequently, the P-wave interval velocities (V_{LP}) on Fig. 3.6 were determined by a linear least square fit of the a contiguous set of picked transit times the slope of which provides a local tangent used to estimate the interval velocity (Schmitt et al., 2007).

Window lengths of 50 depth points (i.e. over 100 m) was chosen for the least square fitting and the results are shown as the black line in Fig. 3.6 (b). Meanwhile, different window lengths were tested. Since the first arrival times are difficult to determine due to the noise, it is unavoidable to have some errors in the picks. As a result, the length of the window needs to be sufficiently large to counterbalance those errors. During the test, with smaller window such as, for example, only 30 points, the interval velocities (Fig. 3.6 (a)) varied dramatically. But with a longer window than 50 points, some detailed variation of velocities (Fig. 3.6 (c)) was lost. 50-point length window made the velocities change smoothly (Fig. 3.6 (b)), and more detail information were observed.

The Pearson's correlation coefficient (Fig. 3.6 (d)) that gives some measure of the quality

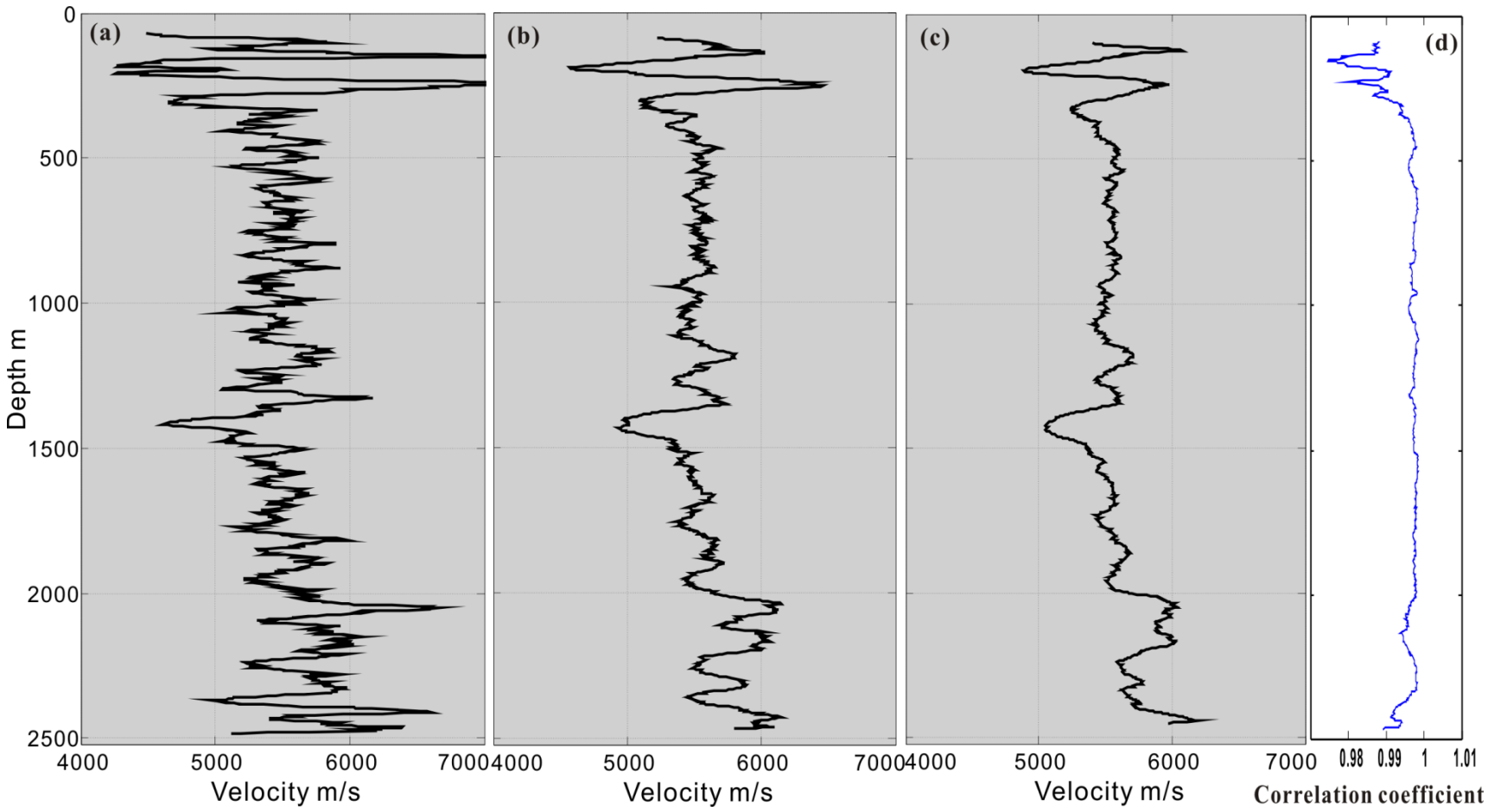

Figure 3.6 P-wave interval velocities calculated from the picked first break time of VSP data with different lengths of windows. (a) with 30-point length window; (b) with 50-point length window; (c) with 70-point length window; (d) the correlation coefficient of the local linear slope method when the length of window is 50 points.

of the fitting is mostly better than 0.99 except for the shallow part before 250 m, which can be considered as the result of the difficult picks on the noisy data. But the correlation coefficient is still higher than 0.97.

Sonic logging is taken to record the interval transit time, or slowness of compressional waves versus depth in downhole formation (Ellis and Singer, 2007). The interval velocity is the reciprocal of the interval transit time. Sonic logging records at frequencies of ~20 kHz (Schmitt *et al.*, 2007) over distances of approximately 1 m with the transit time sampled at a spacing of 0.1 m along the well bore, the direct data is shown in Fig. 3.7a. In contrast, the OKU-1 VSP was acquired at a lower frequency band (20 Hz to 250 Hz) with a spacing of 2.0 m along the wellbore wall.

It is difficult to compare the sonic log velocities to the P-wave interval velocities calculated from VSP data directly. To allow for a better comparison, the sonic log was smoothed by two averaging methods: the simple arithmetic mean

$$V_A(z) = \frac{\sum V_P(z_i)}{N} \tag{3-1}$$

and a long-wavelength approximation based on a ‘Backus’ long-wavelength average (Backus, 1962, Rio *et al.*, 1996):

$$V_B(z) = \left[\frac{\sum V_P^{-2}(z_i)}{N} \right]^{-1/2} \tag{3-2}$$

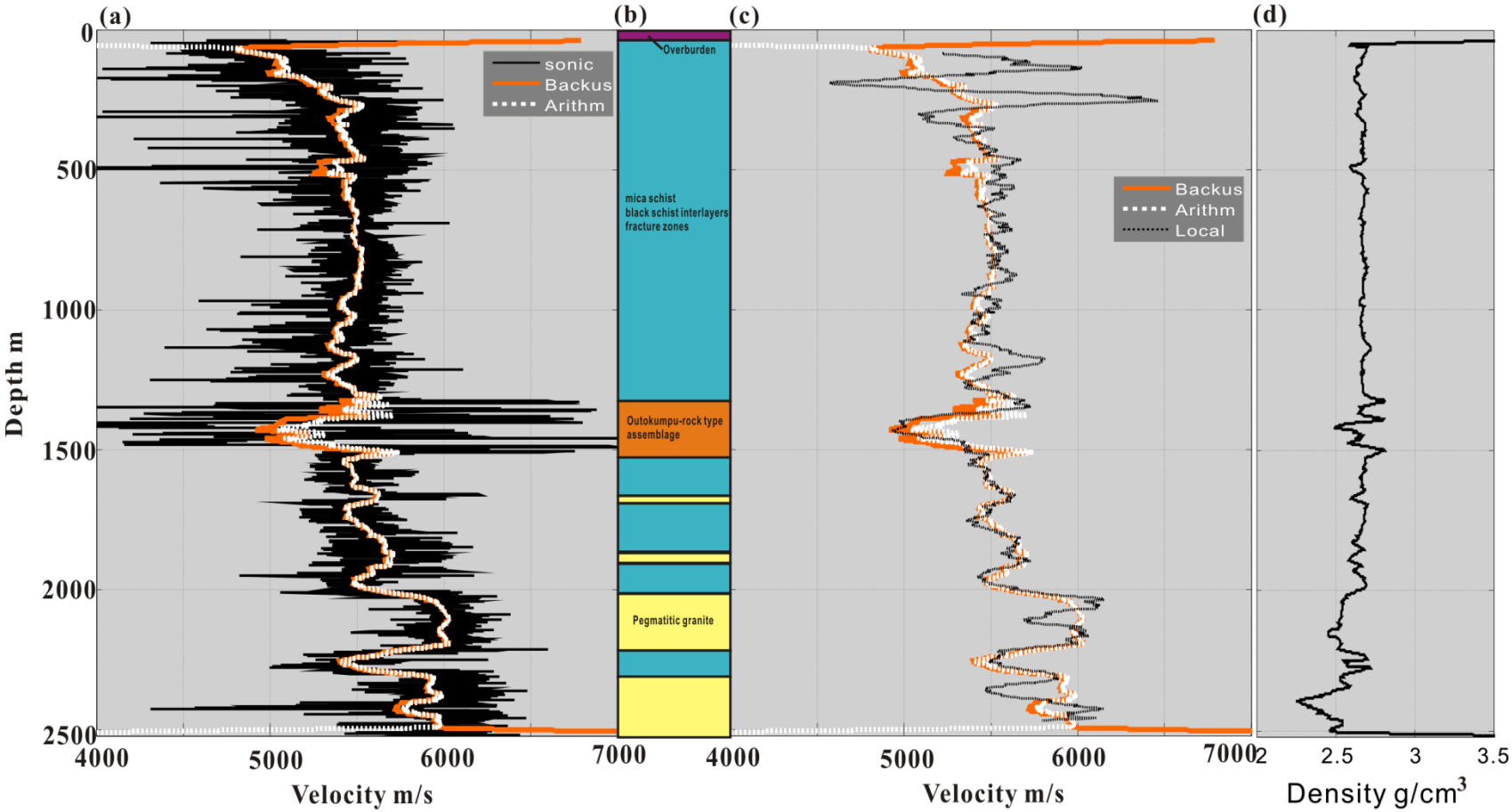

Figure 3.7 Measures of interval velocities in Outokumpu deep drill hole. (a) sonic log interval velocities (black solid line) with corresponding Backus average (orange solid line) and arithmetic average (dotted white line). (b) the geology information. (c) sonic log averages from (a) compared to values of the interval velocities (dotted black line)obtained from the seismic travel time of Figure 3.5 by local linear slope method. (d) density log with Backus average.

where N is the number of sonic log samples $V_P(z_i)$ in a depth window over the range of depths centered on z, a 50 m depth window (250 samples) was selected for the calculations. Fig. 3.7 (a) shows the variable direct sonic log and its two smoothed curves. The sonic velocities from the smoothed curves have the trend of increasing from 5000 m/s to 6000 m/s with depth.

Fig. 3.7 (c) shows the comparison between V_{LP} and V_A, V_B. Broadly, they agree well with each other. The trend of velocities increases with depth from 5000 m/s to 6000 m/s. In the upper schist zone, aside the shallow section affected by the inaccurate picks, sonic smoothed results and VSP measurements, as well as the density (Fig. 3.7 (d)) exhibit a relatively stable variation trend. However, sonic smoothed results display slightly lower velocities than the VSP measurements. The difference between them is around 1% and this is somewhat unexpected as the higher frequency sonic velocities are usually assumed to exceed those of the low frequency seismic data.

The reason for this discrepancy is not completely understood. It may result from the fact that the rock in the immediate vicinity of the wellbore, which is sensed by the sonic log, is damaged by stress concentrations of the borehole, and this damage manifest as increased crack porosity relative to the undisturbed rock mass. This damaged rock has correspondingly lower moduli and hence wave speeds. In contrast, the much larger wavelength seismic energy is sensitive primarily to the undamaged virgin rock mass.

Interestingly, the smoothed sonic velocities match those of the VSP measurements well. Both exhibit a significant drop over the depths of the Outokumpu-type assemblage from about 1300 m to 1500 m. Below 2000 m, the velocities in pegmatitic granite are much higher than those in mica schist zone. This trend of velocities variation remains generally consistent between sonic and VSP measurements. In addition, pegmatitic granite has the lowest densities (Fig. 3.7 (d)) but highest velocities. However, other sections display a relation that rocks with higher densities have higher velocities and rocks with lower densities have lower velocities correspondingly.

3.4.3 Noise Attenuation

Noise in the seismic data is generally classified into two types: random noise or coherent noise. The random noise is uncorrelated from trace to trace. Usually, bandpass filtering and ‘vertical’ stacking of repeated records is applied to attenuate much of random noise. Coherent noise includes linear noise, reverberations and multiples and these can be difficult to remove.

According to the quality of this zero offset VSP data, there are several interference waves we really need to worry about. These include random noise, tube waves, and the harmonic interference from the local electrical system with 50 Hz (from Fig. 3.4 (b)). The random noise is uncorrelated from trace to trace. And usually, much of it can be attenuated after vertical summation or corridor stacking.

The harmonic noise is produced by sources from the electrical grid such as power lines and electric railways. The noise has the fundamental frequency of the local power transmission system (@ 50 Hz) and its harmonics (Butler and Russell, 1993). There are a variety of approaches developed to combat this powerline noise during data acquisition, such as notch filters, spiking deconvolution, and removal by subtracting an estimate of the noise (Butler and Russell, 1993). Butler and Russell (Butler and Russell, 2003) presented a method to fit the noise in a least squares sense by seeking a linear combination of sinusoids that are harmonics of one or more fundamental frequencies to fit the data. This method can handle cases where there is more than one harmonic frequency contaminating the data.

In the present case, the powerline noise has a frequency of 50Hz; and Butler and Russell's method was used to remove this. The harmonic noise was estimated on a trace-by-trace basis over a time window from the record start time to the selected first break time. An example for trace 615 is showed on Fig. 3.8. Fig. 3.8 (c) is the harmonic noise estimated by Butler's method. Then the sinusoid subtraction process was applied to the data (Fig. 3.8 (a)), and Fig. 3.8 (b) shows the trace without harmonic noise. Fig. 3.9 shows the corresponding amplitude spectra and this too demonstrates that the subtraction procedure has largely removed the spike at 50Hz. This type of time domain removal did not damage the desired signal as might techniques such as notch filters that act in the Fourier domain. Evidence for this is shown in Fig. 3.10 (a) and (b) show the difference before and after

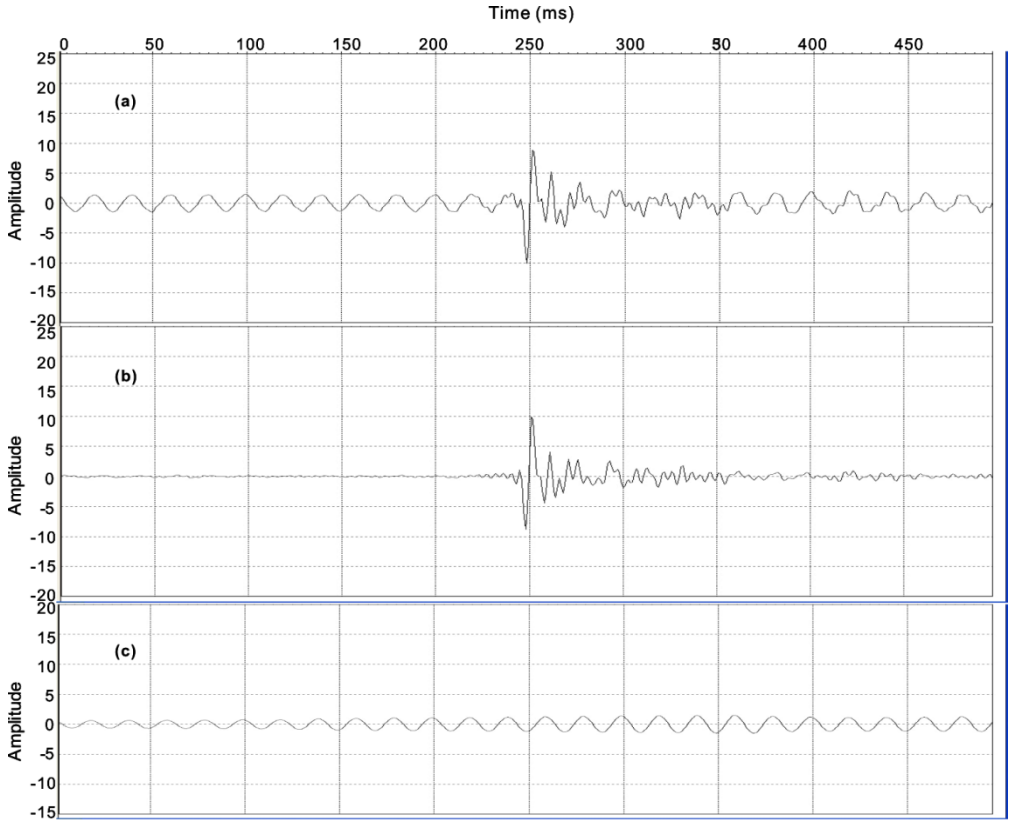

Figure 3.8 (a) Trace 615 from 0 ms to 500 ms. (b) Trace 615 after removing the 50Hz harmonic noise. (c) The harmonic noise estimated from (a).

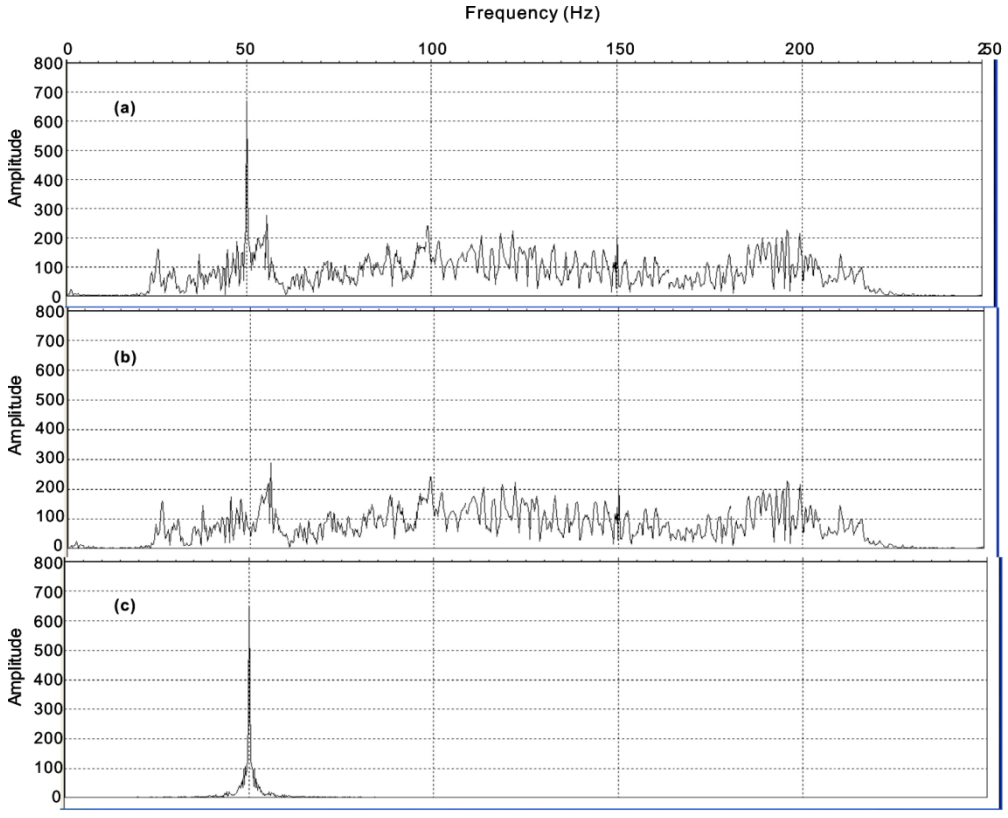

Figure 3.9 (a) Amplitude spectra of trace 615. (b) Amplitude spectra of trace 615 after removing the 50Hz harmonic noise. (c) Amplitude spectra of the harmonic noise estimated from raw data.

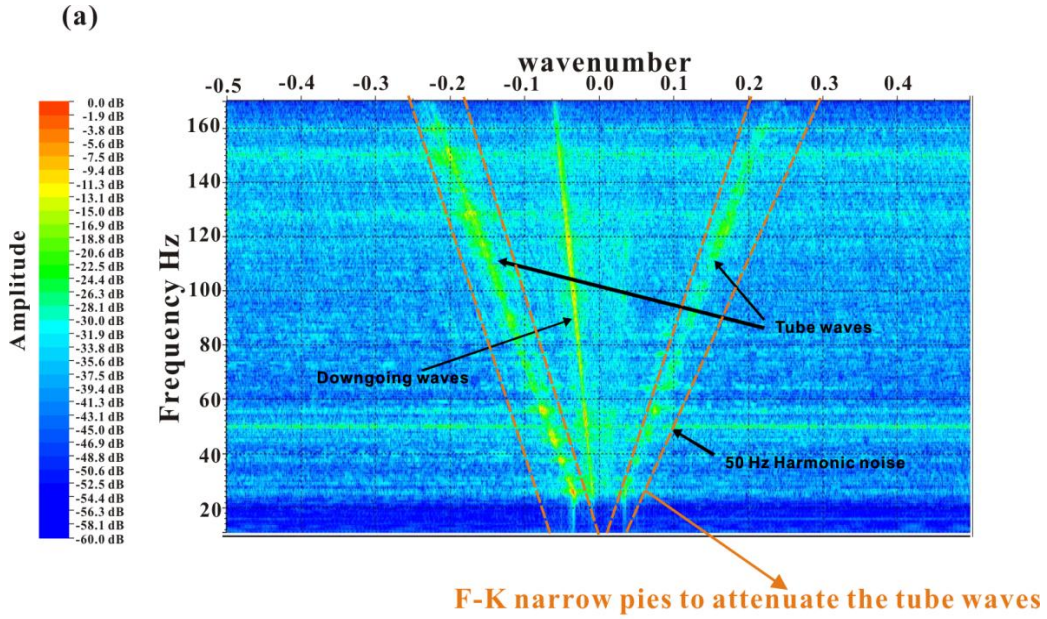

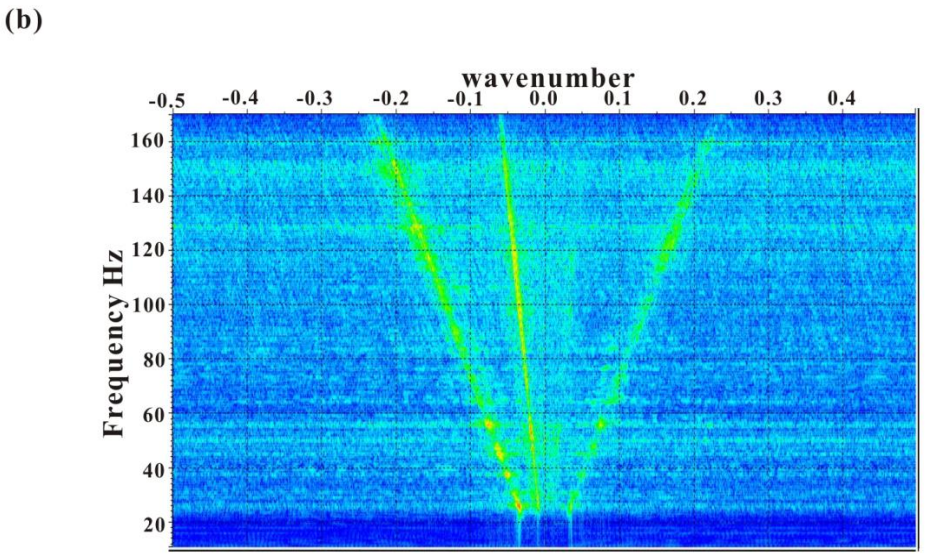

Figure 3.10 (a) The data with noise in frequency and wavenumber domain, and the F-K filter pie slices for tube wave attenuation are displayed. (b) The data without 50Hz harmonic noise in frequency and wavenumber domain.

the harmonic noise removing on whole data in frequency-wavenumber domain.

Tube waves (Fig. 3.4 (a)) are low-velocity, high-amplitude events propagating along the interface between the borehole wall and the borehole fluid. They can be generated by the incident compressional wave energy from a surface source near the borehole, a source in the borehole, or a compression wave in the surrounding solid passing any major discontinuity in the borehole (White and Tongtaow, 1981, Huang and Hunter, 1984). They propagate by displacing fluid particles in the fluid column of a wellbore. These waves are analogous to surface waves in surface reflection profiling; and the physics can be quite complex (Mari and Coppens, 1991, Hardage, 2000) as they are different modes of motion of the borehole wall and fluid and as such they can be dispersive. At the frequencies of this survey, however, they travel at nearly the speed of sound in the wellbore fluid. In Fig. 3.4 (a), several tube waves are seen and designated as Tw1 to Tw6. Tw1 is considered to be generated by downgoing P-wave intersecting fractures at the depth of 494 m. Surface waves may have generated a series of tube waves, Tw2, which are reflected back from the bottom of the well (Tw3). Tw4, Tw5 and Tw6 are generated by reflections of Tw1 from fractures at depths of 966 m, 1446 m and 2248 m, respectively. Tw7 and Tw8 are the multiples of Tw2 and Tw3. The depth points of 494 m, 966 m, 1446 m, and 2248 m could be interpreted as the locations of fractures.

Continuing the analogy with surface waves, tube waves, too, are one of the most damaging types of noise that can exist in vertical seismic profiling. They are a dispersive

and coherent noise mode that repeats itself for every seismic shot. Tube wave amplitudes do not diminish with travel distance as dramatically as do compressional or shear body wave amplitudes. Indeed, the tube waves can be highly problematic when acquiring the VSP data as once they are generated they will continue to progress up and down the borehole for many tens of seconds or even longer; this of course can be disruptive in obtaining the seismic data.

As with surface waves, strategies must be developed to attenuate tube waves in order that the more important reflection data is not overwhelmed. In some cases, the tube waves (coherent noise) energy lies outside or partially outside the signal frequency band and can be effectively suppressed after band-pass filtering by designing the filter to pass only the signal frequency bandwidth (Hardage, 2000, Hardage, 1981). However, the frequencies of most tube waves lie in the signal frequency band in OKU-1 VSP data. Consequently, after testing on different method, a F-K filtering, which has been discussed in Chapter 2, was utilized to the data in frequency-wavenumber domain. A narrow rejection angle (Fig. 3.10 (a)) was chosen in case generating artificial events. Fig. 3.11 is the data after FK filter. The tube waves have been attenuated effectively but incompletely.

The amplitude compensation was carried out after noise attenuation. As discussed earlier, VSP data has less energy loss than seismic surface data due to the different acquisition environment and geometry. Further, considering the zero-offset VSP surveys only provides information about the subsurface only within the Fresnel zone centered at the

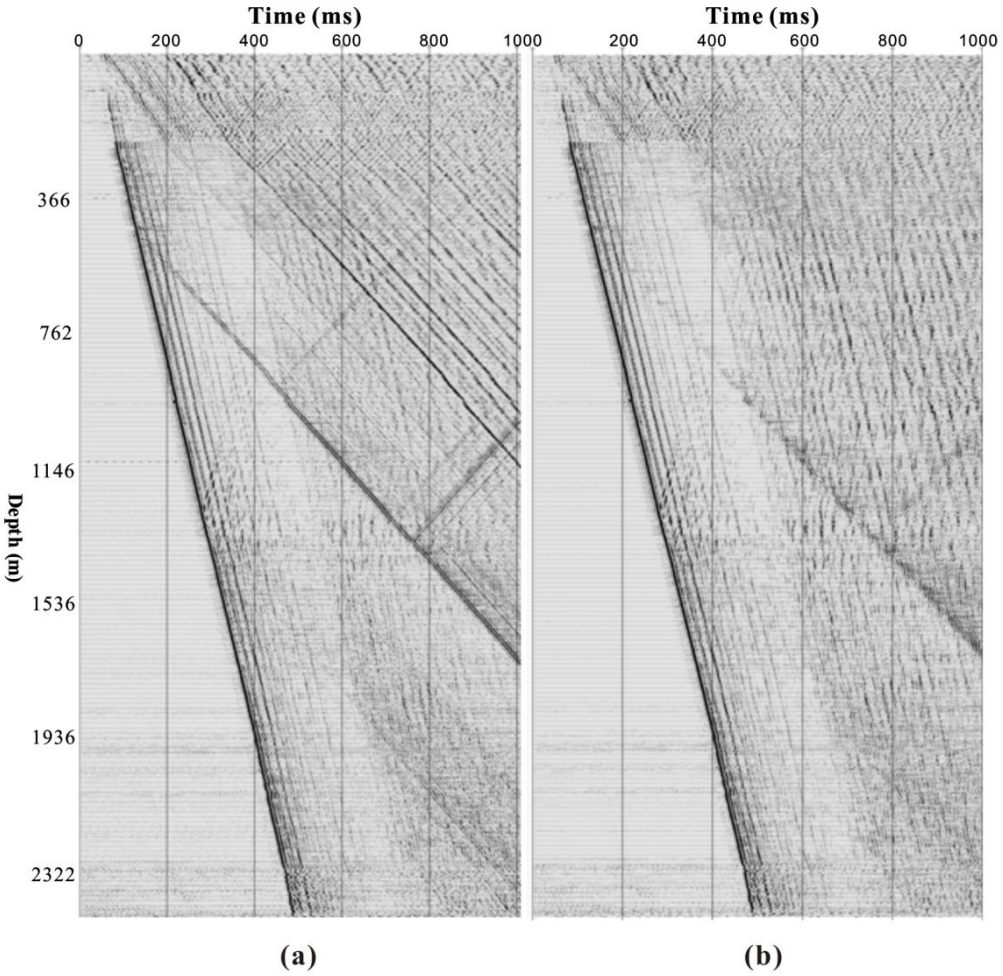

Figure 3.11 Comparison of VSP data before (a) and after (b) tube waves attenuation

well, keeping the true-relative amplitudes becomes meaningless. Consequently, simple AGC gain was added to the data to balance the energy loss.

3.4.4 Wavefield Separation

In conventional seismic exploration, the events of interest recorded on the surface seismograms are upward-traveling waves (reflected events). In VSP the geophones are placed beneath the surface of the earth and measure the downgoing wavefield as well as the reflected upgoing wavefield. These two wavefields of course interfere with each other. The initial downgoing arrivals are much stronger than upgoing events, and camouflage the upgoing events seriously. The analysis of up-going wave mode is particularly important and also complicated. As a result, it is necessary to separate the up-going modes from the down-going modes. Various separation techniques have been published, which include F-K multi-channel velocity filtering (Suprajitno and Greenhalgh, 1985), radon transform (Moon *et al.*, 1986, Miao *et al.*, 1994, Miao *et al.*, 1995), median filter (Stewart, 1985, Hardage, 2000), wave-by-wave optimization approach (Blias, 2007), the recursive-approaching signal filter (RASF) (Sun *et al.*, 1997), and using local slopes attribute to separate wavefields (Du *et al.*, 2009). Kommedal and Tjøstheim (1989) presented a general study on some common used methods for wavefield separation. Each method can work well depending on the VSP data set. In this research, two methods, F-K multichannel velocity filtering and median filter, were tested on OKU-1 VSP data.

The F-K approach involves the design of velocity filter in frequency-wavenumber space. Since upgoing events and downgoing events have different propagation direction, their co-ordinates in the frequency-wavenumber domain. Upgoing waves show negative velocities in frequency-wavenumber space, and can be revealed in the negative wavenumber half plane. On the contrary, downgoing waves show positive velocities (Fig. 3.4 (b)), and can be revealed in positive wavenumber half plane. Thus, the recording events are separated into two different half planes depending on the direction of their travel. So, the downgoing waves can be rejected from F-K domain by using a surgical F-K muting. And upgoing events are isolated. A disadvantage of F-K velocity filtering is that spatial mixing may exist when the pass band of the velocity filter is narrow.

The median filter was developed as a means of smoothing data (Hardage, 2000), In particular it attempts to remove anomalous amplitudes without disrupting the overall trend within a series. In application to VSP processing, it is used to provide an estimate of the strongest wave mode (i.e. the direct downgoing P-wave) that must be separated. Once this estimate is calculated it is then subtracted from each VSP trace. In the median filter method, the median value of an ascending value sequence will be the one in the middle. As such, the median filter entirely rejects the single spikes but it is still able to pass 'boxcar' functions. Any spike or perturbation on the trace that is less than N/2 points long, where N is the filter lengthen, will be rejected (Stewart, 1985). These properties make it very useful in seismic data processing and in the broader field of image processing as a

whole.

The procedure of the wavefield separation by median filter was shown on Fig. 3.12. Briefly, the flow the technique follows the steps (Hinds *et al.*, 1996, Hardage, 2000).

- Flattening (i.e., time shifting) all of the traces to a common fiducial time (see transition from Fig 3.12a to Fig. 3.12b). This employs the already measured first break times (See Fig. 3.5 (b)). Downgoing waves are shown as solid arrows; upgoing waves are shown as dotted arrows.

- The purpose of this flattening is to align all of the downgoing events (Fig. 3.12 (b)) in order to ease the application of the median filter across a number of shifted traces. Then the median filter is applied to emphasize the downgoing events and attenuate the upgoing events (Fig. 3.12 (c)). On Fig. 3.12 (c), enhanced downgoing waves are shown as heavier solid arrows, and attenuated upgoing waves are shown as lighter dotted arrows. This constructs an estimate to the downgoing wavefield.

- Next, the estimated downgoing wavefield from the median filter (Fig. 3.12c) is subtracted from the original shifted wavefield (Fig. 3.12b) leaving as a residual an estimate of the upgoing wavefield. (Fig. 3.12 (d)). As a result, the downgoing events are strongly attenuated, which are shown as dotted arrows, and the upgoing events are now isolated, which are shown as solid arrows.

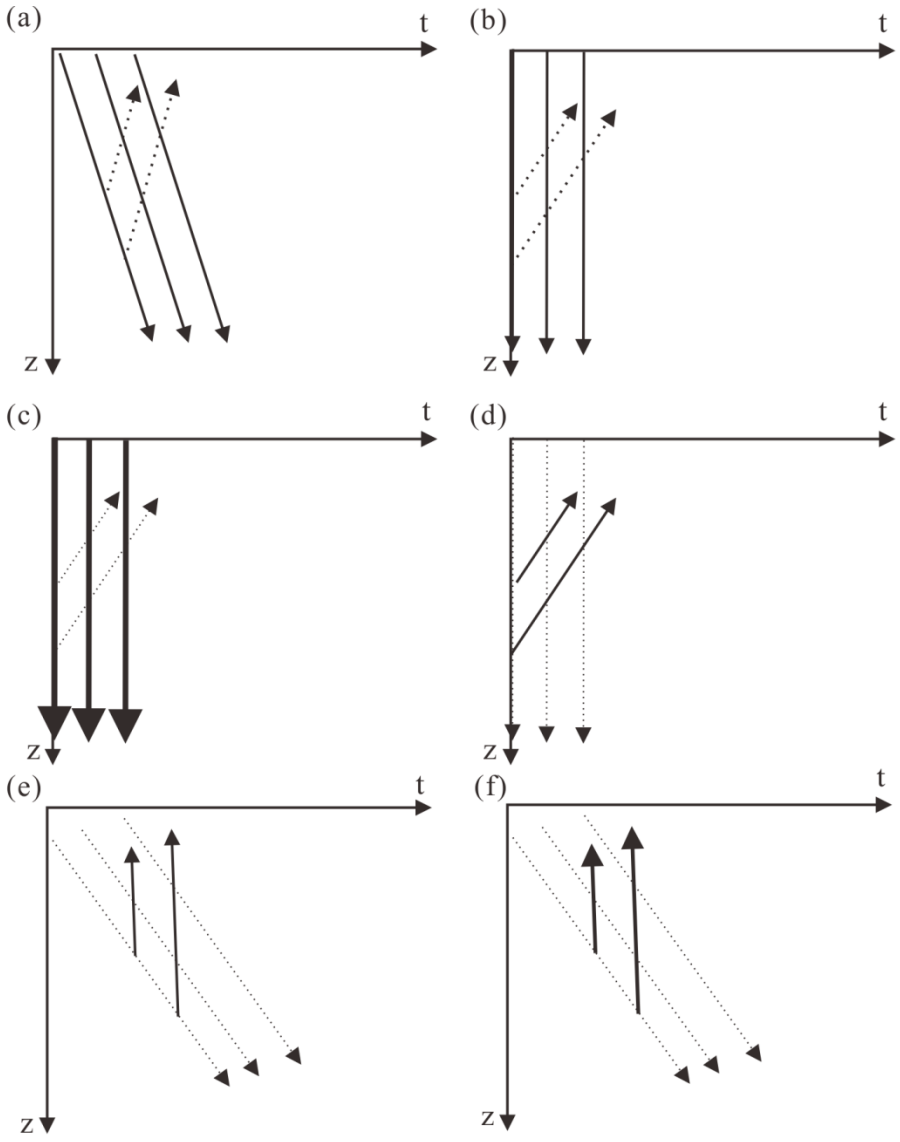

(Modified from Hardage, 2000)

Figure 3.12 A cartoon of the wavefield separation by median filter. Lines with upward arrows are upgoing waves; Lines with downward arrows are downgoing waves. (a) raw data. (b) data after static correction to flatten downgoing waves (solid arrows). (c) enhanced downgoing wavefield (heavier solid arrows) by median filter. (d) upgoing wavefield (solid arrows) after subtracting the downgoing wavefield. (e) data after static correction to flatten upgoing waves (solid arrows).(f) enhanced upgoing wavefield (heavier solid arrows) by median filter. Reproduced with the permission of Elsevier.

- This residual data is then shifted back by twice the original time shift. This has the effect of flattening the upgoing events to emphasize the upgoing events (Fig. 3.12 (e)).

- At last, a median filter is applied a second time in order to enhance the upgoing events (Fig. 3.12 (f)) which are shown as heavier solid arrows.

The median filtering is an effective method to separate the wavefield. But there are two concerns when using the median filter. One is the first break time. Another is the length of the median filter. (i.e., over how many traces should be applied). Improper first break picks or unsuitable median filter length could generate false events.

Comparing the results of both the F-K and the median filters, it was found that the median filter generated a better upgoing wavefield than the F-K filtering. The reason is considered as the low data quality. The downgoing events were better estimated since they were emphasized by the median filter, and the upgoing events were able to be enhanced by the median filter, too. As a result, the median filter method was finally chosen for wavefield separation. Fig. 3.13 shows each step on the Outokumpu VSP data corresponding to the steps in Fig. 3.12. In this data set, a 15-point median filter was first used to estimate the downgoing waves; the downgoing waves are displayed in Fig. 3.13 (c). Next, the downgoing waves were subtracted from VSP data to yield the upgoing waves. Then a 5-point median filter was used on upgoing wavefield to enhance the

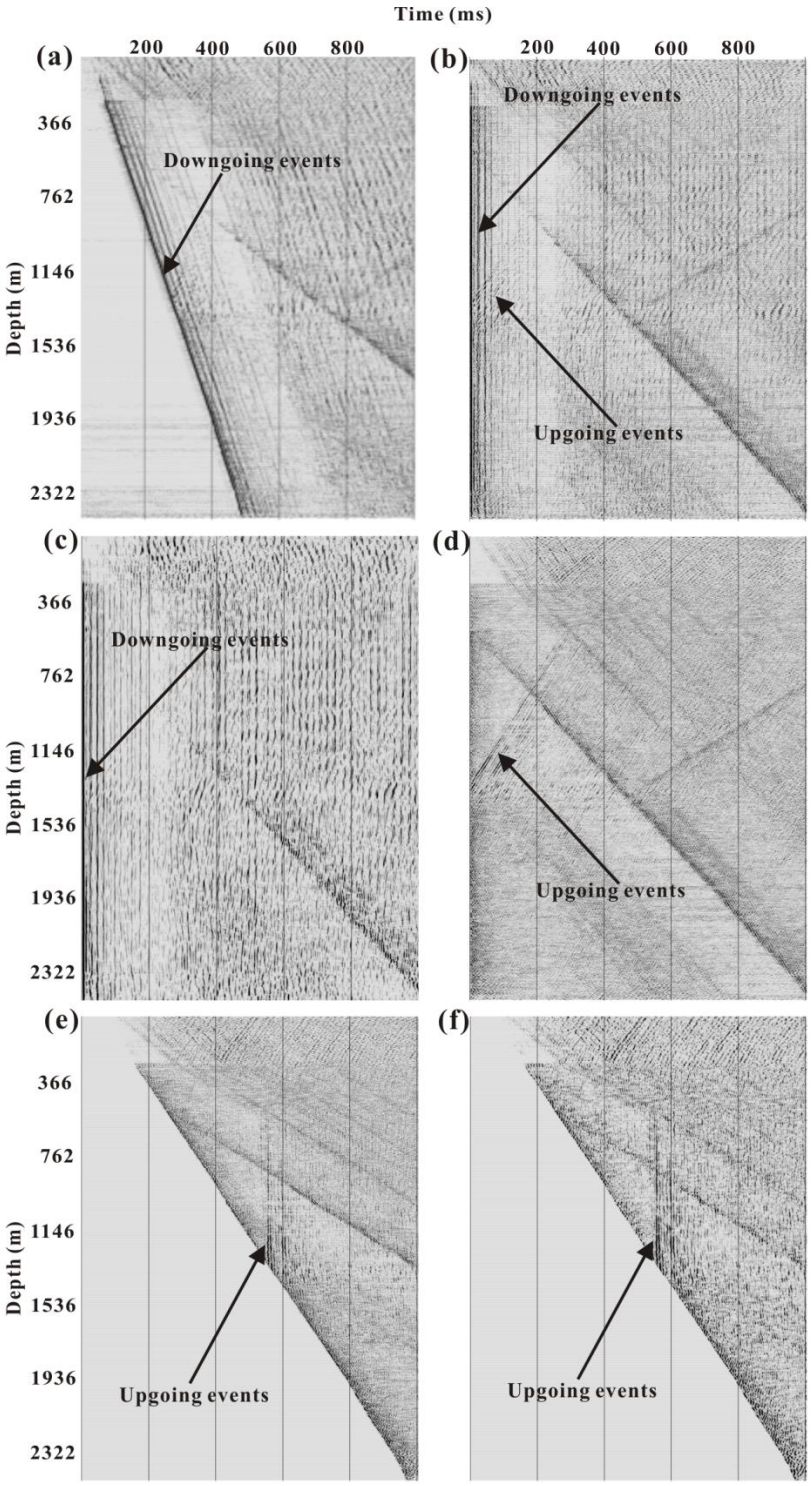

Figure 3.13 The wavefield separation by median filter on Outokumpu VSP data. (a) data after noise attenuation and amplitude compensation. (b) data after static correction to flatten downgoing waves.(c) enhanced downgoing wavefield by median filter. (d) upgoing wavefield after subtracting the downgoing wavefield. (e) data after static correction to flatten upgoing waves.(f) enhanced upgoing wavefield by median filter.

resolution of data. After the separation, the up-going wave field can obviously be seen on the Fig. 3.13 (f). Note that a residual tube wave is still visible within the upgoing data.

3.4.5 Deconvolution

The downgoing P wave is commonly used to design a deconvolution operator to remove multiples from a VSP upgoing wavefield. The reason is the signal strength from the downgoing wavefield is 20 dB to 40 dB greater than the one from the upgoing wavefield (Hardage, 2000). So the calculation is based on the best possible description of the multiple relationships in VSP.

A 200 ms spiking deconvolution operator was designed for the downgoing events to generate the operator (Fig. 3.13 (c)). This operator was then convolved with the upgoing wavefield (Fig. 3.13 (f)) to compress the wavelet. Fig. 3.14 shows the upgoing wavefield after deconvolution. And Fig. 3.15 shows the comparison of autocorrelation from upgoing wavefield before deconvolution and after deconvolution. Deconvolution compressed the wavelet effectively (Fig. 3.15). Meanwhile, the signal-to-noise ratio was increased after deconvolution.

3.4.6 Static Time Shifting

As described above, the recording time of vertical seismic profiling is the one-way travel time. To convert the record to a two-way travel time so that it can be better compared

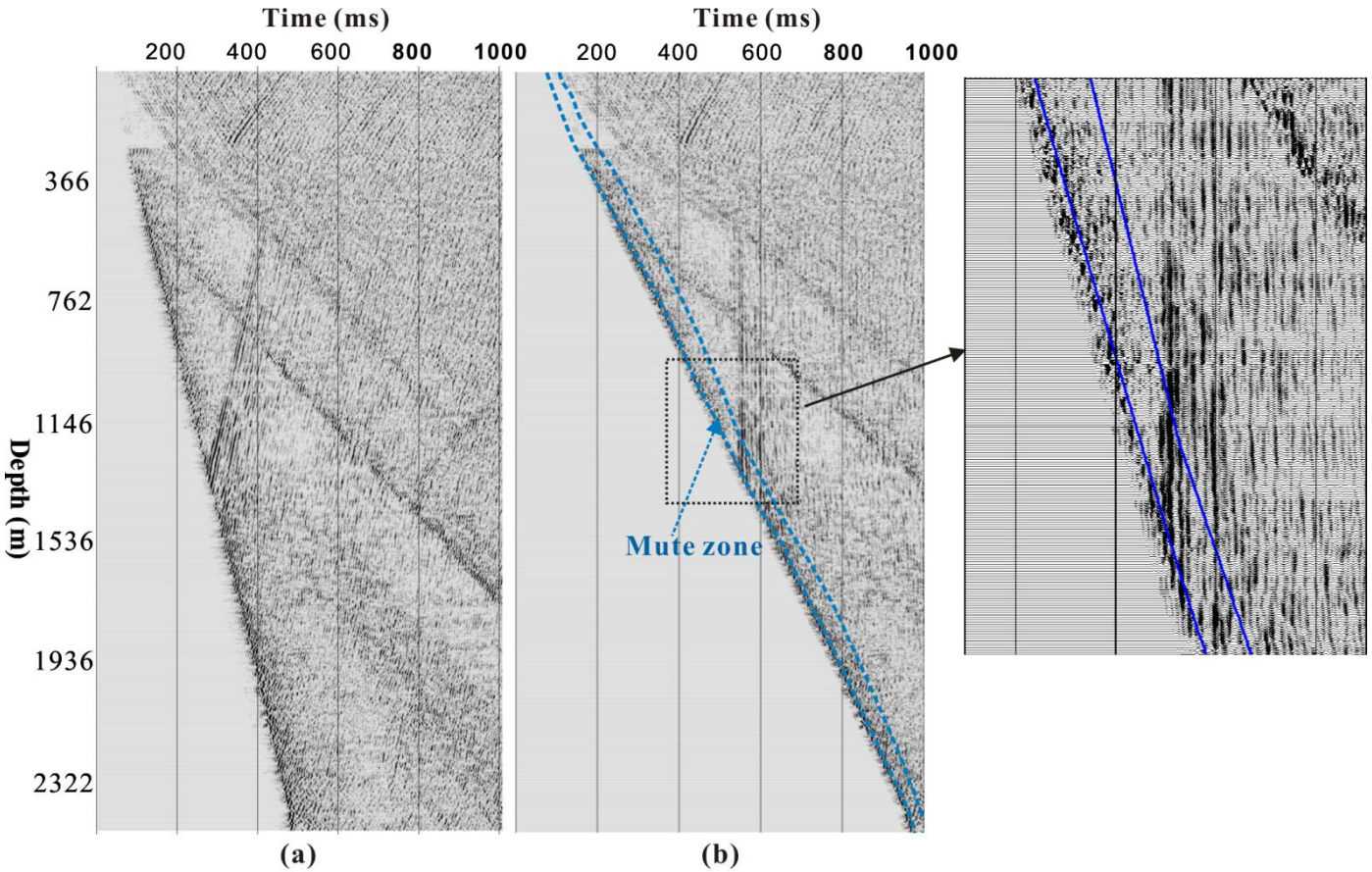

Figure 3.14 (a) upgoing wavefield after deconvolution. (b) upgoing wavefield delayed by twice first breaking time. The mute zone for corridor stacking is displayed on (b).

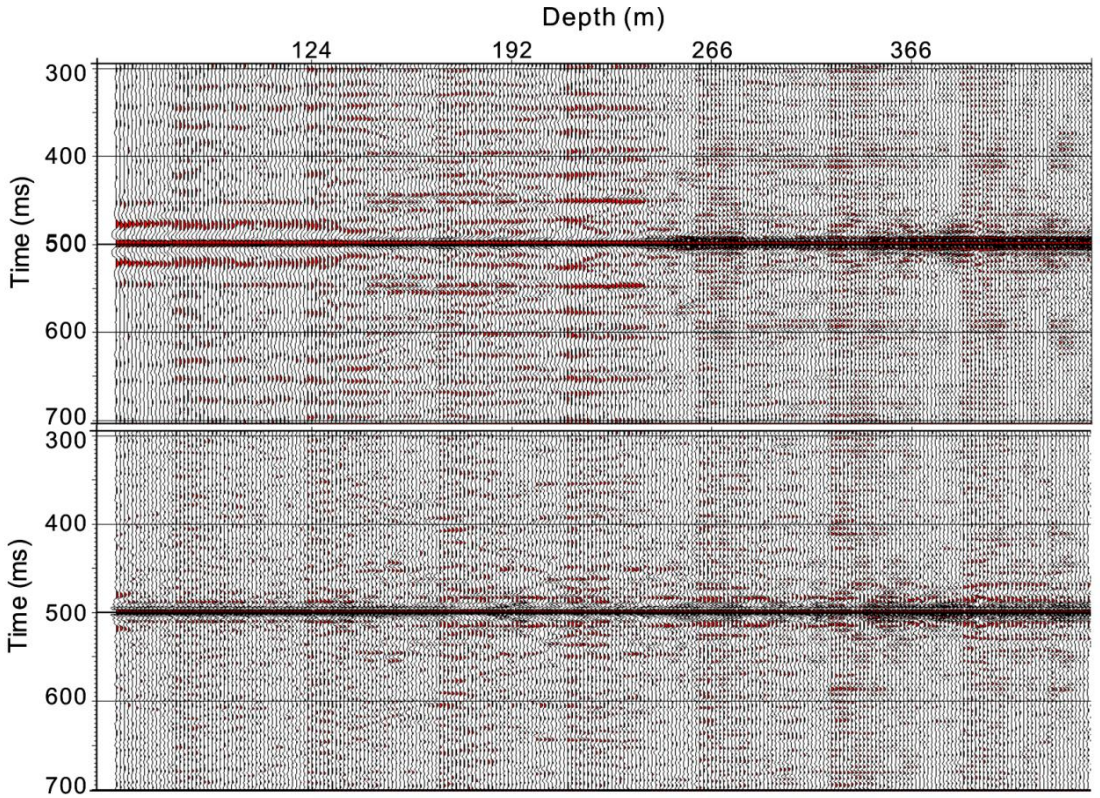

Figure 3.15 Autocorrelation plots: Top is the autocorrelation from upgoing wavefield before deconvolution; Bottom is the autocorrelation from upgoing wavefield after deconvolution.

with the surface reflection images a static time shifting is needed (Hinds *et al.*, 1996). The static time was obtained from the first break time. For upgoing events, the actual recording time was delayed by its first break time to align the upgoing events. For downgoing events, the actual recording time was advanced by its first break time to align the downgoing events. After static time shifting, the time is two-way time (Fig. 3.14 (b)).

3.4.7 Corridor Stack

VSP stack was performed on the delayed data (Fig. 3.14 (b)). Along the depth direction, data can be simply summed together to yield a single stacking trace, which is called the vertical summation. To display, this stacking trace will usually be repeated 10 times; Fig. 3.16 (b) shows the final stack of this vertical summation. During this procedure, the upgoing events are emphasized and downgoing events are attenuated. However, not only are the upgoing primary events aligned, but also are the upgoing multiples. As a result, the vertical summation contains both primary and multiple events. Additionally, some contamination which could not be completely removed by noise attenuation, such as the tube waves, is contained in vertical summation, too.

In order to create a stacking trace with only the primary events and with the least contamination possible, the ‘corridor stack’ was developed meaning that only the data in a narrow corridor near the first break times is stacked. . The corridor stack is also called as restricted vertical summation (Hardage, 2000). It involves a ‘corridor’ zone (Fig. 3.14

(b)) which needs to be designed carefully. Except for a small amount of noise caused by early downgoing and upgoing multiples, this zone contains only predominantly primary upgoing reflection. All the data outside the zone were muted to zero. The remaining data were then vertically summed to produce one trace that is representative of an actual two-way time seismic reflection trace as would be seen in Chapter 2. Subsequently, a bandpass filter and AGC were applied on stack results to attenuate random noise and enhance the resolution of final profiles (Fig. 3.16 (c)).

As mentioned above, the receiver interval along the borehole in this zero-offset VSP survey is only 2 m. This is quite small relative to the 10 m to 20 m of conventional industrial surveys where reducing costs are usually the primary factor in designing field experiments. The close spacing makes it possible to generate a higher resolution stack profile which is shown on Fig. 3.17 (a). This corridor stack reveals a number of reflections and particularly the strong set of events at 550 ms (~1.3 km) associated with ophiolite complex that is potentially ore bearing.

As noted earlier, economic considerations often limit the number of VSP depth stations that may be obtained. The current unique data set offered an opportunity to see how this reduced sampling might influence the final VSP stacked trace. Hence, the full VSP processing procedure was applied to two different receiver gaps at the more conventional 10 m and 20 m receiver increments. This was achieved simply by extracting the traces in different intervals, which was executed from the raw VSP data. The same processing

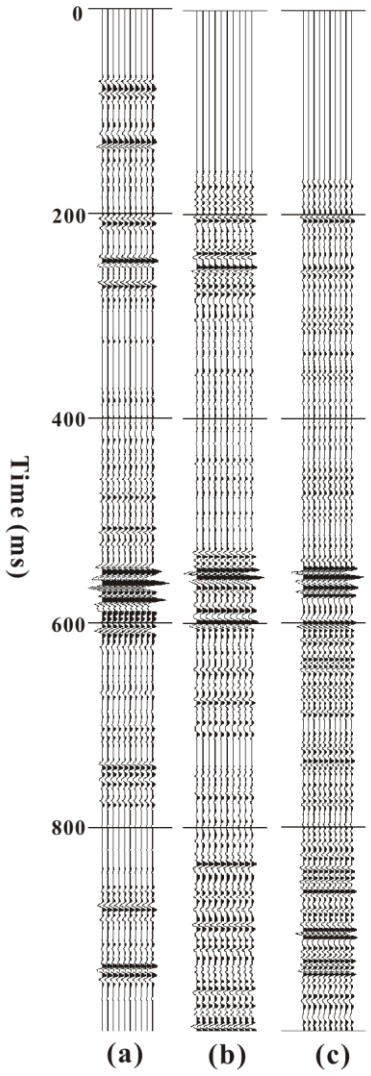

Figure 3.16 Comparison of synthetic (a), vertical summation (b) and the corridor stack (c)

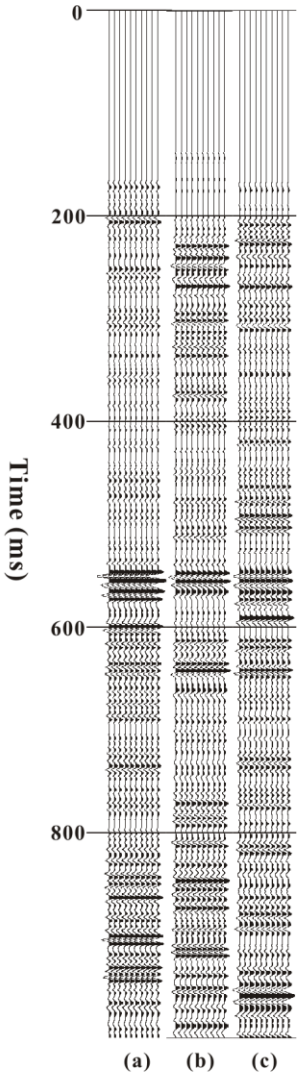

Figure 3.17 Final corridor stack result of VSP data.
(a) with 2m depth receiver increment. (b) with 10m depth receiver increment.
(c) with 20m depth receiver increment

flows and parameters used in 2 m interval data were used for these more sparsely sampled wave fields from the very beginning. And the results are shown in Fig. 3.17 (b) and (c). By the comparison, it is obvious that the stack profile with 2m depth increment shows more detail than the other two stack profiles. Some differences in shallow may be caused by some noise which still exits in mute zone even after noise attenuation.

3.5 Conclusions

The zero-offset VSP survey was carried out to assist in the determination of the detailed structure of bedrock near the deep drill hole. A 2 m depth increment between receiver stations was applied in this new survey to get high resolution data. The signal to noise ratio in VSP data is higher than surface seismic data since receivers were placed in a well environment. However, it has its special noise types. Noise was also a troublesome problem. A series of processing techniques were employed to obtain a high resolution result based on the 2 m depth increment which was also used to compare with two different depth increments. Meanwhile, special effort was made for preserving the high frequency information and wavefield separation by reason of weak upgoing waves. Moreover, the P-wave velocity was determined from the first break picking. By comparison with the sonic log, they match well although they did not represent velocity variations on the same scale. From the corridor stacking results, the final profile shows detailed information about sequence structure which also can be used for the interpretation of surface reflection seismic profiles. The 2 m spacing also allows for a

better determination of the in situ seismic band velocities.

4.0 Joint Interpretation of Seismic Surface and Borehole Data

This chapter begins with an evaluation of the seismic processing with a detailed presentation of the final results of the Outokumpu seismic reflection profiles. The results include a synthetic seismogram calculated from the edited geophysical logs, the final processed images for the two 2D surface seismic profiles, the zero-offset VSP, and P-wave velocities derived from VSP data. These results will be jointly interpreted to understand the properties and structures of the Outokumpu area. Subsequently, discussions and conclusions about this project will be made.

4.1 Evaluation of processing

Seismic reflection methods have been successfully used in exploration for petroleum in layered sedimentary over the last several decades. The geological features are usually quite different in crystalline metamorphic rock terranes, however, that are characterized by much more complex structures. Seismic reflection profiling is further complicated by generally smaller differences in the elastic impedances between the differing lithologies; this results in weaker seismic reflections that are more prone to contamination by noise. Unlike sedimentary structures, crystalline deposits are inherently heterogeneous (L'Heureux *et al.*, 2005) that this tends to scatter seismic data. This high level of scattering together with the low contrasts between reflecting and scattering interfaces causes the signal to noise ratio to always be low. Due to these special characteristics of

hardrock terranes, seismic methods need to be adjusted in order to obtain good images and, in a practical sense, to meet the needs of mineral exploration. As a result, usually high-frequency seismic survey techniques with dense fold coverage are applied in hard rock environments to aim at obtaining high resolution data. Further, special attention needs to be paid to data processing in order to preserve high frequency information and improve the resolution.

In 2006, a high resolution seismic reflection survey was carried out in Outokumpu area. 2D seismic acquisition was carried out on high-frequency vertical seismic vibrator and had relatively dense fold coverage to generate high resolution images. A zero-offset VSP survey was acquired from 50 m to 2500 m deep at a 2 m receiver interval, this is an unusual interval relative to the 10m to 20m spacings normally employed in industry. These acquisition parameters are the first consideration to obtain high resolution images. On top of this, the determination of a proper processing sequence and parameters is also critical. The processing was performed by using Vista^{TM} 2D/3D Seismic Data Processing software and Matlab™. The final processing sequence and parameters were determined after plenty of testing and comparisons; there were a number of failed attempts in gaining this experience. During the processing, every new step is based on the result of the previous actions; so appropriate and careful processing is necessary at each step. Line_2000 and line_3000 had essentially same processing sequence, but with different parameters in each method according to their different data quality (Table 2.1). VSP

processing sequence is different with those two 2D seismic lines due to their different geometry. Nevertheless, some of methods used in VSP processing are borrowed from surface seismic data processing.

The 2D seismic lines were crooked; consequently special attention was paid to their surface mapping, to the construction of the CMP bin grids, to the choice of the bandwidth in bandpass filtering, to the methods and parameters of the various noise attenuation strategies employed, and finally to the deconvolution and migration parameters.

The irregular crooked lines introduced special problems including inconsistent fold coverage, uneven offset distributions, and reflected waveform differences because the CMP gather includes points over a wide area.. This problem would be even more severe if there was significant dip of the reflecting events out of the plane of the 2D profile (Wu *et al.*, 1995, Nedimovic and West, 2003a). As such conventional 2D seismic processing might weaken the efficacy of the final stack with smearing of the reflecting events. In the present case, the target zones were assumed to be mostly flat-lying. For that reason, surface lines were defined by following the density of the CMP with wide CMP bin grids chosen to include as many such points as possible. No special stacking method was used during processing.

The bandwidth parameters were chosen according to the analysis to the acquisition

frequency parameters, the quality of data and the amplitude spectra. A relatively wide bandpass was chosen in order to preserve as high a degree of seismic resolution as possible.

Due to the low signal to noise ratio expected from the crystalline terranes, the abatement of the cultural electrical and the surface wave noise is perhaps the most important part of the seismic processing. It is essential to enhance the quality of the images, especially for low signal to noise ratio data set. It began with the trace editing and penetrated the whole processing. Tests on methods and parameters were performed for each type of noise and different shot gathers from different locations along each data set. The final decisions were made after comparing the effectiveness on data to avoid artificial events. Every method attenuated some of noise, and the resolution was improved progressively.

Deconvolution consisted of two parts, spiking deconvolution and predictive deconvolution. Spiking deconvolution was applied first, and then followed by predictive deconvolution. Thus, the seismic wavelet was compressed in time (i.e. the vertical seismic resolution was improved), and multiples were suppressed after deconvolution. From the quality-control figures (Fig. 2.26 and Fig. 2.27), the frequency range was broadened and data quality was improved at the same time.

During the zero-offset VSP processing in Outokumpu, high frequency information was preserved as it was done in 2D seismic processing. The signal to noise ratio in the VSP

data is relatively higher than for the surface seismic data since the geophones were placed in a well environment. However, the borehole data has its special noise types, and the noise attenuation was also a troublesome problem. After processing, the 50 Hz electrical system harmonic noise was successfully eliminated using the method of cancelling estimated harmonic noise. The tube waves were removed using a F-K filter from the data in part. Further, the corridor stack method prevented the contamination of the multiples from stacking result effectively. In addition, special effort was made for wavefield separation because of the weak upgoing waves. The median filter method was chosen because it not only can remove the downgoing wavefield from data, but also can enhance the signal.

4.2 Final results

Both seismic profiles as well as the final distilled VSP reflectivity are viewed in a series of 3D plots that assist visualization of a general spatial understand about this project (Fig. 4.1). The two 2D seismic lines are almost perpendicular to each other and the problematic crookedness of line_2000 is clearly visible. In depth, line_2000 has the same recording length as line_3000 in field. But line_3000 was only processed from 0 s to 2.5 s because I didn’t acquire the whole data for line_3000 from earlier projects. The VSP data which was recorded in the Outokumpu well drilled at the intersections of line_2000 and line_3000. However, there were no exact crossing points between the VSP and the seismic lines, which makes the correlation between them harder to make. The VSP result

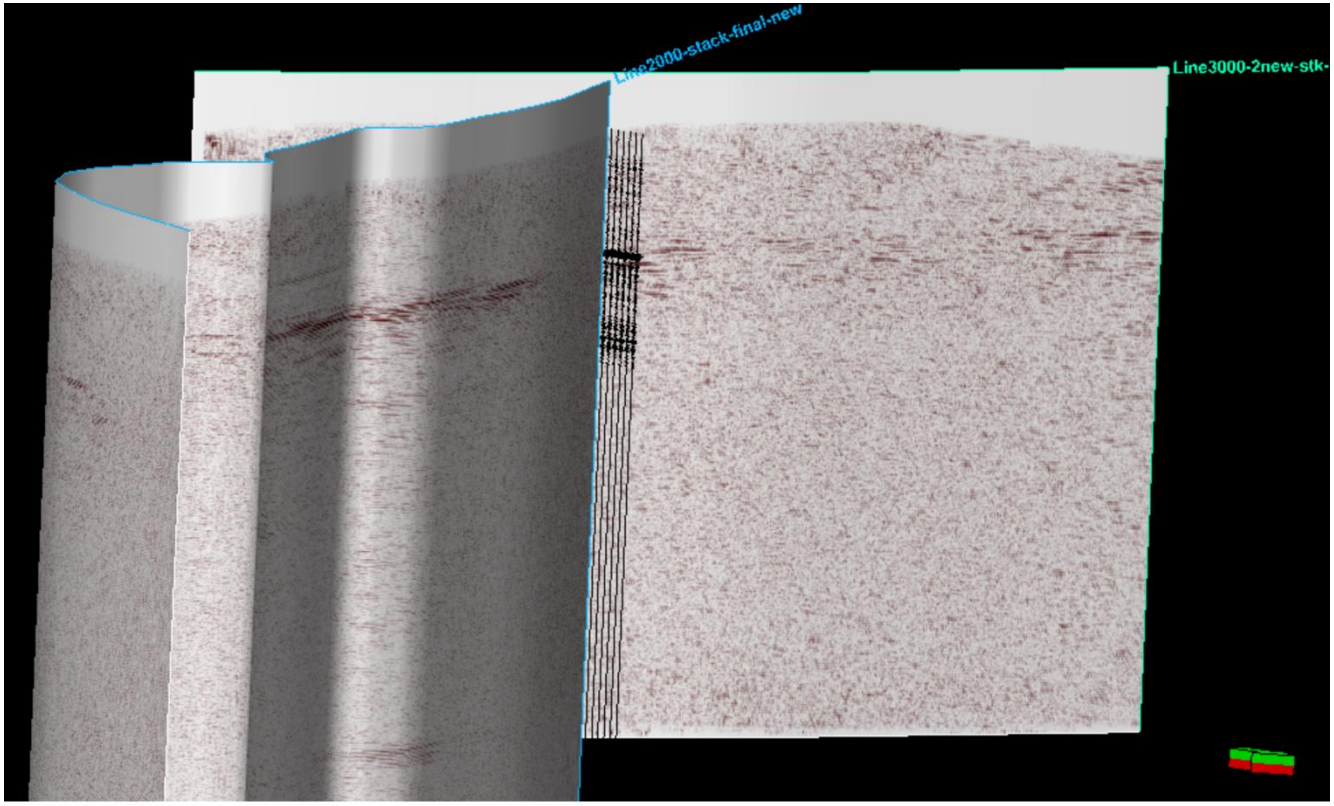

Figure 4.1 A 3D view of the surface seismic and the zero-offset VSP results in Outokumpu.

has a length from 0 s to 1 s. It is much shorter than the surface seismic results. In addition, the target zone is around 500 ms. And strong reflectors can be observed from both seismic results and VSP result. More details will be discussed in later sections.

4.2.1 Crooked 2D Seismic Lines

Line_2000 had almost same acquisition parameters as line_3000, but line_3000 had much lower fold on average than line_2000 due to the fact that line_3000 was not fully covered by receivers and sources. In addition, line_2000 had a relatively better data quality than line_3000. So even though line_2000 crooked more seriously than line_3000, the layers on line_2000 are more observable and continuous than those line_3000.

The final stack and migration results of line_2000 and line_3000 are shown on Fig. 4.2 and 4.3. The full profiles are shown including the edges where the fold is low and coherent events are lost. The most prominent feature on both of these profiles is the strong package of reflectors near 500 ms of two-way travel time. This is associated with the Outokumpu-type assemblage rocks. However, there are additional events that are worth noting particularly in line_2000. A strong event, at 340 ms between CMP 108 to CMP 244 is, likely the same as that seen in the original FIRE line (Fig. 1.11) which was actually one target of the drilling. The depth is about 1000 m. This event is likely generated by the fracture zone at 967 m where tube waves also are observed from zero-offset VSP data (Tw4 on Fig. 3.4). Another coherent event occurs at 900 ms between

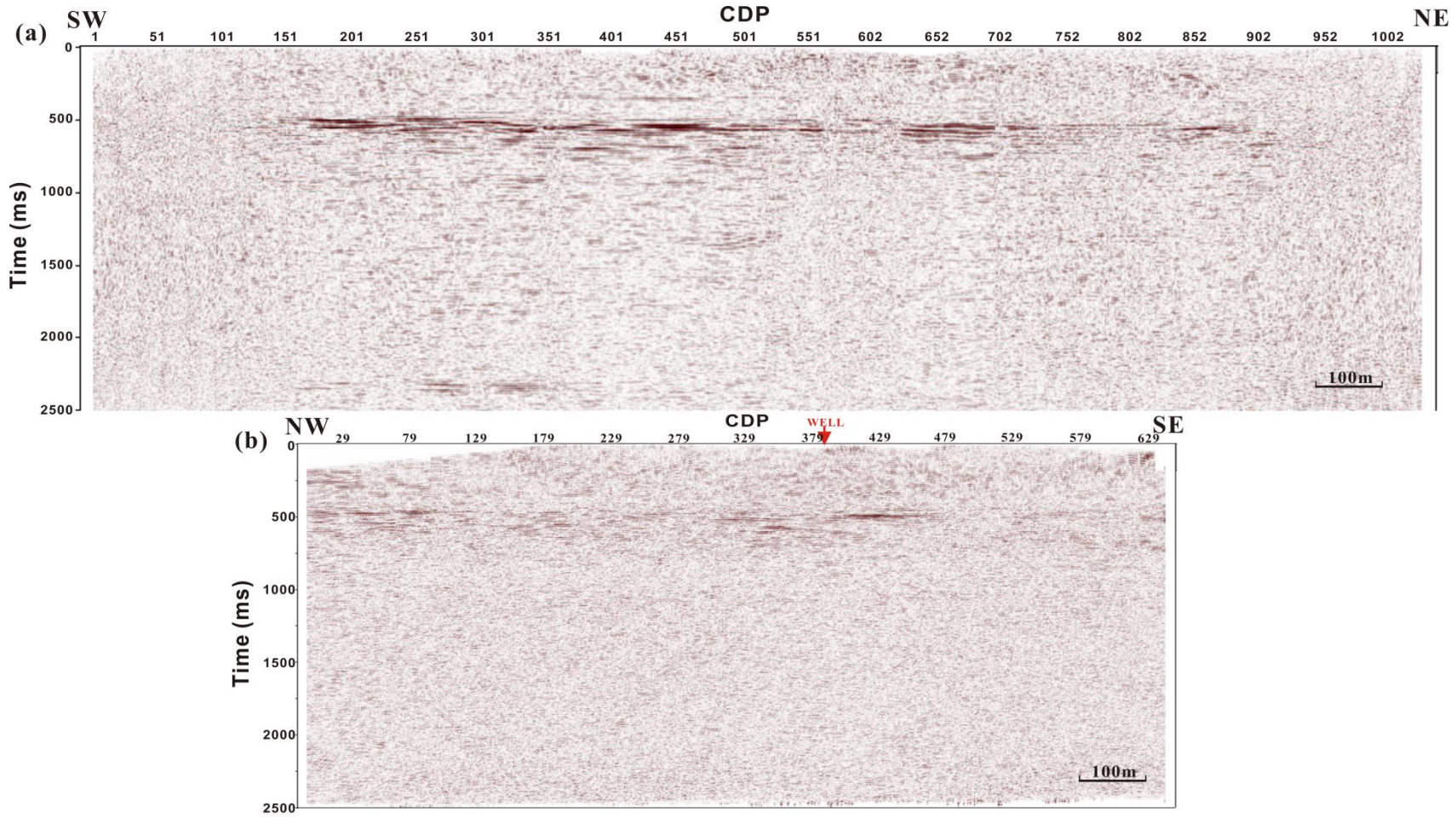

Figure 4.2 The final stack results of line_2000 (a) and line_3000 (b).

CMP 120 to CMP 520. Finally, it is even interesting to note the appearance of a quite deep reflector at 2350 ms which is expected to be at depths greater than 6 km.

The same main 500 ms event associated with the Outokumpu-type assemblage is seen in line_3000. However, the character of the reflectivity appears somewhat different in each line. In line_2000, the Outokumpu assemblage 500 ms reflector packages is characterized by a number of apparently overlapping events; with a time thickness of more than 100 ms. This is considerably thicker than the two-way time of 70 ms that would be expected for the 200 m thick Outokumpu-type assemblage on the basis of the sonic log and the synthetic (Fig. 4.3).In contrast, the reflections in line_3000 are more separated and distinct.

4.2.2 Zero-offset VSP

Zero-offset VSP data was processed also on Vista^{TM} 2D/3D Seismic Data Processing software as discussed in detail in Chapter 3. The final results are shown on Fig. 4.4 (a), (b) and (c) are the final corridor stack with three different geophone increments, 2 m, 10 m, and 20 m. 2 m is the original increment. 10 m and 20 m increments were achieved by extracting the traces in different interval. From the final results, strong reflectors around 500 ms are recognized as Outokumpu-type assemblage rocks. And the final stack with 2 m interval exhibits a highest resolution, and more details can be observed.

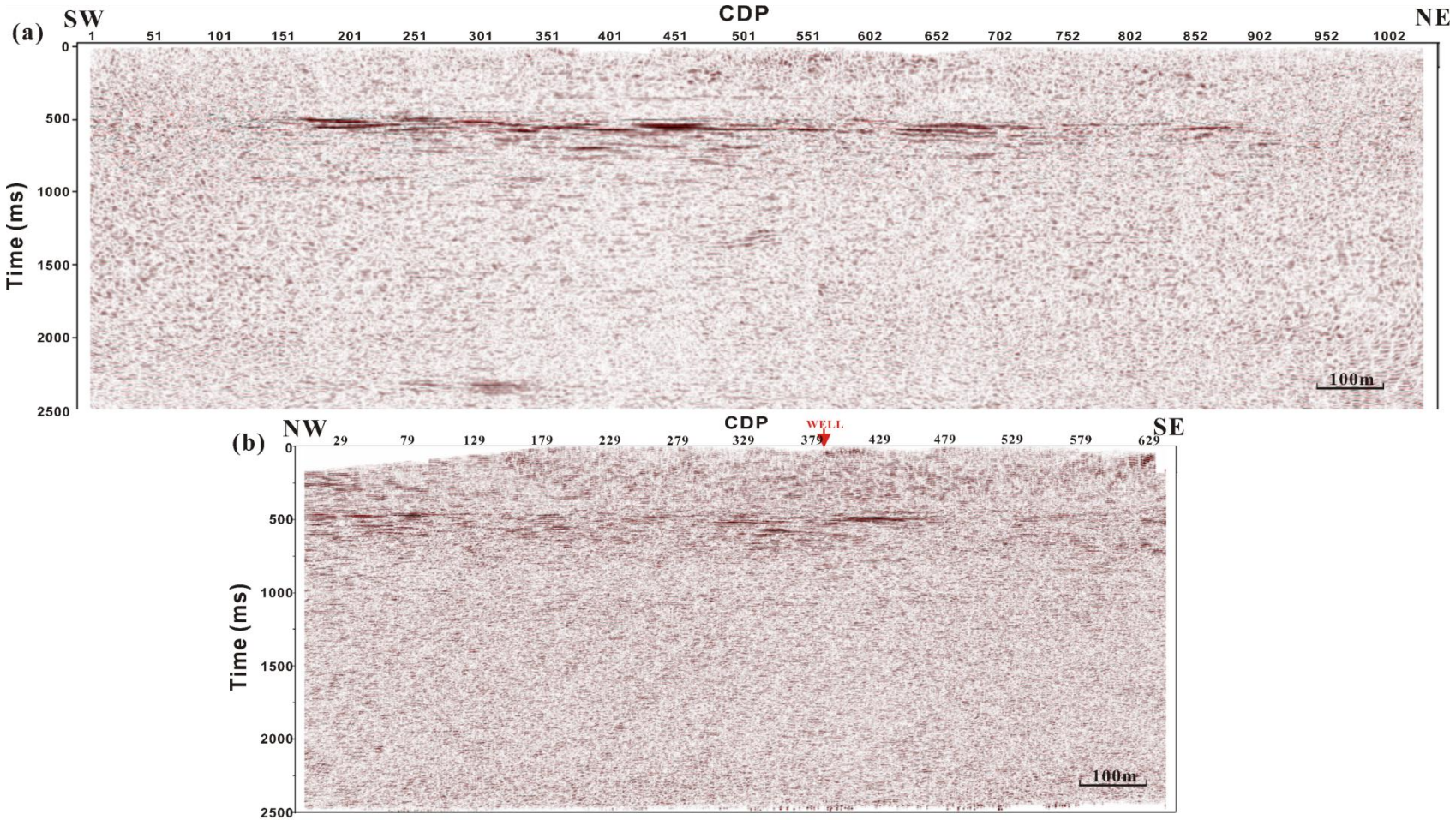

Figure 4.3 The migration profiles of line_2000 (a) and line_3000 (b).

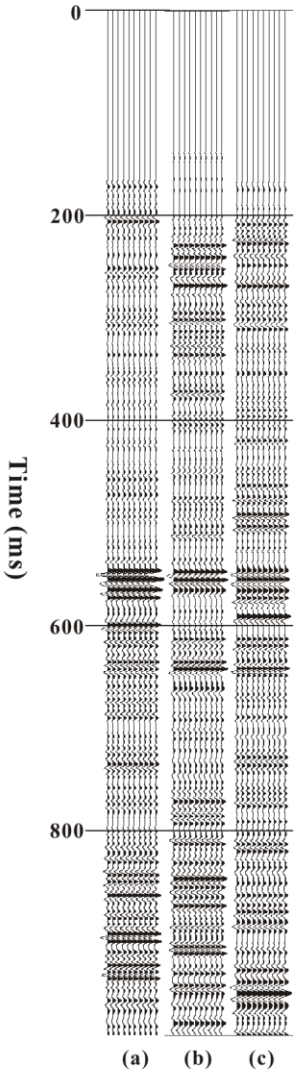

Figure 4.4 Final corridor stack result of VSP data.
(a) with 2m depth receiver increment. (b) with 10m depth receiver increment.
(c) with 20m depth receiver increment

4.2.3 Velocity

The P-wave velocities were derived from the first breaking information. They were calculated based on the estimation of the local tangent slope of the travel time by least squares fitting of a line to a number of contiguous time picks V_{LP} (Schmitt, et al., 2007) with a 0.99 Pearson's correlation coefficient for most of points. Since the frequencies of the VSP data (< 250 Hz) differ from the sonic logging (~10 kHz to 20 kHz) two averaging methods, the simple arithmetic mean and the Backus average, were applied to smooth the latter. The comparison of P-wave velocities and smoothed sonic average curves is shown on Fig. 4.5. The velocity varies from 5000 m/s to 6500 m/s throughout the well. Large variations in velocity are seen through the Outokumpu-type assemblage section from 1314 m to 1515 m. Other sections have a relatively stable velocity variation, and the average velocity value is around 5500 m/s. These values are also supported by recent laboratory measurements (Elbra, et al., 2011).

It is interesting to note that particularly in the upper schist section above the Outokumpu-type assemblage the sonic logging velocities appear lower by 1% on average than the VSP measurements. This is not the normal situation. Usually sonic log velocities are greater than the corresponding seismic velocities. The reason for this anomalous difference here is not known. It could arise due to the fact that the rock in the immediate vicinity of the wellbore is damaged due to stress concentrations produced by the existence of the well itself. This damage would be localized to less than a few borehole

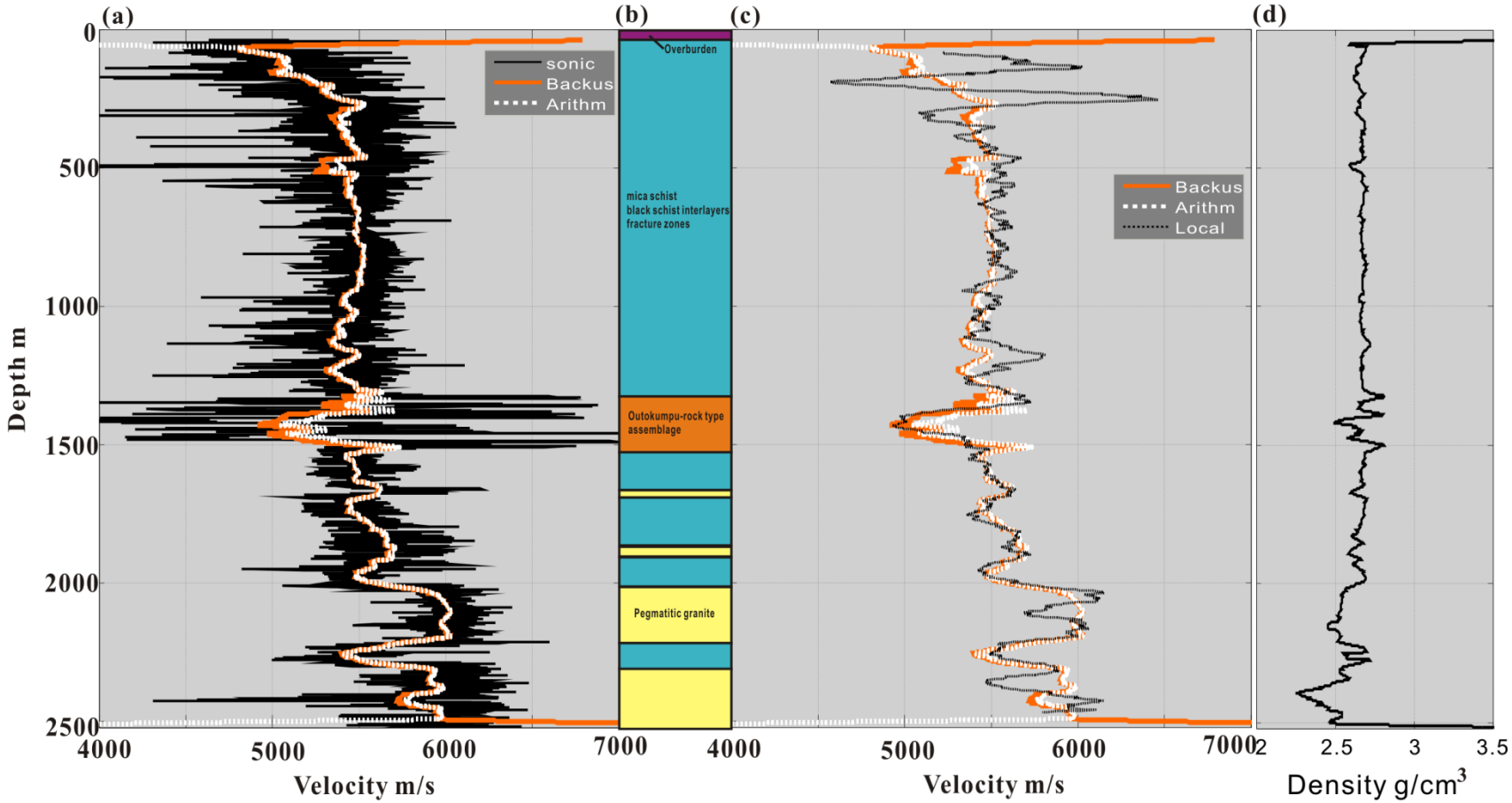

Figure 4.5 Measures of interval velocities in Outokumpu deep drill hole. (a) sonic log interval velocities (black solid line) with corresponding Backus average (orange solid line) and arithmetic average (dotted white line). (b) the geology information. (c) sonic log averages from (a) compared to values of the interval velocities (dotted black line)obtained from the seismic travel time of Figure 3.5 by local linear slope method. (d) density log with Backus average.

radii into the rock mass but still would be measured by the sonic log which does not sample deeply into the formation. In contrast, the VSP seismic frequency waves have longer wavelengths and interrogate a much wider zone that consists of undisturbed and undamaged virgin rock that will have a greater velocity.

4.2.4 Synthetic

A synthetic seismogram is created to simulate seismic data acquisition in the computer. Synthetic seismograms are usually used to tie well logs and seismic reflection data to known lithological interfaces. A synthetic seismogram is calculated using the basic velocities from the sonic log and the mass densities from the γ–γ density log. This allows the acoustic impedances $Z = v\rho$, where ρ is rock density which can be obtained from density log, and v is the P-wave velocity which can be derived from the sonic logs to be easily calculated. Then, the reflection coefficient R as a function of depth may be determined using equation (1-1). The synthetic seismogram is finally generated by convolving the reflectivity with a wavelet representative of the seismic experiment.

The synthetic seismogram was calculated in the geophysical interpretation package Petrel™ and is presented on Fig. 4.6. The acoustic impedance and the reflection coefficient calculated from the density log and the sonic log are also shown. Before the final calculation, both the γ–γ density and the sonic log were edited to remove some abnormal values which could be caused by poor conditions in the borehole such as

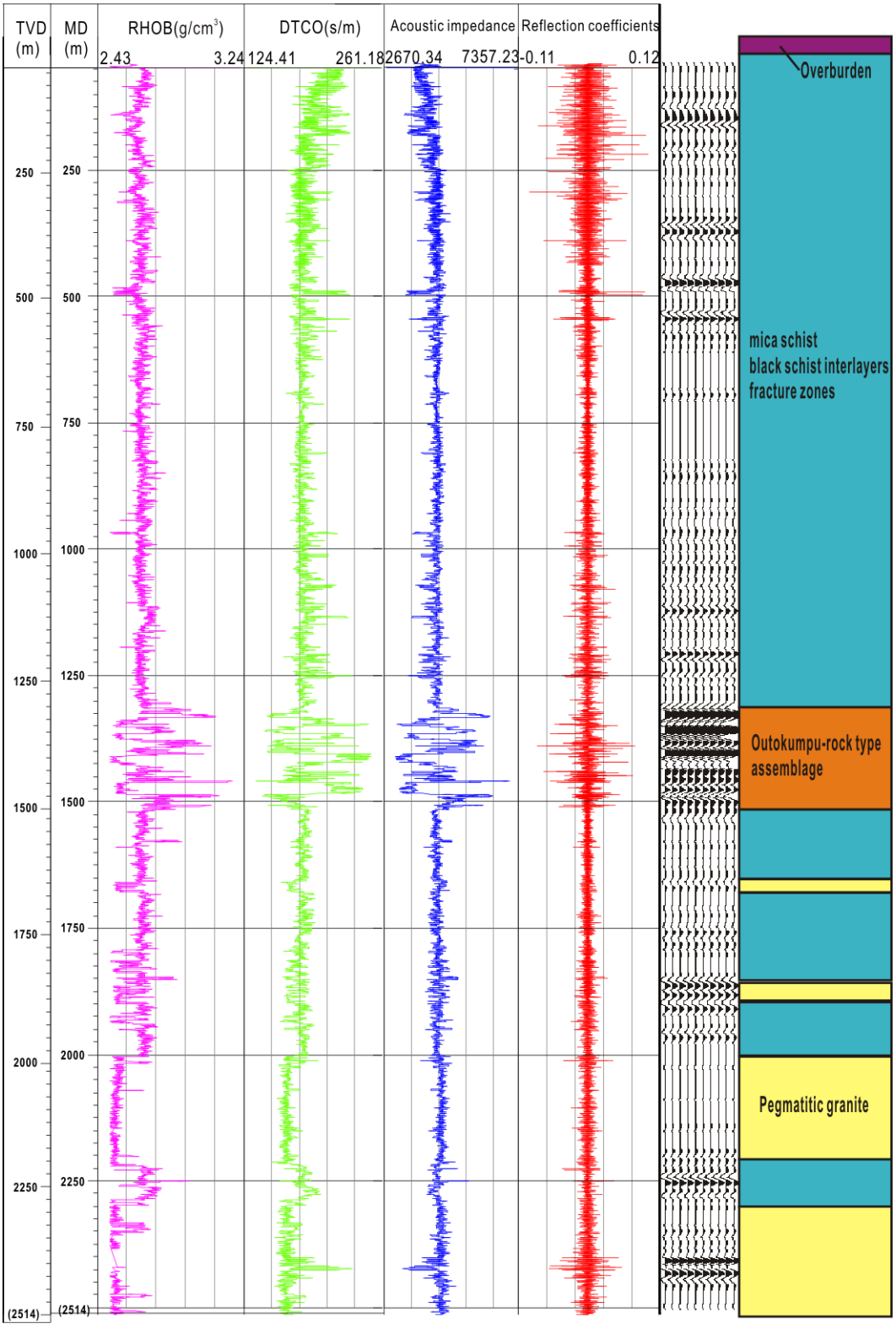

Figure 4.6 Synthetic seismogram: From left to right, they are the density log, the acoustic log, calculated acoustic impedance, reflection coefficient, the synthetic seismogram, and geology information from the deep drill hole

fracture zones. A value was deemed to be abnormal if it deviated significantly from those obtained on core samples in the Elbra, et al's (2011) extensive laboratory measurements. As a result, all the values smaller than 2.5 g/cm^3 in the density log and values bigger than 230 s/m (velocity = 4350 m/s) from 0 m to 1000 m and values bigger than 250 s/m (velocity = 4000 m/s) from 1000 m to the end of the well in the sonic log were eliminated from the raw sonic log data. These values were used to calculate the acoustic impedance that was then converted to a time series of the reflectivity (equation 1-1). Not editing out these aberrant values would produce artificial events in the synthetic seismogram.

To complete the synthetic seismogram, an estimate of the wavelet (equation 1-1) is required. Attempts were made to extract a proper wavelet from line_3000 using the Petrel™ software, however none of these wavelets appeared to provide an appropriate match to the final seismic data. The reason for this may be that the deconvolution process employed in predicting the wavelet must assume that it has zero phase. However, the actual seismic data could not meet this requirement because of the contamination from noise. As such, a zero-phase Ricker wavelet (Costain and Çoruh, 2004) with a peak frequency of 100 Hz was used. And the Ricker wavelet *f(t)* is described by:

$$f(t) = (1 - 2\pi^2 v_0{}^2 t^2) e^{-\pi^2 v_0{}^2 t^2} \tag{4-1}$$

where v_0 is the peak frequency, and t is the time relative to $t = 0$. The resulting synthetic seismogram is shown in Fig. 4.6.

4.3 Joint Interpretation

Hard rocks have more complex properties and structures than sedimentary rocks. The signal-noise ratio and continuity are usually very low, which makes the acquisition and processing challenging. Further, the final profiles also indicate that the interpretation is also not straightforward. Even though seismic reflection technology is not commonly used to in hard rock environment due to its anisotropy and small difference in acoustic impedance, based on the logging information, large density and P-wave velocity variations can be observed in Outokumpu area. Those evident strong reflectors in the synthetic seismogram (Fig. 4.6) increased the possibility that the Outokumpu-type assemblage has large enough differences in the acoustic impedance to be detected on seismic profiles. As noted earlier, the reflectors near 500 ms are associated with the Outokumpu-type assemblage. However, because that all the abnormal values in the γ–γ density and the sonic log, which are caused by poor conditions in the borehole, are hard to remove completely, the comparison would not be exactly consistent. Moreover, according to the vertical and horizontal resolution as described in Fig. 2.10 (a) and Fig. 2.10 (b), it is not possible to image individual rock layers in the seismic profiles because of the limit of resolution, and the alternations of different rocks in Outokumpu hard rock area. Comparing with the VSP result (Fig. 4.7), they match each other well around the Outokumpu-type assemblage zone except a small time difference exists, which could be caused by several factors, such as the quality of well logging and seismic data processing,

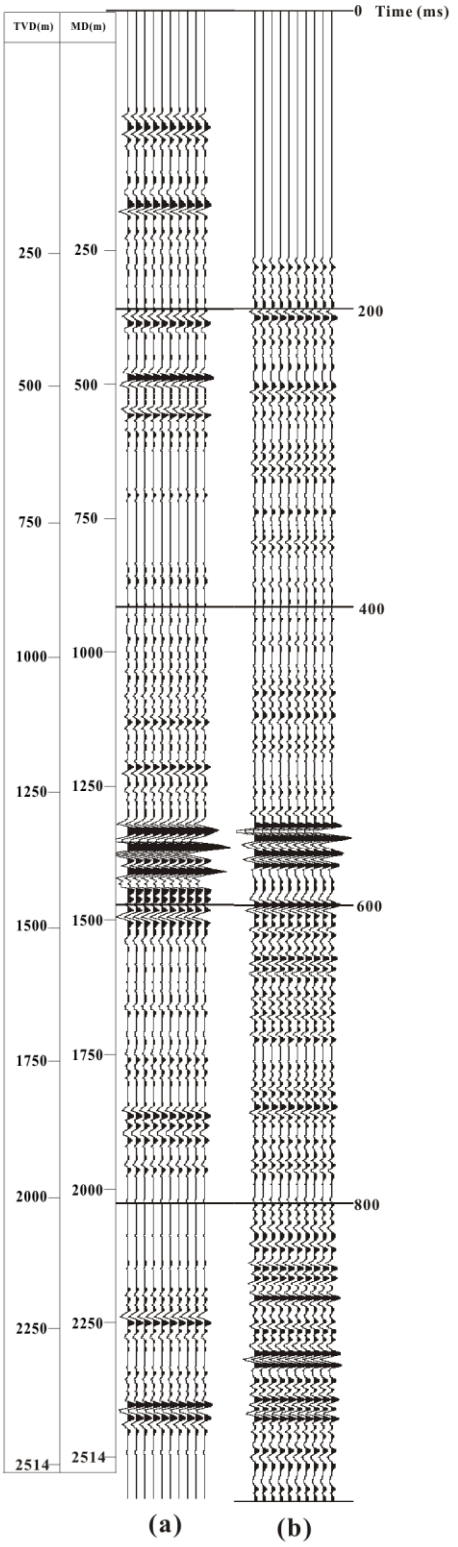

Figure 4.7 Comparison of synthetic seimogram (a) and VSP corridor stack (b).

the frequency band, and the wavelets.

The results were converted from time to depth according the time to depth relationships calculated from the first breaking time. But it is a measured depth (MD) which differs slightly with the true depth (TVD) due to the fact that the deep drill hole slightly drifts towards W and NW by 250 m at the furthest deviation. The biggest difference between them is 18.19 m.

Strong reflectors can also be observed from the reflection seismic profile and VSP results (Fig. 4.4 (a)). Original 2 m increment was employed aimed at high resolution acquisition. And strong and distinct reflectors are exhibited from all of the three stack results from 1300 m to 1500 m at the Outokumpu-type assemblage section. By the comparison, the stack profile with 2 m depth increment shows more details than the other two stack profiles. And the three different corridor stacks have somewhat different character in terms of the apparent waveforms observed. This may be partly due to spatial aliasing effects in the larger receiver spacing.

VSP can provide more convincing evidence that the Outokumpu-type assemblage are sufficiently strong to be detected because VSP survey has the same frequency band with surface seismic surveys. Thus, the high resolution VSP result was compared with surface seismic results for the purpose of seismic event correlation.

On the final stack profile of line_2000 (Fig. 4.2 (a)), the dominant reflectors revealed

around 500 ms are apparently subhorizontal with a possible gentle dip to NE direction, and can be followed from CMP 111 to CMP 915. Before CMP 111 and after CMP 915, the profile has a low signal-to-noise ratio because of the low fold coverage on the edges of the survey line. Besides that, the main Outokumpu-type assemblage reflector package from CMP 620 to CMP 700 appears complex and thick. The reason is considered to be related to the crookedness of the survey line which led to some of CMP points excluded from the final image because they could not be included in a CMP bin. The Outokumpu deep drill hole is located at about 10 m away from the first CMP position of the line_2000. However since no effective reflector is exhibited before CMP 111, it is impossible to make an absolutely definitive correlation between them. The distance between the well and CMP 111 is 226 m far. On the other hand, this roughly 200 m offset is still relatively close and one would expect it to be representative of the character expected in line_2000.

In order to achieve the comparison between surface seismic results and VSP corridor stack, the datum of the VSP stack was corrected from 100 m to 12 m which is the same datum as the surface seismic results.

The corridor stack VSP result is compared to seismic line_2000 in Fig. 4.8 with the stack result placed near the CMP 111 on line_2000. The timing of 480 ms near CMP 111 between the top of strong reflector package in line_2000 agrees well the initial arrivals of the seismic reflections from the top of the Outokumpu-type assemblage at 485 ms in the corridor VSP stack. Thus, the strong reflection package in line_2000 can be interpreted

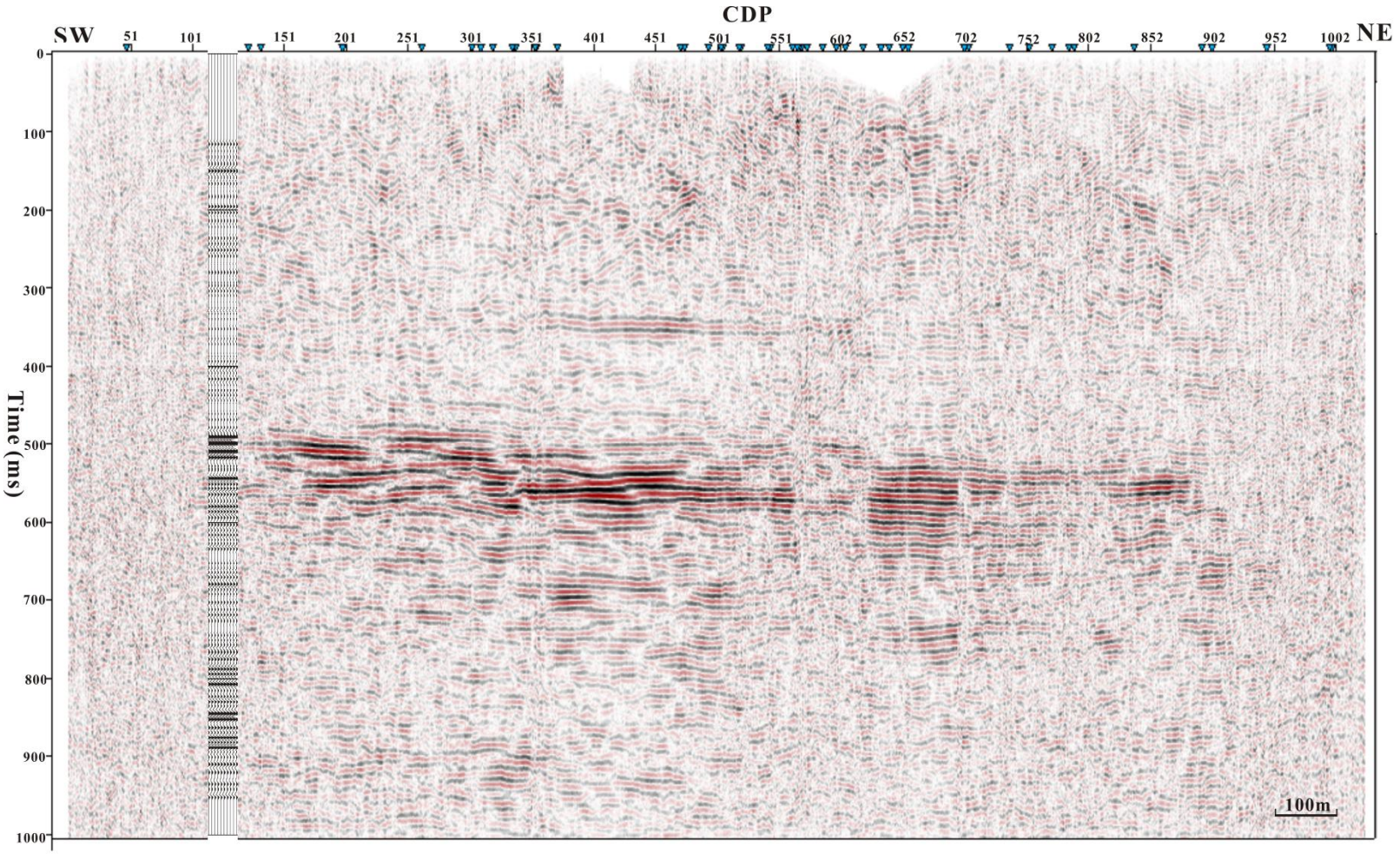

Figure 4.8 Comparison of seismic stack result of line_2000 and VSP result

to be the Outokumpu-type assemblage rocks. However, this reflection package in line_2000 is apparently thicker than one would expect on the basis of the VSP stack. The time thickness of this reflector package can reach a two-way-time of 120 ms which correlates to 330 m thickness assuming an average velocity of 5500 m/s through the assemblage. This contrasts with the 201 m thickness of the Outokumpu-type assemblage observed from core and geophysical logs that corresponds to the approximately 65 ms apparent thickness in the VSP stack.

Before attempting to resolve this possible discrepancy in the apparent thicknesses, it is worthwhile to first review the character of the reflector package in the nearly perpendicular NW-SE running line_3000. The Outokumpu-type assemblage package reflectors are clearly recognized around 500 ms with a gentle dip to the SE (Fig. 4.9). As already mentioned, the 'strength' of the reflector in this line is not as strong and it appears less continuous likely due to the lower fold coverage and hence lower signal to noise. The OKU-1 deep drill hole is immediately west of this profile with its closest point at CMP 386 being only a distance of 73.8 m away. From the correlation (Fig. 4.9 and Fig. 4.10), line_3000 agrees well with the VSP at the Outokumpu-type assemblage zone. However, unlike line_2000, the facevalue time thickness (70 ms) of the reflector package is generally much thinner and, indeed, would appear to be produced by a consistent and nearly flat reflecting event.

To summarize the above last few paragraphs, the seismic character of the Outokumpu

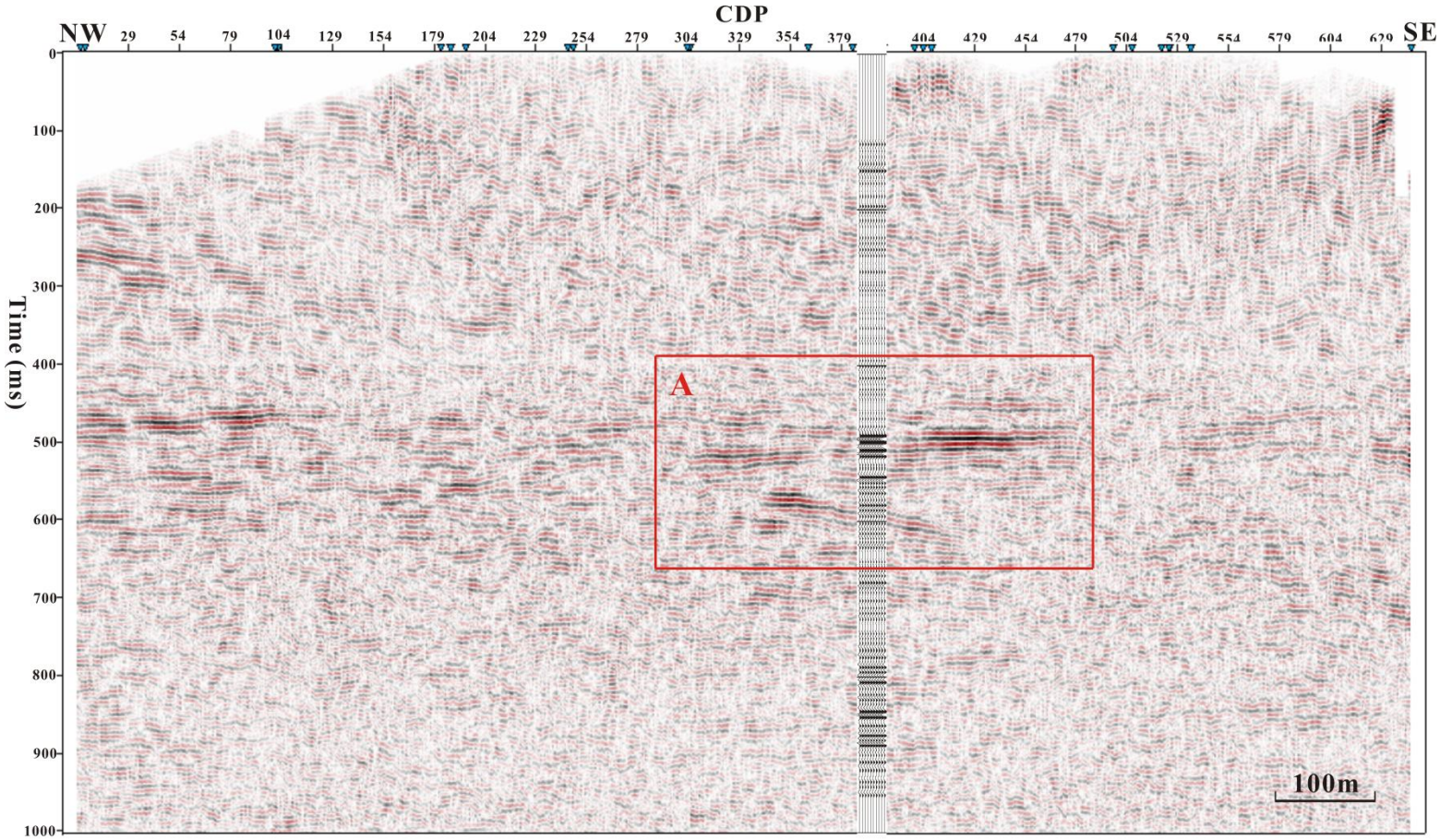

Figure 4.9 Comparison of seismic stack result of line_3000 and VSP result.
In order to reveal details, the comparison in region A is expanded and shown on Figure 4.10

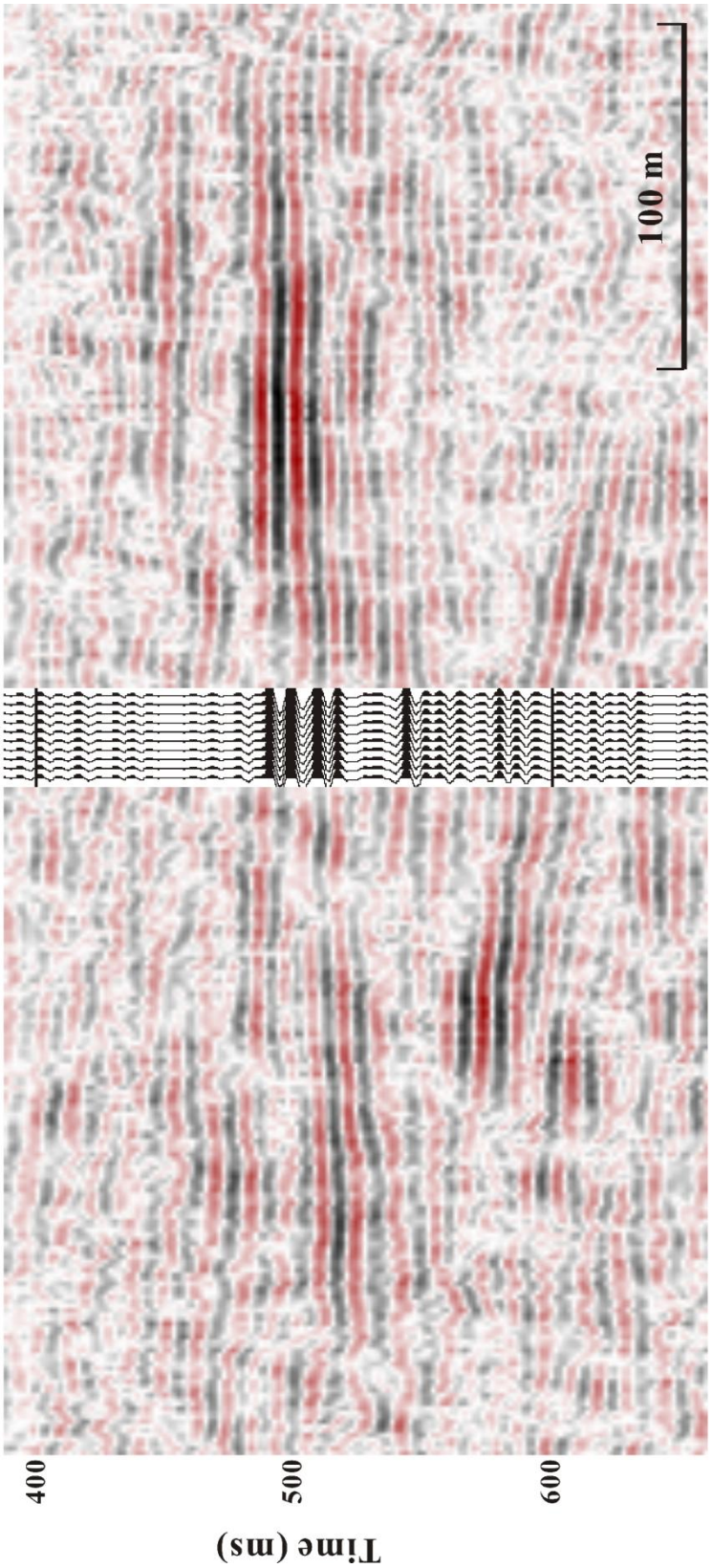

Figure 4.10 An expanded portion of the region A from the Figure 4.9

assemblage in line_3000 agrees well with the ground-truthing of the VSP corridor stack. In contrast, the same reflector package in line_2000 is at face value much thicker. The reasons for this difference are not entirely clear but could include:

- The CMP trend of line_3000 is relatively straighter and this allowed for correspondingly spatially thinner and more densely concentrated CMP bins (Fig. 2.13). In contrast, line_2000 was much more crooked resulting in much wider CMP bins. However, there is no rule that states that the earth's true geological structure must conform to our artificial CMP bin strategy; and the larger the bin the greater will be the variation in the structure over that bin. Hence, the apparent thicker Outokumpu assemblage in line_2000 may be in reality indicative of the variations in the reflected (scattered) waves over a larger area. This might result, for example, from variations in structural dip or actual discrete changes in the topography of the top of the 3D real-world Outokumpu assemblage; the reflected waves from different regions of a given bin would be expected to arrive at different times thus making the entire reflection package apparently thicker. Correspondingly, the Outokumpu assemblage reflections in line_3000 originate from the stacking of CMP points over a smaller area and there is less opportunity for the arrival times to differ.

- Again, nature places little restrictions on what the 3D shape of the Outokumpu assemblage actually is, and given its likely ophiolitic origins it probably

underwent substantial deformation on emplacement that only would have been intensified by later metamorphism. As such, the variations in the reflector package could be reflective of the actual geological variations of the Outokumpu assemblage.

- According to Schijns et al, (2011) measurements in the OKU-1 well, the otherwise uniform schists overlying the Outokumpu assemblage are seismically anisotropic. This anisotropy is also somewhat complex as the symmetry axes are rotated with respect to the vertical and horizontal. However, a conventional analysis that assumes the rock mass is seismically isotropic was employed in developing the stacking velocity $V_{RMS}(t_o)$ functions. Further, an isotropic Kirchhoff migration algorithm was used to make the final corrections to the data. Hence, ignoring the true seismic velocity anisotropy can only result in some error in the seismic image.

It is in reality likely that a combination of these three factors contributes to the differences in the seismic character. However, we believe that most of this comes simply from geometrical effects due to the complex crooked line binning (the second rationalization) because: i) not including anisotropy will most certainly affect the positioning of the seismic events within the image but as long as the differences are consistent one should not expect this to be manifest as a thicker reflector package, and ii) the simplicity of the reflector as seen in both line_3000 and in the VSP would imply that the geology along

line_2000, or at least near its SE end, should also be simple. These discrepancies could only be resolved by first obtaining a proper 3D seismic survey over the area and, second, by additional drilling to sample the true lithologies.

4.4 Discussion

The Outokumpu-type assemblage is located from 1314 m to 1515 m deep according the coring information from the deep drill hole. Seismic reflection techniques were carried out in this area in order to map the structure of the Outokumpu-type assemblage in depth in 2006. According to the borehole logging, small differences in acoustic impedance were found, which makes imaging of the geology challenging. Moreover, the signal-to-noise ratio is usually very low due to the complex properties in hard rock area. As a result, high-frequency and high-fold 2D seismic acquisition techniques including two crooked seismic lines and VSP survey were applied aimed at high resolution data.

The 2D seismic survey is an effective technique to detect the geological structures that could potentially host mineral deposits. 2D seismic profiling is also relatively cheap and easy to implement. After processing, subsurface structure under the line is able to be delineated. However, with only 2D profiles it is difficult to follow the structure in three dimensions. Further, 2D migration is not completely valid for complex structures (Yilmaz, 2001). So the image from a 2D seismic survey might not represent a true geological structure. And it may become worse on a crooked 2D seismic line. Moreover,

reflections are poorly aligned in a CMP gather, which damages the image during stacking and migration as discussed above.

The reprocessing of the Outokumpu data considered the effects caused by crooked line. Special efforts were also made to preserve the high-frequency information and improve the resolution. But from the final results, the impact from irregular geometries still exists. Line_2000 has much apparently thicker Outokumpu-type assemblage than the corresponding VSP result. Line_3000 has less continuity in the entire line due to the low fold coverage but the Outokumpu assemblage there appears much thinner.

Additionally, VSP data are often used to find the depths at which seismic reflections originate and hence assist in the interpretation of surface reflection seismic profiles. Nevertheless, the deep drill hole is not in the middle of any seismic survey lines for the Outokumpu area although it is very close to line_3000. This inevitably brings some errors to the correlation between seismic surface results and VSP result. And another factor that should be considered is the deep drill hole is not perfectly vertical (Fig. 3.2). There is a difference between the measured depth (MD) and the true depth (TVD) in VSP data. The biggest difference is 18.19 m., which is 6 to 8 ms in a two-way time.

4.5 Conclusions

Hard rocks have more complex properties and structures than sedimentary rocks. The signal-noise ratio and continuity are usually very low, which makes the acquisition and

processing challenging. Based on the synthetic result (Fig. 4.6), Outokumpu-type assemblage can be detected by seismic exploration techniques.

P-wave velocities were derived from first-break VSP times, and the 2 m receiver gap allows a detailed determination of the seismic frequency velocity structure variation to be made. They match the smoothed sonic curves well (Fig. 4.5). The velocities increase with depth from 5000 m/s to 6000 m/s except for the lower velocity zone from 1300 m to 1500 m. The variation of velocities corresponds to the lithology.

Despite the effects caused by crooked lines and low signal to noise, the seismic profiles and the VSP were processed successfully. High resolution seismic results are obtained after processing. Strong reflectors can be observed from both the seismic profiles and the VSP. Comparing with the preliminary results obtained by Heinonen et al. (2011), signal-to-noise ratios are improved and finer details can be seen.

Since the geophones in a VSP survey are much closer to the subsurface layers, this VSP measurement is considered to be invaluable for structural, stratigraphic and lithological interpretations. After VSP data is combined with surface seismic data, the features on surface seismic data can be calibrated at the depths. And more reliable and improved seismic characteristics of the subsurface geology near the well can be provided.

From the interpretation of the seismic images, there is consistency between the 2D seismic and VSP results. The strong reflectors around 500 ms on seismic profiles are

associated with the Outokumpu massive sulphide deposits. The comparison of the VSP to line_2000 in particular suggests that the apparent thickness of the Outokumpu-type assemblage on that line is not real and likely results from the crooked geometry. The apparent thickness may be indicative of some cross-dip of the reflecting events or even more complex topography on the top surface of the Outokumpu assemblage. The VSP result also agrees qualitatively with the synthetic result. All in all, our seismic results not only provide a good correlation among 2D surface seismic profiles, the VSP result, and the logging records but also allow a reasonable estimation for the seismic character of the Outokumpu-type assemblage.

4.6 Future work

The seismic surface surveys executed in hard rock environment in Outokumpu, Finland, consist of two crooked 2D seismic lines. The special and complex physical properties of hard rock and the irregular geometry are attributed to the effect of imaging. Even though the final results have some improvements relative to earlier attempts, additional efforts are still warranted. First, different definitions of the survey line could be tested. A smaller bin grid might be able to alleviate the impact of the cross-dip. However the fold coverage would be reduced and a better balance is needed.

Second, the 2D crooked seismic surveys could actually be treated as a partial 3D survey. For a future work, a pseudo-3-D processing technique (Nedimovic and West, 2003a, Wu

et al., 1995) which considers the cross-dip of subsurface structure may remove the adverse effect introduced by irregular geometry during the CMP stacking as well as providing additional geological information. An alternate rebinning technique (Kashubin and Juhlin, 2010) could also reduce the adverse effect of any cross-dip.

Third, the amplitude stack method provided by Nedimovic and West (2003a) could improve the resolution before migration. Additionally, some prestack migration schemes (Nedimovic and West, 2003b, Schmelzbach *et al.*, 2008) might be able to construct a relatively true subsurface structure description.

Finally, we know that there is a substantial seismic anisotropy to the formation as measured by Schijns et al (2011). Such anisotropy is also problematic even in the simplest horizontally layered structures where it produces erroneous estimates of depths to reflectors. When the anisotropy is dipping as it appears to be at Outokumpu, the meaning of the CMP bin becomes even more difficult to define as the true reflection point no longer even lies beneath the midpoint in the earth. To our knowledge, such seismic anisotropy has never before been included in the analysis of seismic data from such hard rock areas and would be an important step forward.

Reference

Adam, E., Perron, G., Milkereit, B., Wu, J.J., Calvert, A.J., Salisbury, M., Verpaelst, P. & Dion, D.J., 2000. A review of high-resolution seismic profiling across the Sudbury, Selbaie, Noranda, and Matagami mining camps, *Canadian Journal of Earth Sciences,* 37**,** 503-516.

Ayarza, P., Juhlin, C., Brown, D., Beckholmen, M., Kimbell, G., Pechnig, R., Pevzner, L., Pevzner, R., Ayala, C., Bliznetsov, M., Glushkov, A. & Rybalka, A., 2000. Integrated geological and geophysical studies in the SG4 borehole area, Tagil Volcanic Arc, Middle Urals: Location of seismic reflectors and source of the reflectivity, *Journal of Geophysical Research-Solid Earth,* 105**,** 21333-21352.

Backus, G.E., 1962. Long-wave elastic anisotropy produced by horizontal layering, *Journal of Geophysical Research,* 67**,** 4427-4440.

Baeten, G. & Ziolkowski, A., 1990. *The vibroseis source*, Vol. 3, Elsevier Science Ltd.

Balch, A.H., 1982. The use of vertical seismic profiles in seismic investigations of the earth, *Geophysics,* 47**,** 906-918.

Balch, A.H. & Lee, M.W., 1984. *Vertical seismic profiling: technique, applications, and case histories*, International human resources development corporation, Boston.

Beaty, K., Schmitt, D. & Sacchi, M., 2002. Simulated annealing inversion of multimode Rayleigh wave dispersion curves for geological structure, *Geophysical Journal International,* 151**,** 622-631.

Bellefleur, G., Calvert, A.J. & Chouteau, M.C., 1998. Crustal geometry of the Abitibi Subprovince, in light of three-dimensional seismic reflector orientations, *Canadian Journal of Earth Sciences,* 35**,** 569-582.

Blatt, H., Tracy, R.J. & Owens, B.E., 1996. *Petrology: igneous, sedimentary, and metamorphic*, WH Freeman & Co.

Blias, E., 2007. VSP wavefield separation: Wave-by-wave optimization approach, *Geophysics,* 72**,** T47-T55.

Boyer, S. & Mari, J.-L., 1997. *Seismic surveying and well logging*, Institut francais du petrole.

Butler, K.E. & Russell, R.D., 1993. Subtraction of powerline harmonics from geophysical records, *Geophysics,* 58**,** 898-903.

Butler, K.E. & Russell, R.D., 2003. Cancellation of multiple harmonic noise series in geophysical records, *Geophysics*, 68**,** 1083-1090.

Carr, B.J., Smithson, S.B., Kareav, N., Ronin, A., Garipov, V., Kristofferson, Y., Digranes, P., Smythe, D. & Gillen, C., 1996. Vertical seismic profile results from the Kola Superdeep Borehole, Russia, *Tectonophysics,* 264**,** 295-307.

Cary, P.W. & Lorentz, G.A., 1993. Four-component surface-consistent deconvolution, *Geophysics,* 58**,** 383-392.

Cassell, B.R., 1984. Vertical seismic profiles-an introduction, *First Break,* 2**,** 9-19.

Chase, M., 1992. Random noise reduction by FXY prediction filtering, *Exploration Geophysics,* 23**,** 51-56.

Cosma, C., Heikkinen, P., Keskinen, J. & Enescu, N., 2001. VSP in crystalline rocks--from downhole velocity profiling to 3-D fracture mapping, *International Journal of Rock Mechanics and Mining Sciences,* 38**,** 843-850.

Costain, J.K. & Çoruh, C., 2004. *Basic theory of exploration seismology*, Vol. 1, Elsevier Science.

Dehghannejad, M., Juhlin, C., Malehmir, A., Skyttä, P. & Weihed, P., 2010. Reflection seismic imaging of the upper crust in the Kristineberg mining area, northern Sweden, *Journal of Applied Geophysics,* 71**,** 125-136.

Dix, C., 1939. INTERPRETATION OF WELL-SHOT DATA, *Geophysics,* 4**,** 24-32.

Dix, C.H., 1945. THE INTERPRETATION OF WELL SHOT DATA—II, *Geophysics,* 10**,** 160-170.

Du, J., Wang, S., Liu, G. & Liu, Y., 2009. VSP wavefield separation using local slopes attribute, *CHINESE JOURNAL OF GEOPHYSICS-CHINESE EDITION,* 52 (7)**,** 1867-1872.

Eaton, D.W., Adam, E., Milkereit, B., Salisbury, M., Roberts, B., White, D. & Wright, J., 2010. Enhancing base-metal exploration with seismic imaging, *Canadian Journal of Earth Sciences,* 47**,** 741-760.

Eaton, D.W.S. & Wu, J., 1996. Relative-amplitude preserving processing for crustal seismic reflection data: an example from western Canada, *Tectonophysics,* 264**,** 357-370.

Elbra, T., Karlqvist, R., Lassila, I., Haeggström, E. & Pesonen, L.J., 2011. Laboratory

measurements of the seismic velocities and other petrophysical properties of the Outokumpu deep drill core samples, eastern Finland, *Geophysical Journal International,* 184**,** 405-415.

Ellis, D.V. & Singer, J.M., 2007. *Well logging for earth scientists*, Springer Verlag.

Gaal, G., Koistinen, T.J. & Mattila, E., 1971. Tectonics and Startigraphy of the vicinity of Outokumpu, North Karelia, Finland., pp. 67.

Gal'perin, E.I., 1974. *Vertical seismic profiling*, Vol. 12, pp. 270, Society of Exploration Geophysicists Special Publication, Tulsa.

Ganchin, Y.V., Smithson, S.B., Morozov, I.B., Smythe, D.K., Garipov, V.Z., Karaev, N.A. & Kristofferson, Y., 1998. Seismic studies around the Kola Superdeep Borehole, Russia, *Tectonophysics,* 288**,** 1-16.

Gu, Y., 2010. *Arrays and array methods in global seismology*, Springer, New York.

Hallenburg, J., 1984. Geophysical Logging for Mineral and Engineering Applications. Tulsa, OklahomaPennWell Books, PennWell Publishing.

Hardage, B.a., 1981. An examination of tube wave noise in vertical seismic profiling data, *Geophysics,* 46**,** 892-903.

Hardage, B.A., 2000. *Vertical seismic profiling: Principles*, Third edn, Vol. 14, pp. 552, Elsevier Science Publications Co., Inc.

Harjes, H.P., Bram, K., Durbaum, H.J., Gebrande, H., Hirschmann, G., Janik, M., Klockner, M., Luschen, E., Rabbel, W., Simon, M., Thomas, R., Tormann, J. & Wenzel, F., 1997. Origin and nature of crustal reflections: Results from

integrated seismic measurements at the KTB superdeep drilling site, *Journal of Geophysical Research-Solid Earth,* 102**,** 18267-18288.

Heinonen, S., Kukkonen, I.T., Heikkinen, P.J. & Schmitt, D.R., 2011. High Resolution Reflection Seismics Integrated With Deep Drill Hole Data in Outokumpu , Finland. *in Geological Survey of Finland, Special Paper 51,*, pp. 105-118.

Hinds, R.C., Anderson, N.L. & Kuzmiski, R.D., 1996. *VSP interpretive processing: theory and practice*, Society of Expolaration Geophysicists.

Huang, C. & Hunter, J., 1984. The tube-wave method of estimating in-situ rock fracture permeability in fluid-filled boreholes, *Geoexploration,* 22**,** 245-259.

Jolly, R.N., 1953. Deep-hole geophone study in Garvin County, Oklahoma, *Geophysics,* 18**,** 662-670.

Kashubin, A.S. & Juhlin, C., 2010. Mapping of crustal scale tectonic boundaries in the Ossa-Morena Zone using reprocessed IBERSEIS reflection seismic data, *Tectonophysics,* 489**,** 139-158.

Kearey, P. & Brooks, M., 1984. *An introduction to geophysical exploration*, Blackwell scientific publications.

Kennett, P., Ireson, R. & Conn, P., 1980. Vertical Seismic Profiles: Their Applications in Exploration GEOPHYSICS•, *Geophysical Prospecting,* 28**,** 676-699.

Kern, H., Mengel, K., Strauss, K., Ivankina, T., Nikitin, A. & Kukkonen, I., 2009. Elastic wave velocities, chemistry and modal mineralogy of crustal rocks sampled by the Outokumpu Scientific Drill Hole: evidence from lab measurements and modeling,

Physics of the Earth and Planetary Interiors, 175**,** 151-166.

Kern, H., Popp, T., Gorbatsevich, F., Zharikov, A., Lobanov, K. & Smirnov, Y.P., 2001. Pressure and temperature dependence of Vp and Vs in rocks from the superdeep well and from surface analogues at Kola and the nature of velocity anisotropy, *Tectonophysics*, 338**,** 113-134.

Klein, C. & Hurlbut Jr, C., 1985. Manual of mineralogy , 596 pWiley, New York.

Koistinen, T., 1981. Structural evolution of an early Proterozoic strata-bound Cu-Co-Zon deposit, Outokumpu, Finland. *in Transactions of the Royal Society of Edinburgh,Earth Sciences 72*, pp. 115-158.

Kommedal, J. & Tjøstheim, B., 1989. a Study of Different Methods of Wavefield Separation for Application to Vsp DATA1, *Geophysical Prospecting*, 37**,** 117-142.

Kontinen, A. & Peltonen, P., 2002. Geomex; Modelling of the Outokumpu type semimassive sulphide deposits. A summary of the results and conclusions of the modelling subproject. *in Unpublished report*, Geological Survey of Finland.

Kontinen, A. & Peltonen, P., 2003. Description and genetic modelling of the Outokumpu type rock assemblage and sulphide ores - a GEOMEX subproject. *in GEOMEX/Preliminary Technical Report*, Geological Survey of Finland.

Kukkonen, I., Heikkinen, P., Ekdahl, E., Hjelt, S., Yliniemi, J. & Jalkanen, E., 2006. Acquisition and geophysical characteristics of reflection seismic data on FIRE transects, Fennoscandian Shield, *geological Survey of Finland*, Special Paper**,**

13–43.

Kukkonen, I.T., 2004. Outokumpu Deep Drilling Project, International Workshop, October 25-26, 2004, Espoo, Finland. Programme and Extended Abstracts. Geological Survey of Finland, Espoo Unit, Geophysical Research, Report Q10.2/2004/1, pp. 49.

Kukkonen, I.T., 2007. Outokumpu Deep Drilling Project, Second International Workshop, May 21-22, 2007, Espoo, Finland. Programme and Extended Abstracts. Geological Survey of Finland, Southern Finland Office, Marine Geology and Geophysics, Report Q10.2/2007/29, pp. 87.

L'Heureux, E., Milkereit, B. & Adam, E., 2005. 3D Seismic Exploration for Mineral Deposits in Hardrock Environments, *cseg.ca***,** 36-39.

Lay, T. & Wallace, T.C., 1995. *Modern global seismology*, Vol. 58, Academic Pr.

Le Maitre, R.W., Bateman, P., Dubek, A., Keller, J., Lameyre, J., Le Bas, M., Sabine, P., Schimid, R. & Sorensen, H., 2002. *A classification of igneous rocks and glossary of terms, recommendations of the International Union of Geological Sciences, Subcommission on the Systematics of Igneous Rocks*, Oxford.

Lee, M.W. & Balch, A.H., 1983. Computer processing of vertical seismic profile data, *Geophysics*, 48**,** 272-287.

Levin, F.K. & Lynn, R.D., 1958. Deep-hole geophone studies, *Geophysics*, 23**,** 639-664.

Lindseth, R.O., 1982. *Digital processing of geophysical data: a review*, SEG Books.

Lowrie, W., 2007. *Fundamentals of Geophysics*, Second edn, Cambridge University

Press.

Lu, Z.W., Gao, R., Kuang, C.Y., Liu, J.K., Hou, H.S., Feng, S.Y. & Wang, H.Y., 2010. Research on deep seismic reflection profile in Luzong ore concentration area: An economical and changeable gathering test, *Acta Petrologica Sinica,* 26**,** 2553-2560.

Luschen, E., Bram, K., Sollner, W. & Sobolev, S., 1996. Nature of seismic reflections and velocities from VSP-experiments and borehole measurements at the KTB deep drilling site in southeast Germany, *Tectonophysics,* 264**,** 309-326.

Main, I.G., 1993. *Vibrations and waves in physics*, Cambridge University Press.

Malehmir, A. & Bellefleur, G., 2009. 3D seismic reflection imaging of volcanic-hosted massive sulfide deposits: Insights from reprocessing Halfmile Lake data, New Brunswick, Canada, *Geophysics,* 74**,** B209-B219.

Mari, J.L. & Coppens, F., 1991. *Seismic well surveying*, Editions Technip.

Miao, X., Moon, W.M., Milkereit, B. & Mwenifumbo, C.J., 1994. 3 Component Vertical Seismic Profiling (Vsp) Experiment in the Sudbury Basin, *Geophysical Research Letters,* 21**,** 939-942.

Miao, X.G., Moon, W.M. & Milkereit, B., 1995. A Multioffset, 3-Component Vsp Study in the Sudbury Basin, *Geophysics,* 60**,** 341-353.

Milkereit, B., Berrer, E.K., King, A.R., Watts, A.H., Roberts, B., Adam, E., Eaton, D.W. & Wu, J.J., 2000. Development of 3-D seismic exploration technology for deep nickel-copper deposits - A case history from the Sudbury basin, Canada,

Geophysics, 65**,** 1890-1899.

Milkereit, B. & Green, A., 1992. Deep geometry of the Sudbury structure from seismic reflection profiling, *Geology,* 20**,** 807-811.

Milkereit, B., White, D.J. & Green, A.G., 1994. Towards an improved seismic imaging technique for crustal structures: The Lithoprobe Sudbury experiment, *Geophysical Research Letters,* 21**,** 927-930.

Moon, W., Carswell, A., Tang, R. & Dilliston, C., 1986. Radon transform wave field separation for vertical seismic profiling data, *Geophysics,* 51**,** 940-947.

Nedimovic, M.R., 2000. Seismic reflection imaging in crystalline terrains, Doctor of Philosophy, Geophysics Laboratory, Department of Physics, University of Toronto.

Nedimovic, M.R. & West, G.F., 2003a. Crooked-line 2D seismic reflection imaging in crystalline terrains: Part 1, data processing, *Geophysics,* 68**,** 274-285.

Nedimovic, M.R. & West, G.F., 2003b. Crooked-line 2D seismic reflection imaging in crystalline terrains: Part 2, migration, *Geophysics*, 68**,** 286-296.

Nelson, H.R., 1983. *New technologies in exploration geophysics*, Gulf publishing company.

Newman, P., 1973. Divergence Effects in a Layered Earth, *Geophysics,* 38**,** 481-488.

Olhoeft, G. & Johnson, G., 1989. Densities of rocks and minerals: in Carmichael, RS, ed., Practical handbook of physical properties of rocks and minerals, Boca Raton, Florida, CRC Press.

Oristaglio, M.L., 1985. A guide to current uses of vertical seismic profiles, *Geophysics,* 50**,** 2473-2479.

Park, A., 1988. Nature of the early proterozoic Outokumpu assemblage, Eastern Finland, *Precambrian Research,* 38**,** 131-146.

Prensky, S.E., 1999. Advances in borehole imaging technology and applications, *Geological Society, London, Special Publications,* 159**,** 1-43.

Rabbel, W., Beilecke, T., Bohlen, T., Fischer, D., Frank, A., Hasenclever, J., Borm, G., Kuck, J., Bram, K., Druivenga, G., Luschen, E., Gebrande, H., Pujol, J. & Smithson, S., 2004. Superdeep vertical seismic profiling at the KTB deep drill hole (Germany): Seismic close-up view of a major thrust zone down to 8.5 km depth, *Journal of Geophysical Research-Solid Earth,* 109.

Riggs, E.D., 1955. Seismic wave types in a borehole, *Geophysics,* 20**,** 53-67.

Rio, P., Mukerji, T., Mavko, G. & Marion, D., 1996. Velocity dispersion and upscaling in a laboratory-simulated VSP, *Geophysics,* 61**,** 584-593.

Ronen, J. & Claerbout, J.F., 1985. Surface-consistent residual statics estimation by stack-power maximization, *Geophysics,* 50**,** 2759-2767.

Ruotoistenmaki, T. & Tervo, T., 2006. Geophysical characteristics of Outokumpu area, SE Finland, Report of Investigation 162. *in GEOMEX Final Report,* Geological Survey of Finland.

Salisbury, M., Milkereit, B., Ascough, G., Adair, R., Schmitt, D. & Matthews, L., 2000. Physical properties and seismic imaging of massive sulphides, *Geophysics,* 65**,**

1882-1889.

Salisbury, M. & Snyder, D., 2007. Application of Seismic Methods to Mineral Exploration, *Mineral deposits of Canada: a synthesis of major deposit-types, district metallogeny, the evolution of geological provinces, and exploration methods. Edited by W. Goodfellow. Mineral Deposits Division, Geological Association of Canada, Special Publication,* 5**,** 971-982.

Salisbury, M.H., Milkereit, B. & Bleeker, W., 1996. Seismic imaging of massive sulfide deposits; Part I, Rock properties, *Economic Geology,* 91**,** 821-828.

Santti, J., Kontinen, A., Sorjonen-Ward, P., Johanson, B. & Pakkanen, L., 2006. Metamorphism and Chromite in Serpentinized and Carbonate-Silica–Altered Peridotites of the Paleoproterozoic Outokumpu-Jormua Ophiolite Belt, Eastern Finland, *International Geology Review,* 48**,** 494-546.

Scheuer, T. & Oldenburg, D.W., 1988. Aspects of time-variant filtering, *Geophysics*, 53**,** 1399–1409.

Schijns, H., Heinonen, S., Schmitt, D.R., Heikkinen, P. & Kukkonen, I.T., 2009. Seismic refraction traveltime inversion for static corrections in a glaciated shield rock environment: a case study, *Geophysical Prospecting,* 57**,** 997-1008.

Schijns, H., Schmitt, D., Heikkinen, P. & Kukkonen, I., 2011. Seismic Anisotropy Observations in the Crystalline Upper Crust: Observations and Modeling from the Outokumpu Scientific Borehole, Finland, *Geophysical Journal International, in press.*

Schmelzbach, C., Horstmeyer, H. & Juhlin, C., 2007. Shallow 3D seismic-reflection imaging of fracture zones in crystalline rock, *Geophysics*, 72**,** B149-B160.

Schmelzbach, C., Simancas, J.F., Juhlin, C. & Carbonell, R., 2008. Seismic reflection imaging over the south Portuguese zone fold-and-thrust belt, SW Iberia, *Journal of Geophysical Research-Solid Earth*, 113.

Schmitt, D., Milkereit, B., Karp, T., Scholz, C., Danuor, S., Meillieux, D. & Welz, M., 2007. In situ seismic measurements in borehole LB-08A in the Bosumtwi impact structure, Ghana: Preliminary interpretation, *Meteoritics & Planetary Science*, 42**,** 755-768.

Schmitt, D., Mwenifumbo, C., Pflug, K. & Meglis, I., 2003. Geophysical Logging for Elastic Properties in Hard Rock: A Tutorial, *Hardrock seismic exploration. Edited by DW Eaton, B. Milkereit, and MH Salisbury. Society of Exploration Geophysicists, Tulsa, Okla***,** 20–42.

Schön, J., 1996. *Physical Properties of Rocks: Fundamentals and Principles of Petrophysics, Volume 18*, Pergamon Press.

Sheriff, R.E., 1989. *Geopgysical methods*, pp. 605, Prentice hall, New Jersey.

Sheriff, R.E. & Geldart, L.P., 1982. *Exploration seismology volume 2: Data-processing and interpretation*, Cambridge university press.

Smithson, S.B., Wenzel, F., Ganchin, Y.V. & Morozov, I.B., 2000. Seismic results at Kola and KTB deep scientific boreholes: velocities, reflections, fluids, and crustal composition, *Tectonophysics*, 329**,** 301-317.

Sorjonen-Ward, P., 1997. An overview of the geological and tectonic evolution of eastern Finland. In: Loukola-Ruskeeniemi, K. & Sorjonen-Ward, P. (eds.) Research and exploration - where do they meet? 4th Biennial SGA Meeting, August 11-13, 1997, Turku, Finland. Excursion guidebook A4: ore deposits in eastern Finland., *Geologian tutkimuskeskus,* Opas 42**,** 11-22.

Stein, S. & Wysession, M., 2003. *An introduction to seismology, earthquakes, and earth structure*, Wiley-Blackwell.

Stewart, R.R., 1984. Vsp Interval Velocities From Traveltime Inversion*, *Geophysical Prospecting,* 32**,** 608-628.

Stewart, R.R., 1985. Median filtering: Review and a new f/k analogue design, *Can. Soc. Expl. Geophys,* 21**,** 54-63.

Stewart, R.R. & Disiena, J.P., 1989. The values of VSP in interpretation, *The Leading Edge,* 8**,** 16-23.

Sun, C., Rabinowitz, P.D. & Griswold, N.C., 1997. Application of the recursive-approaching signal filter (RASF) to VSP data processing, *Geophysics,* 62**,** 1059-1068.

Suprajitno, M. & Greenhalgh, S., 1985. Separation of upgoing and downgoing waves in vertical seismic profiling by contour-slice filtering, *Geophysics,* 50**,** 950–962.

Taner, M.T. & Koehler, F., 1969. VELOCITY SPECTRA—DIGITAL COMPUTER DERIVATION APPLICATIONS OF VELOCITY FUNCTIONS, *Geophysics,* 34**,** 859-881.

Taner, M.T. & Koehler, F., 1981. Surface consistent corrections, *Geophysics,* 46**,** 17-22.

Wang, D.Y. & McCowan, D.W., 1989. Spherical divergence correction for seismic reflection data using slant stacks, *Geophysics,* 54**,** 563-569.

White, D., Boerner, D., Wu, J.J., Lucas, S., Berrer, E., Hannila, J. & Somerville, R., 2000. Mineral exploration in the Thompson nickel belt, Manitoba, Canada, using seismic and controlled-source EM methods, *Geophysics,* 65**,** 1871-1881.

White, D.J., Milkereit, B., Wu, J.J., Salisbury, M.H., Mwenifumbo, J., Berrer, E.K., Moon, W. & Lodha, G., 1994. Seismic Reflectivity of the Sudbury Structure North Range from Borehole Logs, *Geophysical Research Letters,* 21**,** 935-938.

White, J.E. & Tongtaow, C., 1981. Cylindrical waves in transversely istropic media, *J. Acoust. Soc. Am.,* 70**,** 1147-1155.

Widess, M., 1973. How thin is a thin bed?, *Geophysics,* 38**,** 1176-1180.

Willenberg, H., Evans, K.F., Eberhardt, E., Spillmann, T. & Loew, S., 2008. Internal structure and deformation of an unstable crystalline rock mass above Randa (Switzerland): Part II--Three-dimensional deformation patterns, *Engineering Geology,* 101**,** 15-32.

Wu, J., 1996. Potential pitfalls of crooked-line seismic reflection surveys, *Geophysics,* 61**,** 277-281.

Wu, J., Milkereit, B. & Boerner, D.E., 1995. Seismic imaging of the enigmatic Sudbury structure, *Journal of Geophysical Research,* 100**,** 4117-4130.

Wu, R.S., 1989. 1166-1187 Encyclopedia of Geophysics. *in Seismic wave scattering,* ed

James, D. Van Nostrand Reinhold and Comp.

Yilmaz, O., 2001. *Seismic data analysis: processing, inversion, and interpretation of seismic data*, Society of Exploration Geophysicists Tulsa.

Zimmerman, L.J. & Chen, S.T., 1993. Comparison of vertical seismic profiling techniques, *Geophysics*, 58**,** 134-140.

Appendix

Seismic vibrators are sources that generate seismic waves by a servo-controlled hydraulic vibrator, an electrodynamic vibrator, or a magnetic levitation vibrator (Fig. A.1). This 'vibroseis' technique was developed by the Continental Oil Company (Conoco) during the 1950s, and has become an important and commonly used method for seismic data exploration world-wide. Vibroseis overcomes some defects with impulsive seismic sources like dynamite and weight-drop, which are destructive, and introduce unpredictable nonlinear effects in the vicinity of the source (Lindseth, 1982, Baeten and Ziolkowski, 1990) . But it generates less energy at higher frequencies than dynamite and suffers more serious static problems and surface wave interference by the reason of a surface source.

The energy generated by vibrator propagates into the earth in the form of a sweep of varying frequency for several seconds (Fig. A.2). The sweep is usually 7-8 s long. The sweep is commonly given by (Baeten and Ziolkowski, 1990)

$$q(t) = a(t)\sin[2\pi(f_0 + \frac{1}{2}\frac{f_1 - f_0}{T}t)t] \quad \text{.....(A-1)}$$

where f_0 is the starting frequency of the sweep, f_1 is the end frequency and T is the sweep duration. $a(t)$ is a taper function which is usually chosen to be a linear or cosine roll-off taper to reduce truncation effects (Gibbs phenomena) that produce sidelobes and a longer duration wavelet.

Figure A.1 An example of a seismic vibrator.

And the instantaneous frequency is given by

$$f^{inst}(t) = f_0 + \frac{f_1 - f_0}{T} t \quad \text{.....(A-2)}$$

If sweep frequency f_0 is smaller than the frequency f_1, the sweep is called upsweep; if f_0 is larger than f_1, it is called a downsweep.

The recorded data in this way must be correlated with the sweep in order to collapse the extended source signal to an impulse (Fig. A.3). Figure A.3 shows how the vibroseis works. Trace 7 (blue) is the vibroseis source sweep. Trace 6 (pink) is an earth reflection impulse response from three interfaces. Trace 3, 4, and 5 (black) are the reflection responses. And trace 2 (green) is the recorded uncorrelated seismogram. Then the uncorrelated seismogram is cross-correlated with the sweep to collapse the sweeps into wavelets and also reduce the length of the seismogram. The correlated seismogram is showed in trace 1 (pink).

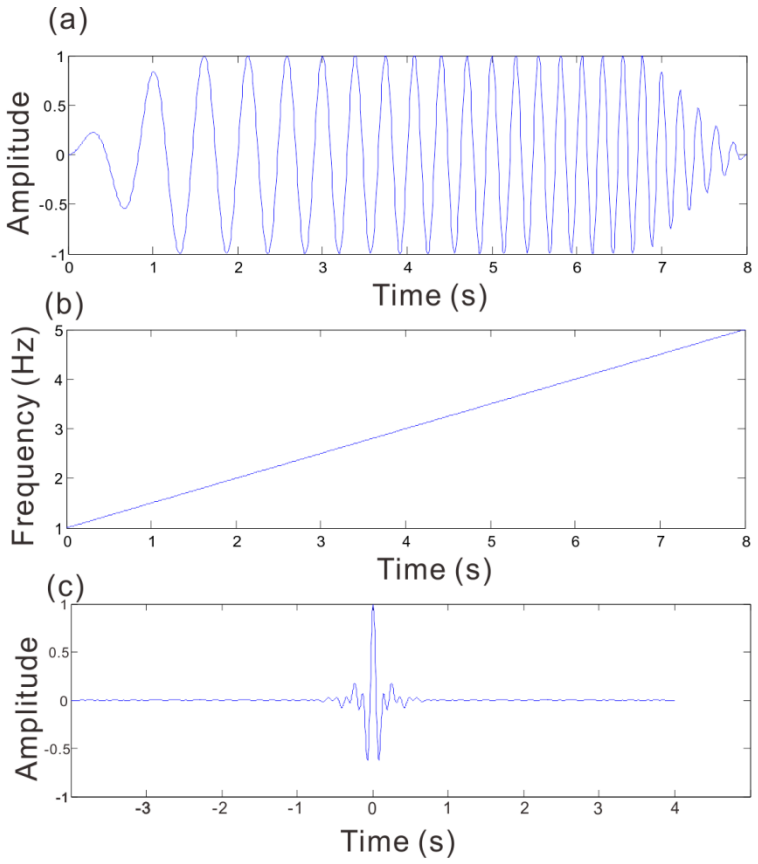

Figure A.2 (a) An 8 s sweep in the time domain; the frequency range for this figure is 1-5 Hz for display purpose, (b) the instantaneous frequency of the sweep as a function of time, (c) the autocorrelation of the sweep.

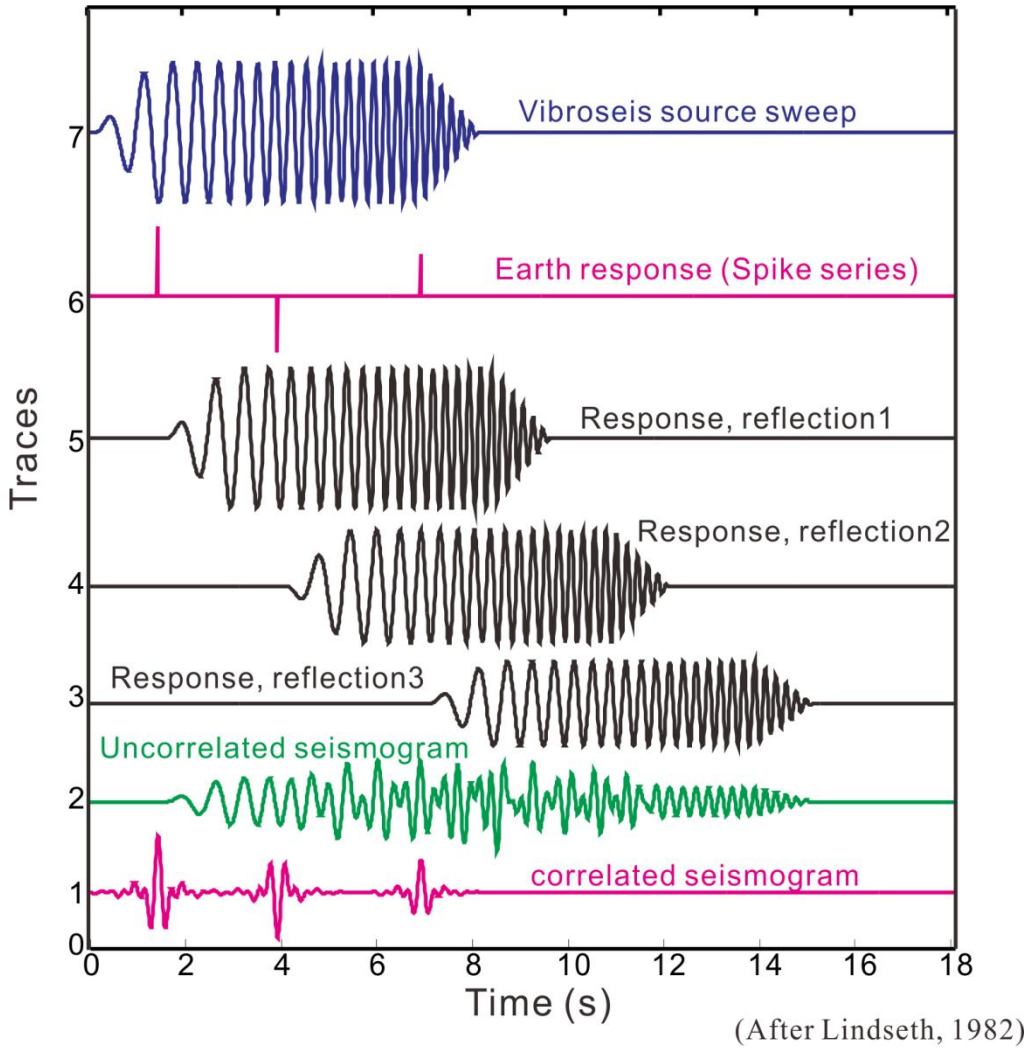

Figure A.3 Vibroseis source sweep, response and correlation